Radiation Damage and Helium Diffusion in Mineral Chronometers

by

Alyssa J. Anderson

A Dissertation Presented in Partial Fulfillment
of the Requirements for the Degree
Doctor of Philosophy

Approved May 2019 by the
Graduate Supervisory Committee:

Kip Hodges, Chair
Matthijs van Soest
Sang-Heon Shim
Tom Sharp
Christy Till

ARIZONA STATE UNIVERSITY

August 2019

ABSTRACT

A mineral's helium content reflects a balance between two competing processes: accumulation by radioactive decay and temperature-dependent diffusive loss. (U-Th)/He dating of zircon and other uranium and thorium-bearing minerals provides insight into the temperature histories of rocks at or near Earth's surface that informs geoscientists' understanding of tectonic and climate-driven exhumation, magmatic activity, and other thermal events. The crystal structure and chemistry of minerals affect helium diffusion kinetics, recorded closure temperatures, and interpretations of (U-Th)/He datasets. I used empirical and experimental methods to investigate helium systematics in two minerals chronometers: zircon and xenotime.

The same radioactivity that makes zircon a valuable chronometer damages its crystal structure over time and changes zircon helium kinetics. I used a zircon, titanite, and apatite (U-Th)/He dataset combined with previously published data and a new thermal model to place empirical constraints on the closure temperature for helium in a suite of variably damaged zircon crystals from the McClure Mountain syenite of Colorado. Results of this study suggest that the widely-used zircon damage accumulation and annealing model (ZRDAAM) does not accurately predict helium closure temperatures for a majority of the dated zircons. Detailed Raman maps of Proterozoic zircon crystals from the Lyon Mountain Granite of New York document complex radiation damage zoning. Models based on these results suggest that most ancient zircons are likely to exhibit intracrystalline variations in helium diffusivity due to radiation damage zoning, which may, in part, explain discrepancies between my empirical findings and ZRDAAM.

Zircon crystallography suggests that helium diffusion should be fastest along the crystallographic *c*-axis. I used laser depth profiling to show that diffusion is more strongly anisotropic than previously recognized. These findings imply that crystal morphology af-

fects the closure temperature for helium in crystalline zircon. Diffusivity and the magnitude of diffusive anisotropy decrease with low doses of radiation damage.

Xenotime would make a promising (U-Th)/He thermochronometer if its helium kinetics were better known. I performed classic step-wise degassing experiments to characterize helium diffusion in xenotime FPX-1. Results suggest that this xenotime sample is sensitive to exceptionally low temperatures ($\sim$50 °C) and produces consistent (U-Th)/He dates.

DEDICATION

In any event, wherever he might go, it was unknown territory, a white spot on the geologic map... a tiny piece in the vast, colorful mosaic of the world ... Who could tell, it might be that just at this one place some of the most essential threads of the earth's structural web were running together (Hans Cloos, 1947).

To Frank Mikan for teaching me that Earth and space are full of endless wonders. Your passion for science is contagious. I can never thank you enough.

ACKNOWLEDGMENTS

This dissertation represents five years of dedicated work that would not have been possible without the love and support of family, friends, and colleagues and an untold number of failed experiments. I would first like to thank my advisor Kip Hodges for offering me the opportunity to work on a project that combines my two great loves − minerals and geologic time − and for his guidance that allowed me to complete it. I would also like to give a heartfelt thanks to Matthijs van Soest for his years of mentorship in the lab and for the hours spent designing experiments and pondering results. Thijs, you made me the scientist that I am today.

I want to thank my other committee members − Christy Till, Tom Sharp, and Dan Shim − for their advice and encouragement along the way. I extend a big thank you to John Hanchar for all his words of wisdom. My visit to Newfoundland re-inspired me and helped to push me through my final two years.

Thank you Michelle Aigner for all your training, help, and many years of friendship. Thank you also to Chris McDonald for all the morning shifts on the SFT and the funny faces that kept my spirits bright. I am fortunate to have been part of a fantastic research group: Nate Borneman, Cameron Mercer, Mary Schultz, Alex Horne, Audrey Horne, Anna Brunner, Alex Pye, and Stephanie Sparks. I would not have survived this wild ride without you.

I am grateful to the SESE graduate student community who made Arizona my home. I'd like to give a special thanks to my incoming class of strong women scientists who saw me through the lows and helped me celebrated the highs: Aleisha Johnson, Nari Miller, Emilie Dunham, Kara Brugman, Meghan Guild, Jessica Noviello, Crystyl Fudge, and Margo Reiger in addition to those already named. Many thanks also go to Sean Peters, Hannah Shamloo, and Ronnie Pena who have been my family these past few years.

I would like to thank my fiancé Tyler McKanna for his love, fortitude, patience, and ceaseless optimism. This is the first chapter of many to come. I would like to thank my sister Addie and my grandma Kay for their love and support throughout my life. Lastly, I would like to thank my parents, Sudie and Brad, for truly everything. You taught me to reach for the stars and supported me every step of the way. I love you.

TABLE OF CONTENTS

LIST OF TABLES

LIST OF FIGURES

Chapter 1

INTRODUCTION

The break-down, or decay, of many radioactive isotopes in minerals occurs at a slow, predictable rate. In the early 1900s scientists first recognized the exciting potential of using radioactivity in minerals to measure geologic time (Holmes, 1913). Today, the earth science community depends on radiometric dating of mineral chronometers to understand the timing and tempo of the geological and biological processes that have shaped Earth throughout its 4.5 billion year history (Condon and Schmitz, 2013).

Different mineral chronometers record different types of geologic events. Some date the crystallization or formation age of a rock (the study of geochronology), while others offer insight into a rock's thermal history (the study of thermochronology) (e.g. Faure and Mensing, 2005; Hodges, 2014; Reiners et al., 2017). Whether a chronometer qualifies as either a geochronometer or a thermochronometer depends on how the radioactive parent and the radiogenic daughter isotopes behave within that mineral's structure. Noble gases such as helium (^{4}He) and argon (^{40}Ar) in minerals are produced by the radioactive decay of uranium (^{238}U and ^{235}U), thorium (^{232}Th), and/or potassium (^{40}K) isotopes. These gases are chemically inert, volatile, and generally incompatible. The radiogenic noble gas content of a mineral at any given time reflects a balance between two competing processes: accumulation by radioactive decay and temperature-dependent diffusive loss (Hodges, 2014). Most noble gas mineral chronometers therefore fall under the umbrella of thermochronology. My dissertation research focuses on one these noble gas systems: (U-Th)/He dating.

(U-Th)/He dating was the first radiometric dating method ever attempted in Earth science back in the early 1900s (Strutt, 1905; Rutherford, 1906). The method, however, was quickly abandoned after scientists recognized that minerals "leaked" helium, yielding

anomalously young crystallization ages (Strutt, 1905; Strutt, 1908; Strutt, 1909; Hurley et al., 1956). It wasn't until the late 1980s and early 1990s that researchers realized that helium loss was a predictable diffusive process and recognized (U-Th)/He dating's potential as a thermochronometer (Zeitler et al., 1987; Wolf et al., 1997). Shortly thereafter, work began in earnest to characterize helium diffusion kinetics in common U and Th-bearing minerals such as apatite, zircon, and titanite through empirical and experimental study (e.g. Wolf et al., 1996; Reiners and Farley, 1999; Farley, 2000; Stockli et al., 2000; Reiners et al., 2004). Since helium is isotopically light, researchers found that helium in most minerals was sensitive to very low temperatures (below $\sim$ 300 °C). (U-Th)/He dating was therefore applied to the study of thermal events occurring at or near Earth's surface, such as mountain building, tectonic and climate-driven exhumation, magmatic activity, and meteor impacts (e.g. Farley, 2002; Reiners et al., 2017).

Interpreting the geologic significance of (U-Th)/He datasets requires an accurate and precise understanding of helium systematics in minerals. Over the past decade or so, there has been growing recognition within the thermochronology community that intrinsic factors such as radiation damage caused by the radioactive decay of parent isotopes, crystallography, crystal chemistry, and compositional heterogeneity affect the temperature sensitivity of helium in minerals (e.g. Shuster et al., 2006; Cherniak et al., 2009; Gautheron et al., 2009; Cherniak and Watson, 2011; Guenthner et al., 2013; Baughman et al., 2017). These poorly understood effects manifest as complicated (U-Th)/He datasets that are often challenging to interpret (e.g. Flowers, 2009; Guenthner et al., 2013; Enkelmann and Garver, 2016). In the chapters outlined below, we use an array of mass spectrometric and microanalytical techniques combined with empirical study to investigate helium diffusion in two minerals: zircon ($ZrSiO_4$) and xenotime ([Y,HREE]PO_4).

Ancient zircon (U-Th)/He datasets from slowly cooled or thermal disturbed environments

often exhibit date-radionuclide content correlations that are generally attributed to the effects of radiation damage on zircon helium closure temperatures (Hurley, 1952; Guenthner et al., 2013; Guenthner et al., 2014). Researchers at the University of Arizona recently developed an experiment-based damage-diffusivity model that allows users to derive thermal histories from such affected datasets (Guenthner et al., 2013). Though widely used, this model (ZRDAAM) has not been rigorously tested. Chapter 2 presents a zircon, apatite, and titanite (U-Th)/He dataset for the Cambrian McClure Mountain Syenite of south-central Colorado (Anderson et al., 2017). Zircon (U-Th)/He dates for the syenite are dispersed by $\sim$520 million years and generally decrease with increasing zircon radionuclide content and estimated radiation damage dose. An independent thermal model is used to assign each dated zircon a closure temperature and derive an empirical relationship between temperature and estimated radiation damage dose. These results are then used to evaluate ZRDAAM's effectiveness.

Largely inspired by some of the results presented in Chapter 2, Chapter 3 examines complex radiation damage zoning in zircon. Most zircon crystals have some degree of U and Th compositional zoning (Hanchar and Miller, 1993; Corfu et al., 2003). In ancient zircons, this zoning results in the heterogeneous accumulation of radiation damage. Zircon Raman spectra are highly sensitive to variations in radiation damage (Zhang et al., 2000; Nasdala et al., 2001; Palenik et al., 2003). The arrival of a new confocal Raman microscope with mapping capabilities to Group 18 Laboratories afforded a unique opportunity to produce high-resolution, radiation damage maps for a suite of Proterozoic zircon crystals with distinct compositional zoning from the Lyon Mountain Granite of the Adirondack Mountains of New York. We use these quantitative maps to model intracrystalline variations in helium diffusivity and laser ablation rates in the these crystals due to radiation damage zoning.

We discuss the implications of our findings for single crystal (U-Th)/He dating and laser ablation (U-Th)/He and U/Pb chronology of variably damaged zircon.

Based on zircon's crystal structure, we expect there to be crystallographically-controlled variations in helium diffusivity (Reich et al., 2007; Cherniak et al., 2009; Saadoune et al., 2009). Traditional step-wise degassing experiments cannot directly evaluate these important crystallographic effects (Reiners et al., 2002; Reiners et al., 2004; Guenthner et al., 2013). In Chapter 4, we present a laser depth profiling study that characterizes helium diffusion along the *a*- and *c*- crystallographic axes in zircon samples with low to moderate amounts of radiation damage. Our findings provide evidence for strong diffusive anisotropy that affects zircon (U-Th)/He closure temperatures in crystals with low radiation damage contents.

Chapter 5 of this dissertation evaluates xenotime's potential as a new (U-Th)/He thermochronometer (Anderson et al., 2019). This mineral can incorporate up to weight percent levels or uranium and thorium, so xenotime (U-Th)/He dating has great promise for dating young, low temperature geologic events (Farley and Stockli, 2002). Xenotime and zircon also share the same crystal structure, offering a chance to investigate how crystal chemistry affects helium diffusivity (Farley, 2007). We demonstrate that FPX-1, a highly crystalline xenotime from Pakistan, yields consistent (U-Th)/He dates and present two step-wise degassing experiments that characterize this sample's bulk helium diffusivity.

Chapter 6 reflects upon the findings of the preceding chapters and discusses open questions in (U-Th)/He thermochronology. The chapter also outlines future research opportunities.

References

Anderson, A. J., K. V. Hodges, and M. C. van Soest (2017). Empirical constraints on the effects of radiation damage on helium diffusion in zircon. *Geochimica et Cosmochimica Acta* 218, pp. 308–322.

Anderson, A. J., K. V. Hodges, M. C. van Soest, and J. M. Hanchar (2019). Helium diffusion in natural xenotime. *Geochemistry, Geophysics, Geosystems* 20, pp. 417–433.

Baughman, J., R. M. Flowers, J. R. Metcalf, and T. Dhansay (2017). Influence of radiation damage on titanite He diffusion kinetics. *Geochimica et Cosmochimica Acta* 205, pp. 50–64.

Cherniak, D. J. and E. B. Watson (2011). Helium diffusion in rutile and titanite, and consideration of the origin and implications of diffusional anisotropy. *Chemical Geology* 288, pp. 149–161.

Cherniak, D. J., E. B. Watson, and J. B. Thomas (2009). Diffusion of helium in zircon and apatite. *Chemical Geology* 268, pp. 155–166.

Condon, D. J. and M. D. Schmitz (2013). One Hundred Years of Isotope Geochronology, and Counting. *Elements* 9 (1), pp. 15–17.

Corfu, F., J. M. Hanchar, P. W. O. Hoskin, and P. Kinny (2003). Atlas of Zircon Textures. *Zircon: Reviews in Mineralogy & Geochemistry*. Ed. by J. M. Hanchar and P. W. O. Hoskin. Chantilly, VA: Mineralogical Society of America, pp. 469–500.

Enkelmann, E. and J. I. Garver (2016). Low-temperature thermochronology applied to ancient settings. *Journal of Geodynamics* 93, pp. 17–30.

Farley, K. A. (2000). Helium diffusion from apatite: General behavior as illustrated by Durango fluorapatite. *Journal of Geophysical Research* 105 (B2), p. 2903.

Farley, K. A. (2002). (U-Th)/He dating: Techniques, calibrations, and applications. *Noble Gases in Geochemistry and Cosmochemistry: Reviews in Mineralogy & Geochemistry*. Ed. by P. D., C. J. Ballentine, and R. Wieler. 47. Washington, DC: Mineralogical Society of America, pp. 819–844.

Farley, K. A. (2007). He diffusion systematics in minerals: Evidence from synthetic monazite and zircon structure phosphates. *Geochimica et Cosmochimica Acta* 71 (16), pp. 4015–4024.

Farley, K. A. and D. F. Stockli (2002). (U-Th)/He dating of phosphates: Apatite, monazite, and xenotime. *Phosphates - Geochemical, Geobiological, and Materials Importance: Reviews in Mineralogy & Geochemistry*. Ed. by M. J. Kohn, J. Rakovan, and J. M. Hughes. 48. Mineralogical Society of America, pp. 559–577.

Faure, G. and T. Mensing (2005). *Isotopes: Principles and Applications*. Ed. by 3. Hoboken, New Jersey: John Wiley & Sons, INC.

Flowers, R. M. (2009). Exploiting radiation damage control on apatite (U-Th)/He dates in cratonic regions. *Earth and Planetary Science Letters* 277, pp. 148–155.

Gautheron, C., L. Tassan-Got, J. Barbarand, and M. Pagel (2009). Effect of alpha-damage annealing on apatite (U–Th)/He thermochronology. *Chemical Geology* 266 (3-4), pp. 157–170.

Guenthner, W. R., P. W. Reiners, R. A. Ketcham, L. Nasdala, and G. Giester (2013). Helium diffusion in natural zircon: Radiation damage, anisotropy, and the interpretation of zircon (U-TH)/He thermochronology. *American Journal of Science* 313 (3), pp. 145–198.

Guenthner, W. R., P. W. Reiners, and Y. Tian (2014). Interpreting date-eU correlations in zircon (U-Th)/He datasets: A case study from the Longmen Shan, China. *Earth and Planetary Science Letters* 403, pp. 328–339.

Hanchar, J. M. and C. F. Miller (1993). Zircon zonation patterns as revealed by cathodoluminescence and backscattered electron images: Implications for interpretation of complex crustal histories. *Chemical Geology* 110 (1-3), pp. 1–13.

Hodges, K. V. (2014). Thermochronology in Orogenic Systems. *Treatise on Geochemistry*. 2nd ed. 4. Elsevier Ltd., pp. 281–308. URL: http://dx.doi.org/10.1016/B978-0-08-095975-7.00308-9.

Holmes, A. (1913). *The Age of the Earth*. London: Harper & Brothers.

Hurley, P. M. (1952). Alpha ionization as a cause of low helium ratios. *Eos, Transactions American Geophysical Union* 33 (2), pp. 174–183.

Hurley, P. M., E. S. J. Larsen, and D. Gottfried (1956). Comparison of radiogenic helium and lead in zircon. *Geochimica et Cosmochimica Acta* 9, pp. 98–102.

Nasdala, L., M. Wenzel, G. Vavra, G. Irmer, T. Wenzel, and B. Kober (2001). Metamictisation of natural zircon: Accumulation versus thermal annealing of radioactivity-induced damage. *Contributions to Mineralogy and Petrology* 141 (2), pp. 125–144.

Palenik, C. S., L. Nasdala, and R. C. Ewing (2003). Radiation damage in zircon. *American Mineralogist* 88, pp. 770–781.

Reich, M., R. C. Ewing, T. A. Ehlers, and U. Becker (2007). Low-temperature anisotropic diffusion of helium in zircon: Implications for zircon (U-Th)/He thermochronometry. *Geochimica et Cosmochimica Acta* 71 (12), pp. 3119–3130.

Reiners, P. W., R. W. Carlson, P. R. Renne, K. M. Cooper, D. E. Granger, N. M. McLean, and B. Schoene (2017). The (U-Th)/He System. *Geochronology and Thermochronology*. John Wiley & Sons Ltd. Chap. 11, pp. 291–363.

Reiners, P. W. and K. A. Farley (1999). Helium diffusion and (U-Th)/He thermochronometry of titanite. *Mineralogical Magazine* 62A (2), pp. 1249–1250.

Reiners, P. W., K. A. Farley, and H. J. Hickes (2002). He diffusion and (U-Th)/He thermochronometry of zircon: Initial results from Fish Canyon Tuff and Gold Butte. *Tectonophysics* 349 (1-4), pp. 297–308.

Reiners, P. W., T. L. Spell, S. Nicolescu, and K. A. Zanetti (2004). Zircon (U-Th)/He thermochronometry: He diffusion and comparisons with ^{40}Ar/^{39}Ar dating. *Geochimica et Cosmochimica Acta* 68 (8), pp. 1857–1887.

Rutherford, E. (1906). *Radioactive Transformations*. New York: Charles Scribner's Sons.

Saadoune, I., J. A. Purton, and N. H. de Leeuw (2009). He incorporation and diffusion pathways in pure and defective zircon $ZrSiO_4$: A density functional theory study. *Chemical Geology* 258 (3-4), pp. 182–196.

Shuster, D. L., R. M. Flowers, and K. A. Farley (2006). The influence of natural radiation damage on helium diffusion kinetics in apatite. *Earth and Planetary Science Letters* 249 (3-4), pp. 148–161.

Stockli, D. F., K. A. Farley, and T. A. Dumitru (2000). Calibration of the apatite (U-Th)/He thermochronometer on an exhumed fault block, White Mountains, California. *Geology* 28 (11), pp. 983–986.

Strutt, R. J. (1905). On the radio-active minerals. *Proceedings of the Royal Society of London* 76 (508), pp. 88–101.

Strutt, R. J. (1908). On the accumulation of helium in geologic time. *Proceedings of the Royal Society of London* 81, pp. 272–277.

Strutt, R. J. (1909). The leakage of helium from radio-active minerals. *Proceedings of the Royal Society of London* 82, pp. 166–169.

Wolf, R. A., K. A. Farley, and L. T. Silver (1996). Helium diffusion and low-temperature thermochronometry of apatite. *Geochimica et Cosmochimica Acta* 60 (21), pp. 4231–4240.

Wolf, R. A., K. A. Farley, and L. T. Silver (1997). Assessment of (U-Th)/He thermochronometry: The low-temperature history of the San Jacinto mountains, California. *Geology* 25 (1), pp. 65–68.

Zeitler, P. K., A. L. Herczeg, I. McDougall, and M. Honda (1987). U-Th-He dating of apatite: A potential thermochronometer. *Geochimica et Cosmochimica Acta* 51, pp. 2865–2868.

Zhang M S, E. K. H., G. C. Capitani, H. Leroux, A. M. Clark, J. Schluter, and R. C. Ewing (2000). Annealing of α-decay damage in zircon: A Raman spectroscopic study. *Journal of Physics: Condensed Matter* 12, pp. 3131–3148.

Chapter 2

EMPIRICAL CONSTRAINTS ON THE EFFECTS OF RADIATION DAMAGE ON HELIUM DIFFUSION IN ZIRCON

Alyssa J. Anderson,[1] Kip V. Hodges,[1] Matthijs C. van Soest,[1]

[1]School of Earth and Space Exploration, Arizona State University, Tempe, AZ 85287, USA.

Citation: A. J. Anderson, K. V. Hodges, and M. C. van Soest, (2017). Empirical Constraints on the Effects of Radiation Damage on Helium Diffusion in Zircon. *Geochimica et Cosmochimica Acta* 218, pp. 308-322.

2.1 Abstract

In this study, we empirically evaluate the impact of radiation damage on zircon (U-Th)/He closure temperatures for a suite of zircon crystals from the slowly cooled McClure Mountain syenite of south-central Colorado, USA. We present new zircon, titanite, and apatite conventional (U-Th)/He dates, zircon laser ablation (U-Th)/He and U-Pb dates, and zircon Raman spectra for crystals from the syenite. Titanite and apatite (U-Th)/He dates range from 447 to 523 Ma and 88.0 to 138.9 Ma, respectively, and display no clear correlation between (U-Th)/He date and effective uranium concentration. Conventional zircon (U-Th)/He dates range from 230.3 to 474 Ma, while laser ablation zircon (U-Th)/He dates show even greater dispersion, ranging from 5.31 to 520 Ma. Dates from both zircon (U-Th)/He datasets decrease with increasing alpha dose, indicating that most of the dispersion can be attributed to radiation damage. Alpha dose values for the dated zircon crystals range from effectively zero to 2.15 x 10^{19} α/g, spanning the complete damage spectrum.

We use an independently constrained thermal model to empirically assign a closure temperature to each dated zircon grain. If we assume that this thermal model is robust, the zircon radiation damage accumulation and annealing model of Guenthner et al. (2013) does not accurately predict closure temperatures for many of the analyzed zircon crystals. Raman maps of the zircons dated by laser ablation document complex radiation damage zoning, sometimes revealing crystalline zones in grains with alpha dose values suggestive of amorphous material. Such zoning likely resulted in heterogeneous intra-crystalline helium diffusion and may help explain some of the discrepancies between our empirical findings and the Guenthner et al. (2013) model predictions. Because U-Th zoning is a common feature in zircon, radiation damage zoning is likely to be a concern for most ancient, slowly cooled zircon (U-Th)/He datasets. Whenever possible, multiple mineral-isotopic systems should be employed to add additional, independent constraints to a sample's thermal history.

2.2 Introduction

Helium diffusion in U- and Th-bearing accessory minerals is sufficiently rapid at low temperatures that (U-Th)/He dating has evolved into a powerful tool for reconstructing cooling histories in the upper crust, informing our understanding of surface and near-surface processes (e.g. Farley, 2002; Ehlers and Farley, 2003; Reiners and M. T. Brandon, 2006). Although most commonly applied to geologic problems in active orogenic systems, (U-Th)/He thermochronology also has proven useful for studies of the development and long-term stability of continental interiors (Enkelmann and Garver, 2016; Flowers, 2009; Flowers et al., 2006).

Applications of low temperature thermochronology to slowly cooled terrains however, present unique challenges. (U-Th)/He datasets from Precambrian and Paleozoic settings are

often dispersed well beyond what is expected based on analytical uncertainty alone, making datasets difficult to interpret unambiguously (Flowers et al., 2006). Zircon (U-Th)/He (ZrnHe) datasets in particular are often problematic in this regard. Dispersion has been attributed to: 1) the effect of U-Th zonation on alpha ejection corrections, (Bargnesi et al., 2016; Hourigan et al., 2005); 2) anisotropic diffusion (Cherniak et al., 2009); 3) multidomain diffusion, (Reiners et al., 2004); and 4) radiation damage (Guenthner et al., 2013). Of these, radiation damage predominantly attributed to alpha decay of U and Th may be especially significant for slowly cooled zircons (Guenthner et al., 2013).

During an alpha decay event, kinetic energy is lost through the emission of an alpha particle and recoil of the heavy daughter nuclide (Ewing et al., 2003; W. J. Weber, 1990). Alpha recoil results in a cascade of atomic-scale collisions, damaging the crystal structure. Damage accumulates over time, affecting material properties. Importantly, however, radiation damage can also anneal over time at elevated temperatures (Murakami et al., 1991; Zhang et al., 2000), such that the amount of damage to a crystal's structure is a function of U and Th concentration, age, and thermal history (Guenthner et al., 2013; Nasdala et al., 2001).

For years, researchers have noted correlations between U and Th content and zircon (U-Th)/He dates (e.g. Hurley, 1952; Hurley and Fairbairn, 1953; Guenthner et al., 2013; Guenthner et al., 2014; Guenthner et al., 2015; Orme et al., 2016; Powell et al., 2016; Johnson et al., 2017). Guenthner et al. (2013) recently attempted to quantify the effects of radiation damage on helium diffusion kinetics through a series of step-heating experiments on crystallographically oriented zircon slabs with varying degrees of structural damage. Results indicated that He retentivity increases at low damage doses from $\sim$1 x 10^{16} to 1.5 x 10^{17} α/g. At greater damage doses, however, their data suggested that He diffusivity dramatically increases. The authors proposed that the low-dosage increases in He retentivity

reflect progressive obstruction of fast pathways for helium diffusion parallel to the c-axis. They posited that, as radiation damage levels increase, the damage zones interconnect to create a series of new fast paths, increasing He diffusivity. Their findings demonstrated that radiation damage has important implications for ZrnHe thermochronology, namely, that heavily damaged zircon grains may be sensitive to temperatures far lower than the previously accepted 180-200 °C closure temperature for helium in zircon (Guenthner et al., 2013; Reiners et al., 2002; Reiners et al., 2004).

From these data, Guenthner et al. (2013) developed a zircon radiation damage accumulation and annealing model (ZRDAAM) designed to calculate helium diffusivity as a function of temperature history based on each zircon crystal's measured U-Th content. ZRDAAM has been applied to a number of bedrock and detrital ZrnHe datasets, yielding valuable information about the thermal history of the regions studied (e.g. Guenthner et al., 2014; Guenthner et al., 2015; Orme et al., 2016). A few recent studies however, have acknowledged that applications of the model are not uniformly successful, especially for zircons with higher damage doses (Johnson et al., 2017; Powell et al., 2016). For example, Powell et al. (2016) has suggested that the damage threshold for increased helium diffusivity may be too high. Johnson et al. (2017), in turn, reported a dataset in which heavily damaged zircons appeared more helium retentive than predicted by ZRDAAM.

The McClure Mountain syenite of south-central Colorado, USA affords an opportunity to empirically test ZRDAAM on a suite of variably damaged zircons from a single sample with a simple, independently constrained thermal history. In this study, we present new zircon, titanite, and apatite conventional (U-Th)/He dates, zircon laser ablation (U-Th)/He and U-Pb dates, and zircon Raman spectra for crystals separated from a sample of the syenite. We modeled the cooling history of the syenite by combining our TtnHe and ApHe dataset with previously published geochronologic and thermochronologic data. We then

used this information to derive empirical constraints on the relationship between radiation damage and ZrnHe closure temperature for comparison with the Guenthner et al. (2013) model.

2.3 The McClure Mountain Syenite

Located in the northern Wet Mountains of south-central Colorado, the McClure Mountain Complex spans $\sim$74 km^2 from McClure Mountain and Deer Mountain in the southwest to Iron Mountain in the northeast (Olson et al., 1977; Parker and Hildebrande, 1963). Originally discovered and named by the U.S. Geological Survey in the 1960s, this concentrically zoned, alkalic complex intrudes Precambrian granitic gneisses and metamorphic rocks. The complex consists of pyroxene-olivine-plagioclase cumulates intruded by the syenite (E. C. J. Alexander et al., 1978; Olson et al., 1977; Parker and Hildebrande, 1963). Major-rock forming minerals in the syenite include K-feldspar, plagioclase, hornblende, biotite, and clinopyroxenes, but significant amounts of titanite and apatite occur in most samples as well (Samson and J. Alexander E. C., 1987; Schoene and Bowring, 2006). Zircon, baddeleyite, zirconolite, ilmenite, magnetite, nepheline, calcite, iron-sulfides, and alteration products are minor constituents (Schoene and Bowring, 2006).

The syenite has been the subject of numerous geochronologic studies, mostly aimed at establishing its intrusive age. Zircon isotope dilution, thermal ionization mass spectrometry (ID-TIMS) ^{207}Pb/^{235}U dates are interpreted to indicate a crystallization age of 523.98 $\pm$ 0.12 Ma (Schoene and Bowring, 2006). (Throughout this paper, all uncertainties are presented at the 2σ level.) ID-TIMS ^{207}Pb/^{235}U data for titanite and apatite yield dates of 523.26 $\pm$ 0.65 Ma and 523.5 $\pm$ 1.5 Ma respectively, implying rapid cooling of the intrusive body following crystallization (Schoene and Bowring, 2006). Laser ablation inductively coupled

plasma mass spectrometry (LA-ICPMS) analyses of McClure Mountain apatite yield a U-Pb Tera-Wasserburg concordia date of 524.5 $\pm$ 3.7, which, while less precise, is consistent with the ID-TIMS U/Pb results (Chew et al., 2014).

Although MMhb is one of the most widely known ^{40}K/^{40}Ar standards (Samson and J. Alexander E. C., 1987), it is now well-established that MMhb is isotopically heterogeneous at the single-crystal scale (Baksi et al., 1996; Renne et al., 1998; Spell and McDougall, 2003). Renne et al. (1998) and Spell and McDougall 2003 have reported total fusion ^{40}Ar/^{39}Ar-hornblende dates for the syenite of 523.1 $\pm$ 5.2 Ma and 523.3 $\pm$ 1.8 Ma, respectively, using the more homogeneous G-1550 biotite as a primary standard. Based on a cooling history inferred from the U/Pb thermochronometric data referred to in the previous paragraph, Schoene and Bowring (2006) predicted that the actual ^{40}Ar/^{39}Ar closure age of MMhb might be ca. 522.98 Ma. Olson et al. (1977) also reported two biotite K-Ar ages for the McClure Mountain syenite: 506 $\pm$ 13 Ma and 510 $\pm$ 13 Ma.

Relatively few thermochronological data have been published for the syenite. Olson et al. (1977) reported fission track dates for titanite and apatite of 506 $\pm$ 43 Ma and 293 $\pm$ 62 Ma, respectively. Both dates have large uncertainties, but are reasonable in light of the dates obtained for higher temperature thermochronometers and estimates of nominal FT closure temperatures for titanite (ca. 300°C) and apatite (110°C) (K. A. Brandon et al., 1998; Coyle and Wagner, 1998; Laslett et al., 1987). The apatite fission track date is also similar to two other dates, 299 $\pm$ 20 Ma and 290 $\pm$ 14, reported by Kelley and Chapin (2004) for granodiorite samples collected at nearby Curley Peak at 2241 m and 2108 m elevation. The latitude-longitude coordinates for the syenite sample collected by Olson et al. (1977) indicate that it was collected at a similar elevation, $\sim$2350 m.

Most recently, Weisberg and colleagues (2014) presented (U-Th)/He dates for zircon, titanite, baddeleyite, and apatite separated from the syenite. Although the baddeleyite dates

were unrealistically older than the $^{207}Pb/^{235}U$ ID-TIMS zircon intrusive age - something the authors tentatively interpreted as a consequence of uncertain alpha ejection corrections. The remaining dates were significantly younger, with reported mean dates of 498 $\pm$ 18 Ma for titanite and 459 $\pm$ 40 Ma for zircon. Apatite (U-Th)/He dates range from 70 to 150 Ma (2014). Combined with information from other isotopic systems and approximate closure temperatures for the various chronometers, these data suggest that the syenite cooled relatively rapidly following crystallization at ca. 524 Ma to temperatures below 200 °C by ca. 500 Ma, but subsequently cooled much more slowly throughout the remainder of the Paleozoic and at least most of the Mesozoic.

2.4 Analytical Methods and Results

2.4.1 Conventional (U-Th)/He Dating

Although the collection locality for the original aliquot of MMhb (E. C. J. Alexander et al., 1978) has been lost for many years, many recent re-collections have been done on boulders sourced from the original collection site but presently deposited in a nearby parking area. The sample used for this study was broken from one of these boulders. Apatite, titanite, and zircon grains were extracted by standard crushing, wet sieving, magnetic separation, and gravimetric separation.

Ten euhedral apatite crystals, eight euhedral zircon crystals, and nineteen subhedral titanite crystals were picked by hand under a binocular microscope for conventional (U-Th)/He dating. None contained obvious inclusions at high magnification. The dimensions of the apatite and zircon crystals were measured prior to analysis to allow for alpha ejection corrections (Farley et al., 1996; Hourigan et al., 2005). Such corrections were not necessary

for the titanite crystals because, prior to analysis, they were abraided with compressed air to remove their outer rims. Dimensions of the abraided titanite crystals were then measured for volume approximations. Selected crystals were analyzed using instrumentation in the Group 18 Laboratories at Arizona State University. Details of analytical and data reduction procedures are provided in the Supplementary Materials. All conventional (U-Th)/He analytical data are reported in Table 2.1.

Dated titanite grains were orange to orange-brown, transparent to translucent, subhedral crystals or anhedral shards. The average grain radius prior to abrasion was $\sim$200 μm. TtnHe dates are dispersed over 76 Ma, ranging from 447 $\pm$ 12 Ma to 523 $\pm$ 14 Ma. The inverse-variance weighted mean date for these grains is 491 $\pm$ 11 Ma. Apatite crystals were colorless and transparent with equivalent spherical radii ranging from 71 - 94 μm and a mean radius of 75 μm. ApHe dates are dispersed by over 50 Ma, ranging from 88.0 $\pm$ 2.4 Ma to 138.9 $\pm$ 3.6 Ma. ApHe dates do not appear to correlate with grain radii. The inverse-variance weighted mean date is 110 $\pm$ 10 Ma.

Zircons selected for conventional (U-Th)/He dating were semi-translucent, yellowish brown, di-pyramid crystals that represent the Group 1 zircon population defined by Schoene and Bowring (2006). Our crystals had equivalent spherical radii ranging from 38 to 78 μm with a mean radius of 56 μm. Conventional ZrnHe dates show greater dispersion than conventional TtnHe and ApHe dates, ranging from 230.3 $\pm$ 7.7 Ma to 474 $\pm$ 15 Ma. There is no apparent correlation between grain radius and ZrnHe date.

2.4.2 Raman Spectroscopy and Laser Microprobe Zircon Dating

As described in detail by Horne et al. (2016), it is possible to combine sequential laser ablation microsampling of zircon for helium isotopic analysis and laser ablation

Table 2.1. Conventional (U-Th)/He dates for McClure Mountain titanite, apatite, and zircon.

Sample	^{238}U (atoms)	^{232}Th (atoms)	^{147}Sm (atoms)	^{4}He (atoms)	Radius Eq. Sphere (μm)	eU (ppm)	Th/U	F_T[a]	Date (Ma)[b]	2σ[c]
Titanite										
Ttn01	5.985E+12	1.412E+13	3.070E+12	6.476E+12	382	4	2.3		523	14
Ttn02	1.949E+12	4.713E+12	9.423E+11	2.112E+12	238	6	2.4		519	14
Ttn04	1.468E+12	4.498E+12	1.285E+12	1.737E+12	218	6	3.0		518	14
Ttn05	4.245E+12	1.074E+13	3.097E+12	4.032E+12	180	31	2.5		450	12
Ttn06	3.019E+12	9.048E+12	2.431E+12	3.263E+12	169	28	3.0		479	13
Ttn07	3.216E+12	7.876E+12	2.105E+12	3.412E+12	142	46	2.4		506	13
Ttn08	2.275E+12	6.861E+12	1.788E+12	2.575E+12	141	37	3.0		499	13
Ttn09	1.258E+12	3.961E+12	3.991E+10	1.466E+12	97	63	3.1		506	17
Ttn10	3.003E+12	6.914E+12	1.487E+12	3.152E+12	147	38	2.3		511	13
Ttn11	2.911E+12	7.449E+12	2.266E+12	2.918E+12	138	46	2.5		472	12
Ttn12	2.383E+12	7.181E+12	1.945E+12	2.662E+12	135	44	3.0		493	13
Ttn13	1.152E+12	2.579E+12	6.744E+11	1.173E+12	107	38	2.2		501	13
Ttn14	1.207E+12	3.279E+12	1.005E+12	1.268E+12	118	32	2.7		483	13
Ttn15	4.824E+12	1.022E+13	2.914E+12	4.480E+12	149	58	2.1		467	12
Ttn16	1.207E+12	3.538E+12	1.068E+12	1.305E+12	105	46	2.9		483	13
Ttn17	1.720E+12	5.057E+12	1.440E+12	1.962E+12	126	38	2.9		508	13
Ttn18	1.210E+12	4.027E+12	1.451E+12	1.445E+12	117	36	3.3		505	13
Ttn19	1.456E+12	4.121E+12	1.708E+12	1.616E+12	114	43	2.8		501	13
Ttn20	1.824E+12	3.574E+12	1.669E+12	1.585E+12	120	40	1.9		447	12
Weighted Mean[d]									491	11
Apatite										
Ap01	3.563E+11	1.048E+12	8.761E+11	6.104E+10	71	22	2.9	0.78	100.0	2.6
Ap02	2.566E+11	6.832E+11	4.972E+11	5.573E+10	72	19	2.6	0.79	131.1	3.5
Ap03	3.403E+11	1.087E+12	9.810E+11	8.206E+10	78	18	3.2	0.80	132.5	3.4
Ap04	3.199E+11	8.270E+11	7.959E+11	5.981E+10	72	21	2.6	0.79	113.9	3.0
Ap05	2.380E+11	6.754E+11	7.765E+11	3.573E+10	73	13	2.8	0.79	88.0	2.4
Ap06	4.720E+11	1.493E+12	9.053E+11	9.652E+10	86	19	3.1	0.82	110.7	2.9
Ap07	3.584E+11	1.007E+12	5.363E+11	7.635E+10	76	21	2.8	0.80	124.4	3.3
Ap08	4.594E+11	1.344E+12	1.234E+12	8.103E+10	86	13	2.9	0.82	98.5	2.6
Ap09	9.926E+11	2.688E+12	1.407E+12	1.887E+11	94	33	2.7	0.83	107.8	2.8
Ap10	4.448E+11	1.219E+12	1.157E+12	1.066E+11	80	21	2.7	0.81	138.9	3.6
Weighted Mean[d]									110	10
Zircon										
Zr01	1.895E+13	4.036E+13		6.817E+12	64	1458	2.1	0.80	230.3	7.7
Zr02	3.648E+13	7.808E+13		1.481E+13	78	1578	2.1	0.83	248.7	8.5
Zr03	1.674E+13	2.126E+13		1.131E+13	74	734	1.3	0.83	474	15
Zr04	1.280E+13	2.924E+13		5.993E+12	50	2161	2.3	0.75	312.0	8.8
Zr05	8.241E+12	2.361E+13		6.232E+12	59	949	2.8	0.78	441	12
Zr06	4.287E+12	9.329E+12		1.716E+12	38	1542	2.2	0.68	300.8	8.2
Zr07	7.060E+12	1.691E+13		3.184E+12	43	1781	2.4	0.71	312.2	8.3
Zr09	4.663E+12	9.482E+12		1.523E+12	42	1350	2.0	0.70	242.8	6.4

[a]Alpha ejection corrections calculated following Hourigan et al. (2005).
[b]ApHe and ZrnHe dates with F_T correction applied. F_T corrections were not made for TtnHe dates.
[c]2σ represents propagated analytical uncertainties.
[d]Inverse-variance weighted mean date. Uncertainties for the inverse-variance weighted mean date have been expanded by multiplying by the square root of the MSWD (Wendt and Carl, 1991; Ludwig, 2003).

microsampling of the same crystal for U, Th, and Pb analysis to simultaneously determine (U-Th)/He and U/Pb dates for domains within individual zircons. Eleven additional, $>$ 60 μm zircon crystals were picked for laser microprobe dating using the approach of Horne et al. (2016). The Horne et al. (2016) procedure is conceptually similar to the approach described

by Evans et al. (2005) but distinctive in that the Horne et al. (2016) procedure more completely accounts for the effects of intracrystalline U-Th zoning. For laser microprobe dating, we picked zircons representative of both McClure Mountain zircon Groups 1 and 2 of Schoene and Bowring (2006); Group 1 crystals were semi-translucent, yellowish brown, and di-pyramidal, while Group 2 crystals were translucent, colorless to pinkish, and anhedral. Selected crystals were mounted in Torr Seal (a low vapor-pressure epoxy) and polished to a depth of 20 to 30 μm to remove crystal rims that might have experienced alpha particle ejection or implantation (Farley et al., 1996).

Prior to laser microprobe dating, selected portions of the polished surface of each crystal were mapped using an HORIBA Scientific XploRA PLUS Raman microscope. Details of the mapping procedure are provided in the Supplementary Materials. Specifically, we mapped variations in the full width at half maximum (FWHM) of the zircon ν_3 (SiO_4) Raman band near 1000 cm^{-1} because this peak is known to broaden with increasing radiation damage (Nasdala et al., 2004; Nasdala et al., 2001). Using the calibration suggested by Palenik et al. (2003), we converted each FWHM measurement to an alpha dose, which we will refer to as a 'Raman alpha dose' (α_r), and report in units of alpha particles (α) per gram (Table 2.2).

Raman maps reveal significant crystal-to-crystal variations in the FWHM of the ν_3 (SiO_4) Raman band, from sharp peaks indicative of highly crystalline domains (FWHM = 4.7 cm^{-1}) to broad spectra characteristic of amorphous material. This variation corresponds to α_r values ranging from 0.2 x 10^{18} α/g to $\geq$10 x 10^{18} α/g (Palenik et al., 2003). Importantly, Raman maps also document highly variable ranges in FWHM and α_r values within individual crystals (Table 2.2 & Figure 2.1). We infer that these intracrystalline variations reflect U-Th zonation that given sufficient time has resulted in the spatially heterogeneous accumulation of radiation damage. The implications of this observation for ZrnHe ther-

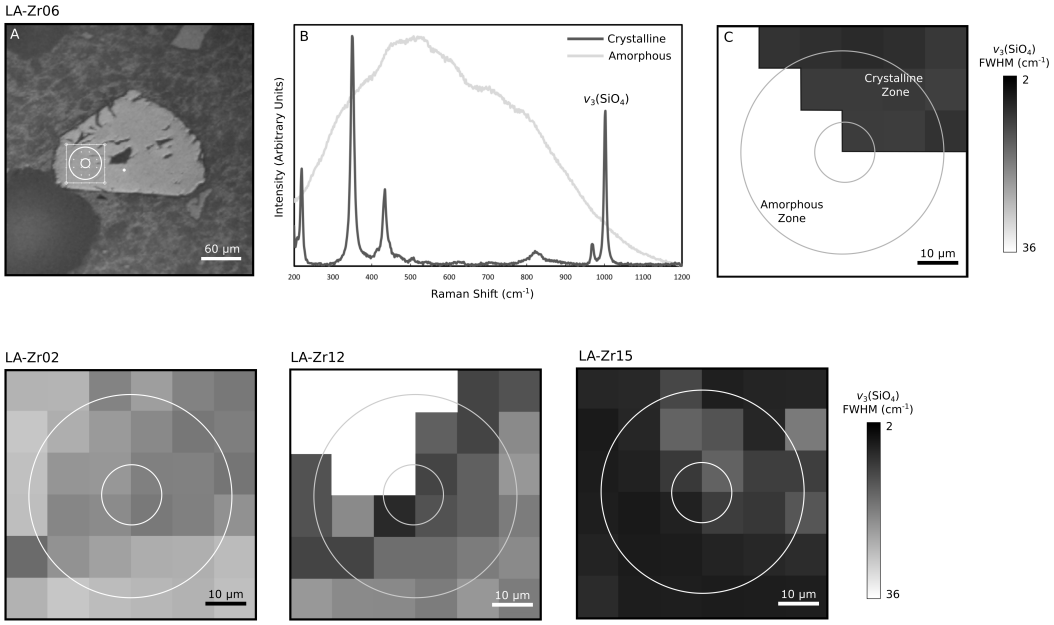

Figure 2.1. The top panel depicts Raman results for LA-Zr06. A. Magnified image of the polished grain mounted in Torr Seal and the 60 μm x 60 μm square grid over which Raman measurements were acquired. B. Representative Raman spectra from the crystalline and amorphous zones in the crystal. C. v_3 (SiO_4) FWHM map for the area designated by the square in Frame A. (For this and other Raman maps in the figure, a laser beam integration footprint of 10 x 10 μm was used.) Dark gray to black regions are moderately to highly crystalline, whereas the white regions are so heavily damaged by radiation as to be amorphous. The bottom panel shows FWHM maps for McClure Mountain syenite zircons LA-Zr02, LA-Zr12, and LA-Zr15. Note the large intra- and inter-crystalline variability of damage. Superimposed on all Raman maps are the locations of ablation spots used in laser microprobe dating of these crystals. The smaller, 15 μm-diameter circles represent He measurement spots, whereas the larger, 50 μm-diameter circles represent U, Th, and Pb measurement spots.

mochronology in slowly cooled rocks like the McClure Mountain syenite are discussed in detail in a later section of the paper.

Laser ablation dating of these crystals employed an ultraviolet (193 nm) excimer laser and involved two separate measurements. First, a ca. 15 μm diameter pit was ablated in vacuuo for helium isotopic analysis using a magnetic sector, gas-source mass spectrometer. This pit was positioned in the center of the region mapped by Raman spectroscopy (Figure 2.1). After precise interferometric measurement of the volume of the resulting pit, a second,

Table 2.2. Modern day alpha dose estimates for McClure Mountain zircon.

Sample	FWHM (cm^{-1})[a]	α_r (10^{18} α/g)[b]	α_i (10^{18} α/g)[c]	2σ[d]
LA-Zr02	16.2 - 28.3	1.1 - 2.9	3.96	0.17
LA-Zr03	4.7 - a	0.2 - ≥10	10.13	0.45
LA-Zr04	7.3 - 20.5	0.4 - 1.6	1.64	0.06
LA-Zr06	7.3 - a	0.4 - ≥10	3.05	0.12
LA-Zr07	16.8 - a	1.2 - ≥10	21.75	1.03
LA-Zr09	7.7 - 27.0	0.4- 2.6	1.92	0.08
LA-Zr12	10.3 - a	0.6 - ≥10	3.00	0.12
LA-Zr14	9.1 - a	0.5 - ≥10	4.39	0.25
LA-Zr15	4.9 - 18.1	0.3 - 1.3	0.76	0.03
LA-Zr17	6.3 - 18.4	0.4 - 1.3	1.00	0.04
LA-Zr19	8.6 - a	0.5 - ≥10	2.09	0.08

[a]Range of measured FWHM values for the $\nu_3(SiO_4)$ Raman band in zircons dated by laser microprobe. The designation 'a' denotes an amorphous spectrum.
[b]Equivalent alpha dose range based on the Raman data following the calibration suggested by Palenik et al. (2013).
[c]Isotopic alpha dose values predicted from the crystals' U-Th concentrations and assuming damage accumulation since the inverse-variance weighted mean TtnHe date (491 ± 11 Ma).
[d]2σ reflects propagated zircon U-Th concentration and TtnHe date uncertainties.

ca. 50 μm - pit centered on the first pit- was ablated at atmospheric pressure to enable U-Th-Pb analysis by ICPMS. The positioning and depth of this second pit was such that the extracted material should represent the U and Th that might have contributed radiogenic ^{4}He to the first pit, thus minimizing the effects of U-Th zoning on the dated domain's apparent (U-Th)/He age. The volume of this second pit was then determined by interferometric measurement. More details about this method may be found in the Supplementary Materials and Horne et al. (2016).

U/Pb and (U-Th)/He results are presented in Table 2.3. Given that the ^{207}Pb/^{235}U age of McClure Mountain zircon was precisely established at 523.98 ± 0.12 Ma by Schoene and Bowring (2006), comparison of that date with laser ablation ^{235}U/^{207}Pb dates obtained using the Horne et al.(2016) method offers a useful check on both our method and data quality.

Table 2.3. Laser microprobe (U-Th)/He and U-Pb dates for McClure Mountain zircon.

Sample	He pit vol. (μm^3)	^{4}He (atoms/g)	U-Th pit vol. (μm^3)	^{238}U (atoms/g)	^{232}Th (atoms/g)	eU	Th/U	ZrnHe Date (Ma)	2σ[a]	^{235}U/^{207}Pb Date (Ma)[b]	2σ[a]
LA-Zr02	1592	9.558E+16	51881	3.774E+18	9.794E+18	2389	2.6	12.28	0.51	521	14
LA-Zr03	1759	2.480E+17	50728	9.131E+18	2.747E+19	6122	3.0	12.42	0.52	529	25
LA-Zr04	1493	1.736E+18	49013	1.958E+18	2.270E+18	985	1.2	520	18	527	11
LA-Zr06	1701	3.722E+17	52769	3.514E+18	4.841E+18	1837	1.4	62.0	2.3	523	11
LA-Zr07	1804	2.283E+17	53746	1.740E+19	6.897E+19	13171	3.9	5.31	0.13	524	14
LA-Zr09	1559	9.354E+17	47756	2.143E+18	3.355E+18	1157	1.6	244.0	9.0	521	13
LA-Zr12	1633	1.961E+18	53138	3.073E+18	6.510E+18	1813	2.1	325	12	528	14
LA-Zr14	1447	1.657E+18	51885	2.891E+18	1.675E+19	2667	5.8	189	10	517	19
LA-Zr15	1456	7.628E+17	47248	9.863E+17	6.777E+17	454	0.7	496	16	514	10
LA-Zr17	1394	1.045E+18	46538	1.231E+18	1.244E+18	603	1.0	511	18	523	9
LA-Zr19	1540	1.834E+18	51048	2.267E+18	3.944E+18	1259	1.7	433	15	529	13
Weighted Mean ZrnPb date[c]										522.7	3.8

[a]Values for 2σ reflect propagated uncertainties for isotopic analyses, laser ablation pit volumes, and the `SynZircon' U-Th concentration standard.
[b] ^{235}U/^{207}Pb dates are corrected for common lead following Andersen (2002).
[c]Inverse-variance weighted mean zircon ^{235}U/^{207}Pb date.

Results for the eleven crystals range from 521 $\pm$ 14 Ma to 529 $\pm$ 13 Ma, display no evidence of excess dispersion beyond what is expected given the analytical uncertainties, and yield an inverse-variance weighted mean of 522.7 $\pm$ 3.8 Ma. This date is well within uncertainty of the Schoene and Bowring (2006) date and of similar precision to the published ICPMS zircon dates of Chew et al. (2014). In contrast, our (U-Th)/He dates for the same crystals are over-dispersed by two orders of magnitude, ranging from a remarkable 5.31 $\pm$ 0.13 Ma to 520 $\pm$ 18 Ma and yielding dates both younger and older than the conventional ZrnHe dataset (230.3 $\pm$ 7.7 Ma to 474 $\pm$ 15 Ma).

2.4.3 Radiation Damage and (U-Th)/He dates

An important parameter in many published explorations of radiation damage in minerals is the effective uranium concentration, eU , where eU = [U] + 0.235 $\cdot$ [Th] where U and Th concentrations are in ppm (Shuster et al., 2006). Effective uranium concentration is assumed to be proportional to the amount of radiation damage in a crystal if all the crystals in the sample have experienced the same thermal history (Flowers, 2009; Guenthner et al., 2013;

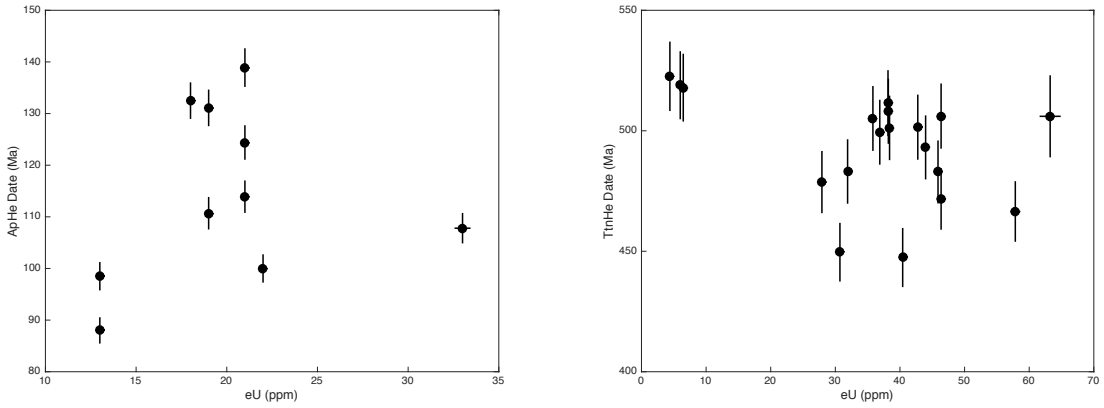

Figure 2.2. Effective uranium concentration vs. (U-Th)/He date for apatite and titanite. Error bars represent 2σ analytical uncertainties.

Guenthner et al., 2014; Shuster et al., 2006). If the dispersion in a set of (U-Th)/He dates is due to radiation damage, we would expect some sort of correlation between (U-Th)/He date and eU. Both positive and negative date-eU correlations are commonly reported in the literature for ApHe and ZrnHe datasets (e.g. Flowers et al., 2009; Guenthner et al., 2013; Orme et al. 2016; Johnson et al., 2017). More recently, Baughman et al. (2017) documented a negative date-eU correlation for TtnHe data.

Our dated apatite crystals have eU values that range from 13 ppm to 33 ppm and show neither a strong positive nor negative correlation with ApHe date (Figure 2.2). This suggests that the over-dispersion in ApHe dates may predominantly reflect significant U-Th zoning that makes simple alpha ejection corrections incomplete (Ault and Flowers, 2012; Farley et al., 2011; Hourigan et al., 2005). Effective uranium values for our dated titanite crystals range from 4 ppm to 63 ppm and also do not exhibit a clear correlation with TtnHe date (Figure 2.2). Thermal modeling results, discussed later in this text, suggest that the McClure Mountain syenite cooled rapidly through the TtnHe partial retention zone (Reiners and Farley, 1999), making it unlikely for the titanite to have had sufficient time to accumulate

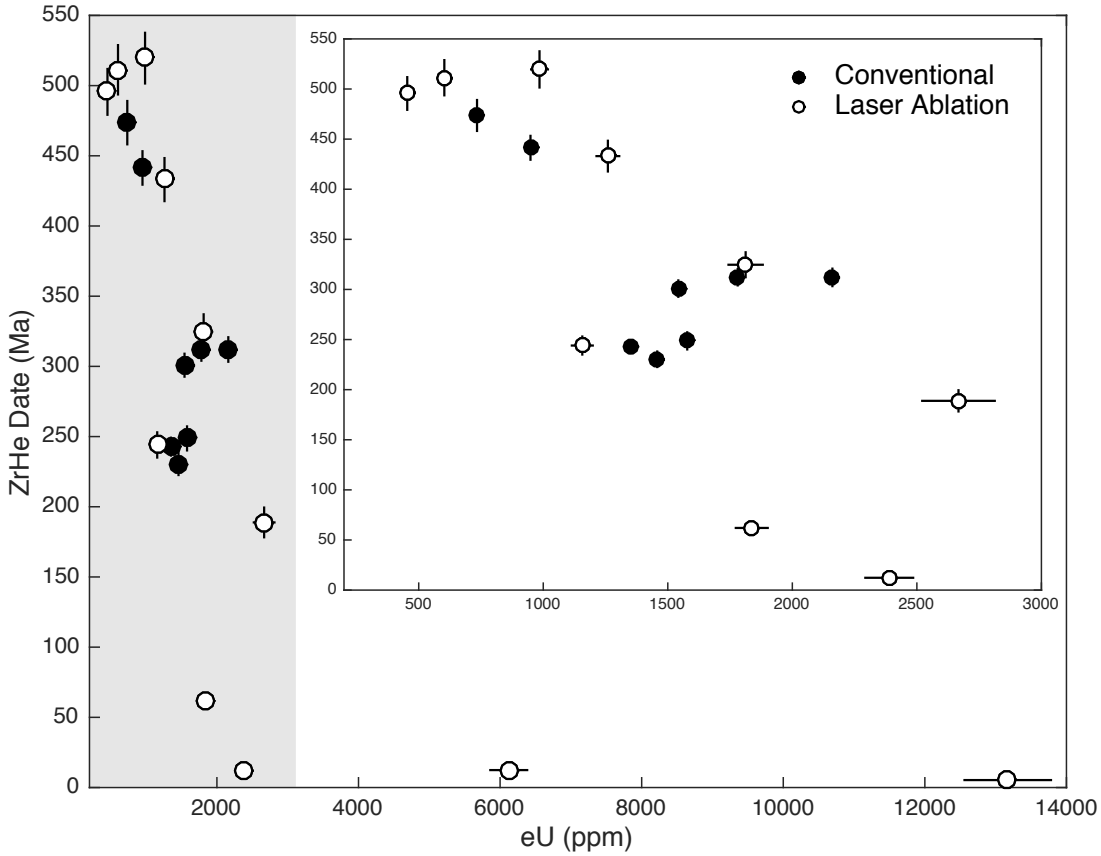

Figure 2.3. Effective uranium concentration vs. (U-Th)/He date for zircon. The gray shaded region highlights the the area of the plot magnified in the overlay. Error bars represent 2σ analytical uncertainties.

significant amounts radiation damage. We thus attribute the TtnHe date dispersion to the effects of U-Th zoning.

Our dated zircon crystals have eU values that range from 454 ppm to 13,170 ppm (Figure 2.3). The conventional and laser ablation ZrnHe data exhibit a strong negative date-eU correlation, which suggests that radiation damage can account for most of their $\sim$515 Ma dispersion. Additional insight is gained by calculating the degree of alpha radiation damage that might be expected for each dated zircon:

$$\alpha_i = \frac{8 \cdot N_A \cdot^{238} U}{M_{238} \cdot 10^6} \cdot (e^{\lambda_{238} t} - 1) + \frac{7 \cdot N_A \cdot^{235} U}{M_{235} \cdot 10^6} \cdot (e^{\lambda_{235} t} - 1) + \frac{6 \cdot N_A \cdot^{232} Th}{M_{232} \cdot 10^6} \cdot (e^{\lambda_{232} t} - 1) \tag{2.1}$$

where N_A is Avogadro's number, ^{238}U, ^{235}U, and ^{232}Th are isotopic concentrations (ppm), λ values are the respective decay constants, M values are the respective atomic masses (g/mol), and t is the time interval over which damage accumulates (Nasdala et al., 2001). We refer to an alpha dose calculated in this manner as an 'isotopic alpha dose', (α_i) and report units in α/g. It is tempting to assume that this interval is the time between zircon crystallization at 523.98 Ma and some subsequent time, but doing so would ignore the probability of alpha recoil damage annealing at high temperatures during cooling. Unfortunately, the rate and temperature dependence of alpha recoil damage annealing in zircon on geologic timescales are poorly constrained (Guenthner et al., 2013). It has been suggested that the kinetics of alpha recoil damage annealing and fission track (FT) annealing are similar, such that the age of zircon FT closure can be taken as a reasonable estimate of the time after which annealing effectively ceases and accumulated damage is retained (Guenthner et al., 2013; Guenthner et al., 2014).

In the absence of available ZrnFT dates for the McClure Mountain syenite, we have followed Johnson et al. (2017) in inferring that the TtnHe date for a sample is a reasonable estimate for the time at which zircons in the same sample began to retain radiation damage. This approach derives from the observation that the nominal closure temperature range for TtnHe (Reiners and Farley, 1999) overlaps significantly with field-based estimates of the closure temperature range for fission tracks in zircon (Bernet, 2009). We evaluated this approach by calculating the present-day α_i for McClure Mountain zircons dated by laser ablation using the sample's TtnHe inverse variance-weighted mean date of 491 $\pm$ 11 Ma as

Table 2.4. Alpha dose at the ZrnHe closure age and closure temperature estimates for McClure Mountain zircon.

Sample	ZrnHe Date (Ma)	2σ	α_i (α/g)[a]	2σ[b]	T_{cb} (°C)[c]	2σ[d]
Zr01	230.3	7.7	1.30E+18	5.8E+16	106	9
Zr02	248.7	8.5	1.31E+18	6.7E+16	111	12
Zr03	474	15	4.43E+16	4.4E+16	137	12
Zr04	312.0	8.7	1.32E+18	9.0E+16	120	14
Zr05	441	12	1.62E+17	4.3E+16	133	12
Zr06	300.8	8.2	1.00E+18	6.2E+16	119	14
Zr07	312.2	8.2	1.09E+18	7.2E+16	120	14
Zr09	242.8	6.4	1.14E+18	5.1E+16	110	11
LA-Zr02	12.28	0.52	3.86E+18	1.6E+17	12	3
LA-Zr03	12.42	0.52	9.88E+18	4.5E+17	12	3
LA-Zr04[e,f]	520	18	--	--	--	--
LA-Zr06	62.0	2.3	2.67E+18	1.1E+17	34	5
LA-Zr07	5.31	0.14	2.15E+19	1.0E+18	9	3
LA-Zr09	244.0	9.0	9.77E+17	8.2E+16	110	11
LA-Zr12	325	12	1.03E+18	1.4E+17	121	14
LA-Zr14	189	11	2.72E+18	2.6E+17	93	7
LA-Zr15[e]	496	16	--	--	157	13
LA-Zr17[e,f]	511	18	--	--	--	--
LA-Zr19	433	15	2.52E+17	1.0E+17	132	13

[a]Reported isotopic alpha doses estimate the degree of alpha radiation damage that might be expected for each zircon crystal at the ZrnHe closure age.
[b]Represents propagated zircon U-Th concentration, TtnHe date, and ZrnHe date uncertainties.
[c]Closure temperature estimates derived from QTQt thermal modeling as discussed in the text.
[d]2σ estimated closure temperature uncertainties based on replicate thermal models.
[e]Isotopic alpha dose could not be estimated at the time of zircon helium closure by the method outlined in 'a' because the ZrnHe date for the crystal falls within uncertainty of the inverse-variance weighted mean TtnHe date. We consider these crystals to have cooled through helium closure with effectively zero damage.
[f]Thermal modeling indicates the ZrnHe date occurs within the period of rapid cooling following crystallization of the syenite. Reasonable closure temperatures for the zircon helium system could not be assigned to these grains.

the integration time and comparing the results to α_r ranges for the same crystals. As Table 2.2 shows, the results are generally consistent, especially considering that the α_r estimates are based on Raman measurements made on polished surfaces, whereas the α_i estimates are based on volumetrically averaged U and Th measurements.

Of most importance to our study is the alpha dose that might have been present in a zircon at the ZrnHe closure age. Three of our ZrnHe dates are indistinguishable (at the 2σ level) from the TtnHe weighted mean date, implying that they had insufficient time to

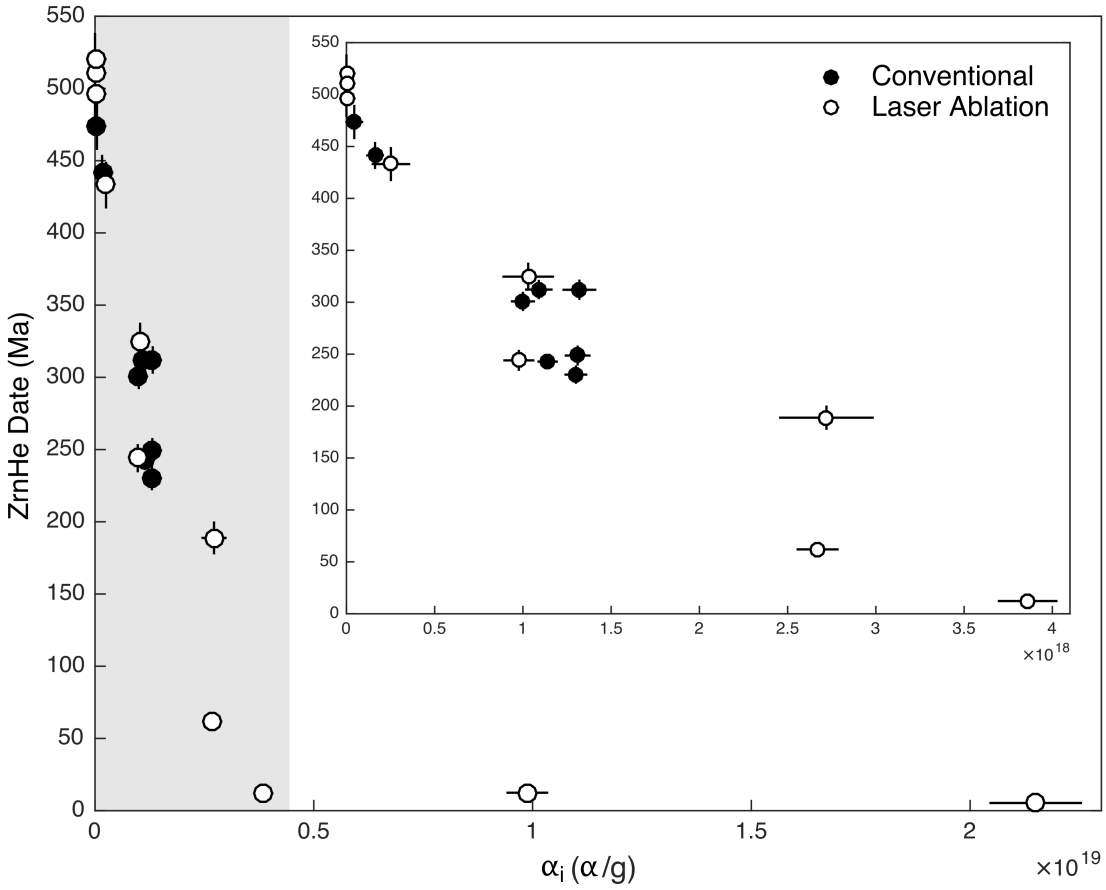

Figure 2.4. Alpha dose at the ZrnHe closure age vs. ZrnHe date. The gray shaded region highlights the the area of the plot magnified in the overlay. Error bars represent 2σ uncertainties.

accumulate significant radiation damage before closure. We use Equation 1 to calculate the α_i accumulated from the TtnHe closure age to the ZrnHe closure age for each of the remaining zircon crystals (Table 2.4). Calculated values range from 4.3 x 10^{16} to 2.1 x 10^{19} α/g, indicating that the nineteen selected zircon crystals comprise the complete radiation damage spectrum from fully crystalline to fully metamict. This finding strongly supports the hypothesis that most of the overdispersion in ZrnHe dates for the McClure Mountain syenite can be attributed to variable closure behavior related to variable alpha radiation damage from grain to grain. As illustrated in Figure 2.4, ZrnHe dates decrease significantly with

increasing alpha dose up to $\sim$4 x 10^{18} α/g. At higher damage doses, the effect becomes less pronounced, and ZrnHe dates decrease by only 7 Ma from $\sim$4 x 10^{18} to 2.1 x 10^{19} α/g.

2.5 Thermal Modeling Methods and Results

If the cooling history of the McClure Mountain syenite can be constrained independently of the ZrnHe data presented here, the relationship in Figure 4 offers a way to relate radiation damage to ZrnHe closure temperature empirically. To estimate that history, we employed a Bayesian Markov Chain Monte Carlo (MCMC) approach to inverse modeling of other available thermochronologic data for the McClure Mountain syenite using the QTQt software package of Gallagher (2012). Full details on the thermal modeling parameters, other assumptions, and modeling procedures may be found in the Supplementary Materials.

Priors (or thermochronologic inputs) for this exercise were the hornblende ^{40}Ar-^{39}Ar date of Spell et al. (2003), the mean biotite K-Ar date of Olsen et al. (1977), and our inverse-variance weighted mean TtnHe date. For our initial modeling run, we also included the inverse-variance weighted mean ApHe date as a prior. The resulting cooling history was characterized by rapid early cooling after crystallization of the syenite, followed by extremely slow cooling for hundreds of millions of years. Under such circumstances, each ApHe date is best modeled as a different proxy due to the potential effects of variable radiation damage on apatite (U-Th)/He closure temperature. We reran the model to include all ten ApHe dates using the radiation damage accumulation and annealing model (RDAAM) developed by Flowers et al. (2009) for each. The expected model produced good fits for the hornblende ^{40}Ar-^{39}Ar, the biotite K-Ar date, our TtnHe date, and some of our ApHe dates (Figure 2.5).

In order to evaluate how well the Guenthner et al. (2013) ZRDAAM model predicts the

temperature of the syenite at the (U-Th)/He closure ages of our analyzed zircons and to test the robustness of our expected thermal model, we found it useful to assign uncertainties to our modeled temperature-time curve. To do so, we repeated the model run until the mean expected thermal model and the standard deviation from the mean converged (a total of twenty repetitions). The mean expected thermal model for these repeated runs (the solid black line in Figure 2.6) indicates rapid cooling after syenite crystallization to temperatures below 200 °C by 500 Ma, followed by protracted slow cooling (at rates of 0.1 - 0.4 °C/Ma) to the present day. The error envelope (the solid gray lines in Figure 2.6) represents two standard deviations from the mean temperature history. We consider this model to be the best available estimate for the cooling history of the syenite.

As is the case for all thermal modeling, the QTQt temperature-time path shown in Figure 2.6 is not necessarily a unique fit. QTQt's Bayesian approach for determining thermal models favors the simplest thermal history that fits the available data (Gallagher, 2012). The McClure Mountain syenite may have experienced a more complex thermal history. Regionally, there is very little additional geological evidence available to help provide useful constraints on the syenite's thermal history. The timing of the Ancestral Rockies overlaps with the interval bracketed by the TtnHe and ApHe closure ages (Kluth and Coney, 1981); however, there is no obvious indication from the thermochronologic data in hand of a signal that may represent an Ancestral Rockies thermal disturbance. Apatite fission track dates from the Wet Mountains range from 300 to 140 Ma (Kelley and Chapin, 2004), suggesting that the area experienced protracted low temperatures over this period, which is consistent with our modeling results. The thermal history of the syenite post-ApHe closure is largely unconstrained. In the absence of lower temperature thermochronological data, the QTQt model assumes a constant cooling rate following ApHe closure to present day. Thus, thermal events associated with Laramide and Rio Grande rift deformation are not recorded by the the

ApHe dataset. The negative ZrnHe date vs. eU correlation strongly supports slow cooling since the late Cambrian, although it is possible the rate of protracted cooling varied some over time. The relatively simple α_i vs. ZrnHe date correlation (Figure 2.4), however, would seem an unlikely occurrence had this cooling rate varied much.

2.6 Discussion

2.6.1 Radiation Damage and Zircon (U-Th)/He Closure Temperature

Assuming that the thermal model is robust, the ZrnHe analytical data may be coupled with the model to derive an empirical relationship between α_i at the ZrnHe closure age and ZrnHe closure temperature. To develop this relationship, we projected the nineteen ZrnHe dates onto the mean expected thermal model to assign a closure temperature (T_{cb}) with 2σ uncertainties to each dated crystal. Results of this exercise are shown in Table 2.4 and Figure 2.7.

The ZrnHe dates for crystals LA-Zr04 and LA-Zr17 fall within the period of rapid cooling following crystallization of the syenite. As such, it is difficult to assign to them reasonable closure temperatures. The apparent closure temperatures for the two grains seem too high, even for undamaged zircon (Reiners et al., 2004).This may indicate that the syenite cooled more rapidly in the $\sim$25 Ma following crystallization than suggested by the thermal model. Alternatively, the two oldest laser ablation dates may not be robust. Although the laser microprobe dating method eliminates the need for alpha ejection corrections it cannot completely account for alpha particle redistribution as some of the crystal rim that might have contributed radiogenic helium to the initial ablation pit was removed during sample polishing (Horne et al., 2016; Tripathy-Lang et al., 2013).

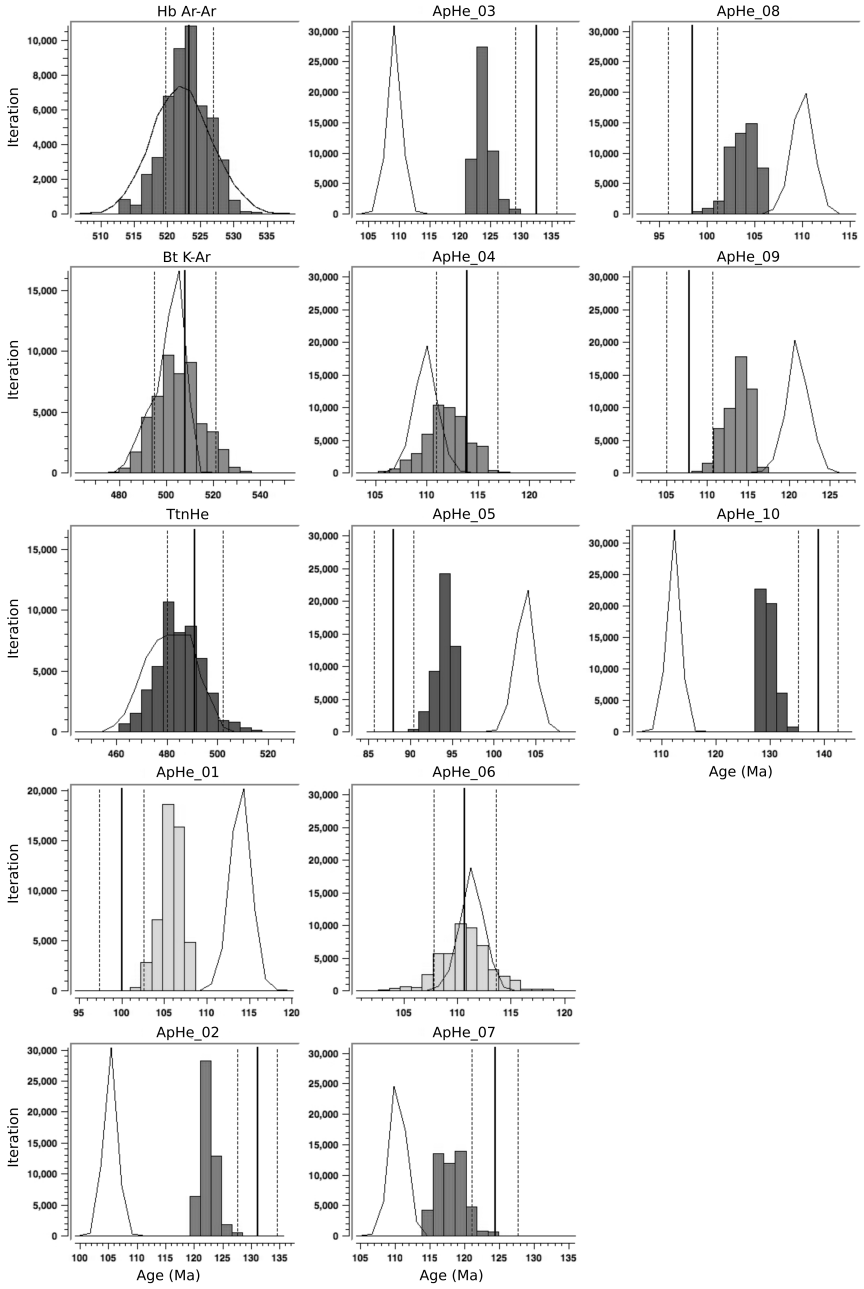

Figure 2.5. Input, sampled, and predicted thermochronometric ages for the QTQt thermal model. The black bars are the input ages and the dashed bars are the associated 2σ uncertainties. The gray histograms represent the distribution of accepted ages, and the curved black lines are the predicted ages (Gallagher, 2012).

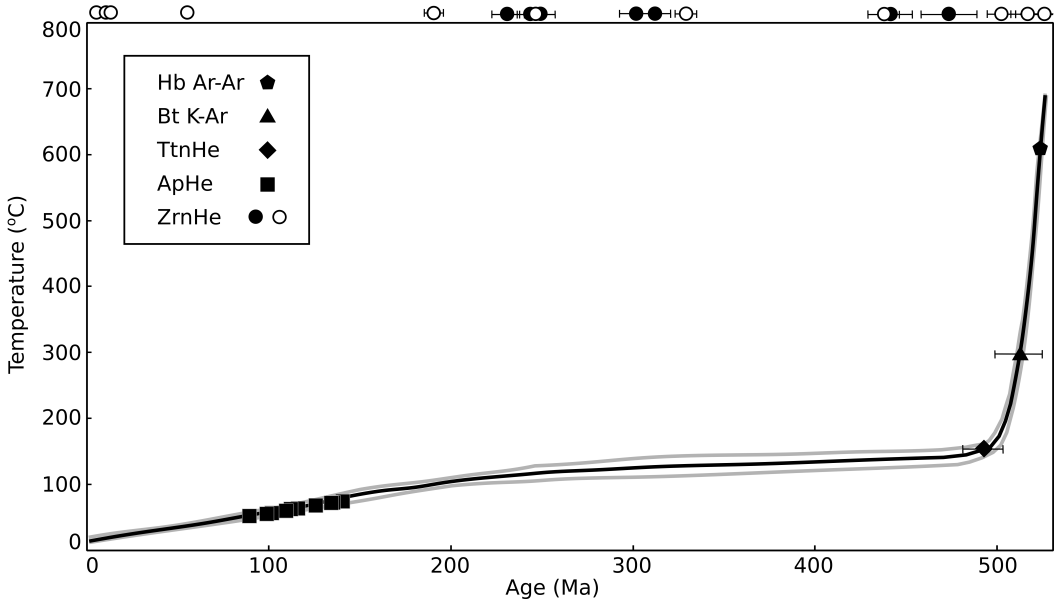

Figure 2.6. QTQt thermal model. The black line is our best estimate thermal model for the McClure Mountain syenite. The gray error envelope represents 2σ uncertainties as discussed in the text. The thermochronometric ages input as priors into the thermal model are plotted as black markers on the cooling curve. The conventional ZrnHe dates (black circles) and laser ablation ZrnHe dates (white circles) are plotted along the top of the model for visual reference.

Excluding the two oldest crystals, closure temperatures steadily decrease from 157 to 12 °C as alpha dose increases from effectively zero damage to $\sim$4 x 10^{18} α/g. At higher damages, the effect of radiation damage on closure temperature is less dramatic; from $\sim$4 x 10^{18} to 2.1 x 10^{19} α/g closure temperatures decrease by only and additional $\sim$3 °C. Four of the laser ablation ZrnHe dates (LA-Zr02, LA-Zr03, LA-Zr06, and LA-Zr07) are younger than the youngest ApHe date and consequently access lower temperatures, $<$35 °C. “Inverted" dates like these have been reported for a dataset from the Front Range, Colorado (Johnson et al., 2017). Those authors cited the utility of using such high damage zircons to detect low temperature thermal events in samples where there is a paucity of apatite crystals or where the thermal event is below the sensitivity of ApHe dating (Johnson et al., 2017).

To compare our empirical findings to the experimental findings of Guenthner et al.

(2013), we calculated closure temperature values using diffusion parameters derived from the ZRDAAM effective diffusivity equation (Guenthner et al., 2013 Equation 8). In these calculations we assume the same range of protracted cooling rates (0.1 - 0.4 °C/Ma) as estimated by our thermal model for the McClure Mountain syenite and a 56 μm effective diffusion dimension (the average radius for an equivalent sphere for the conventional ZrnHe dataset). Results are shown in Figure 2.7.

With the exception of LA-Zr15, ZRDAAM predicts closure temperatures similar to those found in our study for very low doses, $<$ 3 x 10^{17} α/g. The uncertainties in our closure temperature estimates for these low damage crystals, however, preclude our ability to evaluate the inference of Guenthner et al. (2013) that ZrnHe retentivity increases over this low dose range. At doses of $\sim$1 x 10^{18} α/g, our empirical study supports the Guenthner et al. 2013 conclusion that closure temperatures decrease with increasing damage - to a point; ZRDAAM seems to overestimate closure temperatures for most of the McClure zircons for dose levels between 1 x 10^{18} α/g and 4 x 10^{18} α/g. This finding echoes the suggestion of Powell et al. (2016) that the alpha dose required by ZRDAAM to cause a significant increase in He diffusivity may be too high.

At doses $\geq$1 x 10^{19} α/g, our results imply that closure temperature stabilizes at ca. 12-9 °C. In contrast, the ZRDAAM model predicts that zircon should no longer be retentive of radiogenic ^{4}He in this dose range and thus should yield ZrnHe dates of zero. In addition to the non-zero ZrnHe dates for highly damaged zircons reported in this study, the literature contains other examples (e.g., Orme et al., 2016; Johnson et al., 2017).

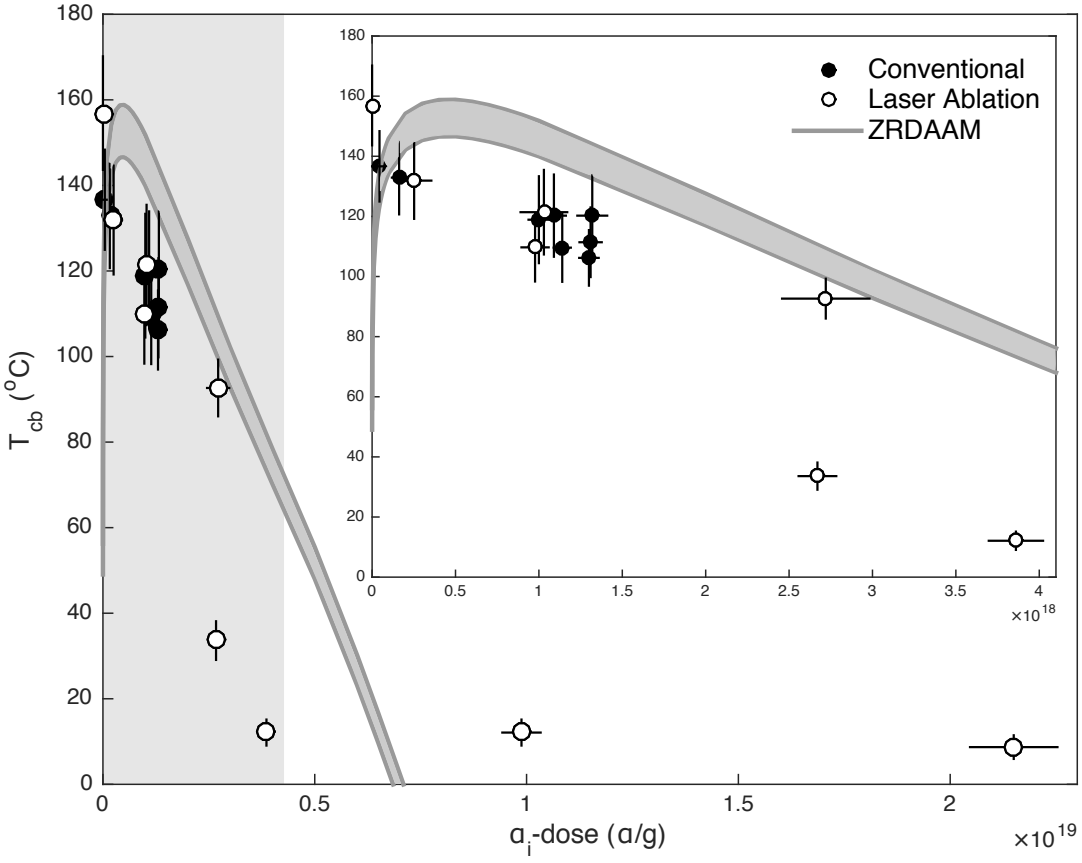

Figure 2.7. Alpha dose at the ZrnHe closure age vs. ZrnHe closure temperature. The light gray rectangular region highlights the area of the plot magnified in the overlay. Circular markers depict the empirical results for the McClure Mountain ZrnHe datasets. Error bars represent 2σ uncertainties. The dark gray shaded curve depicts closure temperature as predicted by ZRDAAM for cooling rates between 0.1 °C/Ma (lower bound) and 0.4 °C/Ma (upper bound) and the same average diffusion dimension (56 μm) as the McClure ZrnHe dataset.

2.6.2 U-Th and Radiation Damage Zoning

U-Th zoning has been known to bias (U-Th)/He dates due to its effect on alpha ejection corrections because standard corrections assume a homogeneous U-Th distribution (Farley et al., 1996; Hourigan et al., 2005). Some researchers have attempted to characterize U-Th zoning in grain populations in order to model more appropriate corrections (e.g.

Hourigan et al., 2005, Orme et al. 2016, Bargnesi et al. 2016). Backscattered electron and cathodoluminescence images of McClure zircon reveal both oscillatory and geometrically complex zoning patterns that are far too irregular for us to consider this approach for our conventional ZrnHe dataset (Schoene and Bowring, 2006). Our laser ablation ZrnHe dataset demonstrates that, even when alpha ejection corrections are eliminated from the equation, ZrnHe dates are still significantly over dispersed.

U-Th zoning can be problematic in a different way for the (U-Th)/He thermochronology of pre-Cenozoic zircons with thermal histories that permit long-term accumulation of radiation damage prior to zircon helium closure. Zones with higher U-Th will accumulate more radiation damage over the same cooling interval, and thus, at any given time during that interval, helium diffusivities in high U-Th zones will differ substantially from those in zones with low U-Th. Depending on how great the intra-crystalline variation in U-Th is and the duration of the damage accumulation interval, the effects on bulk, single-crystal ZrnHe closure could be significant. Recent work by Danišík et al. (2017) demonstrated that radiation damage zoning can result in a heterogeneous distribution of helium in zircon. They reported a laser ablation ^{4}He map for a zircon crystal with a high eU, metamict core. Within the core, no helium was detected, which the authors interpreted as direct evidence of extremely high helium diffusivity in amorphous zones (Danišík et al., 2017). This evidence suggests that radiation damage zoning can indeed result in intra-crystalline variations in helium diffusion kinetics.

Guenthner et al. (2013) explored the implication of this for the case in which zoning is concentric from core to rim, but the implications for more complex and variable zoning like that found in the McClure Mountain syenite zircons are less obvious. We infer that the large variation in radiation damage in the crystals dated by laser ablation, implied by the large range of α_r values (Table 2.2), reflects the complexity of U-Th zoning in these

crystals and the protracted cooling history of the syenite (Figure 2.6). Spatial maps of the FWHM of the $\nu_3(SiO_4)$ Raman band on the polished surfaces ablated for (U-Th)/He and U/Pb dating (Figure 2.1) show, for example, that 10 x 10 μm domains of highly crystalline and amorphous zircon can be found adjacent to one another in the interiors of zircons LA-Zr06 and LA-Zr12. Further, no two of the zircon crystals dated by laser ablation show similar patterns in FWHM variation. The greater dispersion in laser ablation ZrnHe dates may suggest that the laser ablation method is more strongly affected by radiation damage zoning than conventional ZrnHe dating. The conventional ZrnHe dates could be said to reflect the 'bulk' radiation damage of the crystal and may be interpreted as an 'averaging' of the laser ablation dates. Alternatively, the greater dispersion in laser ablation dates may simply be due to the chance selection of older and younger grains.

Thermal histories deduced from radiation damage accumulation and annealing models of apatite and zircon datasets generally assume either a homogeneous U-Th and radiation damage distribution or only simple, concentric zoning patterns. The results of our Raman mapping and that of Danisik et al. (2017) suggest that such approaches may be too simplistic for many zircons of Phanerozoic or Precambrian age that are highly zoned and slowly cooled over hundreds of millions of years. It seems unlikely that any single zircon damage-diffusivity model is applicable to all ZrnHe datasets (Guenthner et al., 2013). This may explain some of the discrepancies between ZRDAAM predictions for closure temperatures of the McClure Mountain zircons and the predictions made by our thermal model, as well as similar discrepancies reported elsewhere (Johnson et al., 2017; Orme et al., 2016; Powell et al., 2016). For example, although the α_i values for laser ablation zircon crystals LA-Zr03 and LA-Zr07 suggest that the crystals are fully amorphous, α_r values show that small crystalline domains have remained intact (Table 2.2 & Table 2.4). These crystalline domains

may still be helium retentive, and they may help to explain why these two zircon crystals record non-zero ZrnHe dates.

The prevalence of ZrnHe date-eU trends in diverse geologic settings, however, suggests that despite intra-crystalline complexities, radiation damage in zircon does provide valuable thermal information. The reported successful applications of ZRDAAM to overdispersed ZrnHe datasets also support this conclusion (Guenthner et al., 2015; Guenthner et al., 2014; Orme et al., 2016). Radiation damage accumulation and annealing models however, should be applied cautiously to slowly cooled, ancient ZrnHe datasets with an understanding of the applied model's limitations. Using laser microprobe zircon dating and Raman microanalytical techniques in conjunction with, or in place of, conventional ZrnHe dating techniques can help to interpret complex ZrnHe datasets. Whenever possible, multiple mineral-isotopic systems should be employed to add additional, independent constraints to a sample's thermal history.

2.7 Conclusions

ZrnHe dates for the McClure Mountain syenite are significantly overdispersed with conventional ZrnHe dates and laser ablation ZrnHe dates ranging from 230.3 to 474 Ma and 5.31 to 520 Ma, respectively. Most of this dispersion can be attributed to the influence of radiation damage on zircon helium systematics. In this contribution, we derive empirical constraints on the relationship between alpha dose (α_i) and ZrnHe closure temperature by coupling our analytical data to an independently constrained thermal model. If we assume that this thermal model is robust, the zircon radiation damage accumulation and annealing model of Guenthner et al. (2013) overestimates closure temperatures for most McClure zircons from $\sim$1 x 10^{18} to 4 x 10^{18} α/g, implying higher helium diffusivity in the McClure

crystals than predicted by their model. At damage doses >7 x 10^{18} α/g, Guenthner et al. (2013) model predicts that zircon should no longer be helium retentive. However, McClure zircon crystals with isotopic alpha doses in excess of this threshold record positive ZrnHe dates and closure temperatures of ca. 9 to 12 °C.

Raman maps of McClure zircon reveal that U-Th zoning coupled with a protracted cooling history has resulted in strong radiation damage zoning. Such zoning suggests intra-crystalline variations in helium diffusion kinetics in the McClure grains and may explain some of the discrepancies between the ZRDAAM predictions for the McClure Mountain dataset and the closure temperatures indicated by our thermal modeling. Radiation damage zoning is likely to be of concern for most ancient, slowly cooled ZrnHe datasets given zircon's propensity for U-Th zonation. However, the possibility that zircons in individual bedrock samples may contain highly variable radiation damage - and this damage is directly related to helium diffusivity - is potentially exciting from the perspective of thermochronology; different crystals essentially may be different (U-Th)/He thermochronometers. However, it appears that our current quantitative understanding of how to relate ZrnHe closure dates to closure temperatures remains inadequate to fully realize this potential. As our community works toward the necessary refinements, we recommend that, whenever possible, multiple thermochronometers should be used to add additional, independent constraints to thermal models.

2.8 Supplementary Materials

2.8.1 Conventional (U-Th)/He Analytical Methods

After selected zircon and apatite crystals were measured for alpha-ejection corrections and titanite crystals were abraided, grains were loaded into niobium tubes for isotopic analysis. Helium measurements were made with an Australian Scientific Instruments (ASI) Alphachron system. This system uses a 45W infrared (980 nm) diode laser for gas extraction and a Balzers Prisma QMS 200 quadrupole mass spectrometer for isotopic analysis. Zircon and titanite grains were heated for ten minutes at 20 A, and apatite grains were heated for five minutes at 9 A. Extracted gases were mixed with a ^{3}He spike of known quantity to allow for isotope-dilution analysis before being purified of reactive gases using hot and cold metal alloy getters. Fish Canyon zircon (28.38 $\pm$ 0.73 Ma, (Horne et al., 2016)), Fish Canyon titanite (27.98 $\pm$ 0.86 Ma, (Horne et al., 2016)), and Durango apatite (32 $\pm$ 1 Ma, (Farley, 2002)) were included as age standards to monitor system performance. Empty niobium tubes were also included in each run to allow for system blank corrections.

Following He measurement, samples were removed from the laser chamber and dissolved for U and Th isotopic analysis. Zircons and titanites were dissolved using a hydrofluoric (HF), nitric (HNO_3), and hydrochloric (HCl) acids mixed with ^{230}Th and ^{235}U spikes at high temperatures and pressures in Parr digestion vessels. Apatites were dissolved using HNO_3 acid mixed with ^{230}Th and ^{235}U spikes. The U and Th content of dissolved samples were measured together with standard spiked solutions on a Thermo Scientific ICAP-Q inductively coupled, plasma source mass spectrometer using isotope dilution.

The concentration of ^{235}U was derived using the natural uranium isotopic ratio. U, Th, and He data were then used to calculate (U-Th)/He dates for each sample iteratively. Raw

zircon and apatite dates were corrected for alpha ejection following the formulations of Hourigan et al. (2005) assuming a uniform U-Th distribution. Reported uncertainties for individual grains represent the propagation of analytical errors at the 2σ level. The Hampel identifier method (Pearson, 2001) was employed in an attempt to identify outliers more than four median average deviations from the median for the titanite and apatite data sets. No outliers were identified. We calculated the inverse-variance weighted mean, the standard deviation of the weighted mean, and the mean squared weighted deviation (MSWD) (Wendt and Carl, 1991) for both the titanite and apatite. The MSWD for both data sets was higher than the ca. 95% confidence range of its predicted value of 1.0. To obtain more realistic uncertainties, we multiplied the 2σ standard deviations for each data set by the square root of its respective MSWD (Ludwig, 2003).

2.8.2 Raman Spectroscopy and Laser Microprobe Zircon Dating

Raman spectra were acquired using a HORIBA Scientific Jobin Yvon XploRA PLUS confocal Raman microscope. The system employs a 532 nm laser, Syncerity 1024 x 256 pixel CCD detector cooled to -60 °C, and Tango motorized XYZ stage. Spectra were acquired using 20-25 mW laser power, 100x magnification, a 2400 gr/mm diffraction grating, a 100 μm slit, and a 100 μm confocal pinhole. The laser spot size was $\sim$1 μm. Acquisition times ranged from 10-35 seconds with 1-3 accumulations. The system was calibrated daily using the silicon 520.7 cm^{-1} Raman peak. Spectral resolution for this setup is 1.4 cm^{-1}. Thirty-six Raman spectra were acquired from the polished surface of each crystal at 10 μm intervals in a 60 μm x 60 μm square grid. Baseline corrections and Gaussian-Lorentzian peak fitting were performed in HORIBA Scientific LabSpec6 software.

Measured FWHM were corrected for instrument bias using the apparatus function (Nasdala et al., 2001).

The Torr Seal mount was then placed under ultrahigh vacuum in the noble gas extraction line. A Photons Machine Analyte G2, 193 nm Atlex 300 ArF excimer laser was focused on the mount's surface through a sapphire window view port. 15 μm diameter cylindrical pits were ablated into each sample. Lasing conditions were 5 mJ laser energy, 50$\%$ output power, and 5 Hz pulse frequency. Eighty shots were fired per sample. The extracted gases were purified using metal alloy getters and a cryogenic trap. Helium isotopic abundances were measured using a GVI/Thermo Electron *Helix SFT* mass spectrometer on an ion-counting electron multiplier detector. The instrument ^{4}He sensitivity was monitored routinely by measuring ^{4}He standard air shots. The mount was then removed from the extraction line, and ablated laser pit topographies were scanned using an ADE PhaseShift *MicroXAM* interferometeric microscope. This data was processed using an in-house *Matlab* script to calculate ablated pit volumes. A nominal uncertainty of 1$\%$ was assigned to all pit volumes. Using this volume, helium isotopic abundances were converted to isotopic concentrations.

The mount was then transferred to a Photon Machines *HelEx Active* two-volume laser ablation cell. A 50 μm diameter laser pit was centered on top of the existing helium pit. Lasing conditions were 4 mJ laser energy, 50 $\%$ output power, and 10 Hz pulse frequency. Four hundred shots were fire per sample. The ablated pits were $\geq$ 20 μm deeper than the helium pit to minimize the effects of intra-crystalline alpha particle redistribution due to parent element zonation given that alpha stopping distances in zircon are $\sim$17 - 20 μm (Horne et al., 2016; Hourigan et al., 2005). The ablated material was analyzed for U, Th, and Pb isotopic abundances using a inductively coupled plasma source Thermo Scientific *iCAP Q* quadropole mass spectrometer. The mount was then removed from the cell, and ablated pit topographies scanned once more using the interferometric microscope. The volume of

material ablated for the U, Th, and Pb analyses was calculated as the volume of the second ablated pit minus the volume of the ablated helium pit. U and Th isotopic concentrations were normalized to a sintered, synthetic rock standard made from micromilled zircon powder, 'SynZircon' (^{238}U = 426 $\pm$ 14 ppm, ^{232}Th = 206 $\pm$ 19 ppm) (Monteleone et al., 2009).

The LA-ICPMS results were processed through the Iolite software package for U/Pb apparent age calculations using the U-Pb Geochronology data reduction scheme (Paton et al., 2010). The reported ^{235}U/^{207}Pb dates were corrected for common lead (Andersen, 2002; Petrus and Kamber, 2012). Plesovice zircon (337.13 $\pm$ 0.37 Ma (Sláma et al., 2008)) and zircon reference 91500 (1065.4 $\pm$ 0.6 Ma (Wiedenbeck et al., 1995)) were employed as U-Pb age standards. In addition to the U-Pb age standards, Fish Canyon Tuff zircon grains (ZrnHe date = 28.38 $\pm$ 0.73 Ma (Horne et al., 2016)) were analyzed alongside the McClure grains to serve as a (U-Th)/He age standard.

2.8.3 QTQt thermal model input parameters and constraints

Ar diffusion in hornblende was modeled assuming a 500 μm diffusion domain, spherical geometry, and diffusivity parameters from Harrison (1981). For biotite, we assumed a 500 μm domain size, infinite cylinder geometry, and diffusivity parameters from Grove and Harrison (1996). For titanite, we used a 200 μm diffusion domain (the average grain size of the dated grains prior to abraision), spherical geometry and He diffusion parameters from Reiners and Farley (1999). The radiation damage accumulation and annealing model (RDAAM) developed by Flowers et al. (2009) was employed to model diffusion kinetics for the ten ApHe dates given each crystal's ^{238}U, ^{232}Th, ^{147}Sm, and ^{4}He concentrations, grain

radius, and assuming a spherical geometry. All thermochronometric dates were re-sampled using MCMC during the course of the model.

The model space sampled 0 to 800 °C from 600 Ma to the present. The thermal history was given three constraints: 1) the syenite crystallized at 700 ± 50 °C at the zircon ID-TIMS U-Pb date of 523.98 ± 0.12 Ma; 2) no reheating events occurred, and 3) the present day temperature is 10 ± 10°C. Proposal scale parameters were 5 °C, 5 Ma, 1 for He diffusion, and a 45 °C birth temperature. A series of 50,000 burn-in and post burn-in iterations were run for each of the twenty model repetitions. Acceptance rates for the time, temperature, and He diffusion proposal moves were between 46 and 63 %. Acceptance rates for birth and death transformations were between 2 and 6%.

2.9 Acknowledgments

This work was supported by the National Science Foundation [EAR-1346321]. We would like to thank David Shuster and two anonymous reviewers for their invaluable feedback that helped to improve this manuscript..

References

Alexander, E. C. J., G. M. Mickelson, and M. A. Lanphere (1978). MMhb-1: A new ^{40}Ar-^{39}Ar dating standard. *Short Papers of the Fourth International Conference, Geochronology, Cosmochronology, and Isotope Geology*. 78-701. U.S. Geological Survey, pp. 6–8.

Andersen, T. (2002). Correction of common lead in U-Pb analyses that do not report ^{204}Pb. *Chemical Geology* 192, pp. 59–79.

Ault, A. K. and R. M. Flowers (2012). Is apatite U-Th zonation information necessary for accurate interpretation of apatite (U-Th)/ He thermochronometry data? *Geochimica et Cosmochimica Acta* 79, pp. 60–78.

Baksi, A. K., D. A. Archibald, and E. Farrar (1996). Intercalibration of ^{40}Ar/^{39}Ar dating standards. *Chemical Geology* 129 (3-4), pp. 307–324.

Bargnesi, E. A., D. F. Stockli, J. K. Hourigan, and C. Hager (2016). Improved accuracy of zircon (U-Th)/He ages by rectifying parent nuclide zonation with practical methods. *Chemical Geology* 426, pp. 158–169.

Baughman, J., R. M. Flowers, J. R. Metcalf, and T. Dhansay (2017). Influence of radiation damage on titanite He diffusion kinetics. *Geochimica et Cosmochimica Acta* 205, pp. 50–64.

Bernet, M. (2009). A field-based estimate of the zircon fission-track closure temperature. *Chemical Geology* 259 (3-4), pp. 181–189.

Brandon, K. A., T. M. Roden-Tice, and J. I. Garver (1998). Late Caneozoic exhumation of the Cascadia accretionary wedge in the Olympic Mountains, northwest Washington State. *Geological Society of America Bulletin* 110 (8), pp. 985–1009.

Cherniak, D. J., E. B. Watson, and J. B. Thomas (2009). Diffusion of helium in zircon and apatite. *Chemical Geology* 268, pp. 155–166.

Chew, D. M., J. A. Petrus, and B. S. Kamber (2014). U-Pb LA-ICPMS dating using accessory mineral standards with variable common Pb. *Chemical Geology* 363, pp. 185–199.

Coyle, D. A. and G. A. Wagner (1998). Positioning the titanite fission-track partial annealing zone. *Chemical Geology* 149 (1-2), pp. 117–125.

Danišík, M., B. I. A. McInnes, C. L. Kirkland, B. J. McDonald, N. J. Evans, and T. Becker (2017). Seeing is believing: Visualization of He distribution in zircon and implications for thermal history reconstruction on single crystals. *Science Advances* 3 (2), e1601121.

Ehlers, T. A. and K. A. Farley (2003). Apatite (U-Th)/He thermochronometry: Methods and applications to problems in tectonic and surface processes. *Earth and Planetary Science Letters* 206 (1-2), pp. 1–14.

Enkelmann, E. and J. I. Garver (2016). Low-temperature thermochronology applied to ancient settings. *Journal of Geodynamics* 93, pp. 17–30.

Evans, N. J., J. P. Byrne, J. T. Keegan, and L. E. Dotter (2005). Determination of uranium and thorium in zircon, apatite,and fluorite: Application to laser (U–Th)/He thermochronology. *Journal of Analytical Chemistry* 60 (12), pp. 1159–1165.

Ewing, R. C., A. Meldrum, L. Wang, W. J. Weber, and L. R. Corrales (2003). Radiation effects in zircon. *Zircon: Reviews in Mineralogy & Geochemistry*. Ed. by J. M. Hanchar and P. W. O. Hoskin. 53. Chantilly, VA: Mineralogical Society of America, pp. 387–425.

Farley, K. A. (2002). (U-Th)/He dating: Techniques, calibrations, and applications. *Noble Gases in Geochemistry and Cosmochemistry: Reviews in Mineralogy & Geochemistry*. Ed. by P. D., C. J. Ballentine, and R. Wieler. 47. Washington, DC: Mineralogical Society of America, pp. 819–844.

Farley, K. A., D. L. Shuster, and R. A. Ketcham (2011). U and Th zonation in apatite observed by laser ablation ICPMS, and implications for the (U-Th)/He system. *Geochimica et Cosmochimica Acta* 75 (16), pp. 4515–4530.

Farley, K. A., R. A. Wolf, and L. T. Silver (1996). The effects of long alpha-stopping distances on (U-Th)/He ages. *Geochimica et Cosmochimica Acta* 60 (21), pp. 4223–4229.

Flowers, R. M. (2009). Exploiting radiation damage control on apatite (U-Th)/He dates in cratonic regions. *Earth and Planetary Science Letters* 277, pp. 148–155.

Flowers, R. M., S. A. Bowring, and P. W. Reiners (2006). Low long-term erosion rates and extreme continental stability documented by ancient (U-Th)/He dates. *Geology* 34 (11), pp. 925–928.

Flowers, R. M., R. A. Ketcham, D. L. Shuster, and K. A. Farley (2009). Apatite (U-Th)/He thermochronometry using a radiation damage accumulation and annealing model. *Geochimica et Cosmochimica Acta* 73 (8), pp. 2347–2365.

Gallagher, K. (2012). Transdimensional inverse thermal history modeling for quantitative thermochronology. *Journal of Geophysical Research* 117 (B2), B02408.

Grove, M. and T. M. Harrison (1996). ^{40}Ar* diffusion in Fe-rich biotite. *American Mineralogist* 81 (7-8), pp. 940–951.

Guenthner, W. R., P. W. Reiners, P. G. DeCelles, and J. Kendall (2015). Sevier belt exhumation in central Utah constrained from complex zircon (U-Th)/He data sets: Radiation damage and He inheritance effects on partially reset detrital zircons. *Bulletin of the Geological Society of America* 127 (3-4), pp. 323–348.

Guenthner, W. R., P. W. Reiners, R. A. Ketcham, L. Nasdala, and G. Giester (2013). Helium diffusion in natural zircon: Radiation damage, anisotropy, and the interpretation of zircon (U-TH)/He thermochronology. *American Journal of Science* 313 (3), pp. 145–198.

Guenthner, W. R., P. W. Reiners, and Y. Tian (2014). Interpreting date-eU correlations in zircon (U-Th)/He datasets: A case study from the Longmen Shan, China. *Earth and Planetary Science Letters* 403, pp. 328–339.

Harrison, T. M. (1981). Diffusion of ^{40}Ar in Hornblende. *Contributions to Mineralogy and Petrology* 78 (3), pp. 324–331.

Horne, A. M., M. C. van Soest, K. V. Hodges, A. Tripathy-Lang, and J. K. Hourigan (2016). Integrated single crystal laser ablation U/Pb and (U-Th)/He dating of detrital accessory minerals - Proof-of-concept studies of titanites and zircons from the Fish Canyon tuff. *Geochimica et Cosmochimica Acta* 178, pp. 106–123.

Hourigan, J. K., P. W. Reiners, and M. T. Brandon (2005). U-Th zonation-dependent alpha-ejection in (U-Th)/He chronometry. *Geochimica et Cosmochimica Acta* 69 (13), pp. 3349–3365.

Hurley, P. M. (1952). Alpha ionization as a cause of low helium ratios. *Eos, Transactions American Geophysical Union* 33 (2), pp. 174–183.

Hurley, P. M. and H. W. Fairbairn (1953). Radiation damage in zircons: A possible age method. *Bulletin of the Geological Society of America* 64 (June), pp. 659–674.

Johnson, J. E., R. M. Flowers, G. B. Baird, and K. H. Mahan (2017). “Inverted" zircon and apatite (U-Th)/He dates from the Front Range, Colorado: High-damage zircon as a low-temperature (<50°C) thermochronometer. *Earth and Planetary Science Letters* 466, pp. 80–90.

Kelley, S. A. and C. E. Chapin (2004). Denudation history and internal structure of the Front Range and Wet Mountains, Colorado, based on apatite fission track thermochronology. *New Mexico Bureau of Geology and Mineral Resources* Bulletin 160, pp. 41–78.

Kluth, C. F. and P. J. Coney (1981). Plate tectonics of the Ancestral Rocky Mountains. *Geology* 9 (1), pp. 10–15.

Laslett, G. M., P. F. Green, I. R. Duddy, and A. J. W. Gleadow (1987). Thermal annealing of fission tracks in apatite 2. A quantitative analysis. *Chemical Geology: Isotope Geoscience section* 65 (1), pp. 1–13.

Ludwig, K. R. (2003). Mathematical–statistical treatment of data and errors for ^{230}Th/U Geochronology. *Uranium-Series Geochemistry: Reviews in Mineralogy & Geochemistry*. Ed. by B. Bourdon, G. M. Henderson, C. C. Lundstrom, and S. P. Turner. 52. Chantilly, VA: Mineralogical Society of America, pp. 631–656.

Monteleone, B. D., M. C. van Soest, K. V. Hodges, G. M. Moore, J. W. Boyce, and R. L. Hervig (2009). Assessment of Alternative [U] and [Th] Zircon Standards for SIMS. *American Geophysical Union Fall Meeting, San Francisco, CA, USA*.

Murakami, T., B. C. Chakoumakos, R. C. Ewing, G. R. Lumpkin, and W. J. Weber (1991). Alpha-decay event damage in zircon. *American Mineralogist* 76, pp. 1510–1532.

Nasdala, L., J. Gotze, J. M. Hanchar, M. Gaft, and M. R. Krbetschek (2004). Luminescence techniques in Earth Sciences. *EMU Notes in Mineralogy* 6, pp. 43–91.

Nasdala, L., M. Wenzel, G. Vavra, G. Irmer, T. Wenzel, and B. Kober (2001). Metamictisation of natural zircon: Accumulation versus thermal annealing of radioactivity-induced damage. *Contributions to Mineralogy and Petrology* 141 (2), pp. 125–144.

Olson, J. C., R. F. Marvin, R. L. Parker, and H. H. Mehnert (1977). Age and tectonic setting of lower Paleozoic alkalic and mafic rocks, carbonatites, and thorium veins in south-central Colorado. *Jour. Research U.S. Geol. Survey* 5 (6), pp. 673–687.

Orme, D. A., W. R. Guenthner, A. K. Laskowski, and P. W. Reiners (2016). Long-term tectonothermal history of Laramide basement from zircon–He age-eU correlations. *Earth and Planetary Science Letters* 453, pp. 119–130.

Palenik, C. S., L. Nasdala, and R. C. Ewing (2003). Radiation damage in zircon. *American Mineralogist* 88, pp. 770–781.

Parker, R. L. and F. A. Hildebrande (1963). Preliminary report on alkalic intrusive rocks in the northern Wet Mountains, Colorado. *Geol Survey Prof Paper*, E8–E10.

Paton, C., J. D. Woodhead, J. C. Hellstrom, J. M. Hergt, A. Greig, and R. Maas (2010). Improved laser ablation U-Pb zircon geochronology through robust downhole fractionation correction. *Geochemistry, Geophysics, Geosystems* 11 (3).

Pearson, R. K. (2001). *Exploring Data in Engineering, the Sciences, and Medicine*. Oxford Univ. Press.

Petrus, J. A. and B. S. Kamber (2012). VizualAge: A Novel Approach to Laser Ablation ICP-MS U-Pb Geochronology Data Reduction. *Geostandards and Geoanalytical Research* 36 (3), pp. 247–270.

Powell, J., D. Schneider, D. Stockli, and K. Fallas (2016). Zircon (U-Th)/He thermochronology of Neoproterozoic strata from the Mackenzie Mountains, Canada: Implications for the Phanerozoic exhumation and deformation history of the northern Canadian Cordillera. *Tectonics* 35 (3), pp. 663–689.

Reiners, P. W. and M. T. Brandon (2006). Using thermochronology to understand orogenic erosion. *Annual Review of Earth and Planetary Sciences* 34 (1), pp. 419–466.

Reiners, P. W. and K. A. Farley (1999). Helium diffusion and (U-Th)/He thermochronometry of titanite. *Mineralogical Magazine* 62A (2), pp. 1249–1250.

Reiners, P. W., K. A. Farley, and H. J. Hickes (2002). He diffusion and (U-Th)/He thermochronometry of zircon: Initial results from Fish Canyon Tuff and Gold Butte. *Tectonophysics* 349 (1-4), pp. 297–308.

Reiners, P. W., T. L. Spell, S. Nicolescu, and K. A. Zanetti (2004). Zircon (U-Th)/He thermochronometry: He diffusion and comparisons with ^{40}Ar/^{39}Ar dating. *Geochimica et Cosmochimica Acta* 68 (8), pp. 1857–1887.

Renne, P. R., C. C. Swisher, A. L. Deino, D. B. Karner, T. L. Owens, and D. J. DePaolo (1998). Intercalibration of standards, absolute ages and uncertainties in ^{40}Ar/^{39}Ar dating. *Chemical Geology* 145 (1-2), pp. 117–152.

Samson, S. D. and J. Alexander E C (1987). Calibration of the interlaboratory ^{40}Ar-^{39}Ar dating standard, MMhb-1. *Chemical Geology: Isotope Geoscience section* 66 (1-2), pp. 27–34.

Schoene, B. and S. A. Bowring (2006). U-Pb systematics of the McClure Mountain syenite: Thermochronological constraints on the age of the ^{40}Ar/^{39}Ar standard MMhb. *Contributions to Mineralogy and Petrology* 151 (5), pp. 615–630.

Shuster, D. L., R. M. Flowers, and K. A. Farley (2006). The influence of natural radiation damage on helium diffusion kinetics in apatite. *Earth and Planetary Science Letters* 249 (3-4), pp. 148–161.

Sláma, J. et al. (2008). Plešovice zircon - A new natural reference material for U-Pb and Hf isotopic microanalysis. *Chemical Geology* 249 (1-2), pp. 1–35.

Spell, T. L. and I. McDougall (2003). Characterization and calibration of ^{40}Ar/^{39}Ar dating standards. *Chemical Geology* 198 (3-4), pp. 189–211.

Tripathy-Lang, A., K. V. Hodges, B. D. Monteleone, and M. C. van Soest (2013). Laser (U-Th)/He thermochronology of detrital zircons as a tool for studying surface processes in modern catchments. *Journal of Geophysical Research: Earth Surface* 118 (3), pp. 1333–1341.

Weber, W. J. (1990). Radiation-induced defects and amorphization in zircon. *Journal of Materials Research* 5 (11), pp. 2687–2697.

Weisberg, W. R., J. R. Metcalf, and R. M. Flowers (2014). Thermochronology of the McClure Mountain syenite; characterization of new He thermochronometers and constraints on the cooling history of the Wet Mountains, Colorado. *Abstracts with Programs - Geological Society of America* 46 (6), p. 512.

Wendt, I. and C. Carl (1991). The statistical distribution of the mean squared weighted deviation. *Chemical Geology* 86, pp. 275–285.

Wiedenbeck, M., P. Allé, F. Corfu, W. L. Griffin, M. Meier, F. Oberli, A. Von Quadt, J. C. Roddick, and W. Spiegel (1995). Three natural zircon standards for U-Th-Pb, Lu-Hf, trace element and REE analyses. *Geostandards Newsletter* 19 (1), pp. 1–23.

Zhang M S, E. K. H., G. C. Capitani, H. Leroux, A. M. Clark, J. Schluter, and R. C. Ewing (2000). Annealing of α-decay damage in zircon: A Raman spectroscopic study. *Journal of Physics: Condensed Matter* 12, pp. 3131–3148.

Chapter 3

MAPPING RADIATION DAMAGE ZONING IN ZIRCON USING RAMAN SPECTROSCOPY

Alyssa J. Anderson,[1], John M. Hanchar[2], Kip V. Hodges[1], and Matthijs C. van Soest[1]

[1]School of Earth and Space Exploration, Arizona State University, Tempe, AZ 85287, USA.

[2]Earth Sciences, Memorial University of Newfoundland, St. John's, NL A1B 3X7, Canada.

3.1 Abstract

Complex U and Th zoning in zircon can result in the heterogeneous accumulation of radiation damage in zircon crystals that have experienced prolonged residence at near-surface temperatures. Because the properties of Raman vibrational spectra in zircons reflect the degree of radiation damage, detailed Raman maps of zircon interiors can be used to quantify the distribution of radiation damage in compositionally zoned crystals. In this contribution, we present high resolution (e.g., 2.5 μm) Raman maps for Proterozoic zircon crystals from the Lyon Mountain Granite (LMG), found in the Adirondack Mountains of New York. Since the $\nu_3(SiO_4)$ stretching vibrational mode commonly used to derive quantitative α dose estimates is only present at very low intensities in some of the zircon crystals mapped, we evaluate the sensitivity of two SiO_4 bending vibrations to radiation damage and establish a useful α dose calibration for the $\nu_4(SiO_4)$ mode. Quantitative α-dose maps of the LMG zircon crystals display complex radiation damage zoning that closely resemble patterns in cathodoluminescence images of the same crystals. These α-dose maps can be used to investigate intracrystalline variations in any damage-dependent material

property. As two example applications, we model helium diffusion and laser ablation rates in the LMG zircon crystals and discuss the implications of these findings for (U-Th)/He and U/Pb chronology of old, zoned zircon.

3.2 Introduction

The typically high U and Th contents of zircon ($ZrSiO_4$), coupled with its persistence in the geologic record, makes it one of earth science's most valuable chronometers. Zircon U/Pb geochronology has played a pivotal role in constraining the timing and tempo of geologic and biologic processes from the Hadean to the Pleistocene (e.g. Bowring and Schmitz, 2003; G. Gehrels, 2014; Schoene, 2014), while zircon (U-Th)/He thermochronology is a powerful technique used to resolve thermal histories of rocks in the upper crust to study tectonic, geomorphic, and climatic processes in diverse geologic settings (e.g. Reiners and M. T. Brandon, 2006; Reiners et al., 2017). The radiation damage content of a zircon crystal depends on its age, U and Th content, and thermal history (e.g. Ewing et al., 2003; W. J. Weber, 1990). Continued accumulation of radiation damage can result in the complete amorphization or metamictization of zircon crystals.

The accumulation of radiation damage strongly affects zircon material properties, including the mineral's ability to retain radiogenic helium (Anderson et al., 2017; Guenthner et al., 2013; Hurley, 1952) and lead (Geisler et al., 2002; Mezger and Krogstad, 1997). Consequently, many zircon studies can benefit from finding a way to easily and quickly characterize accumulated radiation damage in zircon crystals. Raman spectroscopy is a simple, non-destructive technique that rapidly provides information about bonding environments in minerals. Pioneering work by Nasdala et al. (1995) demonstrated that key Raman SiO_4 vibrations predictably broaden and shift to lower frequencies in response to

increasing radiation damage as bonding environments become increasingly irregular. These key spectral features can be used to quantitatively characterize radiation damage in zircon (Nasdala et al., 2001; Palenik et al., 2003).

Zircon's propensity for U and Th zonation, however, suggests that a single Raman microanalysis analysis may not be sufficient to characterize the potential complexities of radiation damage in an individual crystal. In principle, radionuclide zoning can lead to the heterogeneous accumulation of radiation damage in crystals that have spent significant time at near-surface temperatures, such that zones with lower U and Th contents should have less radiation damage than zones with higher U and Th contents (Marillo-Sialer et al., 2016; Nasdala et al., 2005; Palenik et al., 2003). The development of confocal Raman microscopes with high-precision, motorized stages permits the acquisition of thousands of spectra within hours or even minutes (Lehnert, 2000). Such systems afforded us the opportunity to use Raman spectroscopy to quantitatively map radiation damage zoning in zircon crystals and evaluate the potential affects of such zoning on geochronological and thermochronological investigations. In this contribution, we present a case study that evaluates radiation damage zoning in a suite of Proterozoic zircon crystals from the Lyon Mountain Granite (LMG) found in the Adirondack Mountains of New York with strong compositional zoning (Nasdala et al., 2005; Valley et al., 2011).

3.3 Background

3.3.1 Radiation Damage in Zircon

Zircon, $ZrSiO_4$, is a nesosilicate that crystallizes in the tetragonal crystal system (space group $I4_1/amd$). Zircon typically incorporates 10's to 1000's ppm of U and Th into

its crystal structure by the simple substitution $(U,Th)^{4+} \leftrightarrow Zr^{4+}$. Radiation damage is predominantly attributed to alpha decay of ^{238}U, ^{235}U, ^{232}Th, and their radioactive daughter products (Ewing et al., 2003; W. J. Weber, 1990; W. Weber, 1993). During an alpha decay event, kinetic energy is lost via the emission of an alpha particle and the recoil of the heavy daughter nuclide. Alpha recoil results in a cascade of atomic collisions and displacements creating low-density centers surrounded by halos of interstitial defects. Alpha particles, in turn, lose energy primarily through ionization with only some atomic collisions occurring near the end of their $\sim$16 to 20 μm trajectory (Ewing et al., 2003; W. Weber, 1993). Fission of ^{235}U also generates significant structural damage (Ketcham et al., 2013), but fission events occur infrequently relative to alpha decays.

A nominal alpha particle fluence, or α dose, can be calculated for a sample from its measured U and Th contents and an estimate for the damage accumulation interval (t):

$$\alpha\ dose = \frac{8 \cdot N_A \cdot^{238} U}{M_{238} \cdot 10^6} \cdot (e^{\lambda_{238} t} - 1) + \frac{7 \cdot N_A \cdot^{235} U}{M_{235} \cdot 10^6} \cdot (e^{\lambda_{235} t} - 1) + \frac{6 \cdot N_A \cdot^{232} Th}{M_{232} \cdot 10^6} \cdot (e^{\lambda_{232} t} - 1) \tag{3.1}$$

where concentrations are in ppm; λ and M values are the respective decay constants and atomic masses for ^{238}U, ^{235}U, and ^{232}Th; and N_A is Avogadro's number (Holland and Gottfried, 1955).

As α dose increases, SiO_4 tetrahedral bonds lengthen and bonding environments become increasingly irregular as SiO_4 tetrahedra are tilted and distorted (Murakami et al., 1991; Nasdala et al., 2001). Consequently, the unit cell expands and short-range order $-$ and eventually long-range order $-$ decreases, ultimately leading to the amorphization of the zircon structure given a long enough damage accumulation interval and prolonged residence at low temperatures (Meldrum et al., 1998; Murakami et al., 1991; W. J. Weber, 1990). These structural changes affect zircon optical, physical, and chemical properties such as

refractive indices, density, hardness, elastic moduli, thermal conductivity, and solubility (Ewing et al., 2003; Holland and Gottfried, 1955).

Radiation damage in zircon can anneal over time, such that the zircon crystallization age is not always an appropriate estimate for the damage accumulation interval (Equation 3.1). The annealing process strongly depends on the extent of damage present in the crystal structure and the annealing temperature (Ewing et al., 2003; Geisler et al., 2001; Ginster et al., 2019; Zhang et al., 2000), so the amount of damage in a zircon crystal intrinsically depends on the sample's thermal history (Nasdala et al., 2004). Laboratory heating experiments on short timescales (hours to days) have shown that alpha radiation damage partially to fully anneals at temperatures above $\sim$800 °C, with some partial recovery evident at temperatures as low as $\sim$450 °C in heavily damaged samples (Geisler et al., 2001; Zhang et al., 2000). Zircon fission track studies have demonstrated that fission tracks anneal at even lower temperatures ($\sim$200 to 300 °C) on geologic timescales (Bernet, 2009; Yamada et al., 2007), but alpha radiation damage low-temperature annealing kinetics on geologic timescales are poorly understood at present.

3.3.2 Radiation Damage and Raman Spectroscopy

Zircon has twelve Raman-active vibrational modes (Dawson et al., 1971). The four most intense bands occur at Raman shifts of 1008, 974, 439, and 357 cm^{-1}. These bands were assigned by Dawson et al. (1971) to internal SiO_4 stretching (1008 and 974 cm^{-1}) and bending (439 and 357 cm^{-1}) vibrations: ν_3 (B_{1g} mode), ν_1 (A_{1g} mode), ν_2 (A_{1g} mode), and ν_4(E_g mode), respectively. In this contribution, we have chosen to follow the band assignments presented by Dawson et al. (1971), but we note that other researchers have

assigned the 357 cm^{-1} band as an external E_g mode, a vibrational mode that involves zirconium-silicate bonds (Nasdala et al., 2003; Syme et al., 1977).

In well-ordered, highly crystalline zircon Raman bands are distinct and narrow (Nasdala et al., 2001). All main bands in the zircon Raman spectrum broaden, shift to lower frequencies, and decrease in intensity as atomic positions, bond angles, and bond lengths become increasingly irregular as radiation damage accumulates (Nasdala et al., 2001; Nasdala et al., 1995; Nasdala et al., 2003).This effect is best characterized for the ν_3 stretching mode (Nasdala et al., 2001; Palenik et al., 2003). In highly crystalline zircons, this mode has a spectral position near $\sim$1008 cm^{-1} and a FWHM (full width at half-maximum) of < 3 cm^{-1}. In completely metamict zircon, its spectral position down-shifts to 1000 to 955 cm^{-1}, and its FWHM broadens to >30 cm^{-1}.

Nasdala et al. (2001) established the first Raman-based radiation damage calibration by relating measured $FWHM_{\nu_3}$ values to α dose values for Saxonian rhyolite and lunar zircon crystals calculated from their measured U and Th contents (Equation 3.1). These crystals were considered to have experienced minimal annealing, so their respective U/Pb ages were used as the estimated damage accumulation interval. Results yielded the equation:

$$\alpha\ dose = \frac{FWHM_{\nu_3} - 1.2}{140} \cdot 10^{19} \tag{3.2}$$

where α dose is in α/g and $FWHM_{\nu_3}$ is in cm^{-1}. This calibration is only appropriate for highly crystalline to moderately damaged zircons with $FWHM_{\nu_3}$ values ranging from 1.2 to 20 cm^{-1}. Palenik et al. (2003) later extended this calibration curve to include higher damage doses by relating measured $FWHM_{\nu_3}$ values from a Sri Lankan zircon crystal with strong radiation damage zoning to α dose values calculated from the crystal's measured U and Th contents and an estimated damage accumulation interval of $\sim$375 Ma. Calculated α doses for this crystal ranged from 2.1 - 10.1 x10^{18} α/g. By pairing these data with that of Nasdala

et al. (2001), the authors established the equation:

$$\alpha\ dose = \frac{1}{-B} \cdot \ln\left(1 - \frac{FWHM_{\nu_3}}{A}\right) \tag{3.3}$$

where A is the asymptotically approached maximum $FWHM_{\nu_3}$ (35.64 cm^{-1}) and B is the mass of damaged material generated per alpha decay event (5.49 x10^{-19} /g) (Palenik et al. (2003) Equation 4). Equation 3.3 reflects the full range of radiation damage observed in natural zircon crystals. Although the authors do no report uncertainties for A and B, a refitting of the data yields 2σ uncertainties for A and B of 1.5 $cm^{-1}$and 0.44 x10^{-19}/g, respectively.

An important limitation of the use of Equation 3.3 to estimate α dose from Raman data is that the intensity of ν_3 strongly depends on the crystallographic orientation of the zircon grain with respect to the incident laser beam and the polarization directions of the incident and scattered energy beams (Dawson et al., 1971; Syme et al., 1977). Consequently, the ν_3 peak is sometimes only present at very low intensities $-$ or is entirely absent from $-$ some spectra, making quantitative Raman-based α dose estimates impossible (Figure 3.1). The other main Raman bands ν_1, ν_2, and ν_4 however, often exhibit strong intensities and well-defined peak shapes. These bands also broaden and shift to lower frequencies in response to radiation damage (Nasdala et al., 1995), and they can be used to quantify radiation damage if appropriately calibrated. A useful calibration for ν_4 is presented in the results section.

3.4 Lyon Mountain Granite Zircon

Proterozoic zircon crystals from a hand sample from the Lyon Mountain Granite (LMG) in the Adirondack Mountains of New York offer a natural laboratory for investigating the

effects of radiation damage zoning in zircon. These crystals, separated from a sample of microcline granite collected along NYS Route 374 Northwest of Dannemora, New York by Valley et al. (2011) (sample LMG-99-6c), exhibit complex U and Th zoning with low actinide cores (UO_2 + $ThO_2 \leq 0.02$ wt.%) and high actinide rims (UO_2 + ThO_2 = 0.1 - 0.4 wt.%) (Nasdala et al., 2005). Reported ion microprobe U/Pb Concordia dates for cores and rims are ca. 1150 Ma and 1050.5 $\pm$ 5.2 (2σ), respectively (Valley et al., 2011). Based on U-Th ion microprobe and Raman $FWHM_{\nu_3}$ measurements reported by others for the cores of two LMG crystals (JHA-1 analyses 1-o and 1-p and JHA-2 analysis 2-t from Nasdala et al. 2005), we estimate that the zircon crystals have acquired an α dose equivalent to a damage accumulation interval of $\sim$560 Ma. This interval is much younger than the U/Pb core and rim crystallization ages, suggesting that the LMG crystals that a significant portion of their radiation damage has been annealed (Nasdala et al. 2004). Nevertheless, previous Raman work by Nasdala et al. (2005) demonstrated that the LMG zircons have acquired strong radiation damage zoning characterized by predominantly low damage cores and high damage rims $-$ consistent with the radionuclide zoning $-$ and α-damage halos along core-rim boundaries.

3.5 Methods

LMG zircons were hand-picked under a transmitted light microscope. Crystal cores and rims were easy to distinguish visibly: cores appeared brown, cracked, and contained mineral inclusions, while rims were colorless and intact with little evidence of mineral inclusions (McLelland et al., 2001; Nasdala et al., 2005; Valley et al., 2011). Selected crystals were mounted in epoxy or Torr Seal (a low vapor pressure epoxy) with their *c*-axes oriented approximately parallel to the mounts' surfaces, polished, and imaged on a scanning electron

microscope using cathodoluminescence (CL). Additional information about our imaging methods can be found in the Supplementary Materials.

High resolution (2.5 μm) Raman maps were acquired for eight LMG zircon crystals using a confocal *XploRa PLUS* Raman system with motorized scanning stage. This system has a 532 nm green diode laser and − in the configuration described in the Supplementary Materials − a lateral laser spot size and a depth of focus of $\sim$1 μm. A total of 2441 to 6406 spectra were acquired per crystal. Maps were batch processed using HORIBA Scientific *LabSpec6* software to generate peak position and FWHM maps for the ν_2, ν_3, and $\nu_4(SiO_4)$ vibrational modes. Estimated uncertainties for reported peak positions are approximately $\pm$1 cm^{-1}. Following Palenik et al. (2003), we assume uncertainties of 5% for FWHM values <22 cm^{-1} and 10% for FWHM values >22 cm^{-1} (2σ).

3.6 Results

3.6.1 Calibrating the SiO_4 Bending Vibrations

Figure 3.1 shows a representative Raman spectrum for each zircon crystal. Results reveal significant crystal-to-crystal variations in the relative and absolute intensities of the ν_2, ν_3, and $\nu_4(SiO_4)$ vibrational modes. The ν_3 stretching mode has strong intensity in spectral maps of Zr01, Zr06, Zr07, and Zr08 , but it has low intensity − or is entirely absent from − spectral maps of Zr02, Zr03, Zr04, and Zr05. The lower frequency bending modes (ν_2 and ν_4) have high intensities in spectral maps Zr01, Zr02, Zr03, Zr04, Zr05, and Zr06 and moderate to low intensities in maps of Zr07 and Zr08. We attribute these variations to minor differences in crystallographic orientation and the microscope stage rotation angle between the eight crystals.

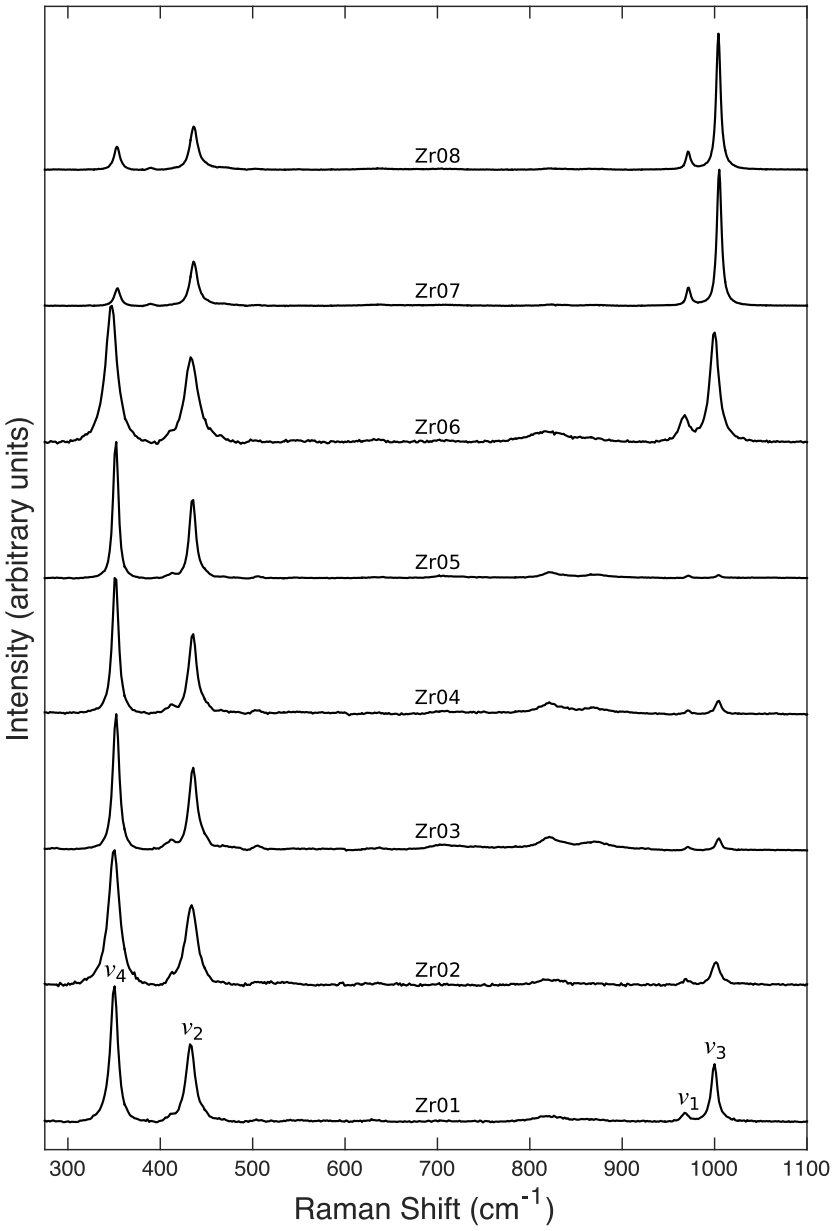

Figure 3.1. Representative Raman spectra for the eight mapped LMG zircon crystals.

Since the ν_3 mode has very low intensity in four of our eight Raman maps, we needed an alternative way in which to quantify radiation damage in these crystals. We first investigated the sensitivity of the ν_4 and ν_2 bending modes to radiation damage. We focused our calibration efforts on samples Zr01 and Zr06, since they are the two Raman maps in which

the ν_2, ν_3 and ν_4 peaks are all three present with strong intensities. Figure 3.3 shows FWHM values for these peaks compared to their respective spectral positions. The data points plotted represent peaks with intensities greater than 1000 counts and FWHM values between 5 and 30 cm^{-1} (for ν_3) or between 5 and 35 cm^{-1} (for ν_2 and ν_4). These constraints were added to help exclude low intensity, poorly-defined, and anomalous peaks due to either surface imperfections, poor automated focus, scattering from mineral inclusions, or scattering from the mounting material.

These results showed that the Raman shift values for the ν_3 and ν_4 peak positions decrease linearly with increasing respective FWHM (Figure 3.2), consistent with previous findings (Nasdala et al., 2001; Nasdala et al., 1995; Palenik et al., 2003). Measured $FWHM_{\nu_4}$ values ($\sim$8 to 34 cm^{-1}) have a greater range than $FWHM_{\nu_3}$ values ($\sim$6 to 25 cm^{-1}), which may suggest that ν_4 is a more sensitive indicator of radiation damage. The range in peak positions for these two vibrational modes is about 12 cm^{-1} ($\sim$1005 to 993 cm^{-1} for ν_3 and $\sim$352 to 340 cm^{-1} for ν_4).

The relationship between FWHM and peak position is more complex for the ν_2 bending mode. Here, there is not a simple, monotonic decrease in Raman shift with increasing $FWHM_{\nu_2}$. The ranges in measured peak position ($\sim$430 to 436 cm^{-1}) and $FWHM_{\nu_2}$ ($\sim$9 to 30 cm^{-1}) values are also more restricted. The observed complexity, in part, likely reflects poor peak fitting. The *LabSpec6* peak fitting algorithm sometimes had difficulty deconvoluting ν_2 from nearby low intensity peaks when batch processing thousands of spectra given a single set of peak fitting parameters (Figure 3.3). The more restricted range in peak parameters may also suggest that ν_2 is less sensitive to radiation damage than ν_3 and ν_4.

Both $FWHM_{\nu_4}$ and $FWHM_{\nu_2}$values increase as $FWHM_{\nu_3}$ values increase (Figure 3.4). The correlation between ν_4 and ν_3 appears strongly linear (r^2 = 0.97 , n = 6374 data pairs),

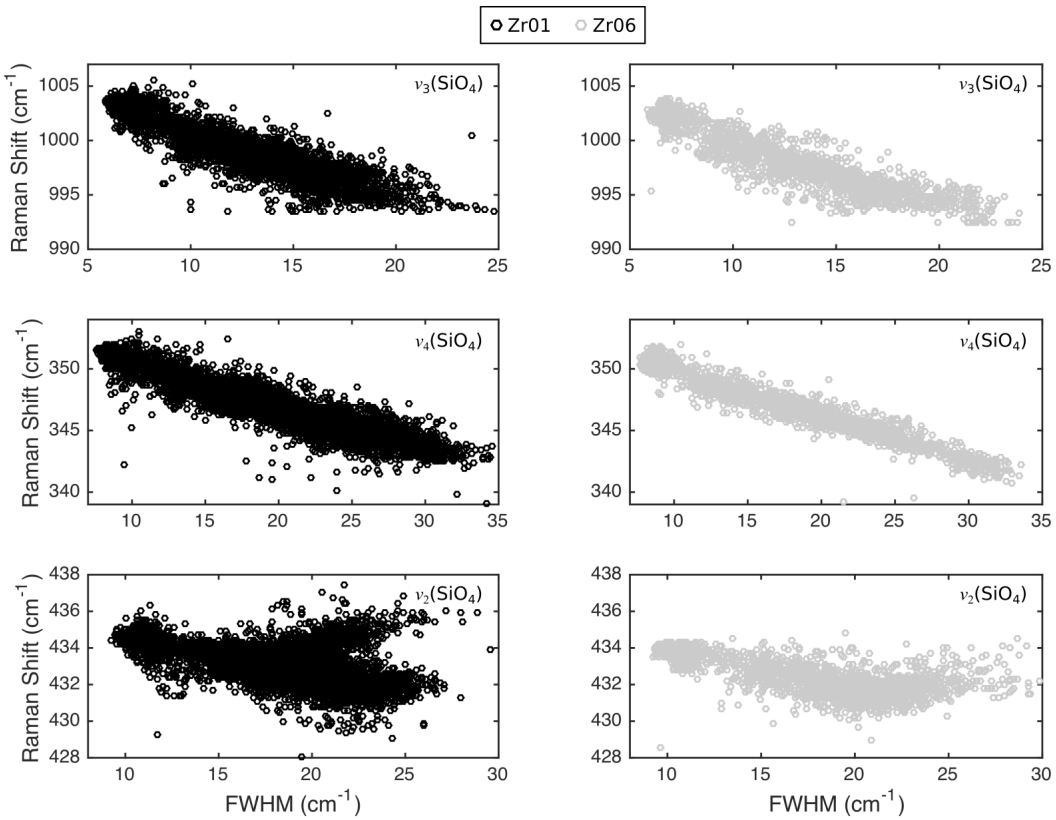

Figure 3.2. FWHM verses spectral position for the ν_3, ν_4, and $\nu_2(SiO_4)$ Raman modes for LMG zircon crystals Zr01 and Zr06.

while the correlation between ν_2 and ν_3, through predominantly linear (r^2 = 0.94, n = 6374 data pairs), exhibits a noticeable kink. We used the Hampel method (Pearson, 2001) to identify statistical outliers more than four median average deviations from the median and a York et al. (2004) linear regression of the remaining data pairs (n = 5046 and n = 5156 for the ν_4 and ν_2 correlations, respectively) to derive lines of the form:

$$FWHM_{\nu_3} = C_1 \cdot FWHM_{\nu_{2,4}} - C_2 \tag{3.4}$$

Constants C_1 and C_2 for the two linear regressions are reported in Table 3.1. These regressions yielded mean squared weighted deviations (MSWDs; Wendt and Carl, 1991)

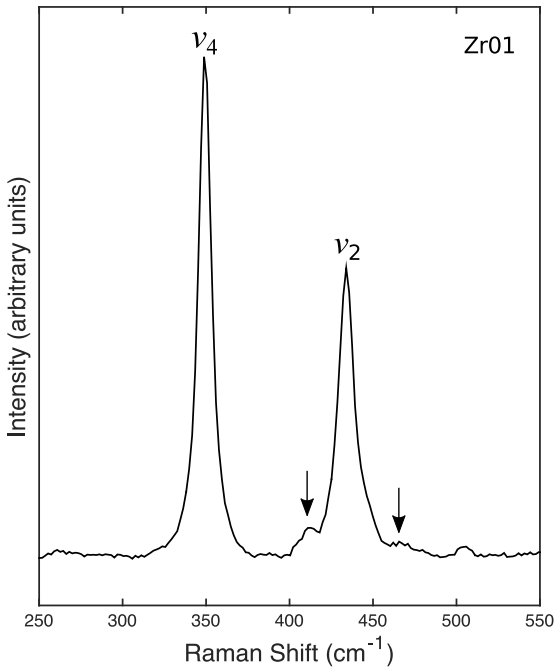

Figure 3.3. Representative Raman spectrum from Zr01 depicting low frequency SiO4 bending vibrations ν_2 and ν_4. Arrows highlight the low intensity shoulder peaks interfering with ν_2 peak fits during batch processing of spectral maps.

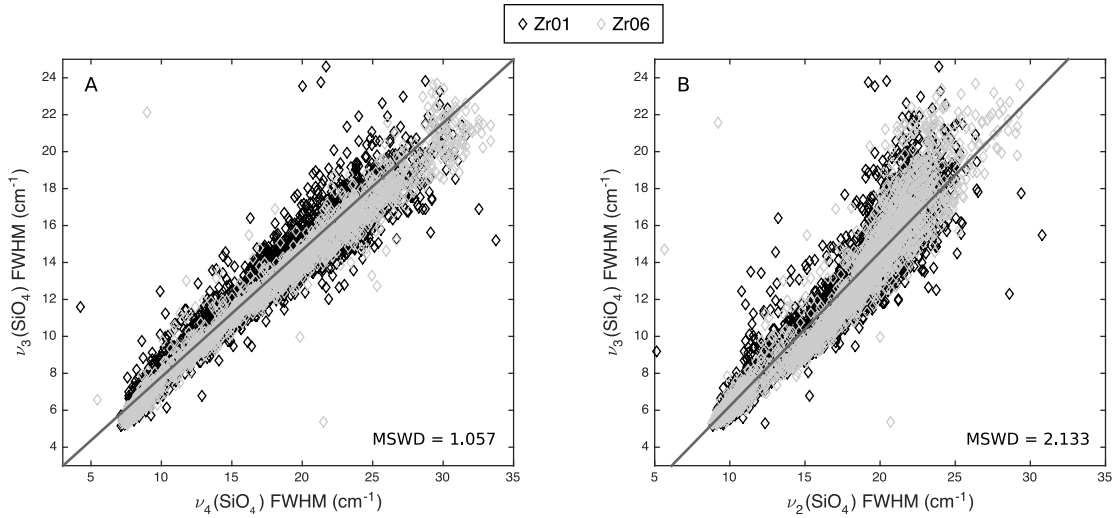

Figure 3.4. A) FWHM$_{\nu_4}$ verses FWHM$_{\nu_3}$ for LMG zircon crystals Zr01 and Zr06 (n = 6043). B) FWHM$_{\nu_2}$ verses FWHM$_{\nu_3}$ for LMG zircon crystals Zr01 and Zr06 (n = 6043). Parameters and estimated uncertainties for the York et al. (2004) linear regressions depicted are reported in Table 3.1.

Table 3.1. Raman FWHM Linear regression results.

Vibrational mode	C_1	2σ[a]	C_2	2σ[a]	N[b]	MSWD
$\nu_4(SiO_4)$	0.6824	0.0022	0.922	0.027	5046	1.057
$\nu_2(SiO_4)$	0.8172	0.0040	-1.926	0.057	5156	2.133

[a]Reported uncertainties have been expanded by the square root of the MSWD (Ludwig, 2003).
[b]Number of data pairs included in each linear regression

of 1.057 and 2.133 for the ν_4 and ν_2 correlations, respectively. The MSWDs for both datasets were slightly higher than the ca. 95% confidence range of its predicted value of 1.0, suggesting that we may have slightly underestimated our FWHM uncertainties. To obtain more realistic uncertainties for C_1 and C_2, the 2σ uncertainties reported in Table 3.1 have been expanded by multiplying by the square root of their respective MSWDs (Ludwig, 2003). We then derived α dose calibration curves for ν_4 and ν_2 by coupling Equations 3.3 and Equation 3.4, such that:

$$\alpha\ dose = \frac{1}{-B} \cdot \ln\left(1 - \frac{C_1 \cdot FWHM_{\nu_{2,4}} - C_2}{A}\right) \tag{3.5}$$

This equation allows quantitative α dose estimates to be made from measured $FWHM_{\nu_4}$ and $FWHM_{\nu_2}$ values. Based on fitting statistics and the higher confidence we have in the quality of our ν_4 peak fits, the calibration presented for ν_4 is considerably more robust than the calibration presented for ν_2.

3.6.2 Quantitative Radiation Damage Maps

Cathodoluminescence images for the eight LMG zircon crystals are presented in Figure 3.5. The imaged zircon crystals have predominantly high-intensity CL cores with faint growth and/or sector zoning and low intensity CL rims with wider, sometimes embayed zones. Although CL images like these are an important tool commonly used to characterize

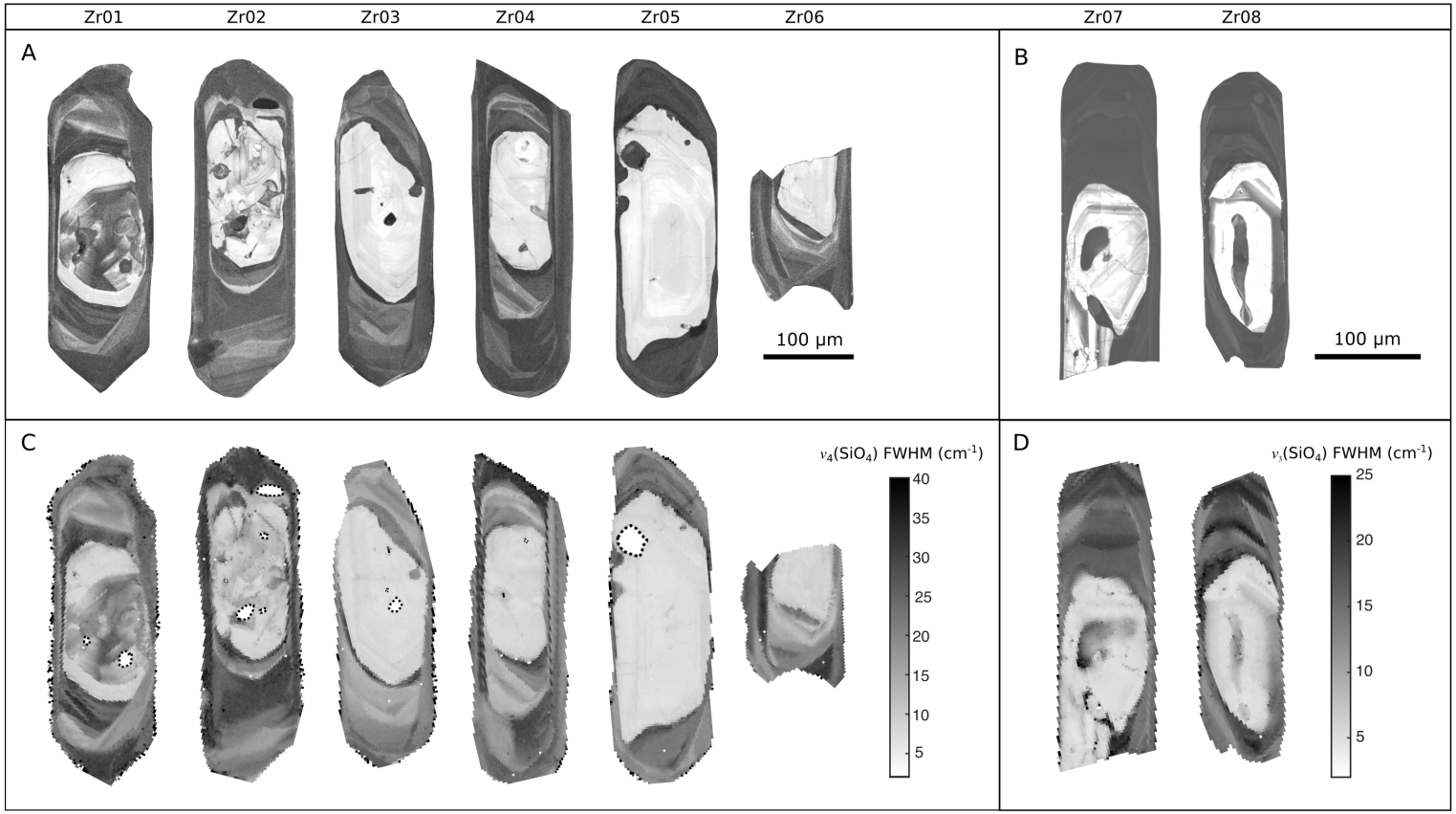

Figure 3.5. A) CL images of LMG zircon crystals Zr01 - Zr06. B) CL images of LMG zircon crystals Zr07 and Zr08. C) Raman maps of Zr01 - Zr06 depicting variations in $\nu_4(SiO_4)$ FWHM values. D) Raman maps of Zr07 and Zr08 depicting variations in $\nu_3(SiO_4)$ FWHM values. White areas with black, dashed outlines in the Raman maps indicate mineral inclusions.

zoning patterns in zircon (Corfu et al., 2003; Hanchar and Miller, 1993), they only provide qualitative information about the distribution of radiation damage in zircon crystals since CL intensity depends on both radiation damage and chemical composition (Hanchar and Rudnick, 1995; Nasdala et al., 2002).

Raman FWHM maps of the eight LMG zircon crystals (Figure 3.5) document complex intracrystalline peak width variations that closely resemble the zoning patterns observed in crystals' corresponding CL images. The maps in Figure 3.5 present the vibrational mode with the highest intensity (either FWHM_{ν_3} and FWHM_{ν_4}). Narrow FWHM values correspond to high intensity CL cores and wide FWHM values correspond to low intensity CL rims. Narrow oscillatory zoning in the crystal cores though evident in some FWHM maps, is faint compared to the CL images.

Although similar in appearance to CL images, these maps allow us to quantitatively investigate radiation damage zoning in the LMG zircon crystals. Using either Equation 3.3 or Equation 3.5, we can convert our Raman FWHM maps into more useful radiation damage maps (Figure 3.7). These α-dose maps reveal significant intracrystalline variations in radiation damage that are consistent with the crystals' radionuclide zoning. Low U-Th cores have accumulated α doses on the order of $\sim$2 to 5 x 10^{17} α/g, while high U-Th rims have accumulated higher damage doses, $\sim$7 to 18 x 10^{17} α/g. We find that damage doses can differ by an order of magnitude over length scales comparable to the spatial resolution of the spectral image (2.5 μm). These Raman-based radiation damage maps have exciting potential $-$ they can be paired with any damage-dependent property to investigate the effects of radiation damage zoning. In the sections below, we use our α-dose maps to explore how radiation damage zoning might affect zircon (U-Th)/He thermochronology and laser ablation U/Pb geochronology.

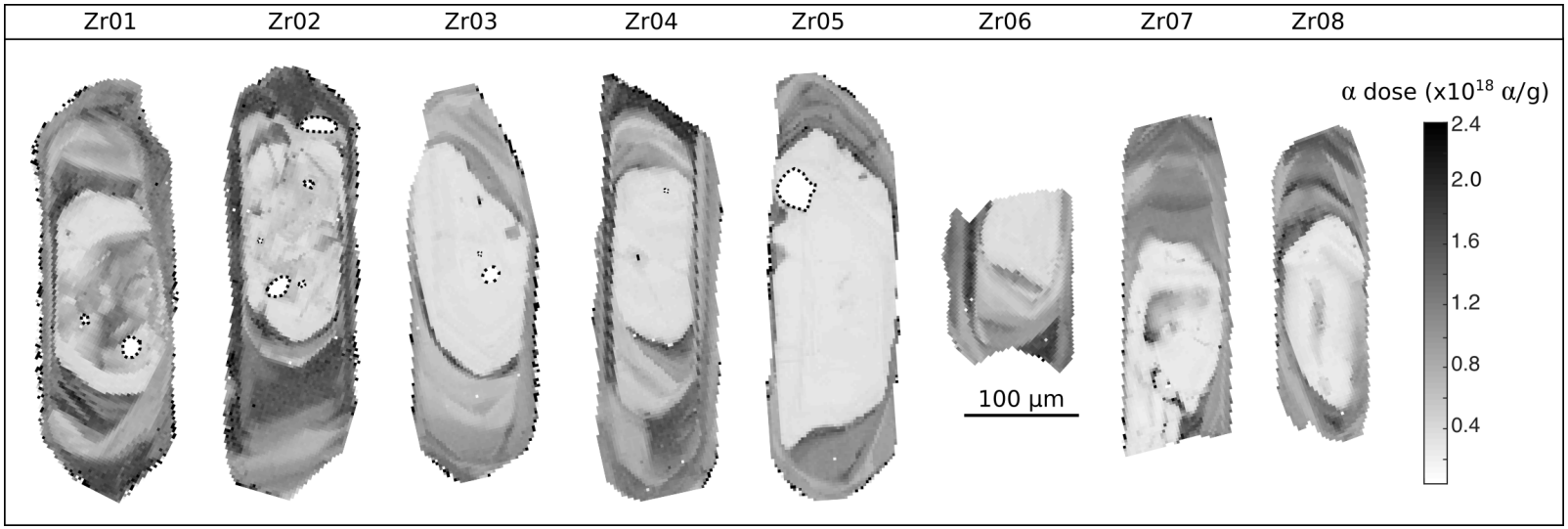

Figure 3.6. Quantitative radiation damage maps of LMG zircon crystals Zr01 - Zr08 based on Raman data presented in Fig. 3.5. White areas with black, dashed outlines in the Raman maps indicate mineral inclusions.

3.7 Radiation Damage Zoning

3.7.1 Implications for Single Crystal (U-Th)/He Thermochronology

The closure temperature for helium in zircon varies from $\sim$190 °C to below 0 °C (i.e. non retentive of helium at Earth surface temperatures) as a function of radiation damage for typical crystal sizes (50 - 100 μm) and cooling rates $\leq$10 °C/Ma (Guenthner et al., 2013). Consequently, zircon (U-Th)/He datasets from slowly cooled or reheated geologic settings often exhibit date-effective uranium (eU = [U] + 0.235 $\cdot$ [Th]) correlations (Anderson et al., 2017; Ault et al., 2018; Guenthner et al., 2015; Guenthner et al., 2013; Guenthner et al., 2014). Based on a series of step-heating experiments, Guenthner et al. (2013) proposed a model in which helium diffusivity initially decreases at low damage doses ($\leq$ 5 x 10^{17} α/g) before increasing dramatically at higher doses (Figure 3.7). This model (ZRDAAM), embedded in thermal modeling programs such as HeFTy (Ketcham, 2005) and QTQt (Gallagher, 2012), allows users to derive thermal histories from overdispersed zircon (U-Th)/He datasets that exhibit date-eU correlations.

Several studies, however, have noted apparent discrepancies between ZRDAAM predictions for zircon helium closure temperatures and empirical observations (Anderson et al., 2017; Johnson et al., 2017; Powell et al., 2016). These studies showed that some zircon grains retain helium despite having α doses $-$ calculated from the crystals' bulk U and Th contents $-$ that suggest that they should have negative closure temperatures and, consequently, zero apparent ages. These discrepancies could be explained, in part, by the effects of radiation damage zoning on zircon helium systematics (Anderson et al., 2017; Danišík et al., 2017; Guenthner et al., 2013; Powell et al., 2016). Recent work by Danišík et al. (2017) unequivocally demonstrated through laser ablation helium mapping of a zoned, Proterozoic

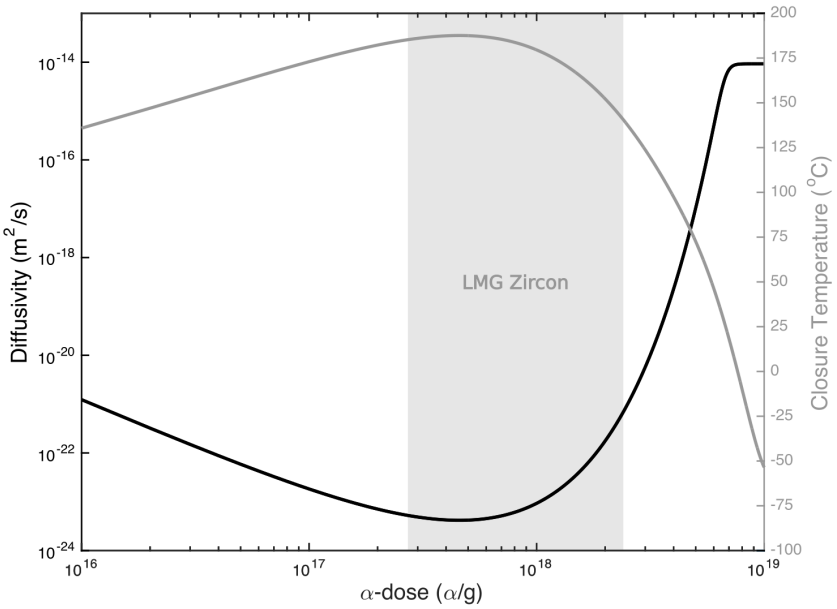

Figure 3.7. ZRDAAM model depicting changes in helium diffusivity (calculated at 200 °C) and bulk closure temperature as a function of radiation damage (Guenthner et al., 2013). Closure temperature calculations assume a 50 μm diffusion dimension, a spherical geometry, and a cooling rate of 10 °C/Ma. The gray shaded region highlights the range in α dose values determined for the eight Raman-mapped LMG zircon crystals.

zircon crystal that metamict zones can lose helium while more crystalline zones retain it, indicating that different zones possess different helium diffusivities. ZRDAAM and other damage accumulation and annealing models commonly used to interpret low-temperature thermochronometric datasets assume a single diffusivity for each (U-Th)/He date based on a crystal's bulk U and Th contents (Flowers, 2009; Gautheron et al., 2009; Guenthner et al., 2013; Willett et al., 2017) and do not account for these potential effects.

Guenthner et al. (2013) attempted to model the effects of radiation damage zoning on (U-Th)/He dates for the simplified case in which a grain has concentric zoning with either high eU rims or high eU cores for a range of bulk eU contents (250 - 1250 ppm). They found that high eU rims produced systematically younger (U-Th)/He dates compared to crystals with homogeneous eU contents, while high eU cores yielded complex date-eU

correlations depending on the magnitude of zoning and the modeled thermal history. The authors suggested that corrections could be applied to (U-Th)/He dates in these "worst case scenarios" if laser ablation U-Th depth profiling were used to characterize zoning patterns in the dated grains. However, many natural zircon crystals like the LMG crystals have complex and decidedly non-concentric zoning patterns which frustrate attempts to use one-dimensional U-Th depth profiling to correct for the effects of intra-crystalline variations in radiation damage.

In Figure 3.8, we depict helium diffusivity maps of two LMG zircons (Zr01 and Zr04) based on their α-dose maps and the ZRDAAM model. These maps reveal complex intracrystalline variations in helium diffusivity with changes occurring over very short length scales ($\sim$5 μm). Predicted diffusivity is more than $\sim$25 times faster in higher damage zones compared to lower damage zones within crystal cores. While these diffusivities were calculated for a single temperature (200 °C), we note that the magnitude of variations is temperature independent, since the activation energy for helium diffusion in zircon is essentially invariant over the α dose range investigated in the LMG crystals (Guenthner et al., 2013). The differences in diffusivity therefore predominantly reflect differences in the pre-exponential diffusivity constant (D_0) as a function of α dose.

Bulk helium closure temperatures calculated using the minimum and maximum predicted diffusivities differ by $\sim$25 °C (T_{cb} calculations assume a 50 μm diffusion dimension, a 1 °C/Ma cooling rate, and a spherical geometry). How much this might impact a (U-Th)/He dataset or geological interpretations invariably depends on the sample's thermal history. We note, however, that a 25 °C difference in bulk helium closure temperature among dated zircon crystals from a single rock sample given a 1 °C/Ma cooling rate would yield a 25 Ma age dispersion.

As highlighted in Figure 3.7, the α dose range in the LMG zircon crystals correlates

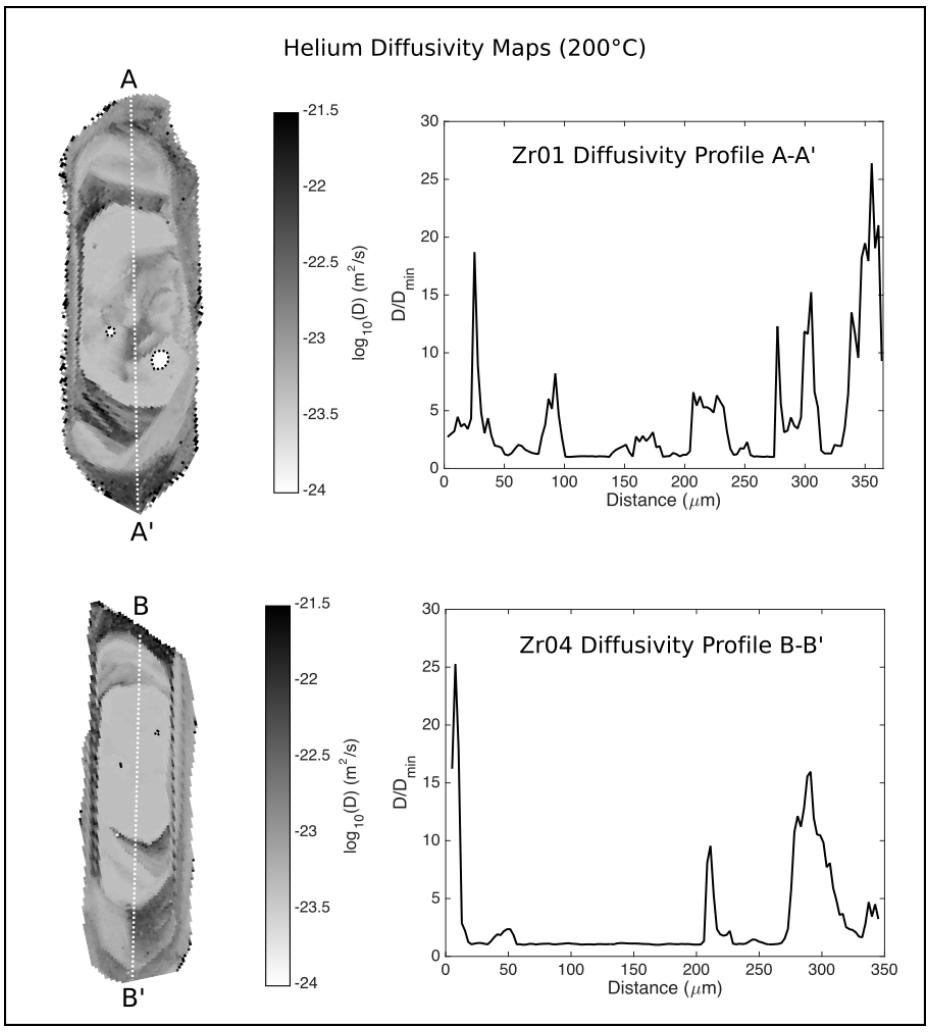

Figure 3.8. Modeled helium diffusivity maps and diffusivity profiles for Zr01 and Zr04 calculated at 200 °C using ZRDAAM (Guenthner et al., 2013). White areas with black, dashed outlines indicate mineral inclusions.

to a relatively restricted range in helium diffusivity. At higher damage doses, helium diffusion increases dramatically (Guenthner et al., 2013), such that we might expect even larger magnitudes of intracrystalline variations in zircon crystals with more enriched U-Th zones or in zircon grains that have experienced longer damage accumulation intervals than the LMG crystals. Given zircon's propensity for complex radionuclide zoning, it is likely that sample-to-sample variations in radiation damage zoning contributes substantially

to the (U-Th)/He age dispersion found in many single bulk crystal datasets for ancient, zoned zircons. The (U-Th)/He datasets most likely to be severely impacted by radiation damage zoning are slowly cooled samples and those that have experienced partial resetting due to burial reheating or other thermal disturbances after having accumulated significant amounts of radiation damage. Damage-diffusivity models − even with modeled zoning corrections based on one-dimensional laser ablation U-Th depth profiles − cannot fully capture the associated complexity in diffusion kinetics in individual zircons and is unlikely to substantially reduce overdispersion in affected datasets.

3.7.2 Implications for Laser Ablation U/Pb and (U-Th)/He Chronology

Ultraviolet laser microprobes are extensively used for high spatial resolution U/Pb and (U-Th)/He dating of zircon (Evans et al., 2015; G. E. Gehrels et al., 2008; Günther et al., 1997; Horn et al., 2000; Horne et al., 2016; Jackson et al., 2004; Tripathy-Lang et al., 2013; Vermeesch et al., 2012). Such studies focus on polished sections of crystals which can be fully characterized prior to laser ablation isotopic analysis using techniques such as wavelength-dispersive spectroscopy X-ray mapping, Raman spectroscopy, and both backscattered electron and cathodoluminescence imaging. Such metadata can permit the avoidance of inclusions and heavily radiation-damaged zones that may have lost excessive amounts of daughter products such as ^{4}He or radiogenic Pb through damage-enhanced diffusion. However, the degree and complexity of radiation damage documented by our studies of LMG zircons underscore some of the special challenges involved in dating ancient zircon grains by laser ablation methods.

Recent studies have demonstrated that even small amounts of radiation damage affect laser ablation rates and the down-hole fractionation of U and Pb isotopes, such that higher

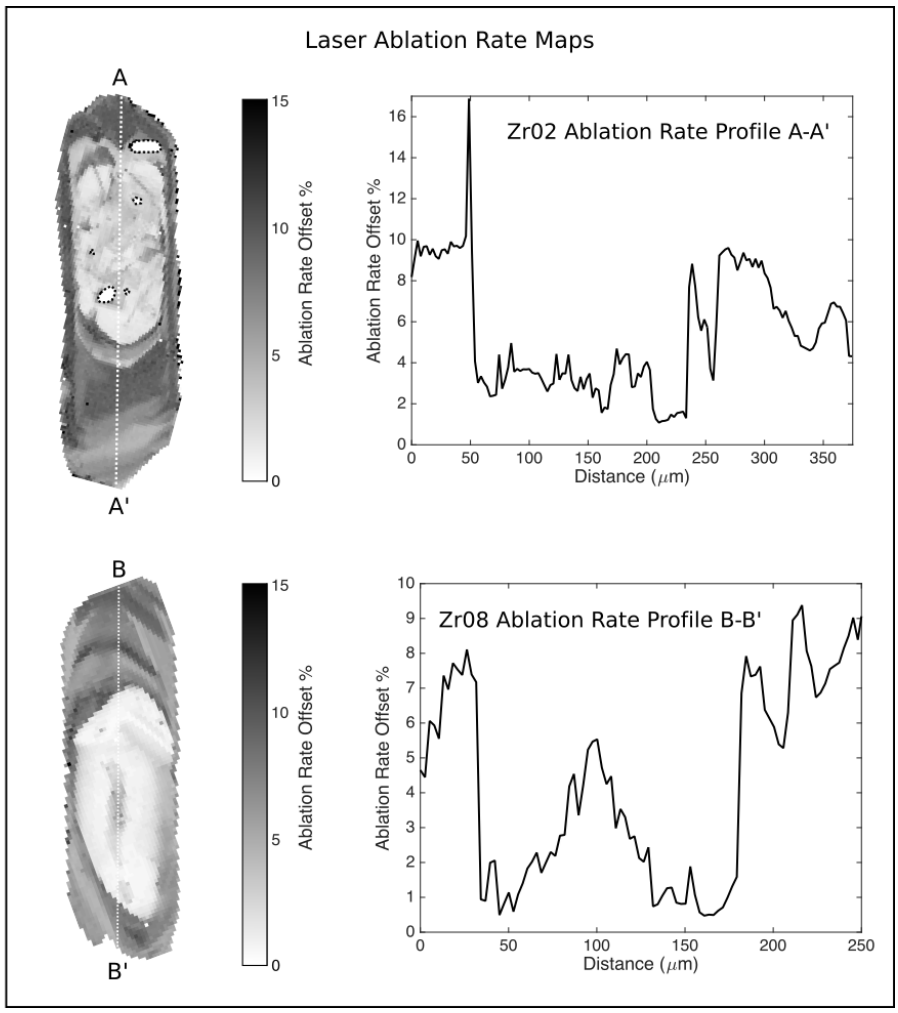

Figure 3.9. Modeled helium diffusivity maps and diffusivity profiles for Zr01 and Zr04 calculated at 200 °C using ZRDAAM (Guenthner et al., 2013). White areas with black, dashed outlines indicate mineral inclusions.

amounts of radiation damage yield higher ablation rates and ^{206}Pb/^{238}U ratios (Marillo-Sialer et al., 2016; Marillo-Sialer et al., 2014; Steely et al., 2014). Compounding the problem is that laser ablation U/Pb dating also relies on external matrix-matched standards for age determinations. To achieve accurate dates, standards and unknowns must behave identically during ablation. Differences in radiation damage between standards and samples can systematically bias U/Pb dates, yielding dates that are up to $\sim$2 to 5 $\%$ too old or too

young when compared to the TIMS U/Pb dates for the same samples (Allen and Campbell, 2012; Marillo-Sialer et al., 2016; Marillo-Sialer et al., 2014).

In zircon crystals with strong radiation damage zoning, different zones should behave differently during ablation. To investigate the potential effects of radiation damage zoning on laser ablation U/Pb analyses, we used the relationship presented by Marillo-Sialer et al. (2016; Figure 4) between Raman FWHM_{ν_3} and percent ablation rate offset − relative to ablation rates determined for Temora-2 zircon, a widely used U/Pb standard (Black et al., 2004) − to model ablation rate offsets in two of our LMG zircon crystals, Zr04 and Zr07 (Figure 3.9). Like our helium diffusivity maps, these ablation rate maps reveal complex intracrystalline variations. Ablation rates in different radiation damage zones in the LMG zircon crystals are predicted to differ by $\sim$10%, and the length-scales for variations are similar to − and sometimes smaller than − the typical laser spot sizes used for U/Pb dating. Marillo-Sialer et al. (2014) found that similar magnitudes of offset between zircon samples and reference standards resulted in $\sim$1 % differences in calculated ^{206}Pb/^{238}U ages. Unfortunately, we cannot test this for the LMG zircons, since crystal cores and crystal rims formed in separate crystallization events.

We might expect even larger age discrepancies in zircon grains with stronger radiation damage zoning. These results suggest that radiation damage zoning could affect the accuracy of − and lower the precision of − U/Pb dates calculated from multiple analyses done on single zoned crystals. Analyses from zones with similar damage contents to the zircon reference standard would be more accurate than analyses from more dissimilar damage zones. Raman-based radiation damage maps (or strategically acquired Raman point spectra guided by CL and BSE imaging) could be used to improve the accuracy of laser ablation zircon U/Pb ages in samples with strong radiation damage zoning. Such information could be used to specifically target more homogenous zones within crystals that have damage

levels similar to the chosen reference standard. Alternatively, a suite of references standards with different damage doses could be analyzed, and the Raman data could be used to select the most appropriate reference standard for each spot analysis (Steely et al., 2014). Another approach would be to use the Raman data to apply a correction factor for the effects of radiation damage during data reduction (T. J. Sliwinski et al., 2017; Steely et al., 2014).

In regards to laser ablation (U-Th)/He dating, α-dose maps of the LMG zircon crystals (Figure 3.6) indicate that variations in radiation damage can occur at smaller length scales than the typical spot sizes used for laser ablation (U-Th)/He analyses (Horne et al., 2016; Tripathy-Lang et al., 2013), suggesting that laser microanalyses could be still be affected by intracrystalline variations in helium production and diffusion (Figure 3.8). Obtaining accurate laser ablation (U-Th)/He dates also requires robust ablation volume estimates for ^{4}He and U+Th concentrations determinations. Variations in ablation rates due to zoning likely affect ablation volumes, and laser analyses that cross damage zones may have non-ideal pit topography. The LMG zircon ablation rate offset maps (Figure 3.9) highlight the need to evaluate ablation volumes on an analysis-by-analysis basis using methods such as white light interferometry. CL and BSE images paired with Raman analyses could be used to better target zones with more homogenous damage contents where helium production, diffusivity, and ablation behavior are more uniform.

Danišík et al. (2017) showed that laser ablation methods can be used to map intra-crystalline ^{4}He zoning in zircons related to both U+Th zoning and radiation damage zoning, although the spatial resolution of ^{4}He measurements made with currently available analytical technology still precludes the quantitative mapping of ^{4}He on the scale of variations in radiation damage revealed through Raman mapping of LMG zircons. The authors presented one promising approach to making the U + Th zoning and radiation damage zoning challenge tractable that involved reducing it to a 1D problem, effectively modeling the parent element

and radiation damage zoning in the crystals they studied as radially concentric. However, in our experience, such zoning in ancient zircon crystals is seldom concentric and more commonly complex and variable, as illustrated by the LMG zircon grains. The robust interpretation of laser ablation helium maps and (U-Th)/He dates for variably and heavily damaged zircons in terms of thermal histories will likely require 2D (or ideally 3D) models of ^{4}He production and diffusion based on microanalytical data.

The acquisition of Raman spectra or spectral maps can represent significant time and cost. While potentially useful for samples with strong radiation damage zoning, acquiring Raman spectra may be less practical for geologically young samples, samples with more uniform distributions of radiation damage, and for detrital datasets that require large numbers of dates. Some studies have suggested that zircon standards and samples should be thermally annealed prior to laser ablation dating to mitigate the effects of radiation damage (Allen and Campbell, 2012; Solari et al., 2015; Steely et al., 2014). As Marillo-Sialer et al. (2016) correctly point out, however, the extent of structural recovery strongly depends on both the annealing temperature and the amount of damage present in the crystal structure, such that zones with different amounts of radiation damage should anneal differently (Ginster et al., 2019; Zhang et al., 2000). To ensure that zones achieve a similar level of crystallinity during annealing, high (>1000°C) annealing temperatures may be required. Even so, some high-damage zones may never achieve complete structural recovery during annealing in laboratory settings. For laser ablation U/Pb and (U-Th)/He double dating (Evans et al., 2015; Horne et al., 2016; Steely et al., 2014; Tripathy-Lang et al., 2013) and some trace element studies, such as studies of lithium isotopes in zircon (J. T. Sliwinski et al., 2018), annealing is not a viable option.

3.8 Conclusions

In this contribution, we presented a case study that examines radiation damage zoning in Proterozoic zircon crystals from the Lyon Mountain Granite using high-resolution Raman mapping. By correlating peak width variations in the $\nu_3(SiO_4)$ stretching vibration (near 1008 cm^{-1}) to peak width variations in the $\nu_4(SiO_4)$ bending vibration (near 357 cm^{-1}) we established a new Raman-based α dose calibration curve that permits α dose estimates to be made for zircon regardless of crystallographic orientation and stage rotation angle. This new calibration also allows users to target the SiO_4 peak with the highest intensity when Raman mapping to help decrease acquisition times.

We produced quantitative α dose maps from the Raman data that reveal strong radiation damage zoning with length scales comparable to our Raman measurement step size (2.5 μm). Using these maps, we modeled to what extent radiation damage zoning might affect helium diffusion and laser ablation rates in the LMG zircon crystals. Model results indicate complex intracrystalline variations in helium systematics in which helium diffusion is more than 25 times faster in high damage zones compared to low damage zones within crystal cores. Given zircon's penchant for complex U and Th zoning, these results suggest that radiation damage zoning is likely a major factor contributing to zircon (U-Th)/He date dispersion in conventional datasets from old, slowly cooled and/or thermally disturbed zircons. Microanalytical techniques including Raman mapping and laser microprobe (U-Th)/He dating may reduce dispersion and help better understand it, but the complexities of ^{4}He distribution in highly damaged zircon crystals make it impractical to fully eliminate such dispersion in the data. Rather than averaging such overdispered dates for a variety of crystals and using the average for thermal modeling, a more productive strategy may be to treat each zircon as a separate thermochronometer and to model its thermal evolution

independently once appropriate 2D or 3D modeling tools are developed. Finally, we note that intra-crystalline variability in radiation damage in ancient, zoned zircon can also complicates laser ablation U/Pb protocols and may adversely affect both the precision and accuracy of geochronologic results.

3.9 Supplementary Materials

3.9.1 Cathodoluminescence Imaging

Cathodoluminescence images (CL) for samples Zr01 through Zr06 were acquired at the Arizona LaserChron Scanning Electron Microscope (SEM) facility at University of Arizona which employs a Hitachi S-3400N tungsten filament source SEM and Gatan ChromaCL2 detector. Images were acquired using a 12 kV accelerating voltage, 83.0 μA emission current, a 12.3 mm working distance, and a 600 μs pixel dwell time. Images have a spatial resolution of $\sim$0.4 μm. CL images for Zr07 and Zr08 were acquired at Memorial University using a JEOL JSM 7100F field emission SEM and a Deben CL system.

3.9.2 Raman Spectroscopy

All Raman spectra were acquired using an HORIBA Scientific Jobin Yvon *XploRA PLUS* confocal Raman microscope at Group 18 Laboratories at Arizona State University. This instrument employs a Olympus BX41 optical microscope with 10x (0.25 numerical aperture) and 100x (0.9 numerical aperture) objectives lenses, a 20-25 mW 532 nm laser, a Marzhauser Wetzlar motorized XY 75 x 50 mm scanning stage that has a TANGO controller with sub-μm position resolution, and a Syncerity 1024 x 256 pixel CCD

detector cooled to $\sim$60 °C. The incident energy beam for this system is vertically polarized, while the scattered energy beam is non-polarized. The system was calibrated daily using the silicon 520.7 cm^{-1} Raman peak, yielding a wavenumber accuracy of about $\pm$1 cm^{-1}. All measurements were made using a 100 μm entrance slit and 100 μm confocal pin hole.

Spectra for oriented zircon sample TZZR3 were acquired at 10x magnification using a 2400 gr/mm diffraction grating. The zircon crystal was oriented under the Raman microscope such that the incident laser beam was perpendicular to either the (100) or the (110) crystals faces.

Raman maps of LMG zircon crystals were acquired at 100x magnification using a 2.5 μm x 2.5 μm step size and the 'autofocus tilt at limit' function in the *LabSpec6* software. Given this setup, the laser has a lateral spot size of $\sim$1 μm and a depth of focus of $\sim$1 μm. Spectra for crystals Zr01 through Zr06 were acquired using a 1800 gr/mm diffraction grating, and spectra for Zr07 and Zr08 were acquired using a 2400 gr/mm diffraction grating, which have spectral resolutions of $\sim$1.9 cm^{-1} and 1.4 cm^{-1}, respectively. Acquisition times ranged from 6 to 12 seconds per spectrum with 2441 to 6406 spectra measured per zircon crystal. Total map accumulation times ranged from $\sim$7 to 21 hours per crystal. Spectral maps were batch processed using HORIBA Scientific *LabSpec6* software. Processing included removal of anomalous spectral artifacts, polynomial baseline corrections, and Gaussian-Lorentzian peak fitting. Measured FWHM values were corrected for instrument bias using the apparatus function (Nasdala et al., 2001). Following Palenik et al. (2003), we assume uncertainties of 5% for FWHM values <22 cm^{-1} and 10% for FWHM values >22 cm^{-1} (2σ). FWHM and peak position maps for key SiO_4 vibrations were generated for each zircon crystal.

3.10 Acknowledgments

This work was supported by the National Science Foundation [EAR-1346321].

References

Allen, C. M. and I. H. Campbell (2012). Identification and elimination of a matrix-induced systematic error in LA–ICP–MS ^{206}Pb/^{238}U dating of zircon. *Chemical Geology* 332-333, pp. 157–165.

Anderson, A. J., K. V. Hodges, and M. C. van Soest (2017). Empirical constraints on the effects of radiation damage on helium diffusion in zircon. *Geochimica et Cosmochimica Acta* 218, pp. 308–322.

Ault, A. K., W. R. Guenthner, A. C. Moser, G. H. Miller, and K. A. Refsnider (2018). Zircon grain selection reveals (de)coupled metamictization, radiation damage, and He diffusivity. *Chemical Geology* 490, pp. 1–12.

Bernet, M. (2009). A field-based estimate of the zircon fission-track closure temperature. *Chemical Geology* 259 (3-4), pp. 181–189.

Black, L. P. et al. (2004). Improved ^{206}Pb/^{238}U microprobe geochronology by the monitoring of a trace-element-related matrix effect; SHRIMP, ID–TIMS, ELA–ICP–MS and oxygen isotope documentation for a series of zircon standards. *Chemical Geology* 205 (1-2), pp. 115–140.

Bowring, S. A. and M. D. Schmitz (2003). High-Precision U-Pb Zircon Geochronology and the Stratigraphic Record. *Zircon: Reviews in Mineralogy & Geochemistry*. Ed. by J. M. Hanchar and P. W. O. Hoskin. Chantilly, VA: Mineralogical Society of America, pp. 305–326.

Corfu, F., J. M. Hanchar, P. W. O. Hoskin, and P. Kinny (2003). Atlas of Zircon Textures. *Zircon: Reviews in Mineralogy & Geochemistry*. Ed. by J. M. Hanchar and P. W. O. Hoskin. Chantilly, VA: Mineralogical Society of America, pp. 469–500.

Danišík, M., B. I. A. McInnes, C. L. Kirkland, B. J. McDonald, N. J. Evans, and T. Becker (2017). Seeing is believing: Visualization of He distribution in zircon and implications for thermal history reconstruction on single crystals. *Science Advances* 3 (2), e1601121.

Dawson, P., M. M. Hargreave, and G. R. Wilkinson (1971). The vibrational spectrum of zircon ($ZrSiO_4$). *Journal of Physics C: Solid State Physics* 4, pp. 240–256.

Evans, N. J., B. I. A. McInnes, B. McDonald, M. Danišík, T. Becker, P. Vermeesch, M. Shelley, E. Marillo-Sialer, and D. B. Patterson (2015). An in situ technique for (U–Th–Sm)/He and U–Pb double dating. *J. Anal. At. Spectrom.* 30 (7), pp. 1636–1645.

Ewing, R. C., A. Meldrum, L. Wang, W. J. Weber, and L. R. Corrales (2003). Radiation effects in zircon. *Zircon: Reviews in Mineralogy & Geochemistry*. Ed. by J. M. Hanchar and P. W. O. Hoskin. 53. Chantilly, VA: Mineralogical Society of America, pp. 387–425.

Flowers, R. M. (2009). Exploiting radiation damage control on apatite (U-Th)/He dates in cratonic regions. *Earth and Planetary Science Letters* 277, pp. 148–155.

Gallagher, K. (2012). Transdimensional inverse thermal history modeling for quantitative thermochronology. *Journal of Geophysical Research* 117 (B2), B02408.

Gautheron, C., L. Tassan-Got, J. Barbarand, and M. Pagel (2009). Effect of alpha-damage annealing on apatite (U–Th)/He thermochronology. *Chemical Geology* 266 (3-4), pp. 157–170.

Gehrels, G. (2014). Detrital Zircon U-Pb Geochronology Applied to Tectonics. *Annual Review of Earth and Planetary Sciences* 42 (1), pp. 127–149.

Gehrels, G. E., V. A. Valencia, and J. Ruiz (2008). Enhanced precision, accuracy, efficiency, and spatial resolution of U-Pb ages by laser ablation-multicollector-inductively coupled plasma-mass spectrometry. *Geochemistry, Geophysics, Geosystems* 9 (3).

Geisler, T., R. T. Pidgeon, W. van Bronswijk, and R. Kurtz (2002). Transport of uranium, thorium, and lead in metamict zircon under low-temperature hydrothermal conditions. *Chemical Geology* 191 (1-3), pp. 141–154.

Geisler, T., R. T. Pidgeon, W. van Bronswijk, and R. Pleysier (2001). Kinetics of thermal recovery and recrystallization of partially metamic zircon: A Raman spectroscopic study. *European Journal of Mineralogy* 13, pp. 1163–1176.

Ginster, U., P. W. Reiners, L. Nasdala, and C. C. N (2019). Annealing kinetics of radiation damage in zircon. *Geochimica et Cosmochimica Acta* 249, pp. 225–246.

Guenthner, W. R., P. W. Reiners, P. G. DeCelles, and J. Kendall (2015). Sevier belt exhumation in central Utah constrained from complex zircon (U-Th)/He data sets: Radiation damage and He inheritance effects on partially reset detrital zircons. *Bulletin of the Geological Society of America* 127 (3-4), pp. 323–348.

Guenthner, W. R., P. W. Reiners, R. A. Ketcham, L. Nasdala, and G. Giester (2013). Helium diffusion in natural zircon: Radiation damage, anisotropy, and the interpretation of zircon (U-TH)/He thermochronology. *American Journal of Science* 313 (3), pp. 145–198.

Guenthner, W. R., P. W. Reiners, and Y. Tian (2014). Interpreting date-eU correlations in zircon (U-Th)/He datasets: A case study from the Longmen Shan, China. *Earth and Planetary Science Letters* 403, pp. 328–339.

Günther, D., R. Frischknecht, C. A. Heinrich, and H.-J. Kahlert (1997). Capabilities of an argon fluoride 193 nm excimer laser for laser ablation inductively coupled plasma mass spectometry microanalysis of geological materials. *J. Anal. At. Spectrom.* 12 (9), pp. 939–944.

Hanchar, J. M. and C. F. Miller (1993). Zircon zonation patterns as revealed by cathodoluminescence and backscattered electron images: Implications for interpretation of complex crustal histories. *Chemical Geology* 110 (1-3), pp. 1–13.

Hanchar, J. M. and R. L. Rudnick (1995). Revealing hidden structures: The application of cathodoluminescence and back-scattered electron imaging to dating zircons from lower crustal xenoliths. *Lithos* 36 (3-4), pp. 289–303.

Holland, H. D. and D. Gottfried (1955). The effect of nuclear radiation on the structure of zircon. *Acta Crystallographica* 8, pp. 291–300.

Horn, I., R. L. Rudnick, and W. F. McDonough (2000). Precise elemental and isotope ratio determination by simultaneous solution nebulization and laser ablation-ICP-MS: application to U–Pb geochronology. *Chemical Geology* 164 (3-4), pp. 281–301.

Horne, A. M., M. C. van Soest, K. V. Hodges, A. Tripathy-Lang, and J. K. Hourigan (2016). Integrated single crystal laser ablation U/Pb and (U-Th)/He dating of detrital accessory minerals - Proof-of-concept studies of titanites and zircons from the Fish Canyon tuff. *Geochimica et Cosmochimica Acta* 178, pp. 106–123.

Hurley, P. M. (1952). Alpha ionization as a cause of low helium ratios. *Eos, Transactions American Geophysical Union* 33 (2), pp. 174–183.

Jackson, S. E., N. J. Pearson, W. L. Griffin, and E. A. Belousova (2004). The application of laser ablation-inductively coupled plasma-mass spectrometry to in situ U–Pb zircon geochronology. *Chemical Geology* 211 (1-2), pp. 47–69.

Johnson, J. E., R. M. Flowers, G. B. Baird, and K. H. Mahan (2017). “Inverted" zircon and apatite (U-Th)/He dates from the Front Range, Colorado: High-damage zircon as a

low-temperature (<50°C) thermochronometer. *Earth and Planetary Science Letters* 466, pp. 80–90.

Ketcham, R. A. (2005). Forward and Inverse Modeling of Low-Temperature Thermochronometry Data. *Low Temperature Thermochronology- Techniques, Interpretations, and Applications: Review in Mineralogy & Geochemistry*. Ed. by P. W. Reiners and T. A. Ehlers. 58 (1). Chantilly, VA: Mineralogical Society of America, pp. 275–314.

Ketcham, R. A., W. R. Guenthner, and P. W. Reiners (2013). Geometric analysis of radiation damage connectivity in zircon, and its implications for helium diffusion. *American Mineralogist* 98 (2-3), pp. 350–360.

Lehnert, R. J. (2000). Beyond Imagination - Image Formation Based on Raman Spectroscopy. *G.I.T. Laboratory Journal* 2, pp. 6–9.

Ludwig, K. R. (2003). Mathematical–statistical treatment of data and errors for ^{230}Th/U Geochronology. *Uranium-Series Geochemistry: Reviews in Mineralogy & Geochemistry*. Ed. by B. Bourdon, G. M. Henderson, C. C. Lundstrom, and S. P. Turner. 52. Chantilly, VA: Mineralogical Society of America, pp. 631–656.

Marillo-Sialer, E., J. Woodhead, J. M. Hanchar, S. M. Reddy, A. Greig, J. Hergt, and B. Kohn (2016). An investigation of the laser-induced zircon 'matrix effect'. *Chemical Geology* 438 (C), pp. 11–24.

Marillo-Sialer, E., J. Woodhead, J. Hergt, A. Greig, M. Guillong, A. Gleadow, N. Evans, and C. Paton (2014). The zircon 'matrix effect': evidence for an ablation rate control on the accuracy of U–Pb age determinations by LA-ICP-MS. *J. Anal. At. Spectrom.* 29 (6), pp. 981–989.

McLelland, J., M. Hamilton, B. Selleck, J. McLelland, D. Walker, and S. Orrell (2001). Zircon U-Pb geochronology of the Ottawan Orogeny, Adirondack Highlands, New York: Regional and tectonic implications. *Precambrian Research* 109, pp. 39–72.

Meldrum, A., L. A. Boatner, W. J. Weber, and R. C. Ewing (1998). Radiation damage in zircon and monazite. *Geochimica et Cosmochimica Acta* 62 (14), pp. 2509–2520.

Mezger, K. and E. J. Krogstad (1997). Interpretation of discordant U-Pb zircon ages: An evaluation. *Journal of Metamorphic Geology* 15 (1), pp. 127–140.

Murakami, T., B. C. Chakoumakos, R. C. Ewing, G. R. Lumpkin, and W. J. Weber (1991). Alpha-decay event damage in zircon. *American Mineralogist* 76, pp. 1510–1532.

Nasdala, L., J. Gotze, J. M. Hanchar, M. Gaft, and M. R. Krbetschek (2004). Luminescence techniques in Earth Sciences. *EMU Notes in Mineralogy* 6, pp. 43–91.

Nasdala, L., M. Wenzel, G. Vavra, G. Irmer, T. Wenzel, and B. Kober (2001). Metamictisation of natural zircon: Accumulation versus thermal annealing of radioactivity-induced damage. *Contributions to Mineralogy and Petrology* 141 (2), pp. 125–144.

Nasdala, L., J. M. Hanchar, A. Kronz, and M. J. Whitehouse (2005). Long-term stability of alpha particle damage in natural zircon. *Chemical Geology* 220 (1-2), pp. 83–103.

Nasdala, L., G. Irmer, and D. Wolf (1995). The degree of metamictization in zircon: A Raman spectroscopic study. *European Journal of Mineralogy* 7 (3), pp. 471–478.

Nasdala, L., C. L. Lengauer, J. M. Hanchar, A. Kronz, R. Wirth, P. Blanc, A. K. Kennedy, and A.-M. Seydoux-Guillaume (2002). Annealing radiation damage and the recovery of cathodoluminescence. *Chemical Geology* 191 (1-3), pp. 121–140.

Nasdala, L., M. Zhang, U. Kempe, G. Panczer, M. Gaft, M. Andrut, and M. Plotze (2003). Spectroscopic methods applied to zircon. *Zircon: Reviews in Mineralogy & Geochemistry*. 53 (1). Chantilly, VA: Mineralogical Society of America, pp. 427–467.

Palenik, C. S., L. Nasdala, and R. C. Ewing (2003). Radiation damage in zircon. *American Mineralogist* 88, pp. 770–781.

Pearson, R. K. (2001). *Exploring Data in Engineering, the Sciences, and Medicine*. Oxford Univ. Press.

Powell, J., D. Schneider, D. Stockli, and K. Fallas (2016). Zircon (U-Th)/He thermochronology of Neoproterozoic strata from the Mackenzie Mountains, Canada: Implications for the Phanerozoic exhumation and deformation history of the northern Canadian Cordillera. *Tectonics* 35 (3), pp. 663–689.

Reiners, P. W. and M. T. Brandon (2006). Using thermochronology to understand orogenic erosion. *Annual Review of Earth and Planetary Sciences* 34 (1), pp. 419–466.

Reiners, P. W., R. W. Carlson, P. R. Renne, K. M. Cooper, D. E. Granger, N. M. McLean, and B. Schoene (2017). The (U-Th)/He System. *Geochronology and Thermochronology*. John Wiley & Sons Ltd. Chap. 11, pp. 291–363.

Schoene, B. (2014). U–Th–Pb Geochronology. *Treatise on Geochemistry*. Ed. by H. D. Holland and K. K. Turekian. Elsevier Ltd., pp. 341–378.

Sliwinski, J. T., N. Kueter, F. Marxer, P. Ulmer, M. Guillong, and O. Bachmann (2018). Controls on lithium concentration and diffusion in zircon. *Chemical Geology* 501, pp. 1–11.

Sliwinski, T. J., M. Guillong, C. Liebske, I. Dunkl, A. von Quadt, and O. Bachmann (2017). Improved accuracy of LA-ICP-MS U-Pb ages of Cenozoic zircons by alpha dose correction. *Chemical Geology* 472, pp. 8–21.

Solari, L. A., C. Ortega-Obregón, and J. P. Bernal (2015). U–Pb zircon geochronology by LAICPMS combined with thermal annealing: Achievements in precision and accuracy on dating standard and unknown samples. *Chemical Geology* 414, pp. 109–123.

Steely, A. N., J. K. Hourigan, and E. Juel (2014). Discrete multi-pulse laser ablation depth profiling with a single-collector ICP-MS: Sub-micron U–Pb geochronology of zircon and the effect of radiation damage on depth-dependent fractionation. *Chemical Geology* 372, pp. 92–108.

Syme, R. W. G., D. J. Lockwood, and H. J. Kerr (1977). Raman spectrum of synthetic zircon ($ZrSiO_4$) and thorite ($ThSiO_4$). *Journal of Physics C: Solid State Physics* 10, pp. 1335–1348.

Tripathy-Lang, A., K. V. Hodges, B. D. Monteleone, and M. C. van Soest (2013). Laser (U-Th)/He thermochronology of detrital zircons as a tool for studying surface processes in modern catchments. *Journal of Geophysical Research: Earth Surface* 118 (3), pp. 1333–1341.

Valley, P. M., J. M. Hanchar, and M. J. Whitehouse (2011). New insights on the evolution of the Lyon Mountain Granite and associated Kiruna-type magnetite-apatite deposits, Adirondack Mountains, New York State. *Geosphere* 7 (2), pp. 357–389.

Vermeesch, P., S. C. Sherlock, N. M. W. Roberts, and A. Carter (2012). A simple method for in-situ U-Th-He dating. *Geochimica et Cosmochimica Acta* 79, pp. 140–147.

Weber, W. J. (1990). Radiation-induced defects and amorphization in zircon. *Journal of Materials Research* 5 (11), pp. 2687–2697.

Weber, W. (1993). Alpha-decay-induced amorphization in complex silicate structures. *J. Am. Ceram. Soc.* 76 (7), pp. 1729–1738.

Willett, C. D., M. Fox, and D. L. Shuster (2017). A helium-based model for the effects of radiation damage annealing on helium diffusion kinetics in apatite. *Earth and Planetary Science Letters* 477, pp. 195–204.

Yamada, R., M. Murakami, and T. Tagami (2007). Statistical modelling of annealing kinetics of fission tracks in zircon; Reassessment of laboratory experiments. *Chemical Geology* 236 (1-2), pp. 75–91.

York, D., N. M. Evensen, M. L. Martinez, and J. De Basabe Delgado (2004). Unified equations for the slope, intercept, and standard errors of the best straight line. *American Journal of Physics* 72 (3), pp. 367–375.

Zhang M S, E. K. H., G. C. Capitani, H. Leroux, A. M. Clark, J. Schluter, and R. C. Ewing (2000). Annealing of α-decay damage in zircon: A Raman spectroscopic study. *Journal of Physics: Condensed Matter* 12, pp. 3131–3148.

Chapter 4

HELIUM DIFFUSION IN ZIRCON: ANISOTROPY AND RADIATION DAMAGE EFFECTS REVEALED BY LASER DEPTH PROFILING

Alyssa J. Anderson[1], Matthijs C. van Soest[1], Kip V. Hodges[1], and John M. Hanchar[2]

[1]School of Earth and Space Exploration, Arizona State University, Tempe, AZ 85287, USA.

[2]Earth Sciences, Memorial University of Newfoundland, St. John's, NL A1B 3X7, Canada.

4.1 Abstract

Laser depth profiling of laboratory induced helium diffusion profiles in proton irradiated, natural zircon confirms that helium diffusivity is crystallographically controlled and significantly anisotropic. Experiments on low-damage Mud Tank zircon (1.44 to 2.23 x 10^{17} α/g) indicate that $c_{\|}$ diffusion is $\sim$400 to 700 times faster that $a_{\|}$ diffusion over the experimental temperature range investigated (400 to 600 °C). This magnitude of diffusive anisotropy implies that zircon crystals with different crystal morphologies record different helium closure temperatures. This effect likely contributes substantially to the commonly observed overdispersion of single-crystal (U-Th)/He dates for different zircon crystals from individual rock samples. Other experiments on pieces of a large Sri Lankan zircon crystal with strong radiation damage zoning − characterized using Raman spectroscopy − show that both $c_{\|}$ and $a_{\|}$ diffusivity − as well as the magnitude of diffusive anisotropy − decrease with increasing radiation damage over the alpha dose range of 4.98 to 9.05 x 10^{17} α/g. Decreases in diffusivity appear to reflect changes in the diffusion coefficient and not the

activation energy for diffusion. Our results also suggest that zircon trace element chemistry may influence helium diffusivity in as yet unquantified ways.

4.2 Introduction

The temperature-dependent diffusivity of radiogenic helium in uranium- and thorium-bearing minerals is commonly used to investigate thermal processes that occur at or near Earth's surface (e.g. Enkelmann and Garver, 2016; Farley and Stockli, 2002; Reiners et al., 2017; Shuster et al., 2003). In addition to temperature, however, many studies have suggested that helium systematics in minerals used for (U-Th)/He thermochronology strongly depends on the mineral's structure and accumulated radiation damage (Baughman et al., 2017; Cherniak and Watson, 2011; Farley, 2007; Flowers, 2009; Shuster et al., 2006). This is especially true for zircon, one of the most widely used low temperature thermochronometers (Anderson et al., 2017; Cherniak et al., 2009; Guenthner et al., 2013).

Most helium diffusion studies of zircon have relied on single crystal, step-wise degassing experiments that measure a crystal's bulk diffusive properties (Guenthner et al., 2013; Reiners et al., 2002; Reiners et al., 2004). While yielding important results, such studies provide only limited and indirect information on crystallographically-dependent variations in diffusivity. Characterizing diffusive loss profiles on crystallographically oriented zircon crystals by depth profiling can provide more direct constraints on diffusive anisotropy (Cherniak et al., 2009), but to date these methods have not been used to investigate how radiation damage affects crystallographic variations in helium diffusion in zircon. In this study, we evaluate the competing effects of radiation damage and crystallographic anisotropy on helium diffusion in natural zircon crystals with low to moderate amounts of radiation

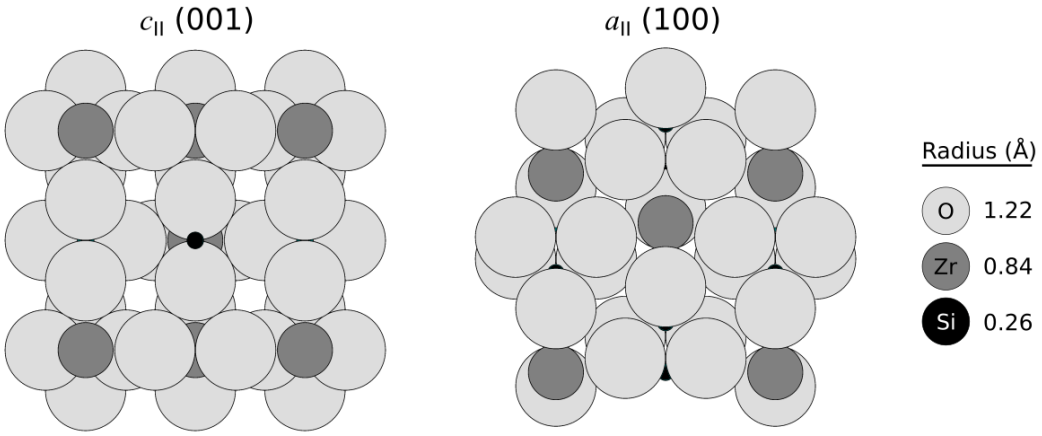

Figure 4.1. The zircon crystal structure as viewed along the *a*- and *c*- crystallographic axes rendered using CrystalMaker software (Hazen and Finger, 1979). Ionic radii are based on recommended values from (Shannon, 1976).

damage using excimer laser ablation depth profiling, largely following the approach of van Soest et al. (2011).

4.3 Background

4.3.1 Zircon Crystal Structure and Radiation Damage

Zircon ($ZrSiO_4$) is a nesosilicate mineral that crystallizes in the tetragonal crystal system (space group $I4_1/amd$) (Finch and Hanchar, 2002; Hazen and Finger, 1979; Robinson et al., 1971). ZrO_8 dodecahedra form edge-sharing chains along <100>. These chains are cross linked by corner sharing SiO_4 tetrahedra. Chains of alternating SiO_4 tetrahedra and ZrO_8 dodecahedra share edges and form along [001]. Aligned interstitial sites between SiO_4 and ZrO_8 polyhedra form continuous open channels along the *c*-axis (Figure 4.1).

Radionuclides are incorporated into the zircon structure by the simple tetravalent substitution of $(U,Th)^{4+} \leftrightarrow Zr^{4+}$ (Finch and Hanchar, 2002). The alpha decay of ^{238}U, ^{235}U, and

^{232}Th, and their radioactive daughters − as well as ^{235}U fission − damage the zircon crystal structure (Ewing et al., 2003). Most damage is attributed to the kinetic recoil of heavy daughter nuclides during alpha decay events which cause thousands of atomic displacements that create low density regions surrounded by interstitial defects (Murakami et al., 1991; W. J. Weber, 1990; W. Weber, 1993). Alpha particles themselves also cause a small number of atomic displacements and interstitial defects near the end of their trajectory. Fission events generate large amorphous tracts; however, they occur infrequently relative to alpha decay events. While radiation damage anneals over time at elevated temperatures, damage accumulates in the crystal structure over time at near-surface temperatures, affecting zircon material properties such as density, hardness, chemical and physical durability, refractive indices, and elastic moduli (Ewing et al., 2003; Geisler et al., 2001; Holland and Gottfried, 1955; Murakami et al., 1991; Zhang et al., 2000). High levels of accumulated radiation damage result in the complete amorphization or metamictization of the zircon structure (Meldrum et al., 1998; Murakami et al., 1991). An accumulated radiation damage dose − commonly referred to as an alpha dose (α decay events/g) − can be calculated for a zircon from its U and Th contents and an estimated damage accumulation interval (Holland and Gottfried, 1955). This interval is generally taken as the zircon's crystallization age if the zircon experienced moderate to rapid cooling and no subsequent annealing due to thermal disturbances. An alpha dose can also be approximated from measured changes in material properties. We used Raman spectroscopy to characterize radiation damage in our zircon samples since key Si-O vibrations in the zircon Raman spectrum, such as the $\nu_3(SiO_4)$ peak near $\sim$1008 cm^{-1}, broaden predictably in response to radiation damage accumulation (Nasdala et al., 2001; Palenik et al., 2003).

4.3.2 Helium Diffusion in Zircon

The first systematic studies of helium diffusion in zircon were presented by Reiners and colleagues (2002; 2004). These bulk step-wise degassing experiments demonstrated that helium diffusive loss is largely consistent with thermally-activated volume diffusion governed by an Arrhenius relationship in which the diffusion dimension is closely related to zircon crystal size. Results of these experiments, calculated assuming isotropic diffusion and a spherical diffusion geometry, yielded a range of values for the activation energy for diffusion (E_a) from 163 to 173 kJ/mol, and for the natural logarithm of the pre-exponential diffusivity constant (D_0) from -11.6 to -8.8 ln(m^2/s). Reiners et al. (2004) reported mean values of 169 $\pm$ 7.6 kJ/mol and -10.0 $\pm$ 2.1 ln(m^2/s), respectively (note that all uncertainties reported throughout the text are quoted at the 2σ level unless otherwise indicated). Those authors, however, also noted some anomalous Arrhenius behavior in early heating steps and minor differences in diffusivity between prograde and retrograde heating steps. They suggested a number of possible interpretations for this behavior, including the presence of multiple diffusion domains, the heterogeneous distribution of radiation damage due to U and Th zoning (McLaren et al., 1994), and crystallographic anisotropy.

Atomic simulations later predicted that helium diffusion in zircon should be strongly anisotropic, with the fastest transport occurring along interstitial channels aligned parallel to the *c* axis (Bengtson et al., 2012; Reich et al., 2007; Saadoune et al., 2009). We refer to this direction throughout the text as "$c_{\parallel}$". One dimensional diffusive loss profiles of ion-implanted ^{3}He measured on crystallographically oriented zircon slabs by nuclear reaction analysis (NRA), in part, confirmed this hypothesis (Cherniak et al., 2009). The NRA study found that $c_{\parallel}$ diffusion was $\sim$75 times faster than in the orthogonal direction ($c_{\perp}$). Cherniak et al. (2009) reported Arrhenius parameters of 148 kJ/mol and -11.0 ln(m^2/s) parallel to

c, but 146 kJ/mol and -15.3 ln(m^2/s) in the orthogonal direction. These results suggested that the dominant effect of crystallographic anisotropy was a substantial change in the pre-exponential constant D_0 with little perceptible change in the activation energy (Cherniak et al., 2009). Since their results nicely bracketed those of Reiners and others (2002; 2004), Cherniak et al. (2009) suggested that diffusive anisotropy might account for the observed anomalies in the bulk diffusion study.

More recently, Guenthner and colleagues (2013) completed a series of bulk ^{4}He degassing experiments to further investigate the role of diffusive anisotropy and to evaluate the effects of radiation damage on helium diffusivity. Zircon slabs with different degrees of radiation damage were oriented parallel and perpendicular to the c-axis and cut with high aspect ratios to, in theory, favor $c_{\parallel}$ or $c_{\perp}$ diffusion. In contrast to the NRA experimental results and atomic model predictions (Cherniak et al., 2009; Reich et al., 2007; Saadoune et al., 2009), Guenthner et al. (2013) found limited evidence for diffusive anisotropy. They instead demonstrated that radiation damage profoundly influences helium diffusion in zircon by first retarding diffusivity at low damage doses and then increasing diffusivity dramatically as damage levels increase (Guenthner et al., 2013). These changes in diffusivity cause the closure temperature for helium in zircon to vary from $\sim$180 °C in highly crystalline zircon to below 0 °C in metamict zircon, assuming typical crystal sizes and the nominal cooling rate of 10 °C/Ma.

Based on their results, Guenthner et al. (2013) suggested a two-part mechanistic model in which low alpha doses ($< \sim$1 x 10^{18} α/g) initially lower diffusivity by obstructing $c_{\parallel}$ interstitial channels, therefore attenuating faster $c_{\parallel}$ transport and diffusive anisotropy. They hypothesized that, at higher doses, low-density damage zones interconnect and serve as diffusive fast pathways (Guenthner et al., 2013; Ketcham et al., 2013). The plausibility of this model is, in part, supported by atomic models which suggest that uranium ions

and defects in the zircon structure can either retard or enhance diffusivity depending on the nature of the defect (Saadoune et al., 2009; Saadoune and Leeuw, 2009). The model developed by Guenthner and others (2013) forms the basis of the zircon radiation damage accumulation and annealing model (ZRDAAM) used to interpret thermal histories from complex zircon (U-Th)/He datasets with date-damage correlations (e.g. Guenthner et al., 2015; Guenthner et al., 2014).

4.4 Experimental Methods and Results

4.4.1 Samples

We selected two centimeter-sized zircon crystals for our diffusion experiments. The first sample was a gem-quality crystal from the Mud Tank carbonatite in Australia (MT) (Crohn and Moore, 1984; Currie et al., 1992). Zircon crystals from this locality are known for their extremely low radionuclide contents (and trace elements in general) and have an established U/Pb age of 732 $\pm$ 5 Ma (Black and Gulson, 1978). The second was a zircon from the Sri Lankan gem gravels (SL3) with pronounced radiation damage zoning (Figure 4.2). A suite of Sri Lankan crystals studied by Nasdala et al. (2004) yielded mean (U-Th)/Pb dates of 555 $\pm$ 11 Ma.

The two samples were crystallographically oriented using either external crystal morphology (SL3) or Laue X-ray diffraction patterns (MT) (see Supplementary Materials). Several slabs oriented perpendicular to the crystallographic a-axis (100) and perpendicular to the crystallographic c-axis (001) were cut and polished for each sample to allow for the characterization of $a_{\parallel}$ and $c_{\parallel}$ diffusive loss profiles by laser depth profiling. Fashioned slabs were generally $\sim$1 to 3 mm across and $\sim$200 to 500 μm thick.

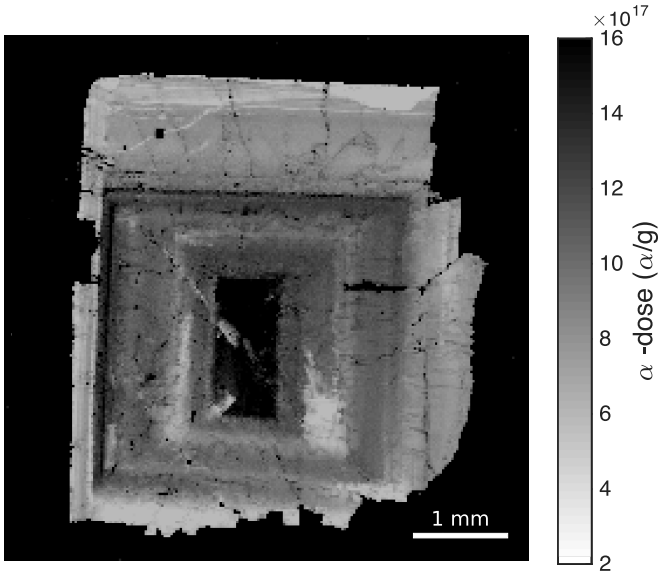

Figure 4.2. Radiation damage map of an un-irradiated SL3 zircon section cut perpendicular to the c-axis (001) based on a Raman spectral map (25 μm resolution) of $\nu_3(SiO_4)$ peak width variations (Nasdala et al., 2001). Peak widths have been converted to alpha dose values using the calibration presented by (Palenik et al., 2003).

4.4.2 Proton irradiation

Uranium and thorium zoning, a common feature in zircon, can produce heterogeneous distributions of radiogenic ^{4}He (Danišík et al., 2017; Tripathy-Lang et al., 2015) which greatly complicates one-dimensional diffusion experiments based on laboratory-induced diffusive loss of ^{4}He. We instead chose to focus the experiments described below on artificial ^{3}He produced by proton irradiation. High- to moderate-energy proton bombardment yields spallogenic ^{3}He in a manner analogous to the way that ^{3}He is produced by cosmic ray bombardment from virtually all nuclei in minerals (Leya et al., 1998; Shuster et al., 2003; Wieler, 2002). In theory, the distribution of proton-induced ^{3}He in a crystal should be uniform. The method, initially devised as a way to recover ^{4}He diffusive loss profiles in apatite crystals through the comparison of ^{3}He/^{4}He ratios during incremental heating

(Shuster and Farley, 2003; Shuster et al., 2003), has since been used to induce ^{3}He in zircon for ^{4}He/^{3}He thermochronology (Tripathy-Lang et al., 2015) and in samples lacking sufficient radiogenic helium for bulk diffusion experiments (Farley, 2007; Shuster and Farley, 2005).

Previous studies of apatite and titanite suggest that proton bombardment neither anneals radiation damage nor causes enough new damage to measurably affect helium diffusion kinetics (Shuster et al., 2003). While shorter irradiations are sufficient to produce enough ^{3}He for bulk (single-crystal) degassing experiments and ^{4}He/^{3}He thermochronology, micro-analytical studies using laser microprobes sample smaller gas volumes and require longer irradiation times to produce enough ^{3}He for analytical measurements; for our studies, three seven-hour sessions at the Francis H. Burr Proton Therapy Center at the Massachusetts General Hospital were required, resulting in a total dose of 3 x 10^{16} protons. Raman $\nu_3(SiO_4)$ peak width measurements acquired both before and after irradiation to characterize samples' radiation damage are statistically indistinguishable, confirming the findings of Shuster et al. (2003) and establishing that proton bombardment did not demonstrably change the amount of radiation damage present in our samples.

4.4.3 Laser Depth Profiling

All laser depth profiling experiments were conducted in the Group 18 Laboratories at Arizona State University. Irradiated samples were heated under vacuum to induce diffusive loss of ^{3}He using either a projector bulb furnace or an infrared laser heated furnace. Experimental temperatures, monitored by a Type K thermocouple, ranged from 400 to 600 °C, and heating durations ranged from 10 to 1440 minutes. Heating temperatures and durations for each diffusion experiment are reported in Table 4.1. More detailed information

Table 4.1. ^{3}He diffusivity and radiation damage estimates for zircon samples.

	Laser Depth Profiling					Raman $\nu_3(SiO_4)$		
	T (°C)	t (min)	Depth (μm)	D (m^2/s)	2σ[a]	Position (cm^{-1})	FWHM (cm^{-1})	α-dose (x10^{17} α/g)
Mud Tank Zircon								
$c_{\|\|}$ Diffusion								
MT 01	400	840	23.7	3.64E-16	7.5E-17	1006.2	2.8	1.49E+17
MT 02	425	480	28.4	2.05E-15	3.3E-16	1005.7	3.4	1.83E+17
MT 03	450	480	22.3	1.26E-15	2.6E-16	1005.6	2.8	1.49E+17
MT 04	475	120	30.8	1.0E-14	1.9E-15	1005.9	4.1	2.23E+17
MT 05	500	30	29.0	3.06E-14	6.7E-15	1005.7	2.8	1.49E+17
MT 06	525	15	28.6	6.6E-14	1.4E-14	1005.8	2.9	1.55E+17
MT 07	550	10	26.4	5.8E-14	1.7E-14	1005.6	2.8	1.49E+17
$a_{\|\|}$ Diffusion								
MT 08	450	1440	8.5	1.52E-17	5.7E-18	1005.6	2.9	1.55E+17
MT 09	475	1200	7.7	1.28E-17	7.6E-18	1006.6	2.8	1.49E+17
MT 10	500	480	5.4	3.4E-17	1.5E-17	1005.6	3.5	1.88E+17
MT 11	525	180	3.4	5.0E-17	1.9E-17	1005.6	3.6	1.94E+17
MT 12	550	90	6.0	2.31E-16	9.3E-17	1005.7	2.8	1.49E+17
MT 13	575	30	3.8	3.8E-16	1.3E-16	1005.7	2.7	1.44E+17
MT 14	600	10	3.2	5.8E-16	2.6E-16	1005.6	2.8	1.49E+17
Unheated								
MT15	-	-	27.0	-	-	1006.3	2.8	1.49E+17
Sri Lankan Zircon								
$c_{\|\|}$ Diffusion								
SL3 01	400	720	83.6	1.36E-14	2.3E-15	1002.2	9.4	5.60E+17
SL3 02	400	840	3.6	4.8E-18	3.1E-18	997.7	13.9	9.05E+17
SL3 03	425	480	15.8	5.6E-16	1.3E-16	999.9	11.2	6.90E+17
SL3 04	425	480	10.2	1.12E-16	3.1E-17	998.6	12.6	7.97E+17
SL3 05	450	180	63.9	3.11E-14	6.1E-15	1001.8	9.2	5.45E+17
SL3 06	475	90	5.9	9.4E-17	4.4E-17	998.1	12.8	8.13E+17
SL3 07	475	90	10.7	7.6E-16	2.3E-16	1001.0	10.9	6.67E+17
SL3 08	500	30	11.0	5.2E-15	1.5E-15	1000.4	10.6	6.44E+17
SL3 09	525	10	3.3	2.3E-16	1.4E-16	998.0	13.5	8.71E+17
$a_{\|\|}$ Diffusion								
SL3 10	450	1440	3.0	3.6E-18	1.5E-18	998.2	13.0	8.30E+17
SL3 11	475	1200	9.3	1.05E-17	3.9E-18	1001.4	10.0	6.02E+17
SL3 12	500	480	10.3	9.23E-17	3.8E-17	1000.1	11.0	6.76E+17
SL3 13	525	300	8.1	1.15E-16	4.0E-17	1000.7	10.4	6.31E+17
SL3 14	550	120	12.7	9.2E-16	3.0E-16	1002.2	8.5	4.98E+17
SL3 15	560	60	8.2	3.1E-16	1.1E-16	1000.8	10.0	6.01E+17
SL3 16	575	30	13.2	4.9E-15	1.2E-15	1002.1	8.9	5.24E+17
Unheated								
SL3 17	-	-	64.3	-	-	997.3	14.4	9.46E+17

[a]2σ values represent propagated analytical uncertainties for ^{3}He abundances, depth measurements, step widths, and t.

on our diffusion experiments may be found in the Supplemental Materials and in van Soest et al. (2011).

After removal from the diffusion cells, the heated zircon slabs were mounted in indium and loaded into a custom-designed laser ablation cell with a synthetic sapphire viewport

with high (70%) transmissivity for 193nm UV laser light. The cell, connected to the noble gas extraction line, was placed under ultrahigh vacuum and positioned beneath a Teledyne Photon Machines *Analyte Exciteor Analyte G2* ultraviolet excimer laser microprobe. Following the approach described by van Soest et al. (2011), we first ablated a shallow pit in the polished zircon surface using multiple laser pulses. The ablated material expanded into the gas purification section of the extraction line, where a combination of metal alloy getters and a cryogenic trap concentrated helium gas for ^{3}He analysis using a Thermo Electron (GV Instruments) *Helix SFT* mass spectrometer. Subsequent ablation steps, using the same laser beam footprint, were used to excavate successively deeper into the sample. Depth profiling was continued until the ^{3}He abundances for at least three consecutive ablation steps were statistically indistinguishable. Isotopic measurements and estimated analytical uncertainties for all diffusion experiments are reported in Table S4.1 in the Supplementary Materials.

Following laser depth profiling, mounts were removed from the laser ablation cell, and ablated profiles were scanned using a white light interferometric microscope to characterize laser pit topography and determine profile depths (Table 4.1). For a given profile, we know the cumulative number of steps responsible for the final profile depth. We calculate an average depth for each profile step by dividing the final measured depth by the number of steps in the given profile.

One complication associated with laser profiling is that pit geometries and ablation volumes change as a function of depth (Hodapp and Fleming, 1998; van Soest et al., 2011). Ideally, a laser profile ablated using a circular spot should have a geometry that closely resembles that of a cylinder. Interferometric scans, however, reveal that profile walls taper inward causing ablation volumes to decrease with increasing depth, such that successive profile steps should sample a smaller and smaller volume of zircon. To accurately estimate helium diffusivity from measured diffusive loss profiles, we had to correct for this effect

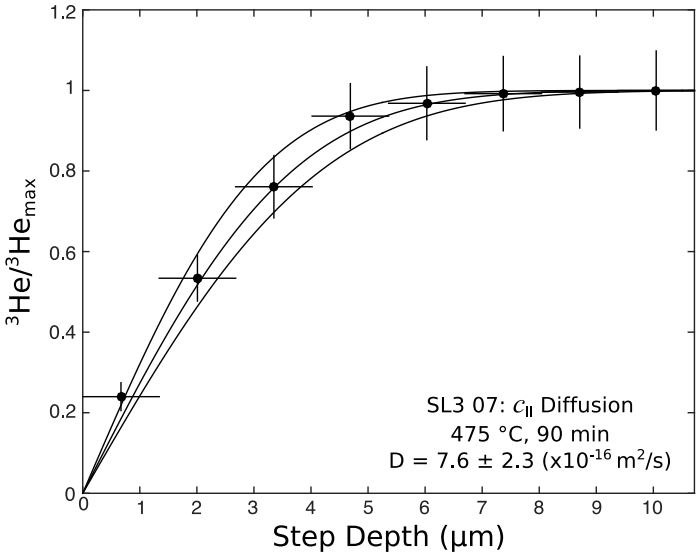

Figure 4.3. Example laser depth profile with best-fit diffusion curve and 2σ uncertainty envelope. Uncertainties on individual data points reflect propagated 2σ analytical uncertainties for ^{3}He measurements and the total width of each profile step, while the uncertainty envelope reflects propagated uncertainties associated with ^{3}He measurements, interferometer depth measurements, step widths, and heating duration.

(van Soest et al., 2011). We established a correction factor (ϕ_z) by measuring $c_{\|}$ depth profiles in one unheated Mud Tank and one unheated Sri Lankan zircon slab (Figure S4.1). This ϕ_z correction was applied to the data reported in Table S4.3 for laser profiles with final profile depths >15 μm; geometry effects on shallower profiles were found to be statistically insignificant. Finally, corrected ^{3}He abundances $-$ or abundances without correction for the shallower profiles $-$ were used to reconstruct the induced ^{3}He diffusion profiles in the directions parallel to the incident beam path. Figure 4.3 shows an example of one of the diffusion profiles; depictions of all profiles are shown in Figures S4.2, S4.3, S4.4, S4.5, and S4.6.

4.4.4 Characterizing Radiation Damage

A Horiba Scientific Jobin Yvon *XploRa Plus* Raman microscope was used to determine accumulated radiation damage in the two samples. After laser depth profiling, spectra were measured at both the polished surface and profile bottoms to evaluate whether laser depth profiles crossed through areas of the crystals with different degrees of radiation damage. Further details on our Raman methods can be found in the Supplementary Materials.

With the exception of SL3 15, all Raman results suggest that profiles sampled areas with relatively uniform damage contents. Mean $\nu_3(SiO_4)$ peak position and FWHM values for each diffusion experiment are reported in Table 4.1. Measured FWHM values range from 2.8 to 4.1 cm^{-1} and 8.5 to 14.4 cm^{-1} for MT and SL3, respectively. Using the calibration curve presented by Palenik et al. (2003) (Eq. 4), we converted these values to equivalent alpha doses. As shown in Table 4.1, estimated alpha doses for zircon diffusion experiments range from 1.44 to 2.23 x 10^{17} α/g (MT) and 4.98 to 9.05 x 10^{17} α/g (SL3). Comparisons of these values to those reported for many zircon samples in the literature suggest that the Mud Tank specimen is highly crystalline, with little radiation damage, while the Sri Lankan specimen has moderate, and spatially variable, amounts of damage.

4.4.5 Diffusivity Calculations

Diffusion profiles, such as that shown in Figure 4.3, were fit with a one-dimensional diffusive loss error function of the form:

$$\frac{^3He}{^3He_{max}} \approx \frac{^3He}{^3He_{init}} = erf\left(\frac{z}{\sqrt{4Dt}}\right) \tag{4.1}$$

where $^3He_{init}$, the initial amount of ^3He in the sample prior to diffusive loss, is approximated by $^3He_{max}$, the maximum ^3He abundance measured in each depth profile, z is the depth of each step, D is diffusivity at the experiment temperature (m^2/s), and t is the heating duration (s). Since the depth associated with each profile step represents a range in depth values (from the bottom of the step above to the top of the step below), a Monte Carlo protocol was used to propagate uncertainties (van Soest et al., 2011). This protocol also propagated analytical uncertainties associated with ^3He measurements, interferometer depth estimates, heating durations, and geometry corrections.

Results of these diffusivity calculations are presented in Table 4.1. Plots for each depth profile experiment with diffusion curve fits and 2σ uncertainty envelopes can be found in Figure 4.3 and Figures S4.2, S4.3, S4.4, S4.5, and S4.6 of the Supplementary Materials. All experiments yielded profiles consistent with error-function governed diffusive loss. Six of the fourteen MT experiments yielded an anomalously high ^3He abundances for the initial step that was excluded from diffusivity calculations. Anomalous first steps are common features in noble gas laser depth profiling studies, and it has been proposed that they may be related to sample preparation (J-A et al., 1999; van Soest et al., 2011). The only other notable outlier was step 17 in SL3 05. We hypothesize that this step may reflect ablation through a mineral or fluid inclusion with a higher ^3He concentration than the surrounding zircon due to its chemistry.

4.5 Results

4.5.1 Diffusive Anisotropy: MT Zircon

Results for $c_{\|}$ and $a_{\|}$ ^{3}He diffusion in MT zircon suggest that helium diffusion in this low-damage crystal is markedly anisotropic. The two directions define offset, near-parallel linear arrays on an Arrhenius diagram in which $c_{\|}$ diffusion is significantly faster than $a_{\|}$ diffusion at equivalent temperatures (Figure 4.4). We derive diffusivity parameters from experimental results for the two crystallographic directions using the Arrhenius relationship:

$$D = D_0 \cdot \exp\left(\frac{E_a}{RT}\right) \tag{4.2}$$

where the pre-exponential constant D_0 represents diffusion at infinite temperature (m^2/s), E_a is the activation energy for diffusion (J/mol), T is the experiment temperature (K), and R is the universal gas constant (8.314 J/mol K). Given a threshold value of 4, the Hampel identifier method (Pearson, 2001) identified MT 03 in the $c_{\|}$ array as a statistical outlier. An error-weighted, Monte Carlo linear regression of the remaining $c_{\|}$ data yielded diffusion parameters of E_a = 160.6 $\pm$ 9.3 kJ/mol and ln(D_0) = -6.4 $\pm$ 1.5 ln(m^2/s). A regression of the $a_{\|}$ data yielded parameters of E_a = 146 $\pm$ 16 kJ/mol and ln(D_0) = -15.0 $\pm$ 2.4 ln(m^2/s). These diffusion parameters indicate that $c_{\|}$ diffusivity is $\sim$400 to 700 times faster than $a_{\|}$ diffusivity at equivalent temperatures over the temperature range investigated by laser depth profiling.

Both Arrhenius regressions have mean squared weighted standard deviations (MSWDs) that are greater than the 95% confidence interval of the predicted value of 1 ($c_{\|}$ = 10.3 and $a_{\|}$ = 5.1), suggesting that the scatter in the datasets cannot be solely explained by our estimated analytical uncertainties (Wendt and Carl, 1991). One possible interpretation

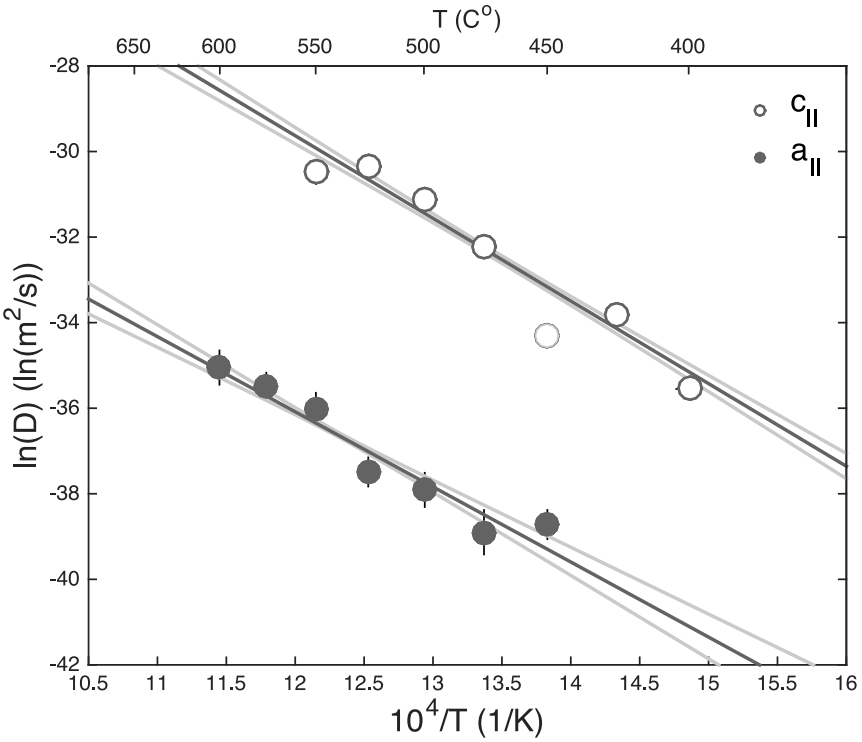

Figure 4.4. An Arrhenius diagram depicting laser depth profile results for $c_{\|}$ and $a_{\|}$ ^{3}He diffusion in Mud Tank zircon (MT). Error bars reflect propagated 2σ analytical uncertainties which are in many cases smaller than the data markers. Best-fit Arrhenius regression lines and 2σ uncertainty envelopes are depicted for the two directions. The lighter open circle marker is a statistical outlier that was not included in the $c_{\|}$ regression.

is that we have underestimated our analytical uncertainties. Alternatively, there may be sources of error not considered by our calculations (please see Section x for a more detailed discussion about error). We note that uncertainties are significant when regression results are extrapolated to the lower temperatures most relevant to zircon helium closure ($\sim$200 to 100 $^{\circ}$C). Providing better constraints on diffusive anisotropy at these lower temperatures would require significantly longer heating durations at lower temperatures, experimental methods capable of resolving shorter diffusive loss profiles (<3 μm) such as NRA, or analytical systems with higher ^{3}He sensitivities that allow for the measurement of smaller ablation volumes.

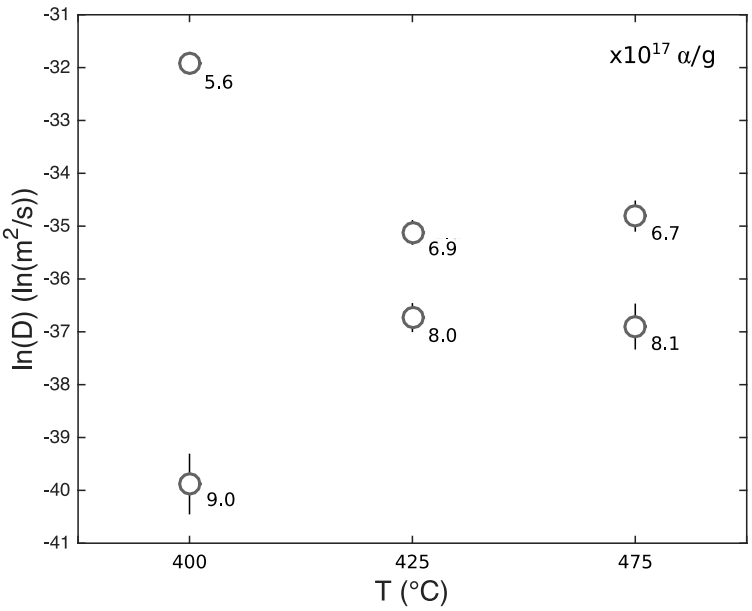

Figure 4.5. Results for Sri Lankan zircon (SL3) isothermal $c_{||}$ diffusion experiments. Data labels represent alpha dose estimates (x10^{17} α/g) for each sample based on Raman data.

4.5.2 Radiation Damage and Diffusive Anisotropy: Sri Lankan Zircon (SL3)

4.5.2.1 $c_{||}$ Diffusivity

Results for our six isothermal $c_{||}$ ^{3}He diffusion experiments in SL3 are shown in Figure 4.5. For each of the three temperature pairs (400 , 425, and 475 °C), the data indicate that diffusion is slower in the sample with higher amounts of radiation damage. Larger variations in radiation damage between data pairs also exhibit larger differences in diffusivity. All $c_{||}$ ^{3}He diffusion experiments in SL3 grouped by estimated alpha dose are shown on an Arrhenius diagram in Figure 4.6. Our data suggest that $c_{||}$ diffusivity appears to decrease systematically with increasing alpha dose.

Simple linear regressions (dotted lines in Figure 4.6) for the two groups with higher alpha doses have similar slopes that closely resemble those for $c_{||}$ and $a_{||}$ helium diffusion

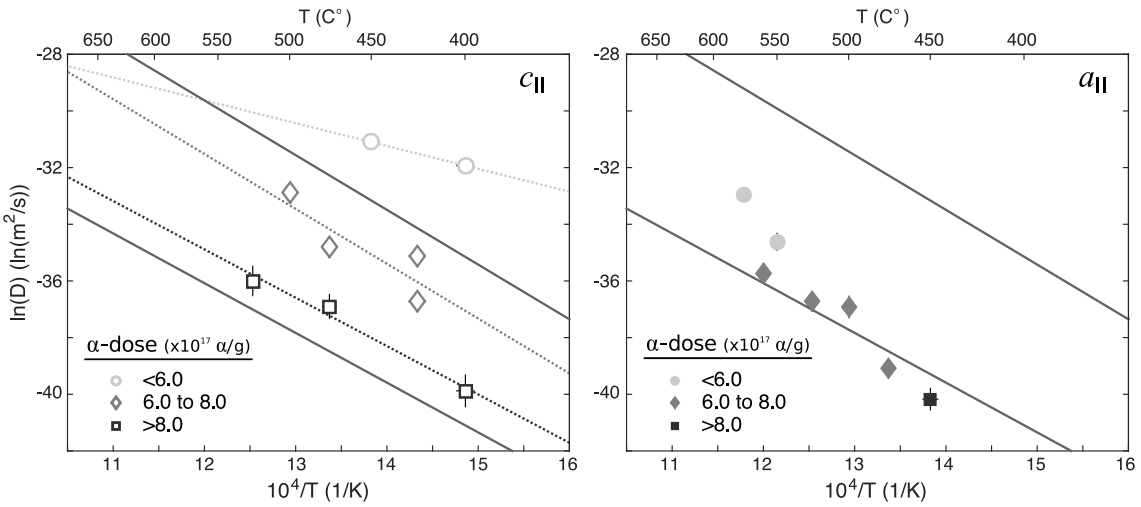

Figure 4.6. An Arrhenius diagram depicting laser depth profile results for $c_{\|}$ and $a_{\|}$ ^{3}He diffusion in Sri Lankan zircon (SL3). Data points have been grouped based on alpha dose estimates determined from Raman measurements. Dotted lines represent simple linear regressions for $c_{\|}$ diffusion in SL3 for each alpha dose group added for visual reference. Solid gray lines represent Arrhenius regressions for $c_{\|}$ and $a_{\|}$ ^{3}He diffusion in Mud Tank zircon for comparison.

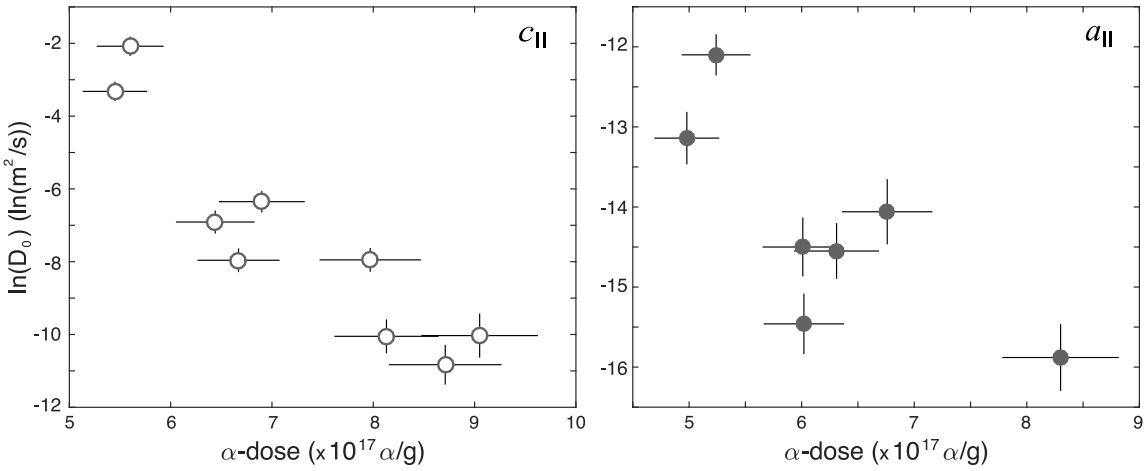

Figure 4.7. Alpha doses vs. projected ln(D_0) values for $c_{\|}$ and $a_{\|}$ helium diffusion in SL3. Error bars reflect propagated $\nu_3(SiO_4)$ FWHM uncertainties and analytical uncertainties for diffusivity calculations as reported in Table 4.1 (2σ).

in MT zircon, suggesting similar activation energies. We interpret this similarity to imply that the apparent decrease in diffusivity with increasing radiation damage is primarily due to a decrease in the diffusivity constant D_0 rather than to changes in E_a. To better evaluate

possible variations in D_0, we apply the best-fit slope for $c_{\|}$ diffusion in MT zircon to each $c_{\|}$ SL3 data point and project a value for D_0. We have chosen to use the slope from our MT results, since there are not enough data points in each alpha dose grouping in SL3 to yield robust Arrhenius regressions. Results of this exercise, shown in Figure 4.7, suggest a steady decrease in $\ln(D_0)$ with increasing radiation damage in the $c_{\|}$ direction.

4.5.2.2 $a_{\|}$ Diffusivity

At first glance, results for $a_{\|}$ diffusivity in SL3 appear to form a linear array on an Arrhenius diagram (Figure 4.6). A simple linear regression of all $a_{\|}$ data points, however, produces an activation energy ($\sim$260 kJ/mol) that is significantly higher than what we would expect for helium diffusion in zircon (Cherniak et al., 2009; Guenthner et al., 2013; Reiners et al., 2004). We interpret this to mean that it is not appropriate to group data points with different damage doses together in single regression. Points derived from experiments on the intermediate alpha dose group (6.0 x 10^{17} to 8.0 x 10^{17} α/g), appear to define a slope that is once again broadly similar to our MT zircon Arrhenius regressions. Similar to before, we try applying the slope for $a_{\|}$ diffusion in MT zircon to each SL3 data point and calculate values for D_0 to investigate possible changes with increasing radiation damage. Although there is significant scatter, we find a weak negative correlation between radiation damage and estimated diffusivity constant.

The decrease in $a_{\|}$ diffusivity with increasing alpha dose is smaller than the change in $c_{\|}$ diffusivity. Consequently, the magnitude of diffusive anisotropy decreases with increasing radiation damage. By an alpha dose of $\sim$9 x 10^{17} α/g, diffusivity in SL3 is only $\sim$20 to 30 times faster along the *c*-axis than along the *a*-axis over the temperature range investigated.

4.5.3 Differences between Zircon Samples

Our SL3 results suggest that low doses of radiation damage will lower helium diffusivity in zircon. However, our four lowest dose SL3 samples (two $c_{\parallel}$ and two $a_{\parallel}$ samples with alpha doses of 1.53 x 10^{17} to 2.31 x 10^{17} α/g) exhibit higher diffusivity than our less damaged MT zircon samples ($\leq$2.31 x 10^{17} α/g). It seems unlikely to us that low doses of radiation damage would first increase and then decrease diffusivity within a very narrow damage range. If this premise is correct, then the noted differences between ^{3}He diffusion in MT and SL3 must be attributed to some other factor. In the next two sections we consider the potential affects of radiation damage annealing and crystal chemistry on zircon helium diffusivity.

4.5.3.1 Radiation Damage Annealing

Annealing radiation damage is not simply the inverse of damage accumulation, but instead involves annealing of different types of crystal defects, epitaxial recrystallization, and the possible appearance and disappearance of additional phases. (Geisler et al., 2001; Ginster et al., 2019; Meldrum et al., 1998; Zhang et al., 2000). Each of these processes have different activation energies, and the extent to which radiation damage anneals strongly depends on the zircon's initial damage content and thermal history. The structural changes associated with various annealing mechanisms could potentially affect helium diffusivity in different ways, so it is important to consider the annealing history of the zircon crystals we studied (Ginster et al., 2019).

Based on previous laboratory annealing studies (Geisler et al., 2001; Ginster et al., 2019; Zhang et al., 2000), we do not expect that the relatively low temperatures (400 to 600 °C)

and short heating durations (10 minutes at the highest temperatures and to 24 hours at lower temperatures) used to induce helium diffusive loss for our laser depth profiling experiments would have caused significant annealing, nor are there correlations between estimated alpha dose and experimental temperature in the two samples. Alpha dose estimates based on Raman measurements indicate that zircon crystals from the Mud Tank carbonatite and the Sri Lankan gem gravels have retained less radiation damage than expected given their crystallization ages and radionuclide contents (Nasdala et al., 2004). Suggested thermal histories for the two localities, however, generally attribute these discrepancies to slow or late cooling rather than to significant late-stage thermal annealing events (Currie et al., 1992; Fernando et al., 2003; Green et al., 2006; Nasdala et al., 2004). We therefore find it unlikely that the noted differences in helium diffusivity between our MT samples SL3 samples can be attributed to the effects of disparate annealing histories.

4.5.3.2 Crystal Chemistry

In addition to uranium and thorium, the zircon structure can accommodate a number of chemical substitutions, resulting in a range of natural compositions and often complex chemical zoning. The most common substitutions are the simple substitutions of (Hf, U, Th)$^{4+} \rightarrow Zr^{4+}$ and $Ti^{4+} \rightarrow Si^{4+}$ and the charge-balanced coupled substitutions of (Y, HREE)$^{3+}$ + $P^{5+} \rightarrow Zr^{4+}$ + Si^{4+} and (Y, HREE)$^{3+}$ + (H,Li)$^{+} \rightarrow Zr^{4+}$ (Finch and Hanchar, 2002; J. T. Sliwinski et al., 2018; Trail et al., 2010). Correspondingly, zircon is isostructural with several tetragonal minerals including heavy rare earth element phosphates ([HREE,Y]PO_4) and end-member xenotime (YPO_4), hafnon ($HfSiO_4$), coffinite, ($USiO_4$), and thorite ($ThSiO_4$).

Farley (2007) demonstrated that crystal chemistry strongly influences helium diffusivity

in synthetic end-member rare earth element phosphates. He showed that diffusivity increases as Y,HREE ionic radii, Y,HREE-P distances, and ionic porosity increased. Anderson et al. (2019) later found that helium diffusion in crystalline natural xenotime time is significantly faster than in isostructural crystalline zircon. The authors attributed these differences to crystal chemistry; since Y^{3+} and other $HREE^{3+}$ have significantly larger ionic radii (0.977 to 1.04 Å) than Zr^{4+} (0.84 Å), Y,HREE-P distances (4.796 to 4.901 Å) are longer than Zr-Si distances (4.670 Å) and interstitial openings are wider and can more easily accommodate helium transport (Shannon1976; Ni et al., 1995). Like HREE ions, U^{4+} and Th^{4+} have large ionic radii (1.00 and 1.05 Å), and U-Si and Th-Si distances in coffinite and thorite (4.946 Å and 5.050 Å) are longer than Zr-Si distances (Fuchs and Gebert, 1958; Shannon, 1976). Consequently, the substitution of U^{4+}, Th^{4+}, and $REEs^{3+}$ for Zr^{4+} in zircon likely widen interstitial sites locally. Although Hf concentrations in zircon are typically higher than U, Th, and REEs, the ionic radii of Hf^{4+} (0.83 Å) is nearly identical to Zr^{4+} and the Hf-Si distance in hafnon is similar (4.647 Å) to the Zr-Si distance in zircon, so we do not expect Hf concentration to significantly affect helium diffusivity (Shannon, 1976; Speer and Cooper, 1982).

To evaluate the potential effects of crystal chemistry, we measured major, minor, and trace element crystal chemistry in one Mud Tank (MT 04) and three Sri Lankan (SL3 01, 08, and 09) slabs used for laser depth profiling by laser ablation inductively coupled plasma mass spectrometry (LA-ICPMS). Details on our LA-ICPMS methods are presented in the Supplementary Materials. The three SL3 samples represent our three alpha dose groups that exhibited differences in helium diffusivity.

Results indicate that the three SL3 samples have significantly higher concentrations of U and Th ($\sim$1100 and 200 ppm, respectively) than MT zircon ($\sim$13 and 30 ppm) and slightly higher concentrations of REEs (Table 4.2, Figure 4.8). Although Raman results suggest

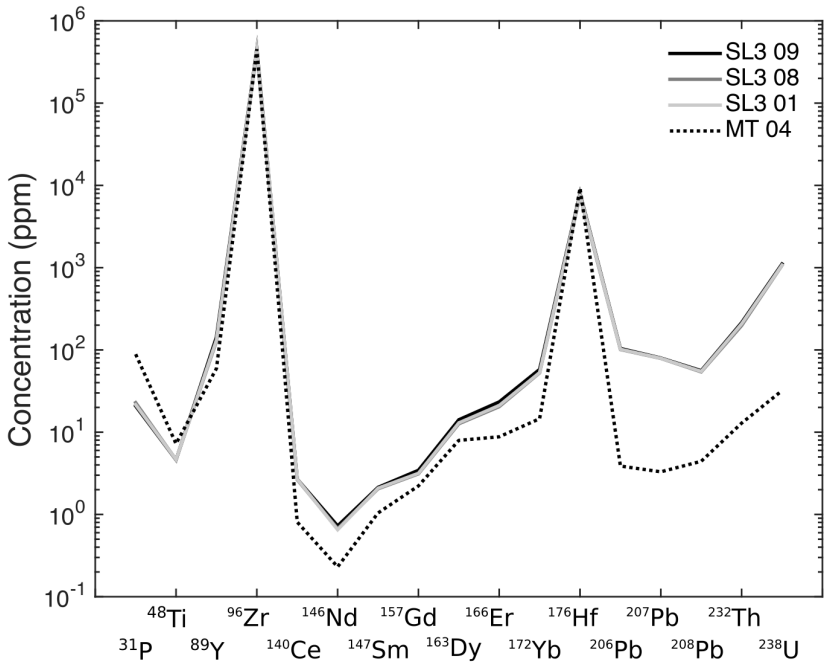

Figure 4.8. LA-ICPMS crystal chemistry results for selected MT and SL3 samples shown on a Spider diagram.

distinct differences in radiation damage between the SL3 samples, isotopic concentrations (including U and Th) are quite similar. LA-ICPMS line scans − which covered large areas around our laser depth profiles pits − however, show that line scans crossed and averaged zones with different chemistries. These results suggest to us that the differences in helium diffusivity between the MT and SL3 zircons may reflect differences in trace element crystal chemistry, particularly U, Th, and REE contents. We propose that the incorporation of U and Th in zircon has two competing effects on diffusivity at low alpha doses: 1) The larger ions widen interstitial sites locally allowing easier helium transport; and 2) alpha decay of U and Th subsequently cause atomic displacements that disrupt helium transport through interstitial sites (Guenthner et al., 2013). Diffusion experiments on zircon crystals with different crystal chemistries and similar amounts of radiation damage with similar annealing

Table 4.2. LA-ICPMS Crystal Chemistry Results.

Isotope	9500	2σ[b]	MT 04	2σ	SL3 09	2σ	SL3 08	2σ	SL3 01	2σ
^{31}P	24.06	0.54	88.68	0.81	20.78	0.47	22.88	0.55	21.56	0.55
^{48}Ti	5.200	0.024	7.243	0.034	4.603	0.029	4.625	0.076	4.641	0.031
^{89}Y	139.98	0.41	59.46	0.29	143.49	0.77	126.86	0.59	131.70	0.71
^{96}Zr[a]	49.53	0.14	45.28	0.18	45.28	0.24	43.16	0.19	44.41	0.22
^{140}Ce	2.600	0.013	0.8072	0.0070	2.689	0.016	2.642	0.015	2.687	0.016
^{146}Nd	0.2402	0.0078	0.2308	0.0081	0.727	0.013	0.672	0.013	0.652	0.013
^{147}Sm	1.000	0.025	1.042	0.025	2.135	0.036	2.051	0.037	2.086	0.038
^{157}Gd	2.199	0.025	2.223	0.025	3.446	0.034	3.115	0.031	3.167	0.034
^{163}Dy	12.000	0.052	7.954	0.048	14.170	0.083	12.652	0.073	12.990	0.080
^{166}Er	24.988	0.084	8.787	0.048	23.358	0.11	20.44	0.10	21.12	0.12
^{172}Yb	73.99	0.22	14.586	0.071	58.06	0.26	52.59	0.22	53.09	0.26
^{176}Hf	5898	20	9291	40	8013	43	7484	35	7788	41
^{206}Pb	15.013	0.045	3.875	0.022	104.07	0.44	101.11	0.40	101.92	0.47
^{207}Pb	15.01	0.11	3.299	0.049	79.77	0.38	78.87	0.39	79.10	0.43
^{208}Pb	15.01	0.10	4.43	0.05	55.91	0.32	54.05	0.29	54.79	0.32
^{232}Th	29.992	0.093	12.876	0.079	214.7	1.2	197.62	0.92	207.5	1.2
^{238}U	80.00	0.22	31.99	0.15	1107.8	5.6	1067.3	4.6	1074.3	5.4

[a]All reported concentrations are in ppm except for ^{96}Zr which is reported in weight %.
[2]All 2σ uncertainties represesnt two standard error analytical uncertainties.

histories are needed to better test to what extent trace element chemistry affects helium diffusivity.

4.5.4 Potential Sources of Uncertainty

In addition to the effects of radiation damage and the potential effects of crystal chemistry on helium diffusion in zircon, there are a number of other factors to consider that may contribute to the scatter in our datasets. Although step-wise degassing studies on single crystals and multi-crystal aliquots suggest that proton-irradiation produces a uniform distribution of ^{3}He in minerals (Shuster et al., 2003), the possibility remains that this distribution is not perfectly homogenous on the shorter length scales relevant to laser micro-sampling ($\sim$1 to 5 μm profile step sizes). Other sources of uncertainties include minor differences in laser ablation behavior between samples due laser focus, color and the related absorption or transparency of the laser energy, crystal chemistry, and the development of complex laser

pit topography in deeper profiles which is evidenced by some interferometer profile images. Erroneous temperature estimates due to temperature gradients forming across zircon slabs or poor sample-thermocouple contact during laboratory heating are also possibilities.

4.6 Comparison with Other Diffusion Data

Our laser depth profile results for $a_{\|}$ diffusion in MT zircon agree well with NRA depth profile results for $c_{\perp}$ diffusion in a different sample of Mud Tank zircon and Australian DR zircon (Figure 4.9) (Cherniak et al., 2009). Our $c_{\|}$ diffusion results, though, imply significantly higher diffusivity $-$ and consequently, a greater magnitude of diffusive anisotropy ($\sim$400 to 700 times faster vs. $\sim$75 times)$-$ than do the $c_{\|}$ NRA results for DR zircon. The NRA results are, however, consistent with a subset of our SL3 dataset with alpha doses between 6.0 - 8.0 x 10^{17} α/g (Figure 4.10). Based on this observation, we posit that DR zircon has more radiation damage than our MT zircon. Neither the U and Th contents nor a U-Pb date were reported by the authors for the sample, but they speculated that it had relatively low amounts of radiation damage based on its locality (Cherniak et al., 2009).

Our $c_{\|}$ diffusion results in MT zircon have somewhat lower diffusivity than that suggested by ^{4}He step-wise degassing of another sample of Mud Tank zircon (Figure 4.9) (Guenthner et al., 2013); however, the activation energy for diffusion for the two datasets agree within uncertainty. The alpha dose (1.22 x 1016 α/g) and U and Th contents reported by Guenthner et al. (2013) for their sample are lower than ours, which may explain their sample's higher diffusivity. Step-wise degassing results for $c_{\perp}$ helium diffusion in Mud Tank zircon (Guenthner et al., 2013), however, are extremely high compared to $a_{\|}$ laser and $c_{\perp}$ NRA depth profile results (Cherniak et al., 2009). We interpret the step-wise degassing results to reflect a strong $c_{\|}$ diffusion component. Our comparisons between depth profiling

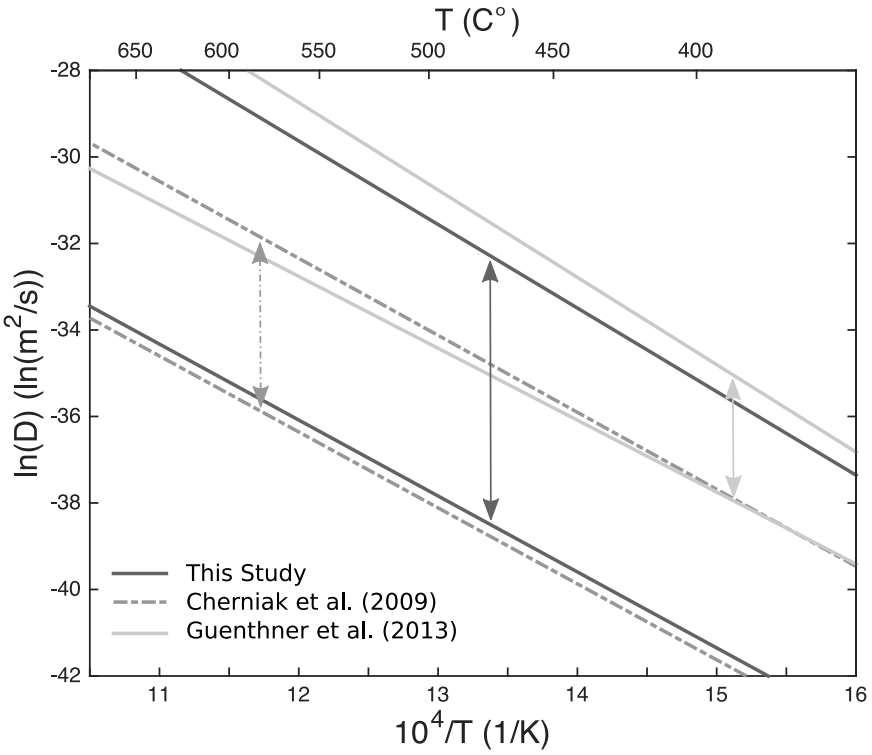

Figure 4.9. An Arrhenius diagram comparing laser depth profiles results for $c_{\|}$ and $a_{\|}$ ^{3}He diffusion in MT zircon to previous studies plotted over the temperature range investigated in this study: 1) NRA results for ^{3}He diffusion in Mud Tank ($c_{\perp}$) and DR ($c_{\|}$ and $c_{\perp}$) zircon (Cherniak et al., 2009), and 2) Step-wise degassing results for ^{4}He diffusion in Mud Tank zircon (Guenthner et al., 2013). Over the illustrated temperature range, the top line in each line pair represents faster $c_{\|}$ diffusion. Arrows have been added as visual cues for comparing the magnitude of diffusive anisotropy

methods and the bulk diffusion study suggest to us that bulk degassing experiments on minerals slabs with elongated crystallographic aspect ratios may successfully characterize the fast component of diffusion when diffusivity is moderately to strongly anisotropic, but do not appear to accurately capture the slow component. Since the step-wise degassing study (Guenthner et al., 2013) shows $c_{\|}$ diffusivity to be even higher in lower damage zircon than suggested by laser depth profiling, the magnitude of diffusive anisotropy may be even higher (more than $\sim$400 to 700 times faster $c_{\|}$ diffusion) in zircon crystals with lower damage doses (<1.5 x 10^{17} α/g).

Although our study and that of Guenthner and colleagues (2013) both suggest that $c_{\|}$

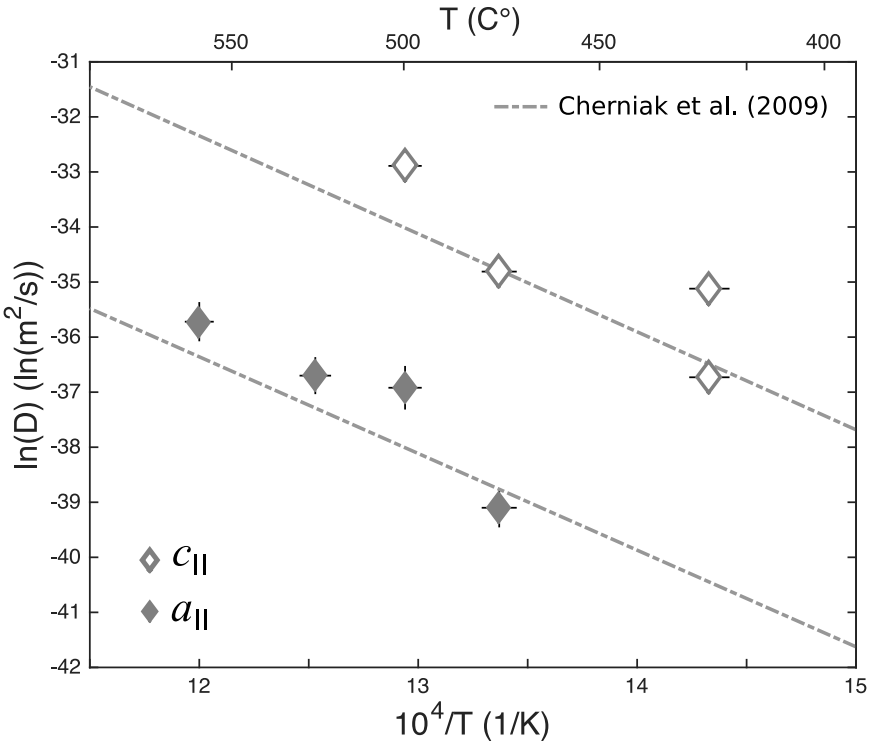

Figure 4.10. An Arrhenius diagram showing NRA results for Cherniak et al. (2009) $c_{\parallel}$ (top line) and $c_{\perp}$ ^{3}He diffusion in zircon compared to laser depth profile results for ^{3}He diffusion in SL3 samples with alpha doses between 6.0 and 8.0 x 10^{17} α/g.

diffusivity and diffusive anisotropy decrease with increasing alpha dose, there are notable inconsistencies between the two studies. For instance, laser depth profiles results for SL3 suggest that diffusive anisotropy remains significant to higher alpha doses than predicted by step-wise degassing results for various Sri Lankan zircons (Figure 4.11). Our intermediate alpha dose group (6.0 x 10^{17} to 8.0 x 10^{17} α/g) indicate that diffusive anisotropy is similar to the NRA study results which found diffusion to be $\sim$75 times faster along the c-axis (Figure 4.10) (Cherniak et al., 2009). Results for RB140 zircon which has a lower alpha dose (4.6 x 10^{17} α/g), however, imply that $c_{\parallel}$ diffusivity is less than 10 times faster. This suggests that step-wise degassing experiments, even on oriented zircon slabs with high aspect ratios, seem to again be underestimating the magnitude of diffusive anisotropy by averaging $a_{\parallel}$ and $c_{\parallel}$ components.

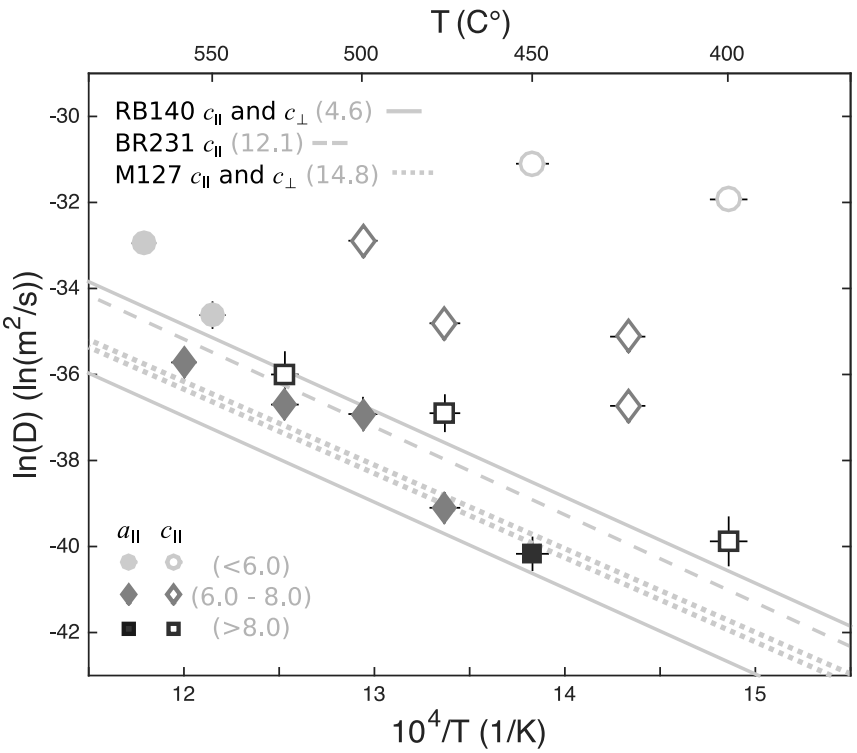

Figure 4.11. An Arrhenius diagram showing depth profile results for ^{3}He diffusion in zircon SL3 compared to results for step-wise degassing experiments for ^{4}He $c_{\parallel}$ (top line in pairs) and $c_{\perp}$ diffusion in Sri Lankan zircons RB140, BR231, and M127 (Guenthner et al., 2013). Numbers in parentheses represent estimated alpha doses (x10^{17} α/g) for samples.

All SL3 experiments have diffusivities that are either higher than or within uncertainty of respective $c_{\parallel}$ and $c_{\perp}$ results for zircon RB140 (Guenthner et al., 2013), even though the SL3 samples have higher estimated alpha doses. We propose that this relative offset might be attributed to the effects of zircon crystal chemistry on helium diffusivity, since SL3 has higher U and Th contents ($\sim$1100 and 200 ppm) and potentially a more open structure than RB140 (288 and 122 ppm). However, as discussed earlier, additional experiments are needed to fully evaluate this hypothesis.

4.7 Implications for Zircon (U-Th)/He Closure Temperatures

In this section, we explore the effects of diffusive anisotropy on helium closure temperature in low damage zircon using the Monte Carlo diffusion model developed by Gautheron and Tassan-Got (2010) and our laser depth profile results for ^{3}He diffusion in MT zircon. This approach allows us to easily model anisotropic diffusivity in crystals with complex geometries as isotropic diffusion in a sphere by expanding the concept of the equivalent spherical radius (R_{eq}) (Farley et al., 1996) to that of the active radius (R_{eq}'). As defined by Gautheron and Tassan-Got (2010), R'$_{eq}$ depends on crystal geometry as well as the ratios of the diffusion coefficients along the *a*-, *b*- and *c*- crystallographic axes. It is important to note that this approach assumes that diffusive anisotropy is controlled by changes to D_0 with crystallographic orientation and not E_a, which is consistent with our results and those of Cherniak et al. (2009). For this model we simply take the average E_a value determined for $a_{\|}$ and $c_{\|}$ diffusivity (153 kJ/mol) as our best estimate for the activation energy.

Since zircon crystallizes in the tetragonal crystal system, D_a equals D_b and the symmetrically averaged diffusion coefficient, D_{avg}, is

$$D_{avg} = \frac{D_c + 2 \cdot D_a}{3} \tag{4.3}$$

where D_a, D_b, and D_c are the diffusion coefficients along the three crystallographic axes. We calculate that D_{avg} equals 5.29 x 10^{-4} m^2/s, and the diffusion coefficient ratio D_c/D_{avg} is 3. Using this final value and the freely available software program developed by Gautheron and Tassan-Got (2010), we calculated R_{eq}' for tetragonal prisms with pyramidal terminations with *c*- to *a*-axis aspect ratios ranging from 1 to 4, about the typical range for natural zircon crystals (Reiners et al., 2017), using the prism dimensions reported in Table 4.3. We then calculated the closure temperature for helium in zircon following Dodson's (1973)

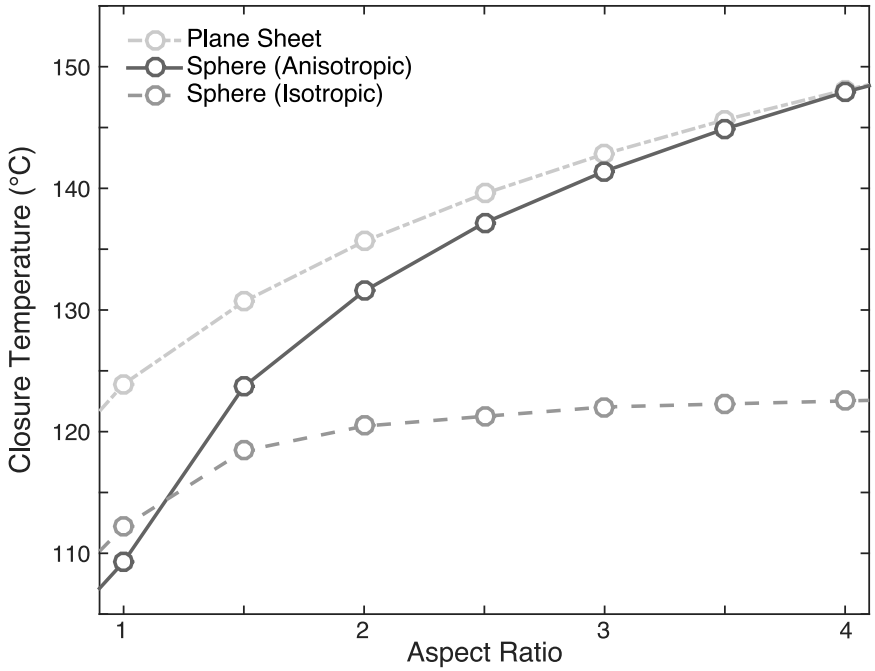

Figure 4.12. Zircon aspect ratio vs. estimated closure temperature for different diffusion models as discussed in text based on laser depth profile results for helium diffusion in Mud Tank zircon. Closure temperature calculations assume a cooling rate of 10 °C/Ma.

Table 4.3. Prism and Modeled Diffusion Dimensions.

Width (μm)	Height (μm)	Aspect Ratio	R_{eq}	R_{eq}'
100	100	1.0	35	29
100	150	1.5	52	72
100	200	2.0	59	115
100	250	2.5	62	159
100	300	3.0	65	202
100	350	3.5	66	245
100	400	4.0	67	289

formulations, assuming a spherical geometry with a diffusion dimension equivalent to our R_{eq}' values and the nominal cooling rate of 10 °C/Ma (Figure 4.12).

Since many thermo-kinematic models used to extract thermal histories from low-temperature thermochronometric datasets assume one of two end member diffusion geometries for dated minerals – either isotropic diffusion in a sphere or perfectly anisotropic diffusion in a plane sheet – we compare our model results using these two scenarios (Cher-

niak et al., 2009; Gautheron and Tassan-Got, 2010; Reiners et al., 2017). For isotropic diffusion in a sphere, our closure temperature calculations assume that the diffusion coefficient is equal to D_{avg} and that the diffusion dimension is equal to the equivalent spherical radius, R_{eq}. In the plane sheet scenario, we assume a diffusion coefficient equal to D_c and a diffusion dimension equal to half the prism's height. All calculations assume 153 kJ/mol as the activation energy for diffusion in the MT zircon.

Our model results demonstrate that neither end-member scenario accurately captures the effects of moderate diffusive anisotropy on the closure temperature for helium in zircon for all prism aspect ratios (Figure 4.12). In nearly equant crystals the closure temperature calculations for anisotropic diffusion in a sphere (the Gautheron and Tassan-Got (2010) model) are more similar to calculations that assume isotropic diffusion in a sphere, whereas more elongated crystals have closure temperatures more similar to those predicted by the plane sheet geometry. Intermediate aspect ratios ($\sim$1.5 to 2.5) have values that fall in between the two end-member scenarios. Our calculations suggest that selecting an inappropriate diffusion model can change zircon helium closure temperature estimates by up to $\sim$25 °C. Whether this difference is enough to significantly affect geologic interpretations ultimately depend on the geologic setting and the question(s) being asked.

Perhaps more importantly, Figure 4.12 demonstrates that because helium diffusion in zircon is anisotropic, low damage zircon crystals with different aspect ratios invariably record different closure temperatures. We find that zircon crystals with high aspect ratios (4:1) have closure temperatures that are $\sim$45 °C higher than perfectly equant crystals. In the isotropic scenario, increasing the prism height to a 4:1 ratio only increases the closure temperature by $\sim$10 °C. This effect could potentially be leveraged to extract a more nuanced understanding of a rock sample's thermal history by dating zircons with different aspect ratios. These results also suggest that the effects of diffusive anisotropy could contribute

significantly to zircon (U-Th)/He date dispersion in datasets with very low amounts of radiation damage and a wide range in aspect ratios where cooling rates are slow to moderate.

4.8 Conclusions

Our results for Mud Tank zircon, obtained by direct measurement of diffusive loss profiles on crystallographically oriented slabs, indicate that the magnitude of diffusive anisotropy in zircon crystals with low amounts of radiation damage is greater than previous experimental results have suggested. These results strongly indicate that bulk diffusion experiments − even when done on oriented crystal slabs with high aspect ratios − consistently underestimate the magnitude of diffusive anisotropy by averaging $a_{\|}$ and $c_{\|}$ diffusivity.

Models based on our depth profile results for Mud Tank zircon suggest that low-damage zircon crystals with different crystal morphologies should record different closure temperatures due to diffusive anisotropy. This effect likely contributes to the scatter in zircon (U-Th)/He dates found in many rock samples. Commonly assumed diffusion geometries used in thermo-kinematic models (such as isotropic diffusion in a sphere and perfectly anisotropic diffusion in a plane sheet) do not properly account for diffusive anisotropy in low-damage zircon and, consequently, do not accurately predict zircon helium closure temperatures for the full range of typical zircon aspect ratios. Thermal-kinematic should either include anisotropic diffusion models (Cherniak et al., 2009; Gautheron and Tassan-Got, 2010), or should be revised to allow diffusion geometry selections that are based on grain aspect ratios.

Depth profiling results for our Sri Lankan zircon sample indicate that both $a_{\|}$ and $c_{\|}$diffusivity decrease as radiation damage increases from 4.98 to 9.05 x 10^{17} α/g, reinforcing previous suggestions that atomic displacements or other structural defects disrupt

helium transport through zircon interstitial sites at low alpha doses (Guenthner et al., 2013). We show that this effect is more complex than a simple change in bulk diffusivity; $c_{\|}$ diffusivity decreases at a faster rate than $a_{\|}$ diffusivity with increasing radiation damage. As a consequence, diffusive anisotropy also decreases with increasing alpha dose. At the highest alpha doses investigated, diffusivity is approaching isotropic.

Finally, our findings suggest that differences in diffusivity between our two zircon samples (MT and SL) cannot be solely attributed to crystallographic anisotropy and radiation damage, suggesting that minor and trace element chemistry may play an under-appreciated role as well. More diffusion experiments are needed on zircon crystals with different crystal chemistries but the same radiation damage to further evaluate this possibility.

4.9 Supplementary Materials

4.9.1 Sample Characterization and Preparation

Laue diffraction patterns were acquired using a PANanalytic X'Pert PRO MRD X-ray diffractometer at the Eyring Materials Center at Arizona State University (ASU) to determine samples' crystallographic orientations. Samples were then fashioned into slabs oriented either (100) or (001) using the table and wire saws in the ASU Experimental Petrology and Igneous Processes Center (EPIC). After polishing and preliminary Raman spectroscopy, oriented zircon slabs were wrapped in aluminum foil jackets, stacked in plastic capsules, which were in turn loaded in silica glass tubes. The packaged samples were proton irradiated at the Francis H. Burr Proton Therapy Center at the Massachusetts General Hospital for three seven-hour sessions of proton irradiation yielding a total dose of 3 x 10^{16} protons. After the samples were returned, Raman spectra were again acquired for comparison.

4.9.2 Inducing Diffusive Loss

Each irradiated sample was placed in a platinum capsule with an Omega Type K thermocouple, loaded into a diffusion cell with a synthetic sapphire viewport, and put under high vacuum. The sample was then heated using either a projector bulb or diode infrared laser positioned above the diffusion cell viewport for a set time and temperature to induce ^{3}He diffusive loss (Farley et al., 1999). Temperature was controlled during heating by a feedback loop between the heating source and the thermocouple. Experimental temperatures and heating durations ranged from 400 to 600 °C and from 10 to 1440 minutes with estimated uncertainties of 4 °C and 2 minutes, respectively. Uncertainties reflect manufacturer-stated thermocouple accuracies, noted temperature fluctuations, and temperature ramp up and cooling down times. All uncertainties are quoted at the 2σ level throughout the text unless otherwise noted. Following heating, zircon samples were unloaded from the diffusion cell, removed from their platinum capsules, and mounted in indium.

4.9.3 Laser Depth Profiling

Indium mounts were then loaded into a custom-designed laser ablation cell with a synthetic sapphire viewport. The cell, connected to the Helix SFT noble gas extraction line, was placed under ultra high vacuum and positioned beneath either a Teledyne Photon Machines *Analyte* Excite or *Analyte* G2 ultraviolet (193 nm) ArF excimer laser for depth profiling. Typical lasing conditions were 4 to 5 mJ laser energy, 100 $\%$ output power, and 5 Hz pulse frequency. Cylindrical pits with either 135 μm (*Analyte* Excite) or 208 μm (*Analyte* G2) diameters were ablated into each sample. These spot sizes represent the largest available for the two laser systems. To generate a large enough volume of ablated material

with sufficient signal for ^{3}He isotopic measurement, groupings of multiple laser spots (2 to 10) were typically ablated per step. The step size for each profile was controlled by the number of laser shots fired per step. Five shots per step were used to characterize the shallowest profiles, and 125 shots per step were used for the deepest $c_{\|}$ profiles. The step size was held constant for all steps within any given profile. The laser focal plane was lowered with each step in accordance with the predicted ablation rate.

The extracted gases for each profile step were purified along the noble gas extraction line using hot and cold metal alloy getters and a cryogenic trap. Isotopic ^{3}He abundances were measured using a Thermo Electron (GV Instruments) *Helix SFT* mass spectrometer on an ion-counting electron multiplier detector. The instrument ^{3}He sensitivity was monitored daily by measuring ^{3}He standard air shots. Measured ^{3}He blanks were at or below detection level, so blank corrections were not necessary. Depth profiling was continued until a 'plateau' was achieved in which at least three steps had ^{3}He abundances within 2σ uncertainty of one another. Helium-3 isotopic measurements for all diffusion experiments are reported in Tables S4.1 and S4.2.

Following laser depth profiling, mounts were removed from the laser ablation cell, and ablated profiles were scanned using a PhaseShift MicroXAM interferometric microscope. These data were processed through an in-house Matlab script to calculate the depth of each ablated profile. Since most profiles consisted of groupings of 2 to 10 laser spots, we took each sample's mean depth value as our best depth estimate (Table 4.1). A 0.4 μm measurement uncertainty was assigned to profiles <5 μm deep and 1 μm uncertainty assigned to profiles >5 μm based on the reproducibility of profile depths determined for different laser spot groupings.

Table S4.1. MT Laser Depth Profile ^{3}He Isotopic Abundances.

Step	^{3}He (atoms)	2σ
MT 01: $c_{\|\|}$ 400 °C, 840 min		
1	1.096E+06	9.9E+04
2	1.659E+06	9.9E+04
3	2.46E+06	1.9E+05
4	3.12E+06	1.6E+05
5	2.91E+06	1.5E+05
6	2.99E+06	1.7E+05
7	2.94E+06	1.5E+05
8	2.94E+06	1.5E+05
MT 02: $c_{\|\|}$ 425 °C, 480 min		
1	6.80E+05	7.3E+04
2	1.105E+06	8.1E+04
3	1.54E+06	1.1E+05
4	1.795E+06	9.4E+04
5	2.356E+06	1.3E+05
6	2.523E+06	1.0E+05
7	2.472E+06	1.2E+05
8	2.395E+06	1.5E+05
MT 03: $c_{\|\|}$ 450 °C, 480 min		
1	1.138E+06	8.6E+04
2	5.61E+05	6.3E+04
3	8.87E+05	7.4E+04
4	1.011E+06	7.5E+04
5	1.213E+06	8.5E+04
6	1.318E+06	9.6E+04
7	1.396E+06	9.9E+04
8	1.46E+06	1.0E+05
9	1.547E+06	9.2E+04
10	1.568E+06	8.4E+04
11	1.506E+06	9.8E+04
MT 04: $c_{\|\|}$ 475 °C, 120 min		
1	7.07E+05	6.8E+04
2	1.388E+06	8.2E+04
3	1.97E+06	1.3E+05
4	2.22E+06	1.3E+05
5	2.53E+06	1.5E+05
6	2.72E+06	1.2E+05
7	2.85E+06	1.4E+05
8	3.18E+06	1.6E+05
9	3.19E+06	1.5E+05
10	3.13E+06	1.9E+05

Step	^{3}He (atoms)	2σ
MT 05: $c_{\|\|}$ 500 °C, 30min		
1	5.48E+05	5.2E+04
2	1.004E+06	7.0E+04
3	1.37E+06	1.1E+05
4	1.71E+06	1.1E+05
5	2.03E+06	1.2E+05
6	2.18E+06	1.1E+05
7	2.43E+06	1.1E+05
8	2.36E+06	1.4E+05
9	2.40E+06	1.3E+05
10	2.57E+06	1.2E+05
11	2.61E+06	1.5E+05
12	2.50E+06	1.3E+05
MT 06: $c_{\|\|}$ 525 °C 15 min		
1	9.32E+05	8.0E+04
2	8.21E+05	7.3E+04
3	1.220E+06	8.2E+04
4	1.58E+06	1.2E+05
5	1.79E+06	1.3E+05
6	1.94E+06	1.3E+05
7	2.14E+06	1.2E+05
8	2.29E+06	1.4E+05
9	2.33E+06	1.2E+05
10	2.29E+06	1.3E+05
11	2.27E+06	1.3E+05
MT 07: $c_{\|\|}$ 550 °C, 10 min		
1	5.10E+05	6.0E+04
2	1.210E+06	8.2E+04
3	2.042E+06	8.9E+04
4	2.31E+06	1.5E+05
5	2.62E+06	1.5E+05
6	2.63E+06	1.6E+05
7	2.76E+06	2.1E+05
8	2.92E+06	1.7E+05
9	2.81E+06	1.6E+05
10	2.78E+06	1.5E+05

Step	^{3}He (atoms)	2σ
MT 08: $a_{\|\|}$ 450 °C, 1440 min		
1	2.06E+06	2.0E+05
2	2.65E+06	2.0E+05
3	3.41E+06	1.9E+05
4	4.29E+06	2.5E+05
5	4.09E+06	2.6E+05
6	4.18E+06	2.7E+05
7	4.20E+06	2.0E+05
8	4.21E+06	2.2E+05
9	4.40E+06	2.3E+05
MT 09: $a_{\|\|}$ 475 °C, 1200 min		
1	4.40E+05	4.8E+04
2	6.31E+05	5.4E+04
3	7.42E+05	6.1E+04
4	8.29E+05	7.6E+04
5	8.97E+05	7.9E+04
6	8.83E+05	5.7E+04
7	9.05E+05	7.6E+04
8	9.12E+05	9.1E+04
9	8.91E+05	9.8E+04
MT 10: $a_{\|\|}$ 500 °C, 480 min		
1	9.85E+05	9.6E+04
2	1.200E+06	7.4E+04
3	1.540E+06	7.6E+04
4	1.660E+06	9.8E+04
5	1.680E+06	7.8E+04
6	1.740E+06	9.7E+04
MT 11: $a_{\|\|}$ 525 °C, 180 min		
1	5.33E+05	5.4E+04
2	4.41E+05	5.9E+04
3	6.89E+05	6.6E+04
4	7.60E+05	6.5E+04
5	8.60E+05	7.5E+04
6	9.08E+05	8.8E+04
7	8.93E+05	8.9E+04
8	8.98E+05	8.2E+04

Step	^{3}He (atoms)	2σ
MT 12: $a_{\|\|}$ 550 °C, 90 min		
1	7.21E+05	5.2E+04
2	1.130E+06	7.4E+04
3	1.460E+06	8.4E+04
4	1.640E+06	8.1E+04
5	1.840E+06	9.6E+04
6	1.85E+06	1.0E+05
7	1.72E+06	1.0E+05
MT 13: $a_{\|\|}$ 575 °C, 30 min		
1	6.21E+05	5.9E+04
2	4.74E+05	5.9E+04
3	5.76E+05	5.9E+04
4	7.25E+05	7.5E+04
5	8.23E+05	7.1E+04
6	8.25E+05	6.3E+04
7	9.05E+05	7.2E+04
8	9.10E+05	6.9E+04
9	8.67E+05	6.2E+04
MT 14: $a_{\|\|}$ 600 °C, 10 min		
1	6.89E+05	6.1E+04
2	5.23E+05	5.9E+04
3	7.61E+05	5.4E+04
4	8.58E+05	8.2E+04
5	9.35E+05	8.5E+04
6	8.95E+05	9.6E+04
7	8.62E+05	7.8E+04
8	9.26E+05	8.0E+04
MT 15: Unheated		
1	1.91E+06	1.2E+05
2	2.08E+06	1.6E+05
3	2.05E+06	1.1E+05
4	2.07E+06	1.1E+05
5	1.99E+06	1.4E+05
6	1.90E+06	1.1E+05
7	1.88E+06	1.4E+05
8	1.87E+06	1.5E+05
9	1.83E+06	1.3E+05
10	1.80E+06	1.2E+05

*Profile geometry corrections have not been applied to the reported isotopic measurements.

Table S4.2. SL3 Laser Depth Profile ^{3}He Isotopic Abundances.

Step	^{3}He (atoms)	2σ
SL3 01: $c_{\|\|}$ 400 °C, 720 min		
1	4.42E+05	5.8E+04
2	1.20E+06	1.0E+05
3	1.67E+06	1.2E+05
4	2.06E+06	1.2E+05
5	2.49E+06	1.6E+05
6	2.84E+06	1.5E+05
7	2.87E+06	1.4E+05
8	3.06E+06	1.1E+05
9	3.05E+06	1.6E+05
10	3.13E+06	1.6E+05
11	3.43E+06	2.0E+05
12	3.16E+06	1.8E+05
13	3.22E+06	1.5E+05
14	3.17E+06	1.5E+05
SL3 02: $c_{\|\|}$ 400 °C, 840 min		
1	4.68E+05	5.7E+04
2	8.7E+05	1.1E+05
3	9.50E+05	9.2E+04
4	1.04E+06	1.0E+05
5	1.160E+06	9.8E+04
6	1.107E+06	7.1E+04
7	1.19E+06	1.0E+05
8	1.044E+06	8.3E+04
SL3 03: $c_{\|\|}$ 425 °C, 480 min		
1	3.06E+05	3.7E+04
2	7.09E+05	8.4E+04
3	9.54E+05	9.1E+04
4	1.206E+06	9.1E+04
5	1.429E+06	8.2E+04
6	1.51E+06	1.0E+05
7	1.558E+06	9.3E+04
8	1.711E+06	9.3E+04
9	1.64E+06	1.2E+05
10	1.675E+06	9.6E+04
SL3 04: $c_{\|\|}$ 425 °C, 480 min		
1	4.03E+05	5.0E+04
2	1.036E+06	6.8E+04
3	1.495E+06	9.8E+04
4	1.81E+06	1.3E+05
5	1.94E+06	1.1E+05
6	2.16E+06	1.3E+05
7	-	-
8	2.06E+06	1.4E+05
9	2.11E+06	1.1E+05
10	2.06E+06	1.2E+05

Step	^{3}He (atoms)	2σ
SL3 05: $c_{\|\|}$ 450 °C, 180 min		
1	2.13E+05	3.3E+04
2	5.73E+05	5.2E+04
3	8.45E+05	9.0E+04
4	1.066E+06	9.2E+04
5	1.319E+06	8.5E+04
6	1.52E+06	1.0E+05
7	1.61E+06	1.3E+05
8	1.87E+06	1.2E+05
9	1.98E+06	1.4E+05
10	1.943E+06	9.8E+04
11	2.05E+06	1.3E+05
12	2.08E+06	1.2E+05
13	2.09E+06	1.2E+05
14	2.14E+06	1.3E+05
15	2.24E+06	1.4E+05
16	2.27E+06	1.4E+05
17	2.77E+06	1.6E+05
18	2.13E+06	1.3E+05
19	2.13E+06	1.5E+05
SL3 06: $c_{\|\|}$ 475 °C, 90 min		
1	8.31E+05	7.4E+04
2	1.62E+06	1.4E+05
3	1.900E+06	9.9E+04
4	1.79E+06	1.4E+05
5	1.93E+06	1.1E+05
6	1.93E+06	1.0E+05
SL3 07: $c_{\|\|}$ 475 °C, 90 min		
1	6.02E+05	7.6E+04
2	1.34E+06	1.1E+05
3	1.91E+06	1.4E+05
4	2.35E+06	1.2E+05
5	2.43E+06	1.5E+05
6	2.49E+06	1.5E+05
7	2.50E+06	1.4E+05
8	2.51E+06	1.7E+05
SL3 08: $c_{\|\|}$ 500 °C, 30 min		
1	1.92E+05	3.4E+04
2	5.42E+05	6.2E+04
3	7.60E+05	6.9E+04
4	8.64E+05	8.4E+04
5	9.8E+05	1.1E+05
6	1.208E+06	9.6E+04
7	1.246E+06	8.3E+04
8	1.381E+06	9.1E+04
9	1.439E+06	9.1E+04
10	1.55E+06	1.1E+05
11	1.71E+06	1.0E+05
12	1.594E+06	7.5E+04
13	1.67E+06	1.3E+05
14	1.586E+06	8.7E+04

Step	^{3}He (atoms)	2σ
SL3 09: $c_{\|\|}$ 525 °C, 10 min		
1	4.45E+05	6.3E+04
2	7.81E+05	6.6E+04
3	9.25E+05	7.8E+04
4	9.07E+05	8.6E+04
5	9.92E+05	8.7E+04
6	9.75E+05	7.9E+04
7	9.07E+05	7.5E+04
SL3 10: $a_{\|\|}$ 450 °C, 1440 min		
1	2.97E+05	4.4E+04
2	6.67E+05	5.7E+04
3	8.83E+05	7.7E+04
4	1.01E+06	8.8E+04
5	9.49E+05	8.2E+04
6	8.83E+05	8.4E+04
SL3 11: $a_{\|\|}$ 475 °C, 1200 min		
1	1.196E+06	8.1E+04
2	2.17E+06	1.2E+05
3	2.39E+06	1.6E+05
4	2.53E+06	1.4E+05
5	2.47E+06	1.4E+05
6	2.46E+06	1.5E+05
7	2.43E+06	1.5E+05
SL3 12: $a_{\|\|}$ 500 °C, 480 min		
1	4.26E+05	3.9E+04
2	9.82E+05	9.2E+04
3	1.27E+06	1.0E+05
4	1.44E+06	1.0E+05
5	1.52E+06	1.5E+05
6	1.462E+06	9.3E+04
7	1.64E+06	1.1E+05
8	-	-
9	1.51E+06	1.2E+05
SL3 13: $a_{\|\|}$ 525 °C, 300 min		
1	4.19E+05	5.5E+04
2	1.06E+06	1.0E+05
3	1.40E+06	1.0E+05
4	1.690E+06	9.7E+04
5	1.53E+06	1.1E+05
6	1.61E+06	1.4E+05
7	1.63E+06	1.1E+05

Step	^{3}He (atoms)	2σ
SL3 14: $a_{\|\|}$ 550 °C, 120 min		
1	3.14E+05	5.4E+04
2	8.09E+05	7.4E+04
3	1.153E+06	8.3E+04
4	1.272E+06	8.7E+04
5	1.459E+06	8.9E+04
6	1.55E+06	1.0E+05
7	1.444E+06	9.7E+04
8	1.415E+06	8.7E+04
SL3 15: $a_{\|\|}$ 560 °C, 60 min		
1	4.35E+05	4.8E+04
2	1.123E+06	8.1E+04
3	1.437E+06	9.5E+04
4	1.61E+06	1.1E+05
5	1.66E+06	1.2E+05
6	1.66E+06	1.2E+05
7	1.69E+06	1.3E+05
8	1.74E+06	1.1E+05
9	1.81E+06	1.1E+05
10	1.61E+06	1.0E+05
SL3 16: $a_{\|\|}$ 575 °C, 30 min		
1	4.11E+05	6.0E+04
2	1.121E+06	8.3E+04
3	1.57E+06	1.1E+05
4	1.90E+06	1.3E+05
5	2.16E+06	1.4E+05
6	2.54E+06	1.4E+05
7	2.47E+06	1.4E+05
8	2.52E+06	1.5E+05
9	2.660E+06	9.9E+04
10	2.62E+06	1.5E+05
SL3 17: Unheated		
1	4.38E+06	2.0E+05
2	4.37E+06	2.2E+05
3	4.16E+06	1.8E+05
4	4.00E+06	1.9E+05
5	3.99E+06	1.6E+05
6	3.96E+06	1.9E+05
7	3.65E+06	1.8E+05
8	3.50E+06	1.7E+05
9	3.53E+06	1.5E+05
10	3.33E+06	1.7E+05
11	3.16E+06	1.6E+05
12	3.13E+06	1.3E+05

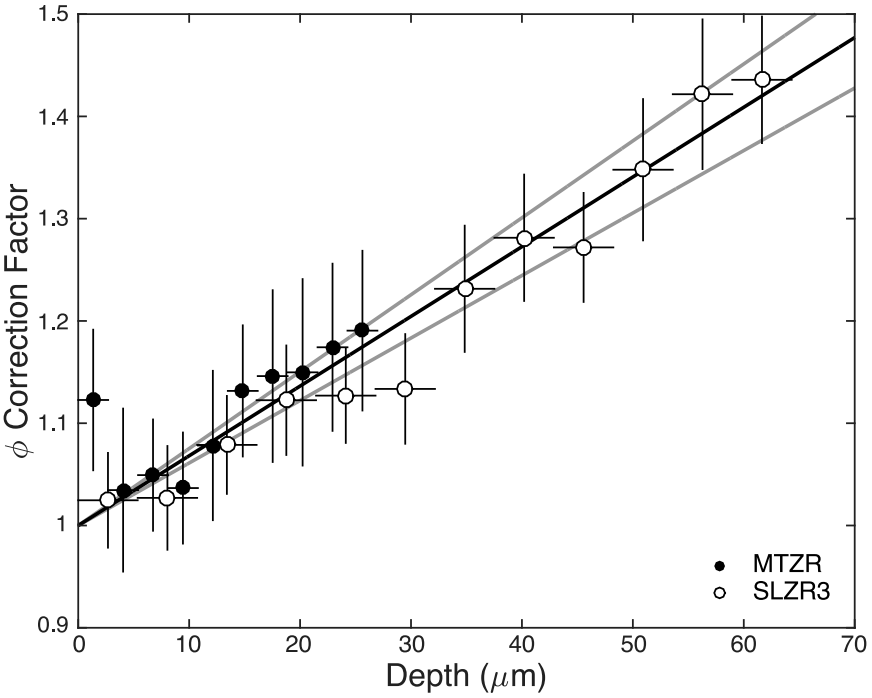

Figure S4.1. Profile geometry correction line (ϕ) with estimated 2σ uncertainty envelope based on two unheated ^{3}He laser depth profiles.

4.9.4 Profile Geometry Corrections

We established a geometry correction factor (ϕ_z) for our deeper diffusive-loss profiles by measuring two $c_{\|}$ depth profiles in two unheated Mud Tank and Sri Lankan zircon slabs. These profiles were ablated using the same excimer laser and lasing conditions as were used for our deeper $c_{\|}$ profiles (>15 μm).

$$\phi_z = \left(\frac{^3He_{expected}}{^3He_{measured}} \right)_z \tag{S4.1}$$

In both profiles, we found ^{3}He abundances to decrease linearly with depth (z), presumably, as ablation volumes decreased (Table S1). We define $^3\text{He}_{expected}$ for the two unheated profiles as the ^{3}He concentration at zero depth as determined by a linear regression. Results

of this exercise, presented in Figure S4.1, yield a simple linear relationship of the form:

$$\phi_z = \beta \cdot z \tag{S4.2}$$

where β, determined by an error-weighted Monte Carlo least squares curve fit, equals 6.82 x $10^{-3} \pm 0.70$ x 10^{-3} (2σ), and z is in microns.

$$({}^3He_{corr})_z = \phi_z({}^3He_{measured})_z \tag{S4.3}$$

The ϕ_z correction was applied to laser profiles with total profile depths >15 μm. Geometry affects on shallower profiles were found to be statistically insignificant. Geometry corrected ^{3}He isotopic abundances are reported in Tables S4.3.

4.9.5 Laser Depth Profile Plots

All depth profiles are plotted in Figures S4.2, S4.3. S4.4, S4.5, and S4.6. Uncertainties on individual data points reflect propagated 2σ analytical uncertainties for ^{3}He measurements, geometry corrections for profiles >15 μm deep, and the total width of each profile step. Open data points represent steps not considered in modeled diffusivities. Best-fit diffusion curves and 2σ uncertainty envelopes are shown for each experiment. Envelopes reflect propagated uncertainties associated with ^{3}He measurements, interferometer depth measurements, step widths, geometry corrections, and heating duration.

Table S4.3. MT & SL3 Laser Depth Profile Geometry-Corrected ^{3}He Isotopic Abundances.

Mud Tank Zircon (MT)						Sri Lankan Zircon (SL3)		
Step	^{3}He (atoms)	2σ	Step	^{3}He (atoms)	2σ	Step	^{3}He (atoms)	2σ
MT 01: $c_{\|\|}$ 400 °C, 840 min			*MT 05: $c_{\|\|}$ 500 °C, 30min*			*SL3 01: $c_{\|\|}$ 400 °C, 720 min*		
1	1.11E+06	1.0E+05	1	5.53E+05	5.3E+04	1	4.51E+05	6.0E+04
2	1.71E+06	1.0E+05	2	1.020E+06	7.3E+04	2	1.27E+06	1.1E+05
3	2.58E+06	2.0E+05	3	1.43E+06	1.2E+05	3	1.84E+06	1.4E+05
4	3.34E+06	1.8E+05	4	1.81E+06	1.2E+05	4	2.35E+06	1.4E+05
5	3.18E+06	1.7E+05	5	2.18E+06	1.4E+05	5	2.95E+06	2.0E+05
6	3.33E+06	1.9E+05	6	2.38E+06	1.2E+05	6	3.48E+06	2.2E+05
7	3.32E+06	1.8E+05	7	2.69E+06	1.3E+05	7	3.63E+06	2.0E+05
8	3.39E+06	1.8E+05	8	2.65E+06	1.6E+05	8	3.99E+06	1.9E+05
			9	2.74E+06	1.6E+05	9	4.11E+06	2.6E+05
MT 02: $c_{\|\|}$ 425 °C, 480 min			10	2.97E+06	1.5E+05	10	4.34E+06	2.6E+05
1	6.88E+05	7.4E+04	11	3.06E+06	1.8E+05	11	4.90E+06	3.4E+05
2	1.150E+06	8.6E+04	12	2.97E+06	1.7E+05	12	4.64E+06	3.0E+05
3	1.63E+06	1.1E+05				13	4.86E+06	2.8E+05
4	1.940E+06	1.1E+05	*MT 06: $c_{\|\|}$ 525 °C 15 min*			14	4.91E+06	3.0E+05
5	2.620E+06	1.5E+05	1	9.40E+05	8.2E+04			
6	2.860E+06	1.3E+05	2	8.43E+05	7.6E+04	*SL3 03: $c_{\|\|}$ 425 °C, 480 min*		
7	2.860E+06	1.4E+05	3	1.270E+06	8.6E+04	1	3.08E+05	3.6E+04
8	2.840E+06	1.9E+05	4	1.68E+06	1.3E+05	2	7.21E+05	8.6E+04
			5	1.93E+06	1.4E+05	3	9.80E+05	9.4E+04
MT 03: $c_{\|\|}$ 450 °C, 480 min			6	2.13E+06	1.4E+05	4	1.260E+06	9.4E+04
1	1.150E+06	8.7E+04	7	2.39E+06	1.4E+05	5	1.500E+06	8.6E+04
2	5.73E+05	6.5E+04	8	2.59E+06	1.7E+05	6	1.60E+06	1.1E+05
3	9.18E+05	7.7E+04	9	2.68E+06	1.4E+05	7	1.67E+06	1.0E+05
4	1.060E+06	7.9E+04	10	2.68E+06	1.6E+05	8	1.85E+06	1.0E+05
5	1.290E+06	9.1E+04	11	2.69E+06	1.6E+05	9	1.79E+06	1.3E+05
6	1.42E+06	1.0E+05				10	1.85E+06	1.1E+05
7	1.53E+06	1.1E+05	*MT 07: $c_{\|\|}$ 550 °C, 10 min*					
8	1.61E+06	1.2E+05	1	5.15E+05	6.0E+04	*SL3 05: $c_{\|\|}$ 450 °C, 180 min*		
9	1.73E+06	1.0E+05	2	1.240E+06	8.6E+04	1	2.15E+05	3.4E+04
10	1.780E+06	9.8E+04	3	2.130E+06	9.4E+04	2	5.93E+05	5.4E+04
11	1.73E+06	1.2E+05	4	2.46E+06	1.6E+05	3	8.93E+05	9.6E+04
			5	2.83E+06	1.6E+05	4	1.16E+06	1.0E+05
MT 04: $c_{\|\|}$ 475 °C, 120 min			6	2.89E+06	1.8E+05	5	1.460E+06	9.6E+04
1	7.14E+05	6.9E+04	7	3.08E+06	2.2E+05	6	1.71E+06	1.2E+05
2	1.430E+06	8.6E+04	8	3.32E+06	2.0E+05	7	1.85E+06	1.5E+05
3	2.07E+06	1.4E+05	9	3.24E+06	1.9E+05	8	2.19E+06	1.4E+05
4	2.38E+06	1.4E+05	10	3.26E+06	1.8E+05	9	2.37E+06	1.8E+05
5	2.77E+06	1.7E+05				10	2.36E+06	1.3E+05
6	3.03E+06	1.5E+05				11	2.54E+06	1.7E+05
7	3.24E+06	1.7E+05				12	2.63E+06	1.7E+05
8	3.68E+06	2.0E+05				13	2.69E+06	1.7E+05
9	3.76E+06	1.9E+05				14	2.80E+06	1.8E+05
10	3.76E+06	2.3E+05				15	2.98E+06	2.0E+05
						16	3.08E+06	2.2E+05
						17	3.82E+06	2.4E+05
						18	2.98E+06	2.0E+05
						19	3.03E+06	2.4E+05

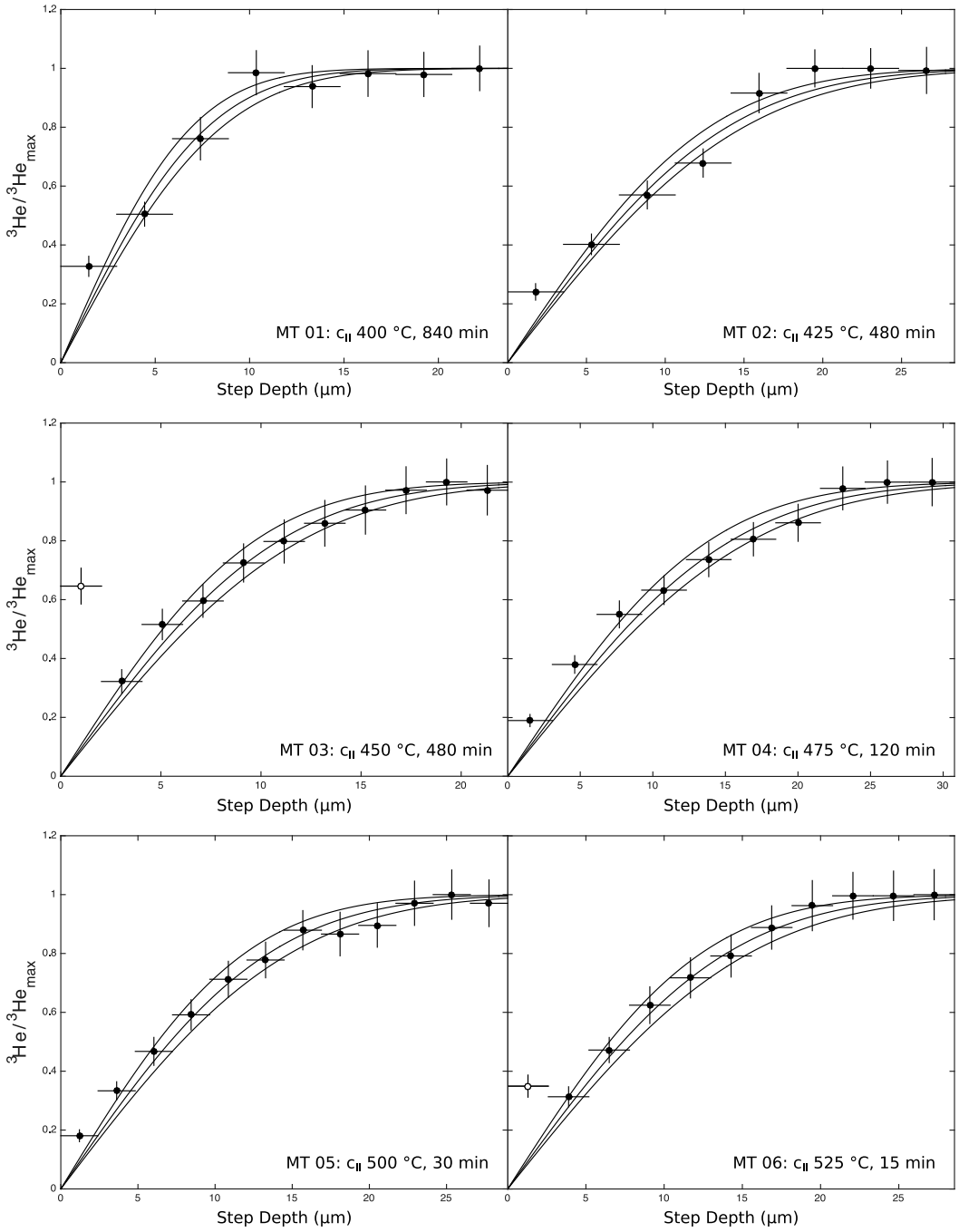

Figure S4.2. Laser depth profiles for diffusion experiments MT 01 through MT 06.

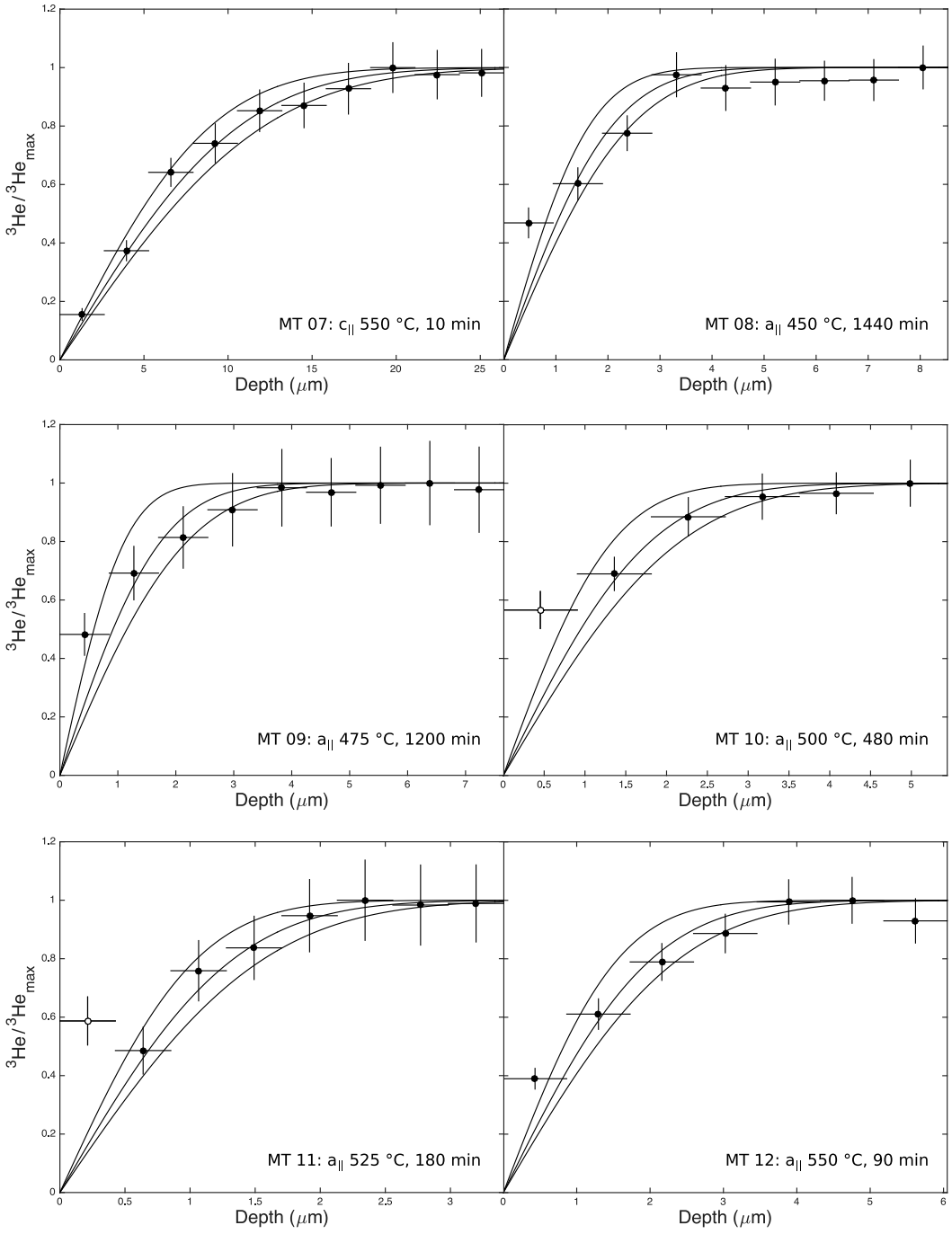

Figure S4.3. Laser depth profiles for diffusion experiments MT 07 through MT 12.

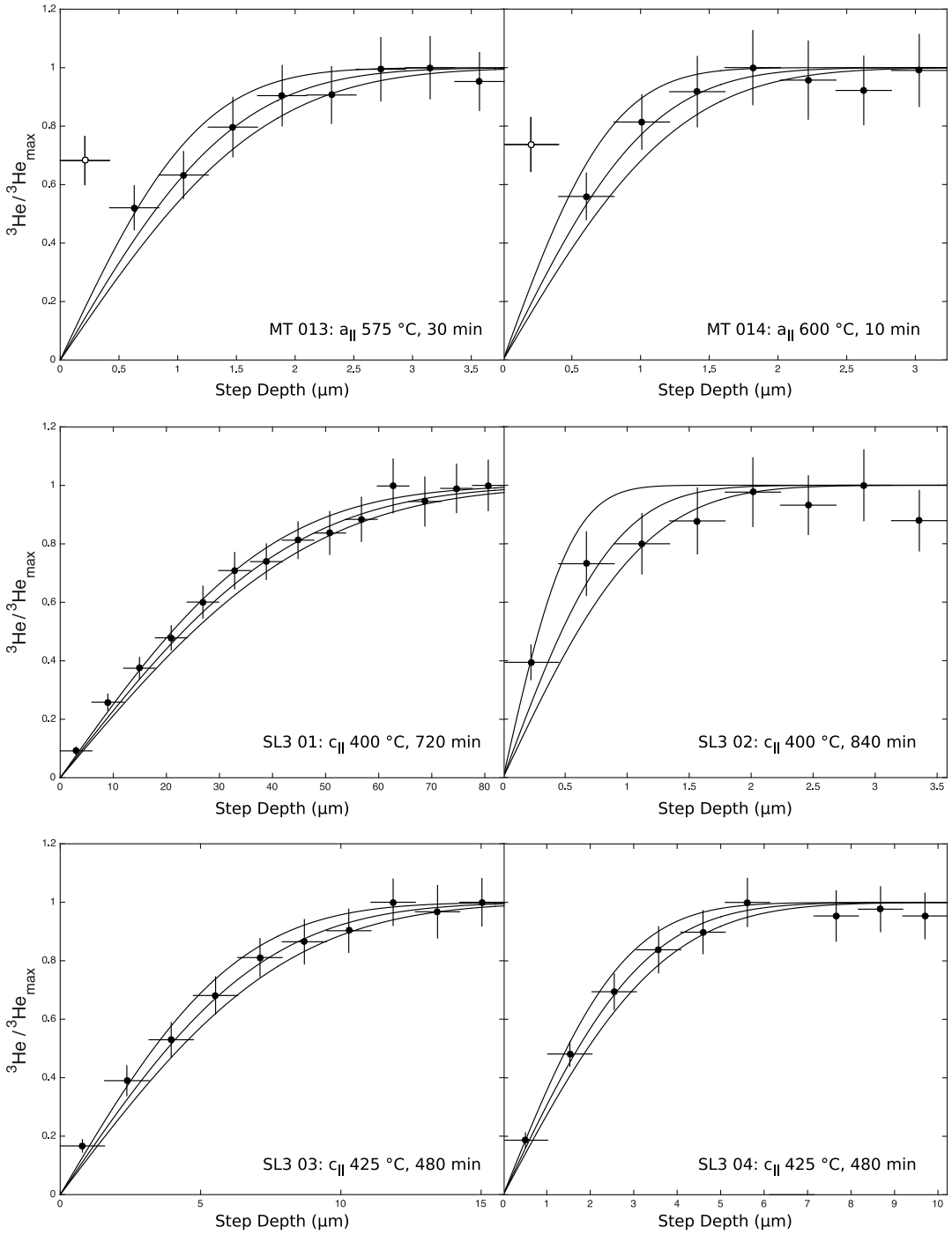

Figure S4.4. Laser depth profiles for diffusion experiments MT 13 through MT 14 and SL3 01 through SL3 04.

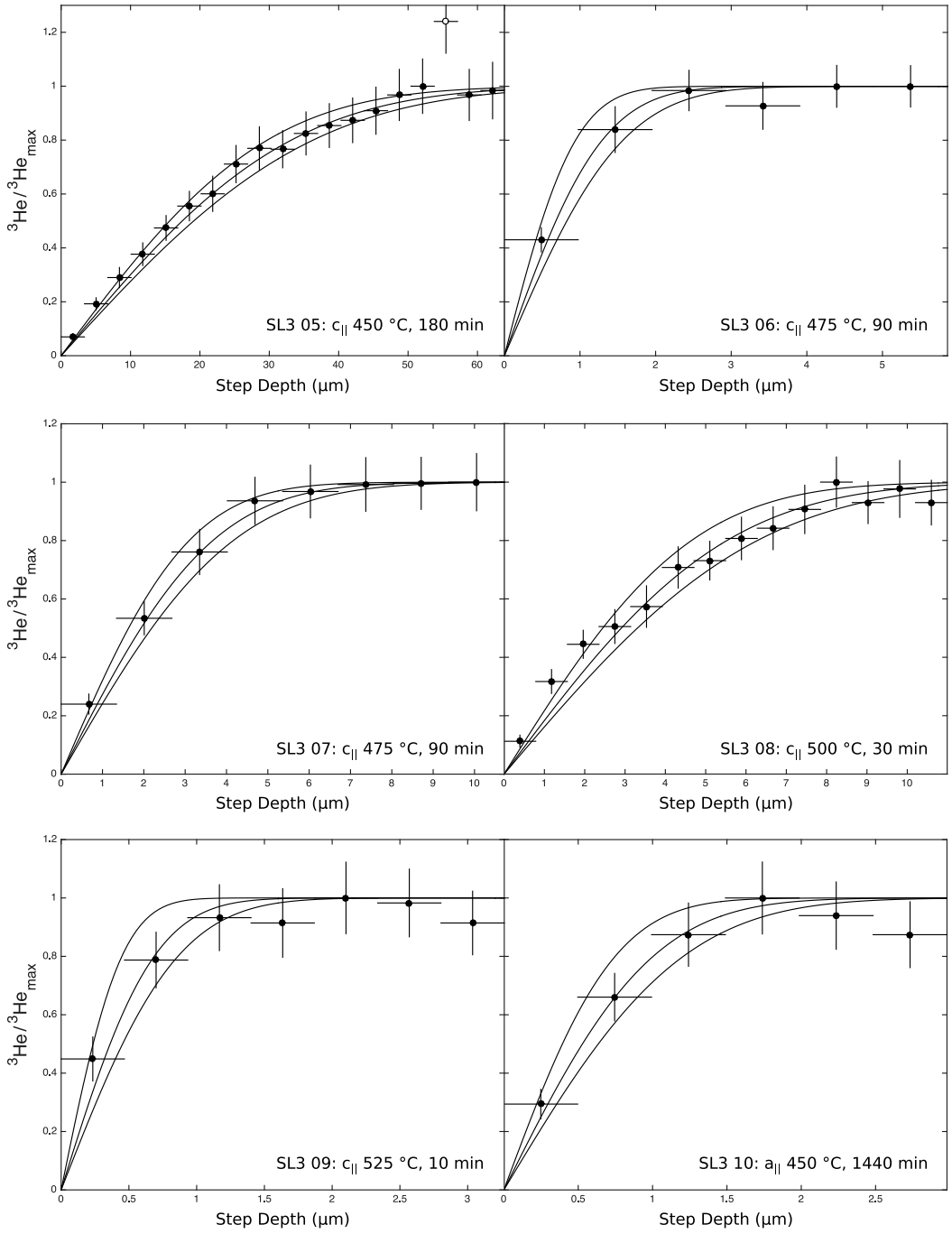

Figure S4.5. Laser depth profiles for diffusion experiments SL3 05 through SL3 10.

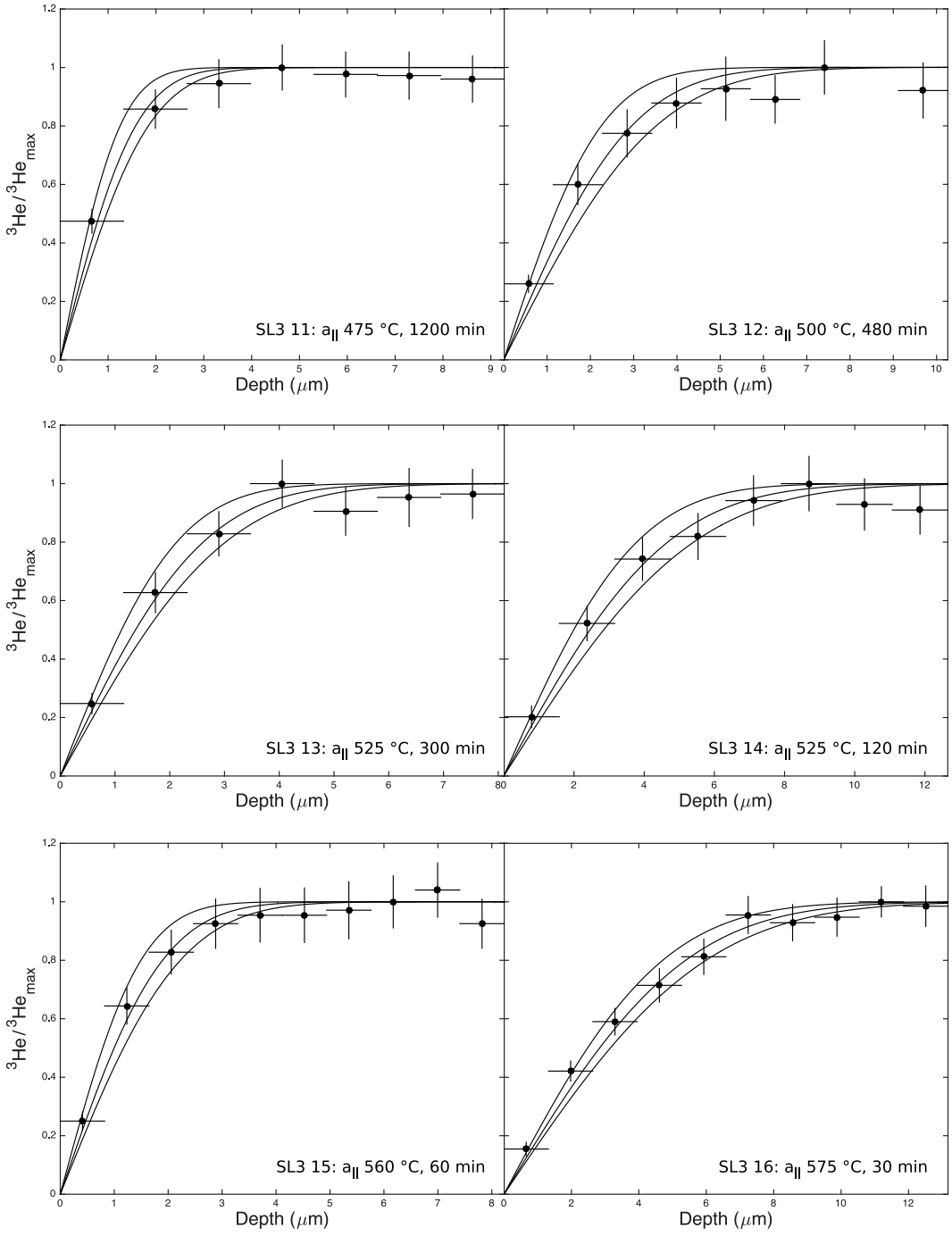

Figure S4.6. Laser depth profiles for diffusion experiments SL3 11 through SL3 16.

4.9.6 Raman Spectroscopy

All Raman spectra were acquired using an Horiba Scientific Jobin Yvon XploRa Plus Raman microscope at Group 18 Laboratories at ASU. This system has an Olympus BX41 optical microscope with 10x and 100x magnification, a 25 mW visible (532 nm) diode laser, a Syncerity 1024 x 256 pixel CCD detector, and a high-precision motorized stage for automated spectral mapping (Figure 1). The system was calibrated daily using the silicon 520.7 cm^{-1} Raman peak, yielding a wavenumber accuracy of about ± 1 cm^{-1}. Reported spectra were measured using either a 1800 gr/mm or 2400 gr/mm diffraction grating which have spectral resolutions of 1.9 and 1.4 cm^{-1}, respectively. Baseline subtractions and Gaussian-Lorentzian peak fitting were done using HORIBA Scientific LabSpec6 software. Reported FWHM values have been corrected for instrument bias using the apparatus function (Nasdala et al., 2001). Following Palenik et al. (2003), we assume uncertainties of 5% for $\nu_3(SiO_4)$ FWHM. FWHM values were converted to alpha dose using the calibration curve presented by Palenik et al. (2003) (Eq. 4). Propagated FWHM uncertainties result in estimated alpha dose uncertainties of $\sim 6\%$. Propagating FWHM measurement uncertainties and uncertainties associated with scatter in the Palenik et al. (2003) calibration curve, yield error estimates of $\sim 11\%$ for our alpha dose values.

4.9.7 LA-ICPMS

The major, minor, and trace element chemistries of samples MT 04 and SL3 01, 08, and 09 were characterized by laser ablation inductively coupled plasma mass spectrometry. Samples, mounted on tape, were placed in a Photon Machines *HelEx Active* two-volume ablation cell. Five lines scans were ablated in each sample and in zircon reference 91500

using an *Analyte* G2 Excimer laser. Line scans, positioned around depth profile laser pits, were made using a 65 μm spot size and 5 μm/s scan speed. Lasing conditions were 4 mJ laser energy and 50% energy output. The isotopic composition of ablated materials was analyzed using a inductively coupled plasma source Thermo Scientific *iCAP-Q* quadropole mass spectrometer. Data were processed through the Iolite software package using the Trace Element IS data reduction scheme (Paton et al., 2011; Woodhead et al., 2007). Silicon was used as our internal standard. Isotopic concentrations in MT and SL3 samples were normalized to zircon reference 91500 (Wiedenbeck et al., 1995). Several line scans in both MT and SL3 samples showed evidence of chemical heterogeneity. Average concentrations for the five line scans were taken as our best estimate for the chemical composition of each sample.

4.10 Acknowledgments

This work was supported by the National Science Foundation [EAR-1346321].

References

Anderson, A. J., K. V. Hodges, and M. C. van Soest (2017). Empirical constraints on the effects of radiation damage on helium diffusion in zircon. *Geochimica et Cosmochimica Acta* 218, pp. 308–322.

Anderson, A. J., K. V. Hodges, M. C. van Soest, and J. M. Hanchar (2019). Helium diffusion in natural xenotime. *Geochemistry, Geophysics, Geosystems* 20, pp. 417–433.

Baughman, J., R. M. Flowers, J. R. Metcalf, and T. Dhansay (2017). Influence of radiation damage on titanite He diffusion kinetics. *Geochimica et Cosmochimica Acta* 205, pp. 50–64.

Bengtson, A., R. C. Ewing, and U. Becker (2012). He diffusion and closure temperatures in apatite and zircon: A density functional theory investigation. *Geochimica et Cosmochimica Acta* 86, pp. 228–238.

Black, L. P. and B. L. Gulson (1978). The age of the Mud Tank Carbonatite, Strangways Range, Northern Territory. *BMR Journal of Australian Geology & Geophysics* 3, pp. 227–232.

Cherniak, D. J. and E. B. Watson (2011). Helium diffusion in rutile and titanite, and consideration of the origin and implications of diffusional anisotropy. *Chemical Geology* 288, pp. 149–161.

Cherniak, D. J., E. B. Watson, and J. B. Thomas (2009). Diffusion of helium in zircon and apatite. *Chemical Geology* 268, pp. 155–166.

Crohn, P. W. and D. H. Moore (1984). The Mud Tank Carbonatite, Strangways Range, central Australia. *Journal of Australian Geology Geophysics* 9, pp. 13–18.

Currie, K. L., J. Knutson, and P. A. Temby (1992). The Mud Tank carbonatite complex, central Australia − an example of metasomatism at mid-crustal levels. *Contributions to Mineralogy and Petrology* 109, pp. 326–339.

Danišík, M., B. I. A. McInnes, C. L. Kirkland, B. J. McDonald, N. J. Evans, and T. Becker (2017). Seeing is believing: Visualization of He distribution in zircon and implications for thermal history reconstruction on single crystals. *Science Advances* 3 (2), e1601121.

Dodson, M. H. (1973). Closure temperature in cooling geochronological and petrological systems. *Contributions to Mineralogy and Petrology* 40 (3), pp. 259–274.

Enkelmann, E. and J. I. Garver (2016). Low-temperature thermochronology applied to ancient settings. *Journal of Geodynamics* 93, pp. 17–30.

Ewing, R. C., A. Meldrum, L. Wang, W. J. Weber, and L. R. Corrales (2003). Radiation effects in zircon. *Zircon: Reviews in Mineralogy & Geochemistry*. Ed. by J. M. Hanchar and P. W. O. Hoskin. 53. Chantilly, VA: Mineralogical Society of America, pp. 387–425.

Farley, K. A. (2007). He diffusion systematics in minerals: Evidence from synthetic monazite and zircon structure phosphates. *Geochimica et Cosmochimica Acta* 71 (16), pp. 4015–4024.

Farley, K. A. and D. F. Stockli (2002). (U-Th)/He dating of phosphates: Apatite, monazite, and xenotime. *Phosphates - Geochemical, Geobiological, and Materials Importance: Reviews in Mineralogy & Geochemistry*. Ed. by M. J. Kohn, J. Rakovan, and J. M. Hughes. 48. Mineralogical Society of America, pp. 559–577.

Farley, K. A., R. A. Wolf, and L. T. Silver (1996). The effects of long alpha-stopping distances on (U-Th)/He ages. *Geochimica et Cosmochimica Acta* 60 (21), pp. 4223–4229.

Farley, K. A., P. W. Reiners, and V. Nenow (1999). An apparatus for high-precision helium diffusion measurements from minerals. *Analytical Chemistry* 71 (10), pp. 2059–2061.

Fernando, G. W. A. R., C. A. Hauzenberger, L. P. Baumgartner, and W. Hofmeister (2003). Modeling of retrograde diffusion zoning in garnet: evidence for slow cooling of granulites from the Highland Complex of Sri Lanka. *Mineralogy and Petrology* 78 (1-2), pp. 53–71.

Finch, R. J. and J. M. Hanchar (2002). Structure and chemistry of zircon and zircon-group minerals. *Zircon: Reviews in Mineralogy and Geochemistry*. Ed. by P. Hanchar, J M and Hoskin. 53. Chantilly, VA: Mineralogical Society of America, pp. 1–25.

Flowers, R. M. (2009). Exploiting radiation damage control on apatite (U-Th)/He dates in cratonic regions. *Earth and Planetary Science Letters* 277, pp. 148–155.

Fuchs, L. H. and E. Gebert (1958). X-ray studies of synthetic coffinite, thorite, and uranothorites. *American Mineralogist* 43, pp. 243–248.

Gautheron, C. and L. Tassan-Got (2010). A Monte Carlo approach to diffusion applied to noble gas/helium thermochronology. *Chemical Geology* 273, pp. 212–224.

Geisler, T., R. T. Pidgeon, W. van Bronswijk, and R. Pleysier (2001). Kinetics of thermal recovery and recrystallization of partially metamic zircon: A Raman spectroscopic study. *European Journal of Mineralogy* 13, pp. 1163–1176.

Ginster, U., P. W. Reiners, L. Nasdala, and C. C. N (2019). Annealing kinetics of radiation damage in zircon. *Geochimica et Cosmochimica Acta* 249, pp. 225–246.

Green, P. F., P. V. Crowhurst, I. R. Duddy, P. Japsen, and S. P. Holford (2006). Conflicting (U–Th)/He and fission track ages in apatite: Enhanced He retention, not anomalous annealing behaviour. *Earth and Planetary Science Letters* 250 (3-4), pp. 407–427.

Guenthner, W. R., P. W. Reiners, P. G. DeCelles, and J. Kendall (2015). Sevier belt exhumation in central Utah constrained from complex zircon (U-Th)/He data sets: Radiation damage and He inheritance effects on partially reset detrital zircons. *Bulletin of the Geological Society of America* 127 (3-4), pp. 323–348.

Guenthner, W. R., P. W. Reiners, R. A. Ketcham, L. Nasdala, and G. Giester (2013). Helium diffusion in natural zircon: Radiation damage, anisotropy, and the interpretation of zircon (U-TH)/He thermochronology. *American Journal of Science* 313 (3), pp. 145–198.

Guenthner, W. R., P. W. Reiners, and Y. Tian (2014). Interpreting date-eU correlations in zircon (U-Th)/He datasets: A case study from the Longmen Shan, China. *Earth and Planetary Science Letters* 403, pp. 328–339.

Hazen, R. M. and L. M. Finger (1979). Crystal structure and compressibility of zircon at high pressure. *American Mineralogist* 64, pp. 196–201.

Hodapp, T. W. and P. R. Fleming (1998). Modeling topology formation during laser ablation. *Journal of Applied Physics* 84 (1), pp. 577–583.

Holland, H. D. and D. Gottfried (1955). The effect of nuclear radiation on the structure of zircon. *Acta Crystallographica* 8, pp. 291–300.

J-A, W., S. P. Kelley, R. A. Brooker, M. R. Carroll, I. M. Villa, and M. R. Lee (1999). Direct measurement of Ar diffusion profiles in a gem-quality Madagascar K-feldspar using the ultra-violet laser ablation microprobe (UVLAMP). *Earth and Planetary Science Letters* 170, pp. 141–153.

Ketcham, R. A., W. R. Guenthner, and P. W. Reiners (2013). Geometric analysis of radiation damage connectivity in zircon, and its implications for helium diffusion. *American Mineralogist* 98 (2-3), pp. 350–360.

Leya, I., H. Busemann, H. Baur, R. Wieler, M. Gloris, S. Neumann, R. Michel, F. Sudbrock, and U. Herpers (1998). Cross sections for the proton-induced production of He and Ne isotopes from magnesium, aluminum, and silicon. *NIM B* 145, pp. 449–458.

McLaren, A. C., J. D. F. Gerald, and I. S. Williams (1994). The microstructure of zircon and its influence on the age determination from Pb/U isotopic ratios measured by ion microprobe. *Geochimica et Cosmochimica Acta* 58 (2), pp. 993–1005.

Meldrum, A., L. A. Boatner, W. J. Weber, and R. C. Ewing (1998). Radiation damage in zircon and monazite. *Geochimica et Cosmochimica Acta* 62 (14), pp. 2509–2520.

Murakami, T., B. C. Chakoumakos, R. C. Ewing, G. R. Lumpkin, and W. J. Weber (1991). Alpha-decay event damage in zircon. *American Mineralogist* 76, pp. 1510–1532.

Nasdala, L., J. Gotze, J. M. Hanchar, M. Gaft, and M. R. Krbetschek (2004). Luminescence techniques in Earth Sciences. *EMU Notes in Mineralogy* 6, pp. 43–91.

Nasdala, L., M. Wenzel, G. Vavra, G. Irmer, T. Wenzel, and B. Kober (2001). Metamictisation of natural zircon: Accumulation versus thermal annealing of radioactivity-induced damage. *Contributions to Mineralogy and Petrology* 141 (2), pp. 125–144.

Palenik, C. S., L. Nasdala, and R. C. Ewing (2003). Radiation damage in zircon. *American Mineralogist* 88, pp. 770–781.

Paton, C., J. Hellstrom, B. Paul, J. Woodhead, and J. Hergt (2011). Iolite: Freeware for the visualisation and processing of mass spectrometric data. *J. Anal. At. Spectrom.* 26 (12), pp. 2508–11.

Pearson, R. K. (2001). *Exploring Data in Engineering, the Sciences, and Medicine*. Oxford Univ. Press.

Reich, M., R. C. Ewing, T. A. Ehlers, and U. Becker (2007). Low-temperature anisotropic diffusion of helium in zircon: Implications for zircon (U-Th)/He thermochronometry. *Geochimica et Cosmochimica Acta* 71 (12), pp. 3119–3130.

Reiners, P. W., R. W. Carlson, P. R. Renne, K. M. Cooper, D. E. Granger, N. M. McLean, and B. Schoene (2017). The (U-Th)/He System. *Geochronology and Thermochronology*. John Wiley & Sons Ltd. Chap. 11, pp. 291–363.

Reiners, P. W., K. A. Farley, and H. J. Hickes (2002). He diffusion and (U-Th)/He thermochronometry of zircon: Initial results from Fish Canyon Tuff and Gold Butte. *Tectonophysics* 349 (1-4), pp. 297–308.

Reiners, P. W., T. L. Spell, S. Nicolescu, and K. A. Zanetti (2004). Zircon (U-Th)/He thermochronometry: He diffusion and comparisons with ^{40}Ar/^{39}Ar dating. *Geochimica et Cosmochimica Acta* 68 (8), pp. 1857–1887.

Robinson, K., G. G V, and P. H. Ribbe (1971). The structure of zircon: A comparison with garnet. *American Mineralogist* 56, pp. 782–790.

Saadoune, I., J. A. Purton, and N. H. de Leeuw (2009). He incorporation and diffusion pathways in pure and defective zircon $ZrSiO_4$: A density functional theory study. *Chemical Geology* 258 (3-4), pp. 182–196.

Saadoune, I. and N. H. de Leeuw (2009). A computer simulation study of the accommodation and diffusion of He in uranium- and plutonium-doped zircon ($ZrSiO_4$). *Geochimica et Cosmochimica Acta* 73 (13), pp. 3880–3893.

Shannon, R. D. (1976). Revised effective ionic radii and systematic studies of interatomic distances in halides and chalcogenides. *Acta Crystallographica Section A* 32 (5), pp. 751–767.

Shuster, D. L. and K. A. Farley (2005). ^{4}He/^{3}He thermochronometry: Theory, practice, and potential complications. *Low Temperature Thermochronology: Techniques, Interpretations, and Applications: Reviews in Mineralogy and Geochemistry*. 58, pp. 181–203.

Shuster, D. L., R. M. Flowers, and K. A. Farley (2006). The influence of natural radiation damage on helium diffusion kinetics in apatite. *Earth and Planetary Science Letters* 249 (3-4), pp. 148–161.

Shuster, D. L. and K. A. Farley (2003). ^{4}He/^{3}He thermochronometry. *Earth and Planetary Science Letters* 217 (1-2), pp. 1–17.

Shuster, D. L., K. A. Farley, J. M. Sisterson, and D. S. Burnett (2003). Quantifying the diffusion kinetics and spatial distributions of radiogenic ^{4}He in minerals containing proton-induced ^{3}He. *Earth and Planetary Science Letters* 217 (1-2), pp. 19–32.

Sliwinski, J. T., N. Kueter, F. Marxer, P. Ulmer, M. Guillong, and O. Bachmann (2018). Controls on lithium concentration and diffusion in zircon. *Chemical Geology* 501, pp. 1–11.

Speer, J. A. and B. J. Cooper (1982). Crystal structure of synthetic hafnon, $HfSiO_4$, comparison with zircon and the actinide orthosilicates. *American Mineralogist* 67, pp. 804–808.

Trail, D., J. B. Thomas, and E. B. Watson (2010). The incorporation of hydroxyl into zircon. *American Mineralogist* 96, pp. 60–67.

Tripathy-Lang, A., M. Fox, and D. L. Shuster (2015). Zircon ^{4}He/^{3}He Thermochronometry. *Geochimica et Cosmochimica Acta* 166, pp. 1–14.

van Soest, M. C., B. D. Monteleone, K. V. Hodges, and J. W. Boyce (2011). Laser depth profiling studies of helium diffusion in Durango fluorapatite. *Geochimica et Cosmochimica Acta* 75 (9), pp. 2409–2419.

Weber, W. J. (1990). Radiation-induced defects and amorphization in zircon. *Journal of Materials Research* 5 (11), pp. 2687–2697.

Weber, W. (1993). Alpha-decay-induced amorphization in complex silicate structures. *J. Am. Ceram. Soc.* 76 (7), pp. 1729–1738.

Wendt, I. and C. Carl (1991). The statistical distribution of the mean squared weighted deviation. *Chemical Geology* 86, pp. 275–285.

Wiedenbeck, M., P. Allé, F. Corfu, W. L. Griffin, M. Meier, F. Oberli, A. Von Quadt, J. C. Roddick, and W. Spiegel (1995). Three natural zircon standards for U-Th-Pb, Lu-Hf, trace element and REE analyses. *Geostandards Newsletter* 19 (1), pp. 1–23.

Wieler, R. (2002). Cosmic-ray-produced noble gases in meteorites. *Noble Gases in Geochemistry and Cosmochemistry: Reviews in Mineralogy and Geochemistry*. Ed. by D. Porcelli, C. J. Ballentine, and R. Wieler. Washington, DC: Mineralogical Society of America, pp. 125–170.

Woodhead, J. D., J. Hellstrom, J. M. Hergt, A. Greig, and R. Maas (2007). Isotopic and elemental imaging of geological materials by laser ablation inductively coupled plasma-mass spectrometry. *Geostandards and Geoanalytical Research* 31 (4), pp. 331–343.

Zhang M S, E. K. H., G. C. Capitani, H. Leroux, A. M. Clark, J. Schluter, and R. C. Ewing (2000). Annealing of α-decay damage in zircon: A Raman spectroscopic study. *Journal of Physics: Condensed Matter* 12, pp. 3131–3148.

Chapter 5

HELIUM DIFFUSION IN NATURAL XENOTIME

Alyssa J. Anderson,[1] Kip V. Hodges[1], Matthijs C. van Soest[1], and John M. Hanchar[2]

[1]School of Earth and Space Exploration, Arizona State University, Tempe, AZ 85287, USA.

[2]Earth Sciences, Memorial University of Newfoundland, St. John's, NL A1B 3X7, Canada.

Citation: A. J. Anderson, K. V. Hodges, M. C. van Soest, and J. M. Hanchar (2019). Helium Diffusion in Natural Xenotime. *Geochemistry, Geophysics, Geosystems* 20, pp. 417-433.

5.1 Abstract

The typically high U and Th contents of xenotime ([Y,HREE]PO_4) make this accessory mineral a promising candidate for (U-Th)/He thermochronometry if the ^{4}He diffusivity can be constrained well enough to estimate its closure temperature. We report new results for two ^{4}He step-heating experiments on different sized fragments of a natural xenotime crystal from the Torghar district of Pakistan (FPX-1). This material, which has a composition within the range of most natural xenotimes (72 mol $\%$ YPO_4), yields a laser ablation ^{238}U/^{206}Pb date of 28.82 $\pm$ 0.13 Ma and a (U-Th)/He date of 15.32 $\pm$ 0.61 Ma (2σ). Results for our more detailed diffusion experiment display excellent linearity on an Arrhenius diagram and indicate kinetic parameters of E = 131.4 $\pm$ 1.1 kJ/mol and $\ln(D_0/a^2)$ = 10.61 $\pm$ 0.20 $\ln(s^{-1})$. These results suggest that the bulk closure temperature for ^{4}He in the degassed crystal fragment is $\sim$75°C for the nominal cooling rate of 10°C/Ma. At equivalent cooling rates and for crystals with equivalent diffusion dimensions, the closure temperature for helium in xenotime is $\sim$20 °C lower than the closure temperature of helium in apatite. Because

xenotime typically has high U and Th contents, it may serve as a high-precision method for dating young, low temperature cooling histories of rocks in which it crystallized. Helium diffusion in xenotime is likely to be moderately anisotropic and moderately dependent on crystal chemistry, so closure temperature interpretations should be made cautiously.

5.2 Introduction

Uranium- and thorium-bearing accessory minerals are frequently targeted for geochronologic, thermochronologic, and petrochronologic study to address a wide range of geologic questions. Xenotime, a tetragonal rare earth element (REE) orthophosphate, occurs as an accessory mineral in granitic rocks, rhyolites, pegmatites, metapelites, and paragneisses and as a diagenetic or detrital mineral in sedimentary rocks. Xenotime can incorporate up to weight percent levels of U and Th (Förster, 1998; Hetherington et al., 2008; Spear and Pyle, 2002; Vallini, D and Rasmussen, B and Krapež, B and Fletcher, I R and McNaughton, N J, 2002), making it a valuable U/Pb geochronometer. Xenotime is commonly dated using *in situ* methods including electron microprobe (Hetherington et al., 2008; Švecová et al., 2016), ion microprobe (Aleinikoff et al., 2012b; Aleinikoff et al., 2015; Aleinikoff et al., 2012c; Fletcher et al., 2004), and laser microprobe (Grand'Homme et al., 2016; Liu et al., 2011) techniques in addition to traditional isotope dilution methods (Hawkins and Bowring, 1997). Xenotime U/Pb dates, often paired with compositional analyses, are used to resolve crystallization, metamorphic, and diagenetic ages in rocks (Aleinikoff and Grauch, 1990; Harrison et al., 2002; Hetherington et al., 2008; Vallini, D A and Rasmussen, B and Krapež, B and Fletcher, I R and McNaughton, N J, 2005; Vallini, D and Rasmussen, B and Krapež, B and Fletcher, I R and McNaughton, N J, 2002) and to constrain the timing of hydrothermal

and mineralization events in ore deposits (Aleinikoff et al., 2012a; Aleinikoff et al., 2012b; Aleinikoff et al., 2012c; Grand'Homme et al., 2016; Švecová et al., 2016).

Despite its success as a U/Pb chronometer, xenotime is seldom used for (U-Th)/He thermochronology, largely because limited data are currently available for ^{4}He diffusion in natural xenotime (Farley, 2002; Farley, 2007). If helium diffusion can be characterized, the prospect of using xenotime for (U-Th)/He dating is very exciting; xenotime's typically high radionuclide content results in the rapid accumulation of radiogenic helium that could potentially allow for the precise dating of very young cooling events in active geologic settings. Most minerals commonly used for (U-Th)/He dating typically incorporate much lower radionuclide concentrations on the order of 10s-100s ppm (apatite and titanite) or 100s-1000s ppm (zircon), which can make such young thermal events challenging to date. Xenotime's likely high concentrations of ^{4}He also make it a promising candidate for laser microprobe (U-Th)/He and U/Pb double dating techniques recently developed for zircon detrital thermochronology (Evans et al., 2005; Horne et al., 2016; Tripathy-Lang et al., 2013). Such techniques could be applied to dating xenotime crystals within petrographic context, which would be particularly useful for petrochronologic studies (Engi, 2017).

To demonstrate the viability of xenotime (U-Th)/He thermochronometry and provide new constraints on the closure temperature for ^{4}He in natural xenotime, we present new results for ^{4}He bulk diffusion experiments on two fragments of a large, gem-quality Oligocene xenotime from the Torghar district of Pakistan. These data imply that the (U-Th)/He closure temperature for this highly crystalline xenotime is low - lower than that for natural apatite. While these results are encouraging, helium diffusivity in xenotime is likely moderately anisotropic and may depend on the specific chemistry of a crystal, so assignment of a nominal (U-Th)/He closure temperature to a natural xenotime should be done cautiously.

5.3 Mineral Chemistry

Xenotime, nominally YPO_4, commonly incorporates other heavy rare earth elements (HREE) (Gd-Lu) into the xenotime crystal structure via the simple substitution $HREE^{3+} \leftrightarrow Y^{3+}$, resulting in a wide range of natural xenotime compositions (Bea, 1996; Förster, 1998; Hetherington et al., 2008; Ni et al., 1995). Typical natural compositions are 70 to 80 mol% YPO_4 and 16 to 25 mol% (Gd-Lu)PO_4; however, up to 45 mol% (Gd-Lu)PO_4 have been reported (Förster, 1998). Because of their larger ionic radii, Light REEs (La-Eu) are generally only present in minor amounts (Boatner, 2002; Förster, 1998; Hetherington et al., 2008; Ni et al., 1995).

U and Th are incorporated into the xenotime structure via the coupled substitutions $(Y,HREE)^{3+} + P^{5+} \leftrightarrow (U,Th)^{4+} + Si^{4+}$ or $2(HREE,Y)^{3+} \leftrightarrow (Th,U)^{4+} + Ca^{2+}$ (Bea, 1996; Förster, 1998; Spear and Pyle, 2002). Typical values for UO_2 and ThO_2 content range from hundreds of parts per million up to $\sim$6 weight percent, although higher concentrations have been reported (Förster, 1998; Hetherington et al., 2008; Švecová et al., 2016).

5.4 Crystallography and Implications for Diffusive Anisotropy

Xenotime is an orthophosphate that crystallizes in the tetragonal crystal system (space group $I4_1/amd$) (Ni et al., 1995). In the xenotime structure, (Y,HREE)O_8 polyhedra form edge-sharing chains along the crystallographic *a*-axis connected by corner-sharing PO_4 tetrahedra. Edge-sharing chains of alternating PO_4 tetrahedra and (Y,HREE)O_8 polyhedra also form along the *c*-axis. Between these chains are interstitial sites that align to form open channels parallel to *c*. Xenotime is isostructural with the mineral zircon, ($ZrSiO_4$), via the coupled substitution $(Y,HREE)^{+3} + P^{+5} \leftrightarrow Zr^{+4} + Si^{+4}$ (Ni et al., 1995) (Figure 5.1). The

most significant difference between the two mineral structures are the differences in cation radii: Y^{3+} and other $HREE^{3+}$ cations are larger (0.977 - 1.04 Å) than Zr^{4+} (0.84 Å), and P^{5+} (0.17 Å) is smaller than Si^{4+} (0.26 Å) (Shannon, 1976).

Helium diffusion in minerals is closely related to the number, size, and arrangement of the interstitial sites available for helium transport (Cherniak and Watson, 2011; Farley, 2007). Since zircon and xenotime are isostructural, differences in helium diffusivity between the two minerals most likely reflect differences in the size of the interstitial sites. The Y-P distance in the xenotime structure (4.875 Å) is longer than the Zr-Si distance in the zircon structure (4.670 Å) (Figure 5.1). Consequently, the open channels along the *c*-axis are significantly wider in the xenotime structure. The interstitial spaces aligned along the *a*-axis are also noticeably wider in xenotime. Since larger interstitial sites can more easily accommodate helium transport, we anticipate helium diffusivity to be higher in xenotime than in zircon.

Crystallographic anisotropy is known to affect helium diffusion in zircon. Atomistic simulation methods predict that helium is preferentially transported through the open channels along the *c*-axis (Reich et al., 2007; Saadoune et al., 2009). Experiments confirm this finding, but disagree on the magnitude of diffusive anisotropy (Cherniak et al., 2009; Guenthner et al., 2013). Nuclear Reaction Analysis (NRA) ^{3}He depth profiles on crystallographically oriented zircon slabs indicate that helium diffusion is nearly two orders of magnitude faster along the *c*-axis than along the *a*-axis (Cherniak et al., 2009), while incremental heating experiments on oriented slabs suggest that helium diffusion is only moderately faster parallel to *c* (Guenthner et al., 2013). Because the two minerals are isostructural, helium diffusion in xenotime may be similarly anisotropic. However, diffusive anisotropy could be less significant in xenotime since the interstitial sites aligned along the *a*-axis are also larger and can potentially accommodate helium transport more easily than in zircon.

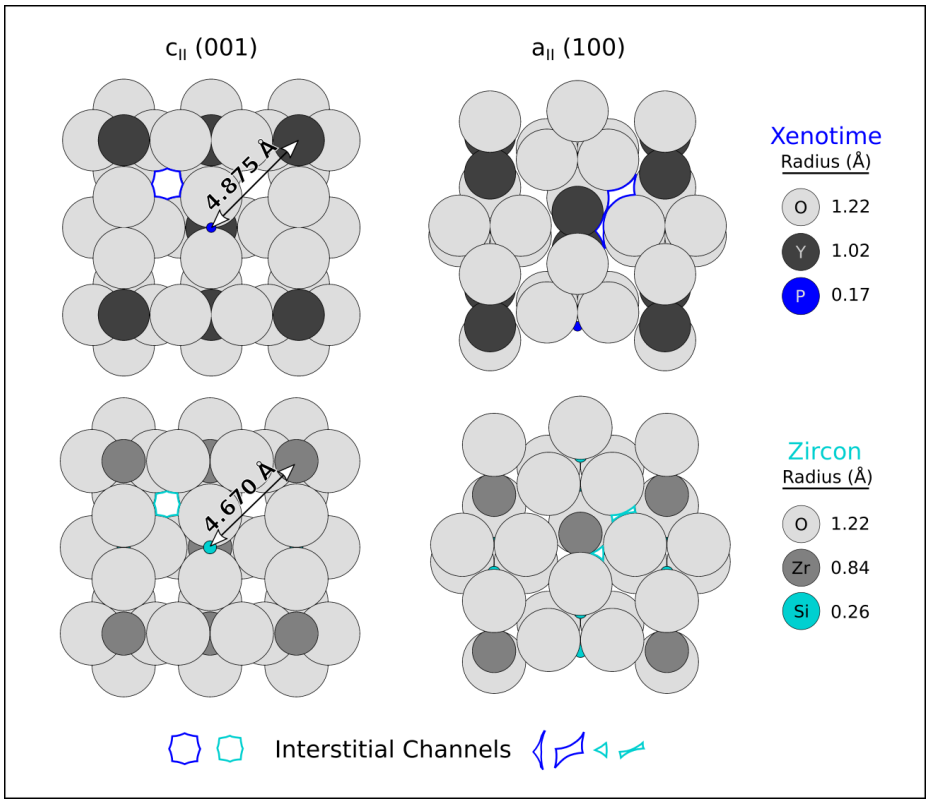

Figure 5.1. Crystal structures for xenotime (Ni et al., 1995) and zircon (Hazen and Finger, 1979) as viewed along the *a*- and *c*- crystallographic axes. Ionic radii are based on recommended values from (Shannon, 1976). Crystal structures were rendered using CrystalMaker software.

5.5 Previous work

Farley (2002) presented an Arrhenius plot for a ^{4}He incremental heating experiment on a sample of natural xenotime (QC-A) from a Miocene Tibetan leucogranite. Based on those data, the authors reported an activation energy of 159 kJ/mol and a 115 °C bulk closure temperature for the sample, but they did not include their experimental results or a description of the sample.

Farley (2007) presented results for a series of bulk ^{3}He diffusion experiments on proton-irradiated, synthetic heavy rare earth (HREE) orthophosphates including end-member xenotime (YPO_4). This comprehensive study demonstrated that ^{3}He diffusivity in HREE

orthophosphates increases systematically as HREE ionic radius, HREE-P distance, and ionic porosity increase. Experimental data for three $YbPO_4$ crystals with different prism aspect ratios showed variations that the author interpreted as evidence for anisotropic helium diffusivity in HREE orthophosphates, with faster transport parallel to *c*. Consequently, the author suggested that plane sheet geometry may be the most appropriate geometry choice for modeling diffusion from experimental data for these phases. Following this approach, Farley (2007) calculated an activation energy of 123 $\pm$ 3 kJ/mol and ln(D_0) of 0.31 $\pm$ 0.80 m^2/s (2σ) for synthetic YPO_4. These parameters suggest a bulk closure temperature of $\sim$7 °C for xenotime assuming a cooling rate of 10 °C/Ma, a 50 μm diffusion dimension, and a plane sheet geometry.

The bulk closure temperature for synthetic xenotime is extremely low compared to that reported by Farley (2002) for natural QC-A xenotime. Citing personal communications with D. Stockli, but without presenting the data, Farley (2007) also referred to new experimental results for QC-A xenotime that suggested a significantly higher activation energy ($\sim$200 kJ/mol) and a ln(D_0) value of $\sim$ -1.2 m^2/s. These values imply an even more discrepant bulk closure temperature of $\sim$190 °C. Farley (2007) speculated that this discrepancy may reflect the influence of radiation damage, different defect densities, and crystallographic anisotropy on diffusion kinetics in natural crystals.

5.6 Xenotime FPX-1

The xenotime specimen used in this study is a large (>1 cm) aggregate of orange and transparent to translucent crystals (FPX-1; Figure 5.2). Individual crystals range in size from 3 to 5 mm and form euhedral, equant to slightly elongated prisms. In the aggregate, these crystals are extensively intergrown and exhibit multiple crystallographic orientations.

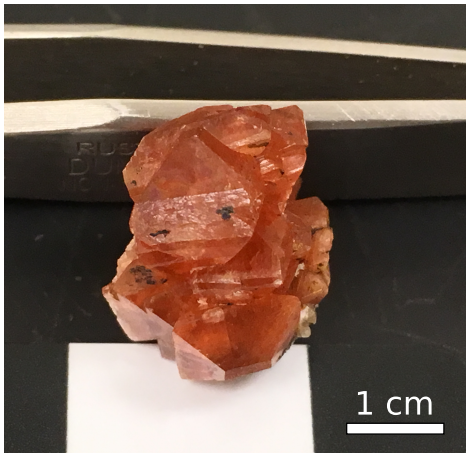

Figure 5.2. Photograph of the xenotime crystal aggregate used as the starting material for this study (FPX-1).

The specimen contains an abundance of thin ($<$ 8 μm), long (50 - $>$500 μm) needle-like inclusions of a gold-colored mineral for which we have no analytical data, but their appearance suggests that they may be rutile. The sample, purchased from a mineral dealer, is purportedly from the Torghar district of the Khyber Agency in the Federally Administered Tribal Areas of Pakistan.

A large section was sawed from the FPX-1 xenotime crystal aggregate. Three multi-millimeter-sized fragments were mounted in epoxy (FPX-1,m1). The mount was polished, and carbon coated for cathodoluminescence (CL) imaging, back-scattered electron (BSE) imaging, and major and minor element chemical characterization by wavelength dispersive X-ray spectroscopy (WDS) with an electron probe microanalyizer (EPMA). Following these analyses, the carbon coat was removed via polishing and the mount was used for Raman spectroscopy and laser ablation U/Pb dating.

Another large fragment was sawed from the aggregate and gently crushed by hand. One fragment (FPX-1,11) weighing 0.35 mg was chosen for solution inductively coupled plasma mass spectrometry (ICPMS) for U and Th concentration determination. Nine smaller

fragments (FPX-1,1-9) were selected for (U-Th)/He dating, and two shards (FPX-1,10 and FPX-1,18) were selected for the bulk diffusion experiments.

5.6.1 Mineral Chemistry

Methods for CL imaging, BSE imaging, WDS chemical characterization, and dissolution ICPMS can be found in the Supplementary Materials. Both CL and BSE images reveal faint growth and sector zoning (Figure S1). Elements measured by WDS include P, Y, Gd, Tb, Dy, Ho, Er, and Yb (Table S5.1). Despite the growth zoning, the WDS results suggest only minor heterogeneity in concentrations of elements present at the weight-percent level. Mean concentrations are 48.58 wt.% P_2O_5, 29.95 wt.% Y_2O_3, and 19.79 wt.% other HREE oxides, with Dy, Er, Gd, and Yb oxides comprising 88% of this total. The P content is slightly higher than predicted by stoichiometry. These wt.% oxide concentrations equate to 72 mol% YPO_4 and 28 mol% (Gd,Tb,Dy,Ho,Er,Yb)PO_4. The mol% YPO_4 is consistent with the range reported by Förster (1998) for typical compositions for natural xenotime (70 to 80 mol% YPO_4).

^{238}U, ^{232}Th, and ^{147}Sm concentrations determined by solution ICPMS are 109.2 $\pm$ 2.2 ppm, 249.4 $\pm$ 7.1 ppm, and 83.52 $\pm$ 0.99 ppm, respectively (2σ analytical uncertainties). These values are very low for typical actinide concentrations in natural xenotime (Förster, 1998; Hetherington et al., 2008; Švecová et al., 2016).

5.6.2 Geochronology and Thermochronology

Full details for our geochronology and thermochronology methods may be found in the Supplementary Materials. Twenty-three laser microprobe analyses yielded an inverse-

Table 5.1. Xenotime Composition - Wavelength Dispersive Spectroscopy

Oxide	Weight %[a]	2σ[b]
P_2O_5	48.6	1.1
Y_2O_3	30.0	2.0
Gd_2O_3	3.65	0.39
Tb_2O_3	0.92	0.13
Dy_2O_3	7.2	1.1
Ho_2O_3	1.36	0.16
Er_2O_3	4.04	0.53
Yb_2O_3	2.65	0.38

[a]Mean weight % oxide determined from 60 WDS analyses.
[b]Two standard deviations of the 60 WDS analyses.

variance weighted mean $^{238}U/^{206}Pb$ date of 28.82 $\pm$ 0.13 Ma with a mean squared weighted deviation (MSWD) (Wendt and Carl, 1991) of 1.52 (Table 5.2). The quoted uncertainty represents propagated analytical uncertainties for the standard deviation of the inverse-variance weighted mean date at the 2σ level. We interpret 28.82 $\pm$ 0.13 Ma as the sample's crystallization age given the known sluggishness of radiogenic Pb diffusion in xenotime (Cherniak, 2006). While the exact geologic setting of the our sample is unknown, the U/Pb date is consistent with crystallization ages previously reported for granitic and pegmatitic rocks from the Pakistani Hindu Kush (Hildebrand, 1998; Hildebrand et al., 2001).

Nine bulk (U-Th)/He analyses yielded an inverse-variance weighted mean (U-Th)/He date of 15.32 $\pm$ 0.14 with a high MSWD of 18.6, implying that the dataset is dispersed beyond what is expected based on analytical uncertainty alone. Therefore, the quoted uncertainty, the standard deviation of the inverse-variance weighted mean at the 2σ level, has been expanded by multiplying by the square root of the MSWD (Ludwig, 2003). We consider the results - 15.32 $\pm$ 0.61 Ma - as our best estimate for the weighted mean (U-Th)/He date and its uncertainty. Even with expanded errors, our (U-Th)/He date precision is

better than 4% which is typical for (U-Th)/He analyses Farley, 2002. Because the selected shards did not show evidence of crystal faces, it is unlikely that a significant quantity of ^{4}He was lost via ejection, so alpha ejection corrections were not made (Farley and Stockli, 2002; Hourigan et al., 2005). Farley (2002), however, do report mean ^{238}U-, ^{235}U-, and ^{232}Th-chain alpha stopping distances of 16.0, 18.6, and 18.3 μm, respectively, for xenotime that can be used to correct for alpha ejection when the chronometer is used for smaller crystals. The (U-Th)/He date for FPX-1 is significantly younger than the ^{238}U/^{206}Pb date, which is consistent with previous findings that suggest that the (U-Th)/He closure temperature for xenotime is significantly lower than its typical crystallization temperature (Farley, 2000; Farley, 2007).

5.6.3 Radiation Damage and Raman Spectroscopy

Radiation damage caused by the recoil of heavy daughter nuclides during U- and Th-series alpha decay events is known to significantly impact helium diffusion kinetics in zircon (Guenthner et al., 2013), apatite (Shuster et al., 2006), and titanite (Baughman et al., 2017), so it was important to attempt to characterize radiation damage in FPX-1. One way to quantify radiation damage is to calculate the alpha dose, or alpha particle fluence, for a sample from its measured ^{238}U, ^{232}Th, and ^{147}Sm concentrations and an estimate for the damage accumulation interval [Nasdala et al. (2001); Equation 5].

Assuming a damage accumulation interval equal to the crystallization age of FPX-1 (28.82 $\pm$ 0.13 Ma), we calculated a maximum radiation damage dose of 1.592 $\pm$ 0.026 x 10^{16} α/g. The quoted uncertainty (2σ) reflects propagated analytical uncertainties for the U and Th concentrations and the laser ablation ^{238}U/^{206}Pb date. Because FPX-1 crystals are likely zoned in U and Th, as suggested by our CL and BSE images, the actual alpha

Table 5.2. Laser Ablation U/Pb Dates

Analysis	$^{206}Pb/^{238}U$	2σ	$^{238}U/^{206}Pb$ Date (Ma)	2σ[a]
1	0.004419	0.000091	28.43	0.58
2	0.004409	0.000090	28.36	0.58
3	0.004416	0.000090	28.40	0.58
4	0.004465	0.000087	28.72	0.56
5	0.004434	0.000086	28.52	0.55
6	0.004580	0.000140	29.45	0.87
7	0.004570	0.000130	29.38	0.81
8	0.00456	0.00011	29.32	0.70
9	0.004522	0.000098	29.08	0.63
10	0.004461	0.000089	28.69	0.57
11	0.004463	0.000088	28.71	0.57
12	0.004530	0.000100	29.13	0.66
13	0.004471	0.000093	28.76	0.59
14	0.00451	0.00011	29.03	0.72
15	0.00448	0.00011	28.83	0.74
16	0.004439	0.000090	28.55	0.58
17	0.004435	0.000091	28.52	0.59
18	0.004449	0.000090	28.62	0.58
19	0.004404	0.000080	28.33	0.52
20	0.004520	0.000094	29.07	0.60
21	0.00454	0.00011	29.19	0.69
22	0.004570	0.000089	29.39	0.57
23	0.004583	0.000085	29.47	0.55
Weighted Mean[b]			28.82	0.13

[a]2σ values represent propagated analytical uncertainties.
[b]Inverse-variance weighted mean date.

dose may vary more than suggested by the quoted uncertainty. In zircon studies, this alpha dose is considered to be very low (Guenthner et al., 2013; Nasdala et al., 2001). The actual radiation damage in the sample may be even lower than the calculated dose due to thermal annealing. It is important to note that different minerals respond differently to radiation damage. Some phosphates, such as monazite, display more resilience to radiation damage than silicates and never fully reach a metamict state (Meldrum et al., 2000; Meldrum et al.,

Table 5.3. (U-Th)/He Dates

Sample	^{4}He (atoms)	2σ	^{238}U (atoms)	2σ	^{232}Th (atoms)	2σ	(U-Th)/He Date (Ma)	2σ[a]
FPX-1,1	6.61E+10	1.6E+09	1.619E+12	1.7E+10	5.925E+12	6.5E+10	17.15	0.44
FPX-1,2	2.060E+10	5.8E+08	6.109E+11	9.2E+09	1.873E+12	2.5E+10	15.30	0.46
FPX-1,3	4.80E+10	1.2E+09	1.337E+12	1.2E+10	4.517E+12	5.6E+10	15.63	0.41
FPX-1,4	1.263E+11	3.1E+09	3.401E+12	3.2E+10	1.262E+13	1.7E+11	15.50	0.40
FPX-1,5	2.119E+10	6.4E+08	6.689E+11	7.9E+09	2.223E+12	2.8E+10	13.89	0.44
FPX-1,6	4.87E+10	1.2E+09	1.306E+12	1.6E+10	5.181E+12	4.9E+10	15.10	0.39
FPX-1,7	2.921E+10	7.8E+08	8.880E+11	8.6E+09	2.992E+12	3.4E+10	14.34	0.40
FPX-1,8	2.144E+10	5.7E+08	5.420E+11	7.4E+09	2.157E+12	3.1E+10	15.99	0.45
FPX-1,9	2.497E+10	6.6E+08	7.41E+11	1.2E+10	2.316E+12	2.5E+10	15.18	0.43
Weighted Mean[b]							15.32	0.61

[a]2σ values represent propagated analytical uncertainties.
[b]Inverse-variance weighted mean date. The quoted uncertainty has been expanded by multiplying by the square root of the MSWD (Wendt and Carl, 1991; Ludwig, 2003).

1998). Experiments on artificially irradiated synthetic xenotime suggest that xenotime is significantly more resistant to radiation damage than zircon, but less so than monazite (Meldrum et al., 1997). Molecular dynamics computer simulations support this finding (Grechanovsky et al., 2013).

Raman spectral characteristics have been used as semi-quantitative proxies for radiation damage in other accessory minerals, including zircon and monazite (Nasdala et al., 2004; Nasdala et al., 2001; Ruschel et al., 2012). The SiO_4 stretching vibration near 1000 cm^{-1} in zircon and the PO_4 stretching vibration near 970 cm^{-1} in monazite, have been shown to predictably broaden with increasing alpha dose (Nasdala et al., 2004; Nasdala et al., 2001; Ruschel et al., 2012). Although this sort of proxy relationship has not yet been calibrated for xenotime, Švecová et al. (2016) has demonstrated that the PO_4 stretching vibration A_{1g} (Giarola et al., 2011) near 999 cm^{-1}, is similarly sensitive to radiation damage; its spectral position decreases and its width increases with increasing damage dose.

Raman methods are described in the Supplementary Materials. In Figure 5.3, we compare a Raman spectrum for FPX-1 to a spectrum for an undamaged synthetic crystal of YPO_4 grown using the MoO_3 flux method (Hanchar et al., 2001). (For more information about the YPO_4 synthesis procedure, readers should refer to the Supplementary Materials.) The low frequency portion of the natural xenotime spectrum is considerably more complex

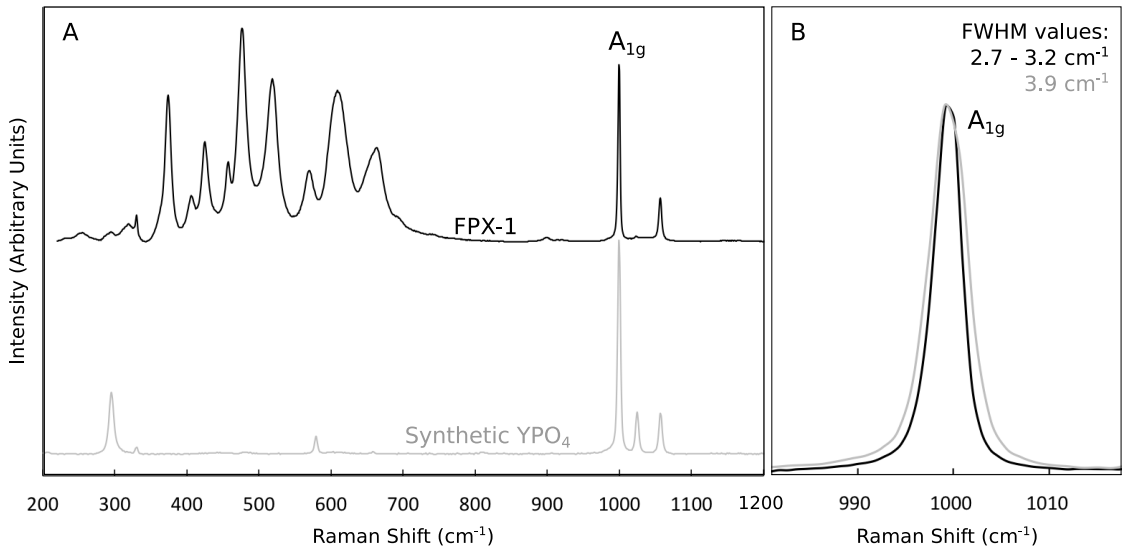

Figure 5.3. A. Raman spectra acquired for our natural xenotime sample, FPX-1 and for synthetic YPO_4. B. Comparison of peak width data for the A_{1g} P-O stretching vibration near 999 cm^{-1} for the two samples.

than that for synthetic YPO_4. Many of these low frequency peaks are not real Raman vibrational modes, but are instead laser-induced photoluminescence artifacts caused by REE^{3+} substitutions (Lenz et al., 2015). Spectral positions and peak widths for the A_{1g} PO_4 stretching vibration range from 999 to 1000 cm^{-1} and 2.7 to 3.2 cm^{-1}, respectively for FPX-1. This peak width range is narrower than the range reported for other natural xenotime samples, 5.5 to 38.0 cm^{-1} (Švecová et al., 2016); however, the other natural samples for which data have been reported have significantly higher calculated alpha doses - 3.1 x 10^{18} to 7.4 x 10^{19} α/g - than FPX-1 (Švecová et al., 2016).

The spectral position for the A_{1g} vibration in synthetic YPO_4 is 998 cm^{-1}, and the peak width (3.9 cm^{-1}) is slightly wider than that of FPX-1. These small differences in peak width and spectral position likely reflect differences in crystal chemistry rather than radiation damage (Ruschel et al., 2012). Paired with the alpha dose calculation, these results suggest that FPX-1 is highly crystalline. The experimental helium diffusion data, discussed below,

should thus provide a reliable indication of intrinsic bulk diffusion parameters for similarly crystalline xenotime with this specific chemical composition.

5.7 Diffusion Experiments

Previous helium diffusion experiments on natural zircon, apatite, and synthetic orthophosphates have consistently indicated that the grain size of a mineral is roughly equivalent to the diffusion domain (a) for helium loss (Farley, 2002; Farley, 2007; Reiners et al., 2004). To confirm this for FPX-1, we performed incremental heating experiments on two differently sized crystal fragments. Both fragments are best described as irregular prisms. The larger fragment (FPX-1, 10) is somewhat elongated, measuring 522 μm by 522 μm by 334 μm, while the smaller (FPX-1, 18) measured 125 μm by 125 μm by 115 μm.

The two crystal fragments were separately loaded in Pt jackets and heated *in vacuo* using a projector bulb furnace. Temperatures were monitored during the experiments using a type K thermocouple through a feedback loop with the bulb power supply. Samples were incrementally degassed in either a series of cycled prograde and retrograde heating steps (FPX-1,10), or a single prograde cycle (FPX-1,18). Additional experimental details can be found in the Supplementary Materials. Diffusivity was calculated from the cumulative fraction of ^{4}He released in each heating step following Fechtig and Kalbitzer (1966). These calculations were done in two ways: 1) assuming plane sheet geometry, based on inferences presented by Farley (2007) regarding the anisotropy of helium diffusivity in synthetic orthophosphates; and 2) assuming spherical geometry. We found empirically that the calculations that assumed a spherical geometry yielded a significantly better fit to our data. As such, all diffusivity values reported in Tables 5.4 and 5.5 and Figure 5.4 reflect the choice of a spherical geometry. Following arguments presented by Gautheron and Tassan-Got

(2010), this suggests to us that diffusion in natural xenotime is only moderately anisotropic. The implications of this finding and our choice in geometry are discussed further in Section 6.

Our larger crystal fragment - FPX-1,10 - yielded enough ^{4}He to allow for a very detailed, 74-step incremental heating experiment (Table 5.4) . Results for this experiment display excellent linearity on an Arrhenius diagram (Figure 5.4) with only five steps at the temperature extremes of the experiment, accounting for less than 4% of the total ^{4}He, clearly falling off the trend. Anomalous initial and final heating steps are common but poorly understood features in many bulk helium diffusion studies (Farley, 2000; Guenthner et al., 2013; Peterman et al., 2014; Shuster and Farley, 2009; Stanley and Flowers, 2016). A Hampel identifier (Pearson, 2001) with a conservative threshold value of six identified these steps (1, 2, 71, 72, and 73) as statistical outliers. Excluding these steps from consideration, a York et al. (2004) linear regression yields values for diffusion parameters $\ln(D_0/a^2)$ and E following the Arrhenius relationship:

$$ln\Big(\frac{D}{a^2}\Big) = \Big(\frac{-E}{R}\Big)\Big(\frac{1}{T}\Big) + ln\Big(\frac{D_0}{a^2}\Big) \tag{5.1}$$

where D_0 is diffusivity at infinite temperature, E is activation energy, a is the diffusion dimension, T is temperature, and R is the universal gas constant (8.314 J/mol K). This regression has a MSWD of 3.06 which is higher than the ca. 95% confidence range of its predicted value of 1.0 (Wendt and Carl, 1991), suggesting that we may have underestimated our analytical uncertainties. To obtain more realistic uncertainties, we expanded the 2σ uncertainties for E and $\ln(D_0/a^2)$ by multiplying by the square root the MSWD (Ludwig, 2003) such that E = 131.4 $\pm$ 1.1 kJ/mol and $\ln(D_0/a^2)$ = 10.61 $\pm$ 0.20 m^2/s $\ln(s^{-1})$ at the 2σ level.

We performed a much shorter diffusion experiment on FPX-1,18 with the exclusive

goal of testing the hypothesis that a smaller crystal fragment should yield systematically higher values for ^{4}He diffusivity at any given temperature. Results for FPX-1,18 support this hypothesis (Figure 5.4, Table 5.5). The six data points plot as a roughly linear array on an Arrhenius diagram. The slope of this line is similar to, albeit less well constrained than, the slope obtained for our study of FPX-1,10, confirming that the activation energy derived from the FPX-1,10 experiment is broadly reproducible for the FPX-1 material. Since anomalous initial and final steps are common features in helium bulk diffusion studies, we do not regard Arrhenius parameters derived from our shorter experiment (n=6) to be as robust as those derived from our longer (n=73), temperature-cycled experiment. As such, we do not report Arrhenius parameters for FPX-1,18. Because the two crystal fragments have different aspect ratios, we might expect there to be minor differences in the Arrhenius behavior of the two samples if diffusive anisotropy is significant in FPX-1. However, the similar slopes defined by the two experiments imply that such effects, if they exist, are impossible to resolve with the data in hand, particularly since the two degassed fragments are irregularly shaped shards and not euhedral crystals.

5.8 Diffusion Domain Size in Natural Xenotime

The simple linear trends on the Arrhenius diagram for the two diffusion experiments are consistent with the interpretation that helium was lost via thermally activated volume diffusion from a single diffusion domain. If we assume that both experimental datasets have the same D_0 value, then the offset in the Arrhenius arrays in Figure 5.4 implies that FPX-1,18 has a smaller diffusion dimension than FPX-1,10. At any given temperature, this offset can be expressed as the ratio a_2/a_1, where a_1 is the diffusion dimension for FPX-1,10 and a_2 is the diffusion dimension for FPX-1,18. The range in values required to explain

Table 5.4. Step-Heating Results for He Diffusion Experiment FPX-1,10

Step	T (°C)	t (minutes)	^{4}He (atoms)	2σ	$f_{cumulative}$[a]	ln(D/a^2)[b]	2σ[c]
1	200	60	1.0042E+09	9.0E+06	0.0003	-26.918	0.018
2	210	60	1.450E+08	4.2E+06	0.0003	-28.090	0.015
3	230	60	1.4840E+10	4.7E+07	0.0046	-21.3851	0.0060
4	250	30	1.5074E+10	4.5E+07	0.0090	-19.6632	0.0038
5	270	20	2.0145E+10	6.2E+07	0.0148	-18.4050	0.0034
6	290	10	1.9241E+10	6.0E+07	0.0204	-17.3621	0.0029
7	310	10	3.340E+10	1.1E+08	0.0300	-16.4450	0.0033
8	330	8	4.532E+10	1.5E+08	0.0431	-15.5346	0.0032
9	350	5	4.919E+10	2.4E+08	0.0573	-14.6541	0.0040
10	340	5	2.6094E+10	6.8E+07	0.0648	-15.0832	0.0023
11	320	8	1.6040E+10	4.8E+07	0.0695	-15.9397	0.0021
12	300	10	7.254E+09	2.6E+07	0.0716	-16.9048	0.0020
13	280	20	5.101E+09	2.3E+07	0.0731	-17.9236	0.0020
14	260	30	2.349E+09	1.4E+07	0.0737	-19.0888	0.0020
15	240	60	1.459E+09	1.0E+07	0.0742	-20.2502	0.0020
16	220	120	8.071E+08	7.8E+06	0.0744	-21.5306	0.0020
17	205	180	4.411E+08	4.3E+06	0.0745	-22.5377	0.0019
18	225	120	1.0310E+09	6.2E+06	0.0748	-21.2802	0.0019
19	245	60	1.785E+09	3.0E+07	0.0753	-20.0326	0.0025
20	265	30	2.887E+09	1.5E+07	0.0762	-18.8490	0.0019
21	285	15	4.257E+09	2.0E+07	0.0774	-17.7530	0.0020
22	305	10	7.595E+09	2.8E+07	0.0796	-16.7451	0.0020
23	315	10	1.1657E+10	3.8E+07	0.0830	-16.2795	0.0020
24	325	8	1.4002E+10	4.3E+07	0.0870	-15.8253	0.0019
25	335	5	1.3334E+10	3.9E+07	0.0909	-15.3554	0.0019
26	345	5	1.8855E+10	5.2E+07	0.0963	-14.9539	0.0019
27	355	5	2.6008E+10	7.3E+07	0.1038	-14.5597	0.0019
28	360	5	2.9270E+10	8.3E+07	0.1123	-14.3578	0.0019
29	365	5	3.2097E+10	9.2E+07	0.1215	-14.1789	0.0019
30	370	5	3.6013E+10	9.7E+07	0.1319	-13.9742	0.0019
31	375	5	3.909E+10	1.0E+08	0.1432	-13.8002	0.0019
32	372	5	3.2074E+10	8.5E+07	0.1525	-13.9167	0.0018
33	367	5	2.6050E+10	7.4E+07	0.1600	-14.0618	0.0018
34[d]	362	5	1.9870E+10	7.5E+07	0.1658	-14.2849	0.0018
35	357	5	1.6516E+10	6.1E+07	0.1706	-14.4331	0.0018
36	362	5	1.9870E+10	7.5E+07	0.1763	-14.2125	0.0018
37	352	5	1.3364E+10	8.5E+07	0.1802	-14.5773	0.0020
38	354	8	2.068E+10	2.8E+08	0.1861	-14.5788	0.0045
39	359	8	2.461E+10	1.3E+08	0.1932	-14.3636	0.0022
40	364	8	2.8045E+10	9.5E+07	0.2013	-14.1861	0.0019
41	369	8	3.386E+10	1.8E+08	0.2111	-13.9447	0.0023
42	374	8	3.907E+10	1.9E+08	0.2224	-13.7411	0.0023
43	380	5	2.972E+10	2.2E+08	0.2310	-13.4902	0.0027
44	385	5	3.361E+10	1.2E+08	0.2407	-13.3183	0.0020
45	390	5	3.812E+10	2.8E+08	0.2517	-13.1387	0.0028
46	395	5	4.478E+10	4.4E+08	0.2647	-12.9176	0.0040
47	400	5	5.046E+10	2.1E+08	0.2792	-12.7318	0.0022
48	397	5	4.266E+10	1.3E+08	0.2916	-12.8370	0.0020
49	392	5	3.276E+10	1.8E+08	0.3010	-13.0515	0.0023
50	405	10	8.443E+10	2.9E+08	0.3254	-12.7233	0.0023
51	410	10	9.010E+10	3.3E+08	0.3515	-12.5518	0.0024
52	415	10	9.464E+10	3.6E+08	0.3788	-12.3949	0.0025
53	420	10	1.0118E+11	5.0E+08	0.4080	-12.2180	0.0029
54	425	10	1.0786E+11	4.9E+08	0.4392	-12.0406	0.0028
55	430	10	1.1233E+11	4.0E+08	0.4717	-11.8835	0.0026
56	435	10	1.1708E+11	4.0E+08	0.5055	-11.7232	0.0026
57	440	10	1.2089E+11	5.8E+08	0.5404	-11.5693	0.0031
58	445	10	1.2305E+11	6.1E+08	0.5760	-11.4268	0.0032
59	450	10	1.2622E+11	6.5E+08	0.6124	-11.2728	0.0034
60	455	10	1.2893E+11	4.4E+08	0.6497	-11.1171	0.0032
61	460	10	1.2863E+11	4.5E+08	0.6868	-10.9790	0.0034
62	465	10	1.2782E+11	5.7E+08	0.7238	-10.8379	0.0039
63	470	10	1.2703E+11	5.1E+08	0.7605	-10.6868	0.0042
64	475	10	1.2052E+11	6.6E+08	0.7953	-10.5714	0.0050
65	480	10	1.1749E+11	4.3E+08	0.8293	-10.4136	0.0054
66	485	10	1.0501E+11	4.1E+08	0.8596	-10.3179	0.0062
67	490	10	9.517E+10	3.4E+08	0.8871	-10.2099	0.0075
68	495	10	8.023E+10	3.1E+08	0.9103	-10.1570	0.0094
69	500	10	7.093E+10	2.7E+08	0.9308	-10.036	0.012
70	505	10	5.900E+10	2.9E+08	0.9478	-9.950	0.016
71	510	10	4.552E+10	2.6E+08	0.9610	-9.923	0.021
72	515	15	4.824E+10	2.4E+08	0.9749	-9.909	0.030
73	520	15	3.054E+10	3.0E+08	0.9837	-9.928	0.047
Final			5.633E+10	1.2E+08	1.0000		

[a]Cumulative fraction of ^{4}He released.

[b]Calculations follow Fechtig and Kalbitzer (1966) and assume a spherical geometry.

[c]2σ values represent propagated analytical uncertainties.

[d]Gas lost after heating. Values reported are estimated from Step 36.

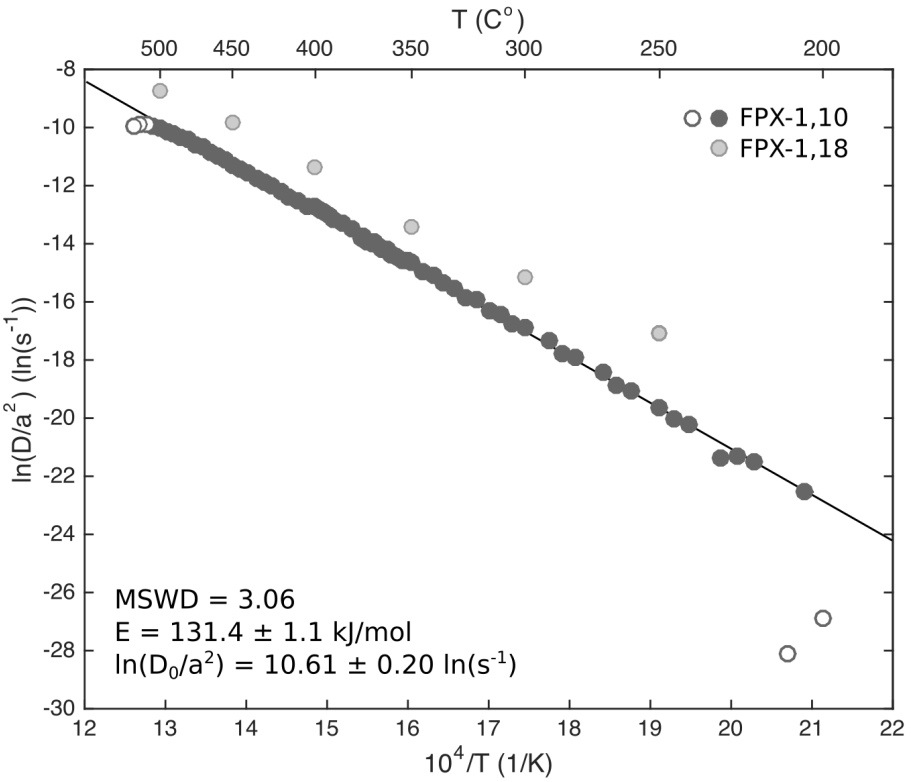

Figure 5.4. Arrhenius diagram for diffusion experiments FPX-1,10 and FPX-1,18. Propagated 2σ uncertainties are smaller than the symbol sizes. Reported kinetic parameters are for FPX-1,10. Open symbols were statistically excluded the linear regression. Quoted uncertainties for $\ln(D/a^2)$ and E represent 2σ propagated analytical errors expanded by the square root of the MSWD.

Table 5.5. Step-Heating Results for He Diffusion Experiment FPX-1,18

Step	T (°C)	t (minutes)	^{4}He (atoms)	2σ	$f_{cumulative}$ [a]	$\ln(D/a^2)$ [b]	2σ [c]	$\ln(D_0/a^2)$ [d]	2σ [e]
1	250	30	2.20E+09	1.8E+08	0.0276	-17.102	0.083	13.11	0.33
2	300	30	3.89E+09	1.7E+08	0.0764	-15.172	0.037	12.40	0.27
3	350	30	8.24E+09	2.6E+08	0.1798	-13.451	0.027	11.91	0.24
4	400	15	1.375E+10	4.1E+08	0.3523	-11.375	0.026	12.10	0.23
5	450	15	2.434E+10	6.7E+08	0.6577	-9.823	0.030	12.03	0.22
6	500	15	2.087E+10	5.9E+08	0.9196	-8.721	0.063	11.72	0.23
Final			6.41E+09	1.9E+08	1.0000				
							Mean:	12.12 [f]	0.34 [g]

[a] Cumulative fraction of ^{4}He released.
[b] Calculations follow Fechtig and Kalbitzer (1966) and assume a spherical geometry.
[c] 2σ values represent propagated analytical uncertainties.
[d] Intercept values calculated by applying the FPX-1,10 slope to each data point.
[e] 2σ values represent propagated analytical uncertainties for FPX-1,18 and for the FPX-1,10 slope.
[f] Inverse-variance weighted mean value.
[g] Uncertainty expanded by the square root of the MSWD.

the offset between the two experiments lies between 0.14 and 0.72. This range reflects the 95% confidence interval given propagated analytical uncertainties. To evaluate whether this range is consistent with the physical grain sizes of the two crystal fragments, we first calculated the equivalent spherical radius for each fragment (R_{eq} = 3V/S, where V is the volume of the crystal fragment and S is the surface area: Meesters and Dunai, 2002; Reiners and M. T. Brandon, 2006). These values are 220 μm and 61 μm for FPX-1,10 and FPX-1,18, respectively. The a_2/a_1 ratio given these dimensions is 0.28, which lies well within the 95% confidence interval of our predicted values. As such, we interpret this to mean that the diffusion dimension for helium loss in natural xenotime is closely related to the physical grain size, which is consistent with findings for helium diffusion in other accessory minerals (Farley, 2000; Farley, 2007; Reiners and Farley, 1999; Reiners et al., 2004).

5.9 Effects of Anisotropy on Inferences for $\ln(D_0)$

To more easily compare our results to other helium diffusion studies, we needed to determine a value for the pre-exponential diffusivity constant, $\ln(D_0)$. To calculate this value from $\ln(D_0/a^2)$ we needed to make an assumption for a. In the previous section, we assumed that a was equal to the equivalent spherical radius, which is only appropriate if diffusivity is essentially isotropic. However, if diffusivity in natural xenotime is moderately anisotropic with faster diffusivity parallel to c, our bulk diffusivity results may be better described as the average of two diffusivities, a-parallel and c-parallel. In this case, the concept of the equivalent spherical radius can be modified following the recommendations of Gautheron and Tassan-Got (2010), such that R_{eq}' = 3V/S', where R_{eq}' is the active radius and S' is the active area. The active area depends on the geometry of the crystal and the ratio of diffusion

coefficients D_a, D_b, D_c, which correspond to diffusion along the crystallographic *a*-, *b*-, and *c*-axes, respectively. Because xenotime has tetragonal symmetry, $D_a = D_b$.

FPX-1,10 is an irregularly shaped prism that is most closely described as a rectangular prism with a *c*-axis dimension of 522 μm and *a*-axes dimensions of 522 μm and 334 μm. Unfortunately, our diffusion experiments do not place direct constraints on the degree of anisotropic diffusivity. It was not possible to explore this through diffusion experiments on differently oriented slabs with very high aspect ratios [e.g. Guenthner et al. (2013)], since FPX-1 crystals are extensively intergrown and cleave when broken off or sawed. Instead, we used the approach of Gautheron and Tassan-Got, 2010 to generally explore how anisotropic diffusivity might affect $\ln(D_0)$ calculations. We modeled values for the active radii for the case in which D_c is 2, 5, 10, 50, and 100 times faster than D_a using the freely available program developed by Gautheron and Tassan-Got (2010). It is important to note that this approach assumes that the activation energies along the *a*- and *c*- crystallographic axes are equal (Gautheron and Tassan-Got, 2010). There is some experimental evidence that this is the case for zircon and rutile (Cherniak and Watson, 2011; Cherniak et al., 2009); however, this has not yet been experimentally or theoretically demonstrated for xenotime. Calculated active radii range from 220 to 363 μm (Table 5.6). Based on this range of values, $\ln(D_0)$ could vary from -6.24 $\pm$ 0.20 to -5.23 $\pm$ 0.20 $\ln(m^2/s)$. Note that the quoted uncertainties reflect propagated analytical uncertainties for $\ln(D_0/a^2)$ at the 2σ level and do not account for measurement uncertainties associated with the irregular shape of the crystal fragment.

Table 5.6. Effects of Diffusive Anisotropy on $\ln(D_0)$ Calculations

D_c/D_a[a]	R_{eq}' (μm)[b]	$\ln(D_0)$ ($\ln(m^2/s)$)	2σ[c]
Isotropic	220	-6.24	0.20
2	227	-6.17	0.20
5	249	-5.98	0.20
10	274	-5.80	0.20
50	338	-5.37	0.20
100	363	-5.23	0.20

[a]Modeled diffusion coefficient ratios.
[b]Calculated active radii following *Gautheron and Tassan-Got* [2010].
[c]Values represent propagated analytical uncertainties for $\ln(D_0/a^2)$.

5.10 Helium Diffusion in Natural Xenotime as Compared to Synthetic Analogues and Other Accessory Minerals

The activation energy for bulk ^{4}He diffusion in FPX-1,10 is similar to that for ^{3}He diffusion in synthetic YPO_4; however, the range in calculated $\ln(D_0)$ values, regardless of the effects of anisotropy (Table 5.6), is significantly lower than that reported for the synthetic material (Farley, 2007). Consequently, helium diffusivity in FPX-1,10 is $\sim$3 orders of magnitude lower than in its synthetic counterpart (Figure 5.5). The FPX-1,10 results are more consistent with experimental findings for helium diffusivity in other natural accessory minerals than they are with synthetic YPO_4 (Boyce et al., 2005; Farley, 2000; Peterman et al., 2014; Reiners et al., 2004). Farley (2007) proposed that radiation damage may explain why helium diffusion is so much slower in natural xenotime than in synthetic analogues. However, we find this explanation to be unlikely since Raman data for FPX-1 suggests little to no radiation damage in the FPX-1 material.

If radiation damage retards diffusivity in xenotime as has been proposed for apatite

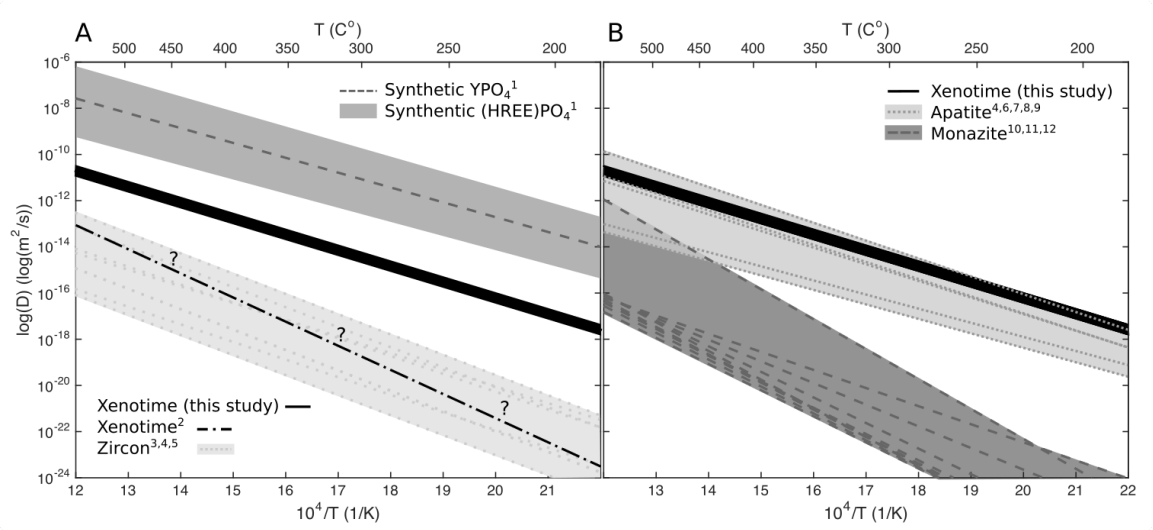

Figure 5.5. A. Arrhenius diagram comparing results for FPX-1,10 given the range of possible ln(D_0) values presented in Table 5.6 to literature results for helium diffusion in synthetic xenotime and HREE phosphates, natural QC-A xenotime (the curve marked with question marks), and isostructural zircon. [1]Farley (2007) step-heating ^{3}He diffusion in synthetic Y, Tb, Dy, Ho, Er, Tm, Yb, and $LuPO_4$; [2] step-heating ^{4}He diffusion in QC-A xenotime reconstructed from the diffusion parameters reported by Farley (2007) based on personal communication with D. Stockli; [3]Reiners et al. (2004) step-heating ^{4}He diffusion in zircon; [4]Cherniak et al. (2009) nuclear reaction analysis *c*-parallel and *c*-perpendicular ^{3}He diffusion in zircon; and [5]Guenthner et al. (2013) step-heating *c*-parallel and *c*-perpendicular ^{4}He diffusion in Mud Tank and RB140 zircon. B. Arrhenius diagram comparing results for FPX-1,10 to literature results for helium diffusion in other natural phosphates. [6]Ouchani et al. (1998) elastic recoil detection analysis ^{3}He diffusion in apatite; [7]Farley (2000) step-heating ^{4}He diffusion in apatite; [8]Shuster et al., 2003 step-heating ^{3}He diffusion in apatite; [4]Cherniak et al. (2009) nuclear reaction analysis ^{3}He diffusion in apatite; [9]van Soest et al., 2011 laser ablation ^{4}He diffusion in apatite;[10]Boyce et al. (2005) step-heating ^{4}He diffusion in monazite; [11]Cherniak and Watson (2013) nuclear reaction analysis ^{3}He diffusion in monazite; [12]Peterman et al. (2014) step-heating ^{4}He diffusion in monazite.

and low-damage zircon (Guenthner et al., 2013; Shuster et al., 2006), it may explain, in part, the discrepancy between our results and those reported by Farley (2002) and Farley (2007) for natural xenotime, if QC-A contained significant radiation damage. It is important to note, however, that there currently is no experimental evidence that radiation damage retards helium diffusivity in xenotime. Radiation damage may enhance helium diffusivity as has been shown for titanite and moderate to high damage zircon (Baughman et al., 2017; Guenthner et al., 2013) or, alternatively, radiation damage may not significantly affect

helium diffusion kinetics in xenotime since this mineral is expected to anneal more readily than zircon and other silicates (Meldrum et al., 1997).

The discrepancy between our results and those previously reported for natural xenotime may, in part, also reflect differences in xenotime chemistry. Although Boyce et al. (2005) speculated that crystal chemistry may strongly influence ^{4}He diffusivity in natural monazite, studies by Cherniak and Watson (2013) and Peterman et al. (2014) found only minor compositional dependency for the range of compositions they studied. The gray shaded region in Figure 5.5 highlights the range in ^{3}He diffusivity observed for synthetic xenotime and synthetic zircon structure phosphates: $TbPO_4$, $DyPO_4$, $HoPO_4$, $ErPO_4$, $TmPO_4$, $YbPO_4$, $LuPO_4$ (Farley, 2007). The activation energies determined for synthetic end-member compositions vary by at most 24 kJ/mol (Farley, 2007). The difference between the activation energy for helium diffusion in FPX-1,10 and that reported for QC-A by Farley (2007) ($\sim$70 kJ/mol) is much larger. The difference in composition between FPX-1 and QC-A is likely to be much smaller that the differences between these synthetic phosphates. While it seems improbable that variations in the relative abundances of HREE could explain the discrepancies in helium diffusivity between FPX-1,10 and QC-A, dramatic differences in U and Th concentrations might.

Helium diffusion in FPX-1,10 is faster than bulk helium diffusion in the isostructural mineral zircon (Reiners et al., 2004). This observation is consistent with our expectation that the interstitial channels through which helium is likely transported are wider in the xenotime structure than in the zircon structure (Figure 5.1). The results reported by Farley (2007) for QC-A seem inconsistent with this expectation. An additional factor that may contribute to the discrepancy in helium diffusivity between zircon and xenotime is solid-solution behavior in the latter involving Y and the other heavy rare earths. For example, FPX-1 xenotime is only 72 mol$\%$ YPO_4, and the substitution of other trivalent heavy rare earths for yttrium

likely increased the [HREE,Y]-P distance in the crystal structure, widening the *c*-parallel open channels further (Farley, 2007).

Somewhat surprisingly, our results also suggest that helium diffusion in FPX-1,10 is faster than helium diffusion in apatite, likely because interstitial sites are more interconnected in the zircon-xenotime structure than in the apatite structure (Cherniak and Watson, 2011). These findings underscore the important role that both size and inter-connectivity of interstitial sites play in controlling noble gas diffusion in minerals (Cherniak and Watson, 2011).

Following Dodson's formulations (Dodson, 1973), we calculated the bulk closure temperature for helium as a function of cooling rate for FPX-1,10 directly from the Arrhenius parameters $\ln(D_0/a^2)$ and E presented in Figure 5.4 without making any assumption about the diffusion domain size or degree of diffusive anisotropy. For cooling rates between 0.1 - 100 °C/Ma, bulk closure temperature ranges from ∼45 - 95 °C, assuming a spherical geometry. For the nominal cooling rate of 10°C/Ma, FPX-1,10 has a bulk closure temperatures of 75 °C. Presuming that these results are at least generally representative of helium diffusion in all xenotimes, Figure 5.6 shows bulk closure temperature as a function of cooling rate for xenotime, apatite, zircon, and titanite, and monazite for typical crystal sizes. The bulk closure temperature for helium in a xenotime crystal with a 50 μm diffusion dimension ranges from ∼25 - 50 °C for cooling rates between 0.1 - 100 °C/Ma. At equivalent cooling rates and for crystals with equivalent diffusion dimensions, the bulk closure temperature for helium in xenotime is ∼20 °C lower than that for helium in apatite. While technically only applicable to highly crystalline xenotime samples with similar chemical composition to FPX-1,10, our results suggest that xenotime (U-Th)/He dating could prove a useful tool for investigating very low-temperature cooling events.

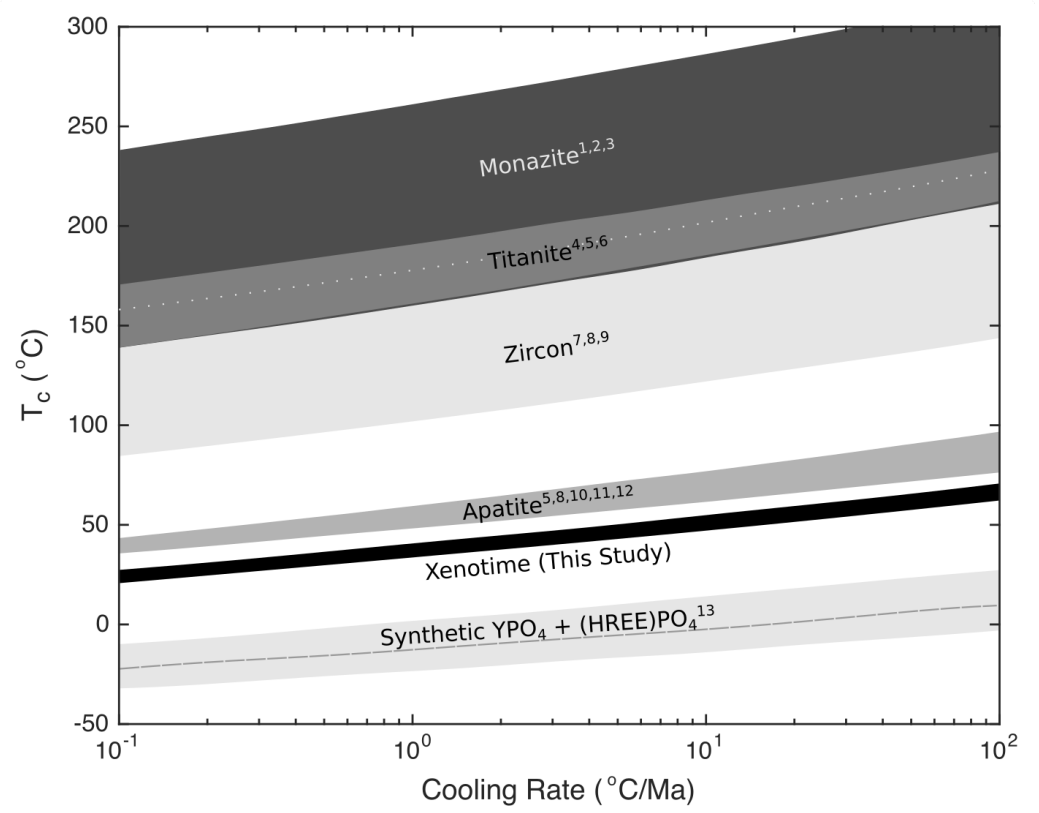

Figure 5.6. Helium bulk closure temperature as a function of cooling rate (Dodson, 1973) for xenotime based on results for experiment FPX-1,10 compared to monazite, titanite, zircon, apatite, synthetic xenotime (dashed line), and synthetic HREE orthophosphates. Bulk closure temperature calculations for xenotime, monazite, zircon, apatite, and synthetic orthophosphates assume a 50 μm diffusion dimension and spherical geometry, while calculations for titanite assume a 250 μm diffusion dimension and spherical geometry. To account for diffusive anisotropy in zircon, bulk closure temperatures were calculated for both *c*-parallel and *c*-perpendicular diffusion parameters to bracket the full range of possible aspect ratios. The dotted line running through 'Titanite' represents the top of the zircon helium bulk closure temperature window. Literature references: [1]Boyce et al. (2005); [2]Cherniak and Watson (2013); [3]Peterman et al. (2014); [4]Reiners and Farley (1999); [5]Shuster et al. (2003); [6]Cherniak and Watson (2011); [7]Reiners et al. (2004); [8]Cherniak et al. (2009); [9]Guenthner et al. (2013) Mud Tank and RB140; [10]Ouchani et al. (1998); [11]Farley (2000); [12]van Soest et al. (2011); [13]Farley (2007).

5.11 Issues and Opportunities

Additional diffusion experiments on natural xenotime crystals with a range of chemical compositions and thermal histories are needed to determine how much crystal chemistry

and radiation damage affect the closure temperature for helium in xenotime. Xenotime crystals from the same rock sample can show significant inter-crystalline variations in chemical composition (Förster, 1998; Švecová et al., 2016). A new analytical method proposed by Idleman et al. (2018) allows for the derivation of diffusion parameters from helium release spectra obtained by continuous ramped heating. This method would be ideal for xenotime (U-Th)/He thermochronology as it would allow the user to derive diffusion parameters from unknown xenotime crystals without needing to characterize the composition of each dated xenotime grain. Besides the limited occurrence of xenotime relative to zircon, apatite, and titanite, the factor most likely to limit the application of xenotime (U-Th)/He thermochronometry is the commonly small grain sizes (<50μm) for natural xenotime which would require large alpha ejection corrections.

5.12 Conclusions

We have assessed the potential of xenotime as a (U-Th)/He thermochronometer through bulk diffusion study of two crystal fragments of a natural, highly crystalline xenotime. Two incremental heating experiments of this material are consistent with ^{4}He being lost by thermally activated volume diffusion from a single diffusion domain related to the physical grain size. Results for experiment FPX-1,10 yield Arrhenius parameters of E = 131.4 $\pm$ 1.1 kJ/mol and $\ln(D_0/a^2)$ = 10.61 $\pm$ 0.20 m^2/s. These results imply a helium bulk closure temperature of 75°C for the degassed crystal fragment for a nominal cooling rate of 10°C/Ma. Our experimental results and an analysis of the xenotime crystal structure, suggest that helium diffusivity may be only moderately anisotropic, with more rapid helium diffusivity in the *c*-parallel crystallographic direction. Additional research is needed to investigate how much crystal chemistry and radiation damage affect xenotime helium closure

and to constrain the magnitude of diffusive anisotropy. Nevertheless, the results reported here suggest that xenotime (U-Th)/He dating could evolve into a valuable tool for low-temperature thermochronometry. Because this mineral typically incorporates more uranium and thorium than apatite, ^{4}He can accumulate much more rapidly in it through radioactive decay. Consequently, xenotime may yield higher precision (U-Th)/He dates than apatite. The greatest challenge to the widespread application of xenotime (U-Th)/He dating is the mineral's limited occurrence and often small grain size.

5.13 Supplementary Materials

5.13.1 Mineral Chemistry

BSE and CL images were acquired for FPX-1,m1 using a JEOL JSM 7100F field emission scanning electron microscope with a Deben CL system at Memorial University of Newfoundland (Figure S1). Images were acquired using a 15.0 kV accelerating voltage, a 25 nA beam current, and a 20 μm beam diameter. Counting times for the analyses were 30 seconds on the peaks and 20 seconds on each background for every element analyzed. Wavelength dispersive spectroscopy (WDS) analyses were done using a JXA-8530F field emission Electron Probe Microanalyzer (EPMA) at the John M. Cowley Center for High Resolution Electron Microscopy at Arizona State University. Elements measured include P, Y, Gd, Tb, Dy, Ho, Er, and Yb (Table S1). Twenty WDS analyses were made on each of the three mounted xenotime crystal fragments across different chemical zones as indicated by the BSE images to evaluate compositional heterogeneity. Smithsonian synthetic rare earth element phosphates NMNH 168485, 168486, 168488, 168489, 168496, 168498, and 168499 were used as concentration standards for P and the REEs (Donovan et al., 2002;

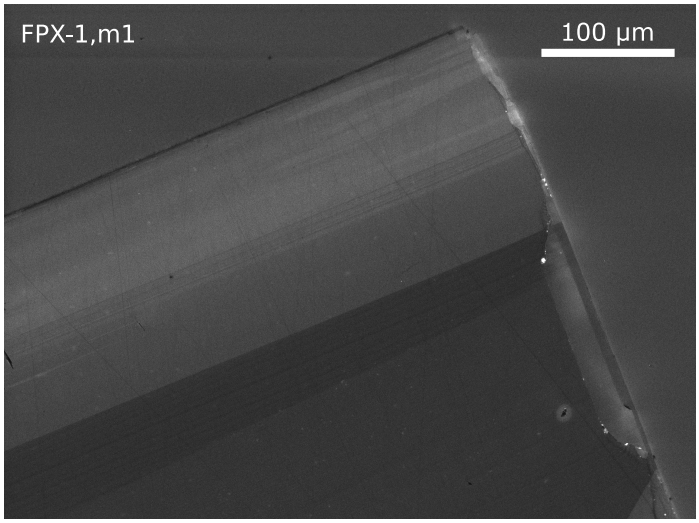

Figure S5.1. Representative cathodoluminescence image of FPX-1,m1.

Donovan et al., 2003; Jarosewich and Boatner, 1991). Pb contamination is a concern in the monoclinic NMNH (LREE)PO_4 standards (Donovan et al., 2003). $GdPO_4$ is monoclinic, but as you go from La to Gd, the Pb contamination decreases significantly. The tetragonal NMNH (HREE)PO_4 have negligible Pb contamination (Donovan et al., 2003). REE glass standards were also analyzed alongside unknowns (Drake and Weil, 1972).

FPX-1,11 was weighed using a METTLER TOLEDO XSE205 DualRange scale and dissolved using hydrofluoric (HF), nitric (HNO_3), and hydrochloric (HCl) acids at high temperatures in Parr digestion vessels. The solution was mixed with ^{230}Th, ^{235}U, and ^{149}Sm spikes prior to isotopic analysis on a Thermoscientific ICAP-Q ICPMS at Group 18 Laboratories at Arizona State University. ^{238}U, ^{232}Th, ^{147}Sm isotopic abundances were determined by isotope dilution, and ^{235}U abundance was calculated assuming the natural uranium isotopic ratio.

Table S5.1. Xenotime Composition - Wavelength Dispersive Spectroscopy

P_2O_5[a]	99%[b]	Y_2O_3	99%	Gd_2O_3	99%	Tb_2O_3	99%	Dy_2O_3	99%	Ho_2O_3	99%	Er_2O_3	99%	Yb_2O_3	99%	Total
49.153	0.059	30.454	0.054	3.521	0.067	0.852	0.019	6.79	0.14	1.358	0.060	3.84	0.18	2.51	0.13	98.48
49.922	0.049	30.213	0.056	3.690	0.067	0.893	0.019	6.93	0.14	1.236	0.061	3.90	0.17	2.49	0.13	99.28
49.528	0.050	30.125	0.055	3.710	0.067	0.917	0.019	6.98	0.14	1.375	0.061	3.80	0.18	2.47	0.13	98.90
48.831	0.051	28.815	0.056	3.601	0.068	0.970	0.019	7.71	0.15	1.405	0.062	4.17	0.18	2.90	0.13	98.40
48.766	0.051	28.930	0.057	3.645	0.068	1.010	0.019	7.76	0.14	1.450	0.062	4.17	0.18	2.78	0.13	98.50
49.139	0.051	29.547	0.055	3.606	0.068	0.978	0.019	7.46	0.14	1.411	0.062	4.27	0.18	2.80	0.13	99.21
48.868	0.050	29.926	0.056	3.599	0.067	0.959	0.019	7.20	0.14	1.372	0.061	3.94	0.18	2.62	0.13	98.47
49.064	0.049	30.197	0.055	3.572	0.068	0.954	0.019	7.23	0.14	1.380	0.061	3.91	0.18	2.63	0.13	98.94
49.260	0.050	30.530	0.056	3.586	0.068	0.886	0.019	6.94	0.14	1.326	0.062	3.81	0.18	2.49	0.13	98.83
49.577	0.051	31.040	0.054	3.580	0.068	0.866	0.019	6.74	0.14	1.322	0.060	3.82	0.17	2.54	0.13	99.49
48.747	0.052	28.906	0.056	3.355	0.068	0.926	0.019	7.80	0.14	1.417	0.062	4.30	0.18	3.04	0.13	98.49
48.315	0.050	29.426	0.056	3.361	0.067	0.924	0.019	7.56	0.14	1.428	0.062	4.17	0.18	2.87	0.13	98.05
48.302	0.050	29.142	0.053	3.472	0.068	0.999	0.019	8.00	0.14	1.429	0.062	4.28	0.18	2.78	0.14	98.40
48.516	0.052	28.913	0.056	3.453	0.068	0.984	0.019	7.97	0.14	1.464	0.062	4.34	0.18	2.75	0.14	98.38
48.468	0.051	29.134	0.055	3.406	0.067	0.950	0.019	8.02	0.14	1.465	0.062	4.36	0.18	2.83	0.13	98.62
48.306	0.051	29.181	0.055	3.421	0.068	0.981	0.019	7.97	0.14	1.491	0.062	4.33	0.18	2.81	0.13	98.49
48.690	0.050	29.862	0.055	3.455	0.067	0.917	0.019	7.29	0.14	1.417	0.061	4.21	0.18	2.95	0.13	98.81
48.917	0.051	29.697	0.057	3.361	0.067	0.903	0.019	7.28	0.14	1.444	0.061	4.17	0.18	2.94	0.13	98.71
48.565	0.051	30.047	0.054	3.374	0.067	0.899	0.019	7.31	0.14	1.400	0.062	4.16	0.18	3.07	0.13	98.83
48.868	0.051	29.893	0.057	3.327	0.068	0.898	0.019	7.34	0.15	1.441	0.061	4.20	0.18	3.00	0.13	98.98
49.441	0.049	32.184	0.053	3.199	0.067	0.760	0.019	5.83	0.14	1.225	0.060	3.54	0.17	2.41	0.13	98.59
49.321	0.049	32.633	0.051	3.306	0.067	0.756	0.019	5.74	0.14	1.201	0.059	3.43	0.17	2.23	0.13	98.62
49.251	0.049	32.528	0.055	3.270	0.067	0.744	0.019	5.81	0.14	1.210	0.060	3.52	0.17	2.40	0.13	98.73
49.377	0.048	32.437	0.054	3.285	0.067	0.783	0.019	5.78	0.14	1.164	0.060	3.39	0.17	2.35	0.13	98.57
48.014	0.050	29.698	0.056	3.886	0.068	0.948	0.019	7.28	0.14	1.299	0.062	3.97	0.18	2.51	0.13	97.61
48.128	0.051	29.781	0.056	3.881	0.068	0.953	0.019	7.26	0.14	1.377	0.061	4.00	0.18	2.62	0.13	98.00
48.113	0.050	29.935	0.055	3.947	0.068	0.974	0.019	7.11	0.15	1.329	0.062	3.90	0.18	2.52	0.13	97.83
48.820	0.051	29.804	0.056	3.804	0.068	0.906	0.019	7.24	0.15	1.389	0.061	4.05	0.17	2.72	0.13	98.74
48.003	0.050	29.714	0.056	3.882	0.068	0.941	0.019	7.27	0.14	1.362	0.061	4.10	0.17	2.56	0.13	97.83
48.809	0.049	30.719	0.054	3.573	0.066	0.817	0.019	6.63	0.14	1.324	0.061	3.84	0.18	2.62	0.13	98.33
49.044	0.049	30.967	0.054	3.529	0.067	0.819	0.019	6.65	0.14	1.274	0.061	3.86	0.17	2.61	0.13	98.75
48.654	0.050	30.670	0.054	3.553	0.067	0.867	0.019	6.59	0.14	1.290	0.061	3.85	0.18	2.53	0.13	98.00
47.675	0.052	28.881	0.057	3.772	0.068	0.938	0.019	7.47	0.15	1.411	0.062	4.30	0.18	2.78	0.14	97.22
47.661	0.050	29.357	0.056	3.690	0.067	0.936	0.019	7.47	0.14	1.460	0.062	4.26	0.18	2.82	0.13	97.65
47.807	0.051	29.616	0.057	3.706	0.067	0.942	0.019	7.46	0.15	1.422	0.061	4.26	0.18	2.84	0.13	98.05
48.054	0.050	29.400	0.055	3.681	0.069	0.938	0.019	7.53	0.14	1.455	0.062	4.32	0.18	2.74	0.13	98.11
48.375	0.051	29.599	0.057	3.934	0.067	0.921	0.019	7.27	0.15	1.356	0.061	3.96	0.18	2.59	0.13	98.01
48.107	0.051	29.772	0.057	3.881	0.068	0.914	0.019	7.33	0.14	1.424	0.061	4.01	0.18	2.54	0.13	97.99
47.626	0.051	29.512	0.055	3.872	0.067	0.957	0.019	7.22	0.14	1.382	0.061	4.05	0.17	2.54	0.13	97.16
47.827	0.050	29.633	0.055	3.885	0.069	0.957	0.019	7.27	0.14	1.348	0.062	4.10	0.18	2.57	0.13	97.59
49.591	0.048	31.645	0.055	3.559	0.067	0.815	0.019	6.13	0.14	1.215	0.060	3.56	0.17	2.40	0.13	98.92
49.108	0.050	31.408	0.055	3.666	0.068	0.855	0.019	6.38	0.14	1.172	0.061	3.55	0.17	2.32	0.13	98.46
49.135	0.050	31.105	0.054	3.818	0.068	0.903	0.019	6.47	0.14	1.232	0.060	3.60	0.17	2.24	0.13	98.51
48.847	0.048	31.366	0.054	3.657	0.067	0.874	0.019	6.42	0.14	1.241	0.060	3.61	0.17	2.36	0.13	98.37
49.024	0.048	31.446	0.055	3.617	0.067	0.833	0.019	6.40	0.14	1.203	0.060	3.63	0.18	2.35	0.13	98.51
48.343	0.050	29.321	0.058	3.854	0.067	0.958	0.019	7.37	0.14	1.418	0.061	4.19	0.17	2.69	0.13	98.15
47.987	0.051	29.813	0.055	3.847	0.068	0.951	0.019	7.40	0.14	1.415	0.062	4.13	0.18	2.71	0.13	98.26
48.570	0.050	29.542	0.056	3.847	0.068	0.922	0.019	7.41	0.15	1.396	0.062	4.11	0.17	2.68	0.14	98.48
48.101	0.049	29.414	0.056	3.796	0.068	0.992	0.019	7.37	0.14	1.392	0.061	4.07	0.18	2.66	0.13	97.79
47.930	0.052	28.915	0.057	3.807	0.067	0.973	0.019	7.48	0.14	1.399	0.061	4.29	0.18	2.67	0.14	97.47
47.717	0.051	29.141	0.056	3.746	0.068	0.950	0.019	7.53	0.15	1.349	0.062	4.31	0.18	2.74	0.13	97.49
48.772	0.051	29.222	0.056	3.721	0.067	0.933	0.019	7.38	0.14	1.428	0.062	4.30	0.17	2.77	0.14	98.53
48.358	0.050	29.374	0.057	3.816	0.068	0.976	0.019	7.48	0.14	1.389	0.062	4.26	0.17	2.73	0.13	98.38
48.173	0.051	29.303	0.054	3.838	0.068	0.981	0.019	7.52	0.14	1.399	0.062	4.19	0.18	2.77	0.14	98.17
48.342	0.050	29.332	0.055	3.859	0.068	0.915	0.019	7.57	0.15	1.375	0.062	4.14	0.18	2.71	0.14	98.24
48.191	0.050	29.430	0.057	3.824	0.068	0.957	0.019	7.51	0.15	1.396	0.062	4.19	0.18	2.63	0.14	98.12
48.091	0.051	29.118	0.057	3.748	0.068	0.940	0.019	7.48	0.14	1.422	0.061	4.35	0.17	2.73	0.14	97.88
48.395	0.051	29.334	0.054	3.764	0.068	0.963	0.019	7.39	0.14	1.373	0.062	4.28	0.18	2.71	0.14	98.21
48.201	0.052	28.929	0.055	3.827	0.068	0.967	0.019	7.51	0.14	1.356	0.062	4.32	0.18	2.74	0.13	97.85
47.951	0.050	29.253	0.056	3.827	0.068	1.013	0.019	7.53	0.14	1.391	0.062	4.26	0.18	2.80	0.13	98.02

[a]All reported values are in weight %
[b]All reported uncertanties represent the 99% confidence interval

5.13.2 Geochronology and Thermochronology

All Geochronologic and Thermochronologic analyses were done using instrumentation at Group 18 Laboratories at Arizona State University. FPX-1,m1 was loaded into a Photon Machines HelEx Active two-volume laser 529 ablation cell for laser ablation $^{238}U/^{206}Pb$ dating. Twenty-three 65 micron spots were ablated using a Teledyne Photons Machine Analyte G2, 193 nm ultraviolet Atlex 300 ArF excimer laser. Lasing conditions were 4 mJ

laser energy, 50% output power, 10 Hz pulse frequency, and 200 shot count per analysis. U, Th, and Pb isotopes were analyzed using a Thermoscientific ICAP-Q quadrupole ICPMS, and results were processed using the U-Pb Geochronology data reduction scheme in the Iolite software package for U-Pb apparent age calculations (Paton et al., 2010). Sri Lankan zircon (562.5 $\pm$ 2 Ma) and MOM monazite (481.8 $\pm$ 0.2 Ma) were used as U-Pb age standards. Results are reported in Table 2. The inverse-variance weighted mean $^{238}U/^{206}Pb$ date for the sample is 28.82 $\pm$ 0.13 Ma with a mean squared weighted deviation (MSWD) of 1.52 (Wendt and Carl, 1991).

Nine xenotime shards with $<$200 μm radii were picked by hand under a binocular microscope (FPX-1,1-9). None of the selected shards showed evidence of crystal growth surfaces. The shards were loaded into niobium tubes and analyzed for ^{4}He on an Australian Scientific Instruments (ASI) 474 Alphachron system. Samples were heated for ten minutes at 20 A using a 45 W infrared (980 nm) diode laser. A known quantity of ^{3}He was added to the extracted gases to allow for isotope dilution analysis. Reactive gases were removed by hot and cold metal alloy getters before isotopic analysis on a Balzers Prisma QMS 200 quadrupole mass spectrometer. Fish Canyon zircon (28.38 $\pm$ 0.73 Ma (Horne et al., 2016), Durango apatite (32 $\pm$ 1 Ma (Farley and Stockli, 2002), and empty niobium tubes were included in the run as age standards to monitor system performance and to allow for system blank corrections, respectively. Degassed samples were dissolved and analyzed for ^{238}U and ^{232}Th isotopic abundances using a Thermoscientific ICAP-Q quadrupole ICPMS in solution mode.

(U-Th)/He dates were calculated for each sample iteratively from the measured ^{238}U, ^{232}Th, and ^{4}He abundances. Because the selected shards did not show evidence of growth surfaces, it is unlikely that a significant quantity of ^{4}He was lost via ejection, so alpha ejection corrections were not made (Farley and Stockli, 2002; Hourigan et al., 2005). Reported

uncertainties for individual shards represent 2σ propagated analytical errors. The nine dates yield an inverse-variance weighted mean date of 15.32 $\pm$ 0.14 Ma with a MSWD of 18.6, which is higher than the ca. 95% confidence range of its predicted value of 1.0 (Wendt and Carl, 1991), indicating that the dataset is overdispersed. We expand this uncertainty to more accurately reflect this dispersion by multiplying by the square root of the MSWD, yielding a date of 15.32 $\pm$ 0.61 Ma (Ludwig, 2003; Wendt and Carl, 1991).

5.13.3 YPO_4 Synthesis and Raman Spectroscopy

Undoped YPO_4 was synthesized in the experimental geochemistry laboratory at Memorial University of Newfoundland. A Li_2MoO_4-MoO_3 flux was mixed with equal molar portions of Y_2O_3 and $NH_4H_2PO_4$ with ethanol in an agate mortar and pestle. A 25 mL platinum crucible with a tightly fitted Pt lid containing the powdered mixture was placed in a Deltech vertical tube furnace, (with a temperature accuracy of $\pm$5 °C confirmed with a Type-S thermocouple), heated to 1250 °C, and held at constant temperature for 8 hr. The crucible was then cooled to 1200 °C at 2 °C/hr before being reheated at 100 °C/hr back up to 1250 °C. The setup was then cooled once more at 2 °C/hr to 1000 °C before the crucible was removed from the furnace and allowed to quench to room temperature. The crucible containing a minor amount of residual flux and the YPO_4 crystals was soaked in boiling concentrated NH4OH to dissolve the residual flux. The YPO_4 crystals were subsequently picked by hand under a binocular microscope.

Raman spectra were acquired from the polished sample surfaces (FPX-1,m1) using a HORIBA Scientific Jobin Yvon XploRA PLUS confocal Raman microscope at Group 18 Laboratories at Arizona State University. The system employs a 532 nm laser with a 20-25 mW power output and a Syncerity 1024 x 256 pixel 506 CCD detector cooled to -60 °C. The

system was calibrated prior to use using the silicon 520.7 cm^{-1} Raman peak for reference. Spectra were measured using 10x magnification, 100 $\%$ laser output, and a 2400 gr/mm diffraction grating with a $\sim$1.4 cm^{-1} spectral resolution. Spectra were measured for two seconds with five accumulations. Polynomial baseline corrections and Gaussian-Lorenztian peak fitting were done using Horiba Scientific LabSpec6 software. Measured peak widths were corrected for instrument bias using the apparatus function (Nasdala et al., 2001). Estimated peak width uncertainties are $<5\%$ (2σ).

5.13.4 Diffusion Experiment

Xenotime shards FPX-1,10 and FPX-1,18 were photographed and measured using a Leica MZ16 binocular microscope. The crystallographic orientation of FPX-1,18 was determined visually under cross-polarized light. The crystallographic orientation of the FPX-1,10 was determined using a Bruker Smart APEX single crystal X-ray diffractometer from the LeRoy Eyring Center for Solid State Studies at Arizona State University. The samples were each placed in a platinum capsule with an Omega type K thermocouple that has a stated accuracy of 2.2°C for temperatures $<$300°C and 0.75$\%$ for higher temperatures. The setup was then loaded into a custom designed diffusion cell with a synthetic sapphire viewport in Group 18 Laboratories.

The samples were incrementally degassed in either a series of cycled prograde and retrograde heating steps (FPX-1,10), or a single prograde series (FPX-1,18). Heating was conducted *in vacuo* using a projector bulb furnace positioned above the diffusion cell viewport. The extracted gasses from FPX-1,10 were purified using metal alloy getters and a cryogenic trap. ^{4}He measurements were made using a GVI/Thermo Electron *Helix SFT* magnetic sector mass spectrometer on either an ion-counting electron multiplier detector or

a Faraday detector depending on each step's ^{4}He abundance. Standard air shots were used to routinely monitor both detectors' ^{4}He sensitivity. The extracted gasses for FPX-1,18 were spiked with a known quantity of ^{3}He to allow for isotope dilution analysis, and purified using hot and cold metal alloy getters using an ASI 474 Alphachron system. He measurements were made using a Balzers Prisma QMS 200 quadrupole mass spectrometer. Hot and cold blanks were run for the FPX-1,10 experiment and cold blanks were run for the FPX-1,18. Hot blanks were not found to change significantly when the heating temperature and duration were varied. Incremental heating was continued until the measured amount of degassed ^{4}He was approaching blank levels and $<1\%$ of the total gas fraction. Final high temperature heating steps, which did not have good temperature control, were grouped and reported as the "Final" step in Tables 4 and 5. The lowest gas yield (besides the final degassing steps) for FPX-1,10 (step 2) and FPX-1,18 (step 1) was greater than $\sim$3x or $\sim$48x the measured blanks, respectively. Heating schedules, ^{4}He measurements, and analytical uncertainties for the experiment is reported in Table 4 and Table 5. All reported measurements and uncertainties have been blank corrected. Reported uncertainties reflect propagated analytical uncertainties for both ^{4}He measurements for the stated t-T step and for the blank corrections.

Diffusivity can be calculated from the cumulative fraction of ^{4}He evolved in each heating step by the equation:

$$f_c = 1 - \Big(\frac{6}{\pi^2}\Big) \sum_{n=1}^{\infty} \Big[\Big(\frac{1}{n^2}\Big) exp\Big(- n^2 \pi^2 \frac{Dt}{a^2}\Big)\Big] \tag{S5.1}$$

where D is diffusivity, t is the heating step duration, and a is the diffusion dimension (Fechtig and Kalbitzer, 1966). This equation assumes a spherical geometry and can be approximated to simplify calculations (e.g., Boyce et al., 2005; Lovera et al., 1997; Lovera and Richter, 1989). Values for ln(D/a^2) are reported in Table 4. Error estimates reflect propagated ^{4}He analytical uncertainties.

5.14 Acknowledgments

This work was supported by the National Science Foundation [EAR-1346321] to KVH, and an NSERC Discovery grant to JMH. All data supporting our conclusions can be found in the tables and figures within the main text. We gratefully acknowledge Axel Wittman for his help with electron microprobe WDS analyses. We would also like to thank Kendra Murray, Daniele Cherniak, Kenneth Farley, and one anonymous reviewer for their valuable feedback.

References

Aleinikoff, J. N. and R. I. Grauch (1990). U-Pb geochronologic constraints on the origin of a unique monazite-xenotime gneiss, Hudson Highlands, New York. *American Journal of Science* 290, pp. 522–546.

Aleinikoff, J. N., R. I. Grauch, F. K. Mazdab, L. Kwak, C. M. Fanning, and S. L. Kamo (2012a). Origin of an unusual monazite-xenotime gneiss, Hudson Highlands, New York: SHRIMP U-Pb geochronology and trace element geochemistry. *American Journal of Science* 312 (7), pp. 723–765.

Aleinikoff, J. N., T. S. Hayes, K. V. Evans, F. K. Mazdab, R. M. Pillers, and C. M. Fanning (2012b). SHRIMP U-Pb ages of xenotime and monazite from the Spar Lake red bed-associated Cu-Ag deposit, western Montana: Implications for ore genesis. *Economic Geology* 107, pp. 1251–1274.

Aleinikoff, J. N., K. Lund, and C. M. Fanning (2015). SHRIMP U-Pb and REE data pertaining to the origins of xenotime in Belt Supergroup rocks: Evidence for ages of deposition, hydrothermal alteration, and metamorphism. *Canadian Journal of Earth Sciences* 52 (9), pp. 722–745.

Aleinikoff, J. N., J. F. Slack, K. Lund, K. V. Evans, C. M. Fanning, F. K. Mazdab, J. L. Wooden, and R. M. Pillers (2012c). Constraints on the Timing of Co-Cu ± Au Mineralization in the Blackbird District, Idaho, Using SHRIMP U-Pb ages of monazite and xenotime plus zircon ages of related mesoproterozoic orthogneisses and metasedimentary rocks. *Economic Geology* 107, pp. 1143–1175.

Baughman, J., R. M. Flowers, J. R. Metcalf, and T. Dhansay (2017). Influence of radiation damage on titanite He diffusion kinetics. *Geochimica et Cosmochimica Acta* 205, pp. 50–64.

Bea, F. (1996). Residence of REE, Y, Th and U in granites and crustal protoliths; implications for the chemistry of crustal melts. *Journal of Petrology* 37 (3), pp. 521–552.

Boatner, L. A. (2002). Synthesis, structure, and properties of monazite, pretulite, and xenotime. *Phosphates - Geochemical, Geobiological, and Materials Importance: Review in Mineralogy & Geochemistry*. Ed. by M. J. Kohn, J. Rakovan, and J. M. Hughes. Washington, DC: Mineralogical Society of America, pp. 87–121.

Boyce, J. W., K. V. Hodges, W. J. Olszewski, and M. J. Jercinovic (2005). He diffusion in monazite: Implications for (U-Th)/He thermochronometry. *Geochemistry, Geophysics, Geosystems* 6 (12), pp. 1–12.

Cherniak, D. J. (2006). Pb and rare earth element diffusion in xenotime. *Lithos* 88 (1-4), pp. 1–14.

Cherniak, D. J. and E. B. Watson (2011). Helium diffusion in rutile and titanite, and consideration of the origin and implications of diffusional anisotropy. *Chemical Geology* 288, pp. 149–161.

Cherniak, D. J., E. B. Watson, and J. B. Thomas (2009). Diffusion of helium in zircon and apatite. *Chemical Geology* 268, pp. 155–166.

Cherniak, D. J. and E. B. Watson (2013). Diffusion of helium in natural monazite, and preliminary results on He diffusion in synthetic light rare earth phosphates. *American Mineralogist* 98 (8-9), pp. 1407–1420.

Dodson, M. H. (1973). Closure temperature in cooling geochronological and petrological systems. *Contributions to Mineralogy and Petrology* 40 (3), pp. 259–274.

Donovan, J. J., J. M. Hanchar, P. M. Picolli, M. D. Schrier, L. A. Boatner, and E. Jarosewich (2002). Contamination in the rare-earth element orthophosphate reference samples. *Journal of Research of the National Institute of Standards and Technology* 107 (6), pp. 693–701.

Donovan, J. J., J. M. Hanchar, P. M. Picolli, M. D. Schrier, L. A. Boatner, and E. Jarosewich (2003). A re-examination of the rare-earth-element orthophosphate standards in use for electron-microprobe analysis. *Canadian Mineralogist* 41 (1), pp. 221–232.

Drake, M. J. and D. F. Weil (1972). New rare earth element standards for electron microprobe analysis. *Chemical Geology* 10, pp. 179–181.

Engi, M. (2017). Petrochronology based on REE-minerals: Monazite, allanite, xenotime, apatite. *Petrochronology - Methods and Applications: Reviews in Mineralogy & Geochemistry*. Ed. by M. J. Kohn, M. Engi, and P. Lanari. 83. Chantilly, VA: Mineralogical Society of America. Chap. 12, pp. 365–418.

Evans, N. J., J. P. Byrne, J. T. Keegan, and L. E. Dotter (2005). Determination of uranium and thorium in zircon, apatite,and fluorite: Application to laser (U–Th)/He thermochronology. *Journal of Analytical Chemistry* 60 (12), pp. 1159–1165.

Farley, K. A. (2000). Helium diffusion from apatite: General behavior as illustrated by Durango fluorapatite. *Journal of Geophysical Research* 105 (B2), p. 2903.

Farley, K. A. (2002). (U-Th)/He dating: Techniques, calibrations, and applications. *Noble Gases in Geochemistry and Cosmochemistry: Reviews in Mineralogy & Geochemistry*. Ed. by P. D., C. J. Ballentine, and R. Wieler. 47. Washington, DC: Mineralogical Society of America, pp. 819–844.

Farley, K. A. (2007). He diffusion systematics in minerals: Evidence from synthetic monazite and zircon structure phosphates. *Geochimica et Cosmochimica Acta* 71 (16), pp. 4015–4024.

Farley, K. A. and D. F. Stockli (2002). (U-Th)/He dating of phosphates: Apatite, monazite, and xenotime. *Phosphates - Geochemical, Geobiological, and Materials Importance: Reviews in Mineralogy & Geochemistry*. Ed. by M. J. Kohn, J. Rakovan, and J. M. Hughes. 48. Mineralogical Society of America, pp. 559–577.

Fechtig, H. and S. Kalbitzer (1966). The diffusion of argon in potassium-bearing solids. *Potassium Argon Dating*. Berlin Heidelberg: Springer, pp. 68–107.

Fletcher, I. R., N. J. McNaughton, J. A. Aleinikoff, B. Rasmussen, and S. L. Kamo (2004). Improved calibration procedures and new standards for U–Pb and Th–Pb dating of Phanerozoic xenotime by ion microprobe. *Chemical Geology* 209 (3-4), pp. 295–314.

Förster, H. (1998). The chemical composition of REE-Y-Th-U-rich accessory minerals in peraluminous granites of the Erzgebirge-Fichtelgebirge region, Germany. Part II : Xenotime. *American Mineralogist* 83, pp. 1302–1315.

Gautheron, C. and L. Tassan-Got (2010). A Monte Carlo approach to diffusion applied to noble gas/helium thermochronology. *Chemical Geology* 273, pp. 212–224.

Giarola, M., A. Sanson, A. Rahman, G. Mariotto, M. Bettinelli, A. Speghini, and E. Cazzanelli (2011). Vibrational dynamics of YPO_4 and $ScPO_4$ single crystals: An integrated study by polarized Raman spectroscopy and first-principles calculations. *Physical Review B* 83 (22), pp. 1–8.

Grand'Homme, A., E. Janots, V. Bosse, A. M. Seydoux-Guillaume, and R. A. Guedes (2016). Interpretation of U-Th-Pb in-situ ages of hydrothermal monazite-(Ce) and xenotime-(Y): Evidence from a large-scale regional study in clefts from the western alps. *Mineralogy and Petrology*, pp. 1–21.

Grechanovsky, A. E., N. N. Eremin, and V. S. Urusov (2013). Radiation resistance of $LaPO_4$ (monazite structure) and $YbPO_4$ (zircon structure) from data of computer simulation. *Physics of the Solid State* 55 (9), pp. 1929–1935.

Guenthner, W. R., P. W. Reiners, R. A. Ketcham, L. Nasdala, and G. Giester (2013). Helium diffusion in natural zircon: Radiation damage, anisotropy, and the interpretation of zircon (U-TH)/He thermochronology. *American Journal of Science* 313 (3), pp. 145–198.

Hanchar, J. M., R. J. Finch, P. W. O. Hoskin, E. B. Watson, D. J. Cherniak, and A. N. Mariano (2001). Rare earth elements in synthetic zircon. 1. Sythesis and rare earth element and phosphorus doping. *American Mineralogist* 86 (667-680), pp. 667–680.

Harrison, T. M., E. J. Catlos, and J. .-.-M. Montel (2002). U-Th-Pb dating of phosphate minerals. *Phosphates - Geochemical, Geobiological, and Materials Importance: Reviews in Mineralogy & Geochemistry*. Ed. by M. J. Kohn, J. Rakovan, and J. M. Hughes. 48. Chantilly, VA: Mineralogical Society of America, pp. 524–558.

Hawkins, D. P. and S. A. Bowring (1997). U-Pb systematics of monazite and xenotime: case studies from the Paleoproterozoic of the Grand Canyon, Arizona. *Contributions to Mineralogy and Petrology* 127 (1-2), pp. 87–103.

Hazen, R. M. and L. M. Finger (1979). Crystal structure and compressibility of zircon at high pressure. *American Mineralogist* 64, pp. 196–201.

Hetherington, C. J., M. J. Jercinovic, M. L. Williams, and K. Mahan (2008). Understanding geologic processes with xenotime: Composition, chronology, and a protocol for electron probe microanalysis. *Chemical Geology* 254 (3-4), pp. 133–147.

Hildebrand, P. R. (1998). Tectonic significance of 24 Ma crustal melting in the eastern Hindu Kush, Pakistan. *Geology* 26 (10), pp. 871–874.

Hildebrand, P. R., S. R. Noble, M. P. Searle, D. J. Waters, and R. R. Parrish (2001). Old origin for an active mountain range: Geology and geochronology of the Eastern Hindu Kush, Pakistan. *Bulletin of the Geological Society of America* 113 (5), pp. 625–639.

Horne, A. M., M. C. van Soest, K. V. Hodges, A. Tripathy-Lang, and J. K. Hourigan (2016). Integrated single crystal laser ablation U/Pb and (U-Th)/He dating of detrital accessory minerals - Proof-of-concept studies of titanites and zircons from the Fish Canyon tuff. *Geochimica et Cosmochimica Acta* 178, pp. 106–123.

Hourigan, J. K., P. W. Reiners, and M. T. Brandon (2005). U-Th zonation-dependent alpha-ejection in (U-Th)/He chronometry. *Geochimica et Cosmochimica Acta* 69 (13), pp. 3349–3365.

Idleman, B. D., P. K. Zeitler, and K. T. McDannell (2018). Characterization of helium release from apatite by continuous ramped heating. *Chemical Geology* 476, pp. 223–232.

Jarosewich, E. and L. A. Boatner (1991). Rare-Earth element reference samples for electron microprobe analysis. *Geostandards Newsletter* 15 (2), pp. 397–399.

Lenz, C., L. Nasdala, D. Talla, C. Hauzenberger, R. Seitz, and U. Kolitsch (2015). Laser-induced REE^{3+} photoluminescence of selected accessory minerals - An “advantageous artefact" in Raman spectroscopy. *Chemical Geology* 415, pp. 1–16.

Liu, Z., F. Wu, C. Guo, Z. Zhao, J. Yang, and J. Sun (2011). In situ U-Pb dating of xenotime by laser ablation (LA)-ICP-MS. *Chinese Science Bulletin* 56 (27), pp. 2948–2956.

Lovera, O. M., M. Grove, T. M. Harrison, and K. I. Mahon (1997). Systematic analysis of K-feldspar $^{40}Ar/^{39}Ar$ step heating results: I. Significance of activation energy determinations. *Geochimica et Cosmochimica Acta* 61 (15), pp. 3171–3192.

Lovera, O. M. and F. M. Richter (1989). The $^{40}Ar/^{39}Ar$ thermochronometry for slowly cooled samples having a distribution of diffusion domain sizes. *Journal of Geophysical Research* 94 (B12), pp. 17917–17935.

Ludwig, K. R. (2003). Mathematical–statistical treatment of data and errors for $^{230}Th/U$ Geochronology. *Uranium-Series Geochemistry: Reviews in Mineralogy & Geochemistry*. Ed. by B. Bourdon, G. M. Henderson, C. C. Lundstrom, and S. P. Turner. 52. Chantilly, VA: Mineralogical Society of America, pp. 631–656.

Meesters, A. G. C. A. and T. J. Dunai (2002). Solving the production–diffusion equation for finite diffusion domains of various shapes. *Chemical Geology* 186 (3-4), pp. 333–344.

Meldrum, A., L. A. Boatner, and R. C. Ewing (2000). A comparison of radiation effects in crystalline ABO4-type phosphates and silicates. *Mineralogical Magazine* 64 (2), pp. 185–194.

Meldrum, A., L. A. Boatner, W. J. Weber, and R. C. Ewing (1998). Radiation damage in zircon and monazite. *Geochimica et Cosmochimica Acta* 62 (14), pp. 2509–2520.

Meldrum, A., L. Boatner, and R. Ewing (1997). Displacive radiation effects in the monazite- and zircon-structure orthophosphates. *Physical Review B* 56 (21), pp. 13805–13814.

Nasdala, L., J. Gotze, J. M. Hanchar, M. Gaft, and M. R. Krbetschek (2004). Luminescence techniques in Earth Sciences. *EMU Notes in Mineralogy* 6, pp. 43–91.

Nasdala, L., M. Wenzel, G. Vavra, G. Irmer, T. Wenzel, and B. Kober (2001). Metamictisation of natural zircon: Accumulation versus thermal annealing of radioactivity-induced damage. *Contributions to Mineralogy and Petrology* 141 (2), pp. 125–144.

Ni, Y., J. M. Hughes, and A. N. Mariano (1995). Crystal chemistry of the monazite and xenotime structures. *American Mineralogist* 80, pp. 21–26.

Ouchani, S., J. C. Dran, and J. Chaumont (1998). Exfoliation and diffusion following helium ion implantation in fluorapatite: implications for radiochronology and radioactive waste disposal. *Applied Geochemistry* 13 (6), pp. 707–714.

Paton, C., J. D. Woodhead, J. C. Hellstrom, J. M. Hergt, A. Greig, and R. Maas (2010). Improved laser ablation U-Pb zircon geochronology through robust downhole fractionation correction. *Geochemistry, Geophysics, Geosystems* 11 (3).

Pearson, R. K. (2001). *Exploring Data in Engineering, the Sciences, and Medicine*. Oxford Univ. Press.

Peterman, E. M., J. K. Hourigan, and M. Grove (2014). Experimental and geologic evaluation of monazite (U–Th)/He thermochronometry: Catnip Sill, Catalina Core Complex, Tucson, AZ. *Earth and Planetary Science Letters* 403 (C), pp. 48–55.

Reich, M., R. C. Ewing, T. A. Ehlers, and U. Becker (2007). Low-temperature anisotropic diffusion of helium in zircon: Implications for zircon (U-Th)/He thermochronometry. *Geochimica et Cosmochimica Acta* 71 (12), pp. 3119–3130.

Reiners, P. W. and M. T. Brandon (2006). Using thermochronology to understand orogenic erosion. *Annual Review of Earth and Planetary Sciences* 34 (1), pp. 419–466.

Reiners, P. W. and K. A. Farley (1999). Helium diffusion and (U-Th)/He thermochronometry of titanite. *Mineralogical Magazine* 62A (2), pp. 1249–1250.

Reiners, P. W., T. L. Spell, S. Nicolescu, and K. A. Zanetti (2004). Zircon (U-Th)/He thermochronometry: He diffusion and comparisons with ^{40}Ar/^{39}Ar dating. *Geochimica et Cosmochimica Acta* 68 (8), pp. 1857–1887.

Ruschel, K., L. Nasdala, A. Kronz, J. M. Hanchar, D. M. Többens, R. Škoda, F. Finger, and A. Möller (2012). A Raman spectroscopic study on the structural disorder of monazite-(Ce). *Mineralogy and Petrology* 105 (1-2), pp. 41–55.

Saadoune, I., J. A. Purton, and N. H. de Leeuw (2009). He incorporation and diffusion pathways in pure and defective zircon $ZrSiO_4$: A density functional theory study. *Chemical Geology* 258 (3-4), pp. 182–196.

Shannon, R. D. (1976). Revised effective ionic radii and systematic studies of interatomic distances in halides and chalcogenides. *Acta Crystallographica Section A* 32 (5), pp. 751–767.

Shuster, D. L., R. M. Flowers, and K. A. Farley (2006). The influence of natural radiation damage on helium diffusion kinetics in apatite. *Earth and Planetary Science Letters* 249 (3-4), pp. 148–161.

Shuster, D. L. and K. A. Farley (2009). The influence of artificial radiation damage and thermal annealing on helium diffusion kinetics in apatite. *Geochimica et Cosmochimica Acta* 73 (1), pp. 183–196.

Shuster, D. L., K. A. Farley, J. M. Sisterson, and D. S. Burnett (2003). Quantifying the diffusion kinetics and spatial distributions of radiogenic ^{4}He in minerals containing proton-induced ^{3}He. *Earth and Planetary Science Letters* 217 (1-2), pp. 19–32.

Spear, F. S. and J. M. Pyle (2002). Apatite, monazite, and xenotime in metamorphic rocks. *Phosphates - Geochemical, Geobiological, and Materials Importance: Reviews in Mineralogy & Geochemistry*. Ed. by M. J. Kohn, J. Rakovan, and J. M. Hughes. 48. Chantilly, VA: Mineralogical Society of America, pp. 293–335.

Stanley, J. R. and R. M. Flowers (2016). Dating kimberlite emplacement with zircon and perovskite (U-Th)/He geochronology. *Geochemistry Geophysics Geosystems* 17, pp. 4517–4533. arXiv: arXiv:1605.08479.

Švecová, E., R. Čopjaková, Z. Losos, R. Škoda, L. Nasdala, and J. Cícha (2016). Multi-stage evolution of xenotime-(Y) from Písek pegmatites, Czech Republic: An electron probe micro-analysis and Raman spectroscopy study. *Mineralogy and Petrology* 110 (6), pp. 747–765.

Tripathy-Lang, A., K. V. Hodges, B. D. Monteleone, and M. C. van Soest (2013). Laser (U-Th)/He thermochronology of detrital zircons as a tool for studying surface processes in modern catchments. *Journal of Geophysical Research: Earth Surface* 118 (3), pp. 1333–1341.

Vallini, D A and Rasmussen, B and Krapež, B and Fletcher, I R and McNaughton, N J (2005). Microtextures, geochemistry and geochronology of authigenic xenotime: constraining the cementation history of a Palaeoproterozoic metasedimentary sequence. *Sedimentology* 52 (1), pp. 101–122.

Vallini, D and Rasmussen, B and Krapež, B and Fletcher, I R and McNaughton, N J (2002). Obtaining diagenetic ages from metamorphosed sedimentary rocks: U-Pb dating of unusually coarse xenotime cement in phosphatic sandstone. *Geology* 30 (12), pp. 1083–1086.

van Soest, M. C., B. D. Monteleone, K. V. Hodges, and J. W. Boyce (2011). Laser depth profiling studies of helium diffusion in Durango fluorapatite. *Geochimica et Cosmochimica Acta* 75 (9), pp. 2409–2419.

Wendt, I. and C. Carl (1991). The statistical distribution of the mean squared weighted deviation. *Chemical Geology* 86, pp. 275–285.

York, D., N. M. Evensen, M. L. Martinez, and J. De Basabe Delgado (2004). Unified equations for the slope, intercept, and standard errors of the best straight line. *American Journal of Physics* 72 (3), pp. 367–375.

Chapter 6

PROSPECTUS

The chapters of this dissertation improve of our understanding of radiation damage and helium diffusion in a well-loved mineral chronometer and demonstrate the potential of a new helium chronometer. Perhaps just as important, the studies in these chapters highlight the promises and limitations of our current experimental and thermochronological methods. In these final sections, I consider the state of (U-Th)/He thermochronology in the context of my findings and discuss future avenues for research.

6.1 Zircon (U-Th)/He Thermochronology

Much of the rock record that could be used to study upper crustal processes has been removed by erosion or thermally overprinted, especially in ancient (Paleozoic - Proterozoic) mountain belts and cratonic interiors (Enkelmann and Garver, 2016; Flowers, 2009). Low temperature thermochronology of zircon and other accessory minerals in basement rocks are some of the few tools available that can help us understand tectonic and climate-driven exhumation in these environments (Reiners et al., 2017). Many researchers have noted that helium thermochronometers − particularly zircon − are strongly affected by radiation damage (Baughman et al., 2017; Guenthner et al., 2013; Shuster et al., 2006). This geologic problem has driven researchers to develop various damage-diffusivity models to help interpret the thermal significance of (U-Th)/He date-damage correlations (Flowers et al., 2009; Gautheron et al., 2009; Guenthner et al., 2013). Chapters 2, 3, and 4 of this dissertation, discussed below, we have attempted through empirical and microanalytical study to investigate the complex and often competing effects of radiation damage, radionu-

clide zoning, crystallographic anisotropy, and crystal chemistry on helium diffusion in zircon (Anderson et al., 2017). Results of these studies indicate that applications of the popular zircon damage-diffusivity model ZRDAAM to ancient rocks have outpaced our understanding of the underlying geochemical kinetics upon which the model is based.

In Chapter 2, we present an empirical study designed to test the effectiveness of ZRDAAM (Anderson et al., 2017). This study focuses on the McClure Mountain syenite of south-central Colorado, a rock that is chock-full of mineral-isotopic and fission track-based thermochronometers that make it, arguably, one of the best rocks available for thermal modeling. We modeled a protracted thermal history for the syenite and used this t-T history to place constraints on the relationship between alpha dose and zircon helium closure temperature. Based on this model, we concluded that ZRDAAM does not accurately predict helium closure temperatures for a majority of our dated zircon grains.

Shortly after publication of Chapter 2, Weisberg and colleagues 2018 published a paper in *Chemical Geology* that refuted our preferred thermal history for the McClure Mountain syenite. The authors instead favored a more complex thermal history characterized by two episodes of burial reheating based on their interpretations of two non-conformities in the Wet Mountains located east of the syenite on the opposite site of the Ilse fault. My co-authors and myself published a comment in response disagreeing with their conclusions (Anderson et al., 2018). In our comment, we showed that ZRDAAM cannot satisfactorily explain the syenite's zircon (U-Th)/He date dispersion given either proposed thermal history or convincingly differentiate between the two, further demonstrating the ineffectiveness of ZRDAAM for the case of the McClure Mountain syenite. The details our arguments and those of the Colorado research group can be found in the comment-and-reply pair published by *Chemical Geology*, and I will not rehash them further here (Anderson et al., 2018; Weisberg et al., 2018b).

As initially proposed in Chapter 2 and reiterated in our published comment, intracrystalline variations in helium diffusion due to radiation damage zoning could, in part, explain the discrepancies between our empirical findings and ZRDAAM predictions for the syenite. ZRDAAM, like most damage-diffusivity models assumes a single diffusivity for a zircon crystal based on its bulk U and Th contents (Guenthner et al., 2013). Given zircon's penchant for complex U and Th zoning, this simplifying assumption may not be valid for many, if not most, ancient zircons.

In Chapter 3, we further investigated the potential impact of damage zoning by producing detailed, quantitative radiation damage maps of zircon crystals from the Lyon Mountain Granite using Raman spectroscopy. Modeled helium diffusivity maps based on these results document complex intracrystalline variations in diffusivity due to the heterogeneous distribution of radiation damage that cannot be reduced to a simple 1D problem. These maps predict that helium diffusion in higher damage zones within the LMG zircons is 25 times faster than in lower damage zones. The magnitude of difference may be even greater in zircons with stronger radiation damage zoning than exhibited by the LMG crystals. These results raise serious questions. How much do intracrystalline variations affect the bulk closure temperature for helium in zircon? What magnitude of variations matter? Are bulk closure temperatures calculated from the mean or median modeled diffusivity geologically meaningful? Future work could use 2D and 3D diffusivity models based on Raman maps to better address these questions.

Our empirical and Raman mapping together studies highlight the limitations of damage-diffusivity models based on a zircon's bulk isotopic composition. Future studies intent on evaluating thermal histories of ancient rocks may be better served by combining conventional bulk thermochronological data with microanalytical work such as laser depth profiling of helium diffusive loss profiles and laser ablation helium mapping coupled with laser ablation

U and Th zoning characterization (Danišík et al., 2017) and/or Raman data. Results paired with 1D, 2D, or 3D helium production-diffusion models (depending on the method and zoning complexity) could be used to more effectively evaluate a sample's thermal history.

While Raman mapping allows us to evaluate possible variations in helium diffusivity based on a zircon's present-day radiation damage distribution, it is not always easy to extrapolate Raman data back to the time of zircon helium closure. Doing so requires not only knowledge of a sample's U and Th contents, its approximate bulk helium closure age, and its thermal history, but also its annealing history. Annealing kinetics of alpha radiation damage at near-surface temperatures on geologic time scales is still an area of active research that merits further investigation (Jonckheere et al., 2019). One challenge associated with using Raman spectroscopy for damage characterization is that Raman peak width data does not fully capture all the structural changes associated with annealing (Murakami et al., 1991; Zhang et al., 2000). While the method tells us something about local bonding environments in minerals, it does not provide information about a sample's long-range order which likely controls bulk helium diffusivity. Understanding how different annealing mechanisms affect helium systematics and how to properly identify them is one of the next fundamental questions for zircon (U-Th)/He thermochronology (Ginster et al., 2019). This problem is especially relevant for applications to geologic settings that have experienced thermal disturbances.

In addition to the effects of radiation damage zoning and the potential effects of annealing on zircon helium kinetics, in Chapter 4 we present evidence for strong crystallographically-controlled variations in helium diffusivity in highly crystalline zircon. Study findings imply that zircons with different crystal morphologies should have different closure temperatures and record different portions of a rock's thermal history. This suggests that diffusive anisotropy likely contributes to zircon (U-Th)/He date dispersion in samples with varied

grain aspect ratios that cooled through helium closure prior to the accumulation of significant amounts of radiation damage. Current thermo-kinetic models do not properly account for diffusive anisotropy. These models, however, could be adapted by incorporating diffusion models already developed by others (Cherniak et al., 2009; Gautheron and Tassan-Got, 2010) or by simply adjusting modeled diffusion geometries based on grain aspect ratios. Importantly, our laser depth profile results also demonstrate that classic step-wise degassing experiments, though fundamental and valuable scientific contributions, can systematically underestimate the role of crystallography on helium diffusion in anisotropic minerals.

Chapter 4 also provides evidence for sample-to-sample variations in helium diffusivity that are not readily explained by crystallography, radiation damage, or annealing. We attribute these differences to the effects of crystal chemistry. Future work should evaluate this hypothesis through a systematic investigation of helium diffusion in zircon crystals with similar damage contents, annealing histories, and crystal morphologies but with different crystal chemistries.

At times my colleagues and I have joked that this dissertation represents the downfall of zircon (U-Th)/He thermochronology. I would argue that that is not the case. Like most mineral-isotopic chronometers, zircon is a complex system − more complex than what some researchers are currently willing to recognize. Some challenges, like diffusive anisotropy, should be relatively easy to account for. Others, like the effects of complicated radiation damage zoning, may be more intractable, although coupling new microanalytical techniques with 2D and 3D helium production-diffusivity models as discussed above provide some hope. To what extent each of the factors discussed influence the closure temperature for helium in zircon invariably depends not only on the a zircon's morphology and internal characteristics but also the geologic setting. In moderately to rapidly cooled environments many of the complexities discussed are unlikely to significantly affect geologic interpretations. Thermal

histories derived solely from overdispersed zircon (U-Th)/He datasets in ancient, slowly cooled and thermal disturbed environments, however, should be considered critically. Pairing zircon (U-Th)/He dates with other thermochronometers would also help to provide more context for interpreting overdispersed zircon (U-Th)/He datasets.

Beyond the need to further improve our understanding of helium diffusion in zircon and acknowledge the limitations of some conventional methods, I would argue that one of the greatest challenges facing low temperature thermochronology is current thermal modeling practices. Too often in the literature individual thermochronometric data points are inappropriately "binned" and geologic hypotheses are incorporated into models as *t*-T constraints through which models are force-fit (e.g. Ketcham et al., 2018; Weisberg et al., 2018a). Such practices effectively pre-determine model outputs. While it is useful to run forward or inverse models with *t*-T constraints to determine whether a hypothesized thermal history is consistent with the thermochronometric data at hand, more researchers need to recognize that other thermal histories could potentially satisfy the data. Elsewise, if there is indeed indisputable geologic evidence that tightly constrains a sample's thermal history, what is the point in collecting thermochronometric data and using thermal models in the first place?

6.2 Xenotime (U-Th)/He Thermochronology

The (U-Th)/He dates and bulk diffusion study presented in Chapter 5 for xenotime FPX-1 successfully demonstrate that xenotime has the potential to be a powerful (U-Th)/He chronometer (Anderson et al., 2019). The lessons learned in Chapters 2 through 4, however, emphasize that the work presented here is simply the beginning. First and foremost, a combination or experimental and empirical work is needed to evaluate whether or not

the closure temperature determined for xenotime FPX-1 is generally applicable to other natural xenotimes. Future studies should focus on characterizing the effects of crystal chemistry (different REE and U+Th contents), crystallography, and radiation damage on helium diffusion in xenotime. Given natural xenotime's notorious compositional variability, new techniques such as measuring helium release spectra during (U-Th)/He dating (Idleman et al., 2018) could be used to evaluate each sample's bulk closure temperature directly, forgoing the need for to characterize each dated crystal's chemistry.

References

Anderson, A. J., K. V. Hodges, and M. C. van Soest (2017). Empirical constraints on the effects of radiation damage on helium diffusion in zircon. *Geochimica et Cosmochimica Acta* 218, pp. 308–322.

Anderson, A. J., K. V. Hodges, and M. C. van Soest (2018). Comment on 'Distinguishing slow cooling versus multiphase cooling and heating in zircon and apatite (U-Th)/He datasets: The case of the McClure Mountain syenite standard' by Weisberg, Metcalf, and Flowers. *Chemical Geology* 498, pp. 150–152.

Anderson, A. J., K. V. Hodges, M. C. van Soest, and J. M. Hanchar (2019). Helium diffusion in natural xenotime. *Geochemistry, Geophysics, Geosystems* 20, pp. 417–433.

Baughman, J., R. M. Flowers, J. R. Metcalf, and T. Dhansay (2017). Influence of radiation damage on titanite He diffusion kinetics. *Geochimica et Cosmochimica Acta* 205, pp. 50–64.

Cherniak, D. J., E. B. Watson, and J. B. Thomas (2009). Diffusion of helium in zircon and apatite. *Chemical Geology* 268, pp. 155–166.

Danišík, M., B. I. A. McInnes, C. L. Kirkland, B. J. McDonald, N. J. Evans, and T. Becker (2017). Seeing is believing: Visualization of He distribution in zircon and implications for thermal history reconstruction on single crystals. *Science Advances* 3 (2), e1601121.

Enkelmann, E. and J. I. Garver (2016). Low-temperature thermochronology applied to ancient settings. *Journal of Geodynamics* 93, pp. 17–30.

Flowers, R. M. (2009). Exploiting radiation damage control on apatite (U-Th)/He dates in cratonic regions. *Earth and Planetary Science Letters* 277, pp. 148–155.

Flowers, R. M., R. A. Ketcham, D. L. Shuster, and K. A. Farley (2009). Apatite (U-Th)/He thermochronometry using a radiation damage accumulation and annealing model. *Geochimica et Cosmochimica Acta* 73 (8), pp. 2347–2365.

Gautheron, C. and L. Tassan-Got (2010). A Monte Carlo approach to diffusion applied to noble gas/helium thermochronology. *Chemical Geology* 273, pp. 212–224.

Gautheron, C., L. Tassan-Got, J. Barbarand, and M. Pagel (2009). Effect of alpha-damage annealing on apatite (U–Th)/He thermochronology. *Chemical Geology* 266 (3-4), pp. 157–170.

Ginster, U., P. W. Reiners, L. Nasdala, and C. C. N (2019). Annealing kinetics of radiation damage in zircon. *Geochimica et Cosmochimica Acta* 249, pp. 225–246.

Guenthner, W. R., P. W. Reiners, R. A. Ketcham, L. Nasdala, and G. Giester (2013). Helium diffusion in natural zircon: Radiation damage, anisotropy, and the interpretation of zircon (U-TH)/He thermochronology. *American Journal of Science* 313 (3), pp. 145–198.

Idleman, B. D., P. K. Zeitler, and K. T. McDannell (2018). Characterization of helium release from apatite by continuous ramped heating. *Chemical Geology* 476, pp. 223–232.

Jonckheere, R., D. Heinz, B. R. Hacker, D. Rafaja, and L. Ratschbacher (2019). A borehole investigation of zircon radiation damage annealing. *Terra Nova* In press.

Ketcham, R. A., P. van der Beek, J. Barbarand, M. Bernet, and C. Gautheron (2018). Reproducibility of thermal history reconstruction From apatite fission-track and (U-Th)/He data. *Geochemistry, Geophysics, Geosystems* 19 (8), pp. 2411–2436.

Murakami, T., B. C. Chakoumakos, R. C. Ewing, G. R. Lumpkin, and W. J. Weber (1991). Alpha-decay event damage in zircon. *American Mineralogist* 76, pp. 1510–1532.

Reiners, P. W., R. W. Carlson, P. R. Renne, K. M. Cooper, D. E. Granger, N. M. McLean, and B. Schoene (2017). The (U-Th)/He System. *Geochronology and Thermochronology*. John Wiley & Sons Ltd. Chap. 11, pp. 291–363.

Shuster, D. L., R. M. Flowers, and K. A. Farley (2006). The influence of natural radiation damage on helium diffusion kinetics in apatite. *Earth and Planetary Science Letters* 249 (3-4), pp. 148–161.

Weisberg, W. R., J. R. Metcalf, and R. M. Flowers (2018a). Distinguishing slow cooling versus multiphase cooling and heating in zircon and apatite (U-Th)/He datasets: The case of the McClure Mountain syenite standard. *Chemical Geology* 485, pp. 90–99.

Weisberg, W. R., J. R. Metcalf, and R. M. Flowers (2018b). Response to comment on "Distinguishing slow cooling versus multiphase cooling and heating in zircon and apatite (U-Th)/He datasets: The case of the McClure Mountain syenite standard". *Chemical Geology* 498, pp. 153–156.

Zhang M S, E. K. H., G. C. Capitani, H. Leroux, A. M. Clark, J. Schluter, and R. C. Ewing (2000). Annealing of α-decay damage in zircon: A Raman spectroscopic study. *Journal of Physics: Condensed Matter* 12, pp. 3131–3148.

REFERENCES

Aleinikoff, J. N. and R. I. Grauch (1990). U-Pb geochronologic constraints on the origin of a unique monazite-xenotime gneiss, Hudson Highlands, New York. *American Journal of Science* 290, pp. 522–546.

Aleinikoff, J. N., R. I. Grauch, F. K. Mazdab, L. Kwak, C. M. Fanning, and S. L. Kamo (2012a). Origin of an unusual monazite-xenotime gneiss, Hudson Highlands, New York: SHRIMP U-Pb geochronology and trace element geochemistry. *American Journal of Science* 312 (7), pp. 723–765.

Aleinikoff, J. N., T. S. Hayes, K. V. Evans, F. K. Mazdab, R. M. Pillers, and C. M. Fanning (2012b). SHRIMP U-Pb ages of xenotime and monazite from the Spar Lake red bed-associated Cu-Ag deposit, western Montana: Implications for ore genesis. *Economic Geology* 107, pp. 1251–1274.

Aleinikoff, J. N., K. Lund, and C. M. Fanning (2015). SHRIMP U-Pb and REE data pertaining to the origins of xenotime in Belt Supergroup rocks: Evidence for ages of deposition, hydrothermal alteration, and metamorphism. *Canadian Journal of Earth Sciences* 52 (9), pp. 722–745.

Aleinikoff, J. N., J. F. Slack, K. Lund, K. V. Evans, C. M. Fanning, F. K. Mazdab, J. L. Wooden, and R. M. Pillers (2012c). Constraints on the Timing of Co-Cu ± Au Mineralization in the Blackbird District, Idaho, Using SHRIMP U-Pb ages of monazite and xenotime plus zircon ages of related mesoproterozoic orthogneisses and metasedimentary rocks. *Economic Geology* 107, pp. 1143–1175.

Alexander, E. C. J., G. M. Mickelson, and M. A. Lanphere (1978). MMhb-1: A new ^{40}Ar-^{39}Ar dating standard. *Short Papers of the Fourth International Conference, Geochronology, Cosmochronology, and Isotope Geology*. 78-701. U.S. Geological Survey, pp. 6–8.

Allen, C. M. and I. H. Campbell (2012). Identification and elimination of a matrix-induced systematic error in LA–ICP–MS ^{206}Pb/^{238}U dating of zircon. *Chemical Geology* 332-333, pp. 157–165.

Andersen, T. (2002). Correction of common lead in U-Pb analyses that do not report ^{204}Pb. *Chemical Geology* 192, pp. 59–79.

Anderson, A. J., K. V. Hodges, and M. C. van Soest (2017). Empirical constraints on the effects of radiation damage on helium diffusion in zircon. *Geochimica et Cosmochimica Acta* 218, pp. 308–322.

Anderson, A. J., K. V. Hodges, and M. C. van Soest (2018). Comment on 'Distinguishing slow cooling versus multiphase cooling and heating in zircon and apatite (U-Th)/He datasets: The case of the McClure Mountain syenite standard' by Weisberg, Metcalf, and Flowers. *Chemical Geology* 498, pp. 150–152.

Anderson, A. J., K. V. Hodges, M. C. van Soest, and J. M. Hanchar (2019). Helium diffusion in natural xenotime. *Geochemistry, Geophysics, Geosystems* 20, pp. 417–433.

Ault, A. K. and R. M. Flowers (2012). Is apatite U-Th zonation information necessary for accurate interpretation of apatite (U-Th)/ He thermochronometry data? *Geochimica et Cosmochimica Acta* 79, pp. 60–78.

Ault, A. K., W. R. Guenthner, A. C. Moser, G. H. Miller, and K. A. Refsnider (2018). Zircon grain selection reveals (de)coupled metamictization, radiation damage, and He diffusivity. *Chemical Geology* 490, pp. 1–12.

Baksi, A. K., D. A. Archibald, and E. Farrar (1996). Intercalibration of ^{40}Ar/^{39}Ar dating standards. *Chemical Geology* 129 (3-4), pp. 307–324.

Bargnesi, E. A., D. F. Stockli, J. K. Hourigan, and C. Hager (2016). Improved accuracy of zircon (U-Th)/He ages by rectifying parent nuclide zonation with practical methods. *Chemical Geology* 426, pp. 158–169.

Baughman, J., R. M. Flowers, J. R. Metcalf, and T. Dhansay (2017). Influence of radiation damage on titanite He diffusion kinetics. *Geochimica et Cosmochimica Acta* 205, pp. 50–64.

Bea, F. (1996). Residence of REE, Y, Th and U in granites and crustal protoliths; implications for the chemistry of crustal melts. *Journal of Petrology* 37 (3), pp. 521–552.

Bengtson, A., R. C. Ewing, and U. Becker (2012). He diffusion and closure temperatures in apatite and zircon: A density functional theory investigation. *Geochimica et Cosmochimica Acta* 86, pp. 228–238.

Bernet, M. (2009). A field-based estimate of the zircon fission-track closure temperature. *Chemical Geology* 259 (3-4), pp. 181–189.

Black, L. P. and B. L. Gulson (1978). The age of the Mud Tank Carbonatite, Strangways Range, Northern Territory. *BMR Journal of Australian Geology & Geophysics* 3, pp. 227–232.

Black, L. P. et al. (2004). Improved ^{206}Pb/^{238}U microprobe geochronology by the monitoring of a trace-element-related matrix effect; SHRIMP, ID–TIMS, ELA–ICP–MS and oxygen

isotope documentation for a series of zircon standards. *Chemical Geology* 205 (1-2), pp. 115–140.

Boatner, L. A. (2002). Synthesis, structure, and properties of monazite, pretulite, and xenotime. *Phosphates - Geochemical, Geobiological, and Materials Importance: Review in Mineralogy & Geochemistry*. Ed. by M. J. Kohn, J. Rakovan, and J. M. Hughes. Washington, DC: Mineralogical Society of America, pp. 87–121.

Bowring, S. A. and M. D. Schmitz (2003). High-Precision U-Pb Zircon Geochronology and the Stratigraphic Record. *Zircon: Reviews in Mineralogy & Geochemistry*. Ed. by J. M. Hanchar and P. W. O. Hoskin. Chantilly, VA: Mineralogical Society of America, pp. 305–326.

Boyce, J. W., K. V. Hodges, W. J. Olszewski, and M. J. Jercinovic (2005). He diffusion in monazite: Implications for (U-Th)/He thermochronometry. *Geochemistry, Geophysics, Geosystems* 6 (12), pp. 1–12.

Brandon, K. A., T. M. Roden-Tice, and J. I. Garver (1998). Late Caneozoic exhumation of the Cascadia accretionary wedge in the Olympic Mountains, northwest Washington State. *Geological Society of America Bulletin* 110 (8), pp. 985–1009.

Cherniak, D. J. (2006). Pb and rare earth element diffusion in xenotime. *Lithos* 88 (1-4), pp. 1–14.

Cherniak, D. J. and E. B. Watson (2011). Helium diffusion in rutile and titanite, and consideration of the origin and implications of diffusional anisotropy. *Chemical Geology* 288, pp. 149–161.

Cherniak, D. J., E. B. Watson, and J. B. Thomas (2009). Diffusion of helium in zircon and apatite. *Chemical Geology* 268, pp. 155–166.

Cherniak, D. J. and E. B. Watson (2013). Diffusion of helium in natural monazite, and preliminary results on He diffusion in synthetic light rare earth phosphates. *American Mineralogist* 98 (8-9), pp. 1407–1420.

Chew, D. M., J. A. Petrus, and B. S. Kamber (2014). U-Pb LA-ICPMS dating using accessory mineral standards with variable common Pb. *Chemical Geology* 363, pp. 185–199.

Condon, D. J. and M. D. Schmitz (2013). One Hundred Years of Isotope Geochronology, and Counting. *Elements* 9 (1), pp. 15–17.

Corfu, F., J. M. Hanchar, P. W. O. Hoskin, and P. Kinny (2003). Atlas of Zircon Textures. *Zircon: Reviews in Mineralogy & Geochemistry*. Ed. by J. M. Hanchar and P. W. O. Hoskin. Chantilly, VA: Mineralogical Society of America, pp. 469–500.

Coyle, D. A. and G. A. Wagner (1998). Positioning the titanite fission-track partial annealing zone. *Chemical Geology* 149 (1-2), pp. 117–125.

Crohn, P. W. and D. H. Moore (1984). The Mud Tank Carbonatite, Strangways Range, central Australia. *Journal of Australian Geology Geophysics* 9, pp. 13–18.

Currie, K. L., J. Knutson, and P. A. Temby (1992). The Mud Tank carbonatite complex, central Australia − an example of metasomatism at mid-crustal levels. *Contributions to Mineralogy and Petrology* 109, pp. 326–339.

Danišík, M., B. I. A. McInnes, C. L. Kirkland, B. J. McDonald, N. J. Evans, and T. Becker (2017). Seeing is believing: Visualization of He distribution in zircon and implications for thermal history reconstruction on single crystals. *Science Advances* 3 (2), e1601121.

Dawson, P., M. M. Hargreave, and G. R. Wilkinson (1971). The vibrational spectrum of zircon ($ZrSiO_4$). *Journal of Physics C: Solid State Physics* 4, pp. 240–256.

Dodson, M. H. (1973). Closure temperature in cooling geochronological and petrological systems. *Contributions to Mineralogy and Petrology* 40 (3), pp. 259–274.

Donovan, J. J., J. M. Hanchar, P. M. Picolli, M. D. Schrier, L. A. Boatner, and E. Jarosewich (2002). Contamination in the rare-earth element orthophosphate reference samples. *Journal of Research of the National Institute of Standards and Technology* 107 (6), pp. 693–701.

Donovan, J. J., J. M. Hanchar, P. M. Picolli, M. D. Schrier, L. A. Boatner, and E. Jarosewich (2003). A re-examination of the rare-earth-element orthophosphate standards in use for electron-microprobe analysis. *Canadian Mineralogist* 41 (1), pp. 221–232.

Drake, M. J. and D. F. Weil (1972). New rare earth element standards for electron microprobe analysis. *Chemical Geology* 10, pp. 179–181.

Ehlers, T. A. and K. A. Farley (2003). Apatite (U-Th)/He thermochronometry: Methods and applications to problems in tectonic and surface processes. *Earth and Planetary Science Letters* 206 (1-2), pp. 1–14.

Engi, M. (2017). Petrochronology based on REE-minerals: Monazite, allanite, xenotime, apatite. *Petrochronology - Methods and Applications: Reviews in Mineralogy & Geo-*

chemistry. Ed. by M. J. Kohn, M. Engi, and P. Lanari. 83. Chantilly, VA: Mineralogical Society of America. Chap. 12, pp. 365–418.

Enkelmann, E. and J. I. Garver (2016). Low-temperature thermochronology applied to ancient settings. *Journal of Geodynamics* 93, pp. 17–30.

Evans, N. J., J. P. Byrne, J. T. Keegan, and L. E. Dotter (2005). Determination of uranium and thorium in zircon, apatite,and fluorite: Application to laser (U–Th)/He thermochronology. *Journal of Analytical Chemistry* 60 (12), pp. 1159–1165.

Evans, N. J., B. I. A. McInnes, B. McDonald, M. Danišík, T. Becker, P. Vermeesch, M. Shelley, E. Marillo-Sialer, and D. B. Patterson (2015). An in situ technique for (U–Th–Sm)/He and U–Pb double dating. *J. Anal. At. Spectrom.* 30 (7), pp. 1636–1645.

Ewing, R. C., A. Meldrum, L. Wang, W. J. Weber, and L. R. Corrales (2003). Radiation effects in zircon. *Zircon: Reviews in Mineralogy & Geochemistry*. Ed. by J. M. Hanchar and P. W. O. Hoskin. 53. Chantilly, VA: Mineralogical Society of America, pp. 387–425.

Farley, K. A. (2000). Helium diffusion from apatite: General behavior as illustrated by Durango fluorapatite. *Journal of Geophysical Research* 105 (B2), p. 2903.

Farley, K. A. (2002). (U-Th)/He dating: Techniques, calibrations, and applications. *Noble Gases in Geochemistry and Cosmochemistry: Reviews in Mineralogy & Geochemistry*. Ed. by P. D., C. J. Ballentine, and R. Wieler. 47. Washington, DC: Mineralogical Society of America, pp. 819–844.

Farley, K. A. (2007). He diffusion systematics in minerals: Evidence from synthetic monazite and zircon structure phosphates. *Geochimica et Cosmochimica Acta* 71 (16), pp. 4015–4024.

Farley, K. A., D. L. Shuster, and R. A. Ketcham (2011). U and Th zonation in apatite observed by laser ablation ICPMS, and implications for the (U-Th)/He system. *Geochimica et Cosmochimica Acta* 75 (16), pp. 4515–4530.

Farley, K. A. and D. F. Stockli (2002). (U-Th)/He dating of phosphates: Apatite, monazite, and xenotime. *Phosphates - Geochemical, Geobiological, and Materials Importance: Reviews in Mineralogy & Geochemistry*. Ed. by M. J. Kohn, J. Rakovan, and J. M. Hughes. 48. Mineralogical Society of America, pp. 559–577.

Farley, K. A., R. A. Wolf, and L. T. Silver (1996). The effects of long alpha-stopping distances on (U-Th)/He ages. *Geochimica et Cosmochimica Acta* 60 (21), pp. 4223–4229.

Farley, K. A., P. W. Reiners, and V. Nenow (1999). An apparatus for high-precision helium diffusion measurements from minerals. *Analytical Chemistry* 71 (10), pp. 2059–2061.

Faure, G. and T. Mensing (2005). *Isotopes: Principles and Applications*. Ed. by 3. Hoboken, New Jersey: John Wiley & Sons, INC.

Fechtig, H. and S. Kalbitzer (1966). The diffusion of argon in potassium-bearing solids. *Potassium Argon Dating*. Berlin Heidelberg: Springer, pp. 68–107.

Fernando, G. W. A. R., C. A. Hauzenberger, L. P. Baumgartner, and W. Hofmeister (2003). Modeling of retrograde diffusion zoning in garnet: evidence for slow cooling of granulites from the Highland Complex of Sri Lanka. *Mineralogy and Petrology* 78 (1-2), pp. 53–71.

Finch, R. J. and J. M. Hanchar (2002). Structure and chemistry of zircon and zircon-group minerals. *Zircon: Reviews in Mineralogy and Geochemistry*. Ed. by P. Hanchar, J M and Hoskin. 53. Chantilly, VA: Mineralogical Society of America, pp. 1–25.

Fletcher, I. R., N. J. McNaughton, J. A. Aleinikoff, B. Rasmussen, and S. L. Kamo (2004). Improved calibration procedures and new standards for U–Pb and Th–Pb dating of Phanerozoic xenotime by ion microprobe. *Chemical Geology* 209 (3-4), pp. 295–314.

Flowers, R. M. (2009). Exploiting radiation damage control on apatite (U-Th)/He dates in cratonic regions. *Earth and Planetary Science Letters* 277, pp. 148–155.

Flowers, R. M., S. A. Bowring, and P. W. Reiners (2006). Low long-term erosion rates and extreme continental stability documented by ancient (U-Th)/He dates. *Geology* 34 (11), pp. 925–928.

Flowers, R. M., R. A. Ketcham, D. L. Shuster, and K. A. Farley (2009). Apatite (U-Th)/He thermochronometry using a radiation damage accumulation and annealing model. *Geochimica et Cosmochimica Acta* 73 (8), pp. 2347–2365.

Förster, H. (1998). The chemical composition of REE-Y-Th-U-rich accessory minerals in peraluminous granites of the Erzgebirge-Fichtelgebirge region, Germany. Part II : Xenotime. *American Mineralogist* 83, pp. 1302–1315.

Fuchs, L. H. and E. Gebert (1958). X-ray studies of synthetic coffinite, thorite, and uranothorites. *American Mineralogist* 43, pp. 243–248.

Gallagher, K. (2012). Transdimensional inverse thermal history modeling for quantitative thermochronology. *Journal of Geophysical Research* 117 (B2), B02408.

Gautheron, C. and L. Tassan-Got (2010). A Monte Carlo approach to diffusion applied to noble gas/helium thermochronology. *Chemical Geology* 273, pp. 212–224.

Gautheron, C., L. Tassan-Got, J. Barbarand, and M. Pagel (2009). Effect of alpha-damage annealing on apatite (U–Th)/He thermochronology. *Chemical Geology* 266 (3-4), pp. 157–170.

Gehrels, G. (2014). Detrital Zircon U-Pb Geochronology Applied to Tectonics. *Annual Review of Earth and Planetary Sciences* 42 (1), pp. 127–149.

Gehrels, G. E., V. A. Valencia, and J. Ruiz (2008). Enhanced precision, accuracy, efficiency, and spatial resolution of U-Pb ages by laser ablation-multicollector-inductively coupled plasma-mass spectrometry. *Geochemistry, Geophysics, Geosystems* 9 (3).

Geisler, T., R. T. Pidgeon, W. van Bronswijk, and R. Kurtz (2002). Transport of uranium, thorium, and lead in metamict zircon under low-temperature hydrothermal conditions. *Chemical Geology* 191 (1-3), pp. 141–154.

Geisler, T., R. T. Pidgeon, W. van Bronswijk, and R. Pleysier (2001). Kinetics of thermal recovery and recrystallization of partially metamic zircon: A Raman spectroscopic study. *European Journal of Mineralogy* 13, pp. 1163–1176.

Giarola, M., A. Sanson, A. Rahman, G. Mariotto, M. Bettinelli, A. Speghini, and E. Cazzanelli (2011). Vibrational dynamics of YPO_4 and $ScPO_4$ single crystals: An integrated study by polarized Raman spectroscopy and first-principles calculations. *Physical Review B* 83 (22), pp. 1–8.

Ginster, U., P. W. Reiners, L. Nasdala, and C. C. N (2019). Annealing kinetics of radiation damage in zircon. *Geochimica et Cosmochimica Acta* 249, pp. 225–246.

Grand'Homme, A., E. Janots, V. Bosse, A. M. Seydoux-Guillaume, and R. A. Guedes (2016). Interpretation of U-Th-Pb in-situ ages of hydrothermal monazite-(Ce) and xenotime-(Y): Evidence from a large-scale regional study in clefts from the western alps. *Mineralogy and Petrology*, pp. 1–21.

Grechanovsky, A. E., N. N. Eremin, and V. S. Urusov (2013). Radiation resistance of $LaPO_4$ (monazite structure) and $YbPO_4$ (zircon structure) from data of computer simulation. *Physics of the Solid State* 55 (9), pp. 1929–1935.

Green, P. F., P. V. Crowhurst, I. R. Duddy, P. Japsen, and S. P. Holford (2006). Conflicting (U–Th)/He and fission track ages in apatite: Enhanced He retention, not anomalous annealing behaviour. *Earth and Planetary Science Letters* 250 (3-4), pp. 407–427.

Grove, M. and T. M. Harrison (1996). ^{40}Ar* diffusion in Fe-rich biotite. *American Mineralogist* 81 (7-8), pp. 940–951.

Guenthner, W. R., P. W. Reiners, P. G. DeCelles, and J. Kendall (2015). Sevier belt exhumation in central Utah constrained from complex zircon (U-Th)/He data sets: Radiation damage and He inheritance effects on partially reset detrital zircons. *Bulletin of the Geological Society of America* 127 (3-4), pp. 323–348.

Guenthner, W. R., P. W. Reiners, R. A. Ketcham, L. Nasdala, and G. Giester (2013). Helium diffusion in natural zircon: Radiation damage, anisotropy, and the interpretation of zircon (U-TH)/He thermochronology. *American Journal of Science* 313 (3), pp. 145–198.

Guenthner, W. R., P. W. Reiners, and Y. Tian (2014). Interpreting date-eU correlations in zircon (U-Th)/He datasets: A case study from the Longmen Shan, China. *Earth and Planetary Science Letters* 403, pp. 328–339.

Günther, D., R. Frischknecht, C. A. Heinrich, and H.-J. Kahlert (1997). Capabilities of an argon fluoride 193 nm excimer laser for laser ablation inductively coupled plasma mass spectometry microanalysis of geological materials. *J. Anal. At. Spectrom.* 12 (9), pp. 939–944.

Hanchar, J. M., R. J. Finch, P. W. O. Hoskin, E. B. Watson, D. J. Cherniak, and A. N. Mariano (2001). Rare earth elements in synthetic zircon. 1. Sythesis and rare earth element and phosphorus doping. *American Mineralogist* 86 (667-680), pp. 667–680.

Hanchar, J. M. and C. F. Miller (1993). Zircon zonation patterns as revealed by cathodoluminescence and backscattered electron images: Implications for interpretation of complex crustal histories. *Chemical Geology* 110 (1-3), pp. 1–13.

Hanchar, J. M. and R. L. Rudnick (1995). Revealing hidden structures: The application of cathodoluminescence and back-scattered electron imaging to dating zircons from lower crustal xenoliths. *Lithos* 36 (3-4), pp. 289–303.

Harrison, T. M. (1981). Diffusion of ^{40}Ar in Hornblende. *Contributions to Mineralogy and Petrology* 78 (3), pp. 324–331.

Harrison, T. M., E. J. Catlos, and J. .-.-M. Montel (2002). U-Th-Pb dating of phosphate minerals. *Phosphates - Geochemical, Geobiological, and Materials Importance: Reviews in Mineralogy & Geochemistry*. Ed. by M. J. Kohn, J. Rakovan, and J. M. Hughes. 48. Chantilly, VA: Mineralogical Society of America, pp. 524–558.

Hawkins, D. P. and S. A. Bowring (1997). U-Pb systematics of monazite and xenotime: case studies from the Paleoproterozoic of the Grand Canyon, Arizona. *Contributions to Mineralogy and Petrology* 127 (1-2), pp. 87–103.

Hazen, R. M. and L. M. Finger (1979). Crystal structure and compressibility of zircon at high pressure. *American Mineralogist* 64, pp. 196–201.

Hetherington, C. J., M. J. Jercinovic, M. L. Williams, and K. Mahan (2008). Understanding geologic processes with xenotime: Composition, chronology, and a protocol for electron probe microanalysis. *Chemical Geology* 254 (3-4), pp. 133–147.

Hildebrand, P. R. (1998). Tectonic significance of 24 Ma crustal melting in the eastern Hindu Kush, Pakistan. *Geology* 26 (10), pp. 871–874.

Hildebrand, P. R., S. R. Noble, M. P. Searle, D. J. Waters, and R. R. Parrish (2001). Old origin for an active mountain range: Geology and geochronology of the Eastern Hindu Kush, Pakistan. *Bulletin of the Geological Society of America* 113 (5), pp. 625–639.

Hodapp, T. W. and P. R. Fleming (1998). Modeling topology formation during laser ablation. *Journal of Applied Physics* 84 (1), pp. 577–583.

Hodges, K. V. (2014). Thermochronology in Orogenic Systems. *Treatise on Geochemistry*. 2nd ed. 4. Elsevier Ltd., pp. 281–308. URL: http://dx.doi.org/10.1016/B978-0-08-095975-7.00308-9.

Holland, H. D. and D. Gottfried (1955). The effect of nuclear radiation on the structure of zircon. *Acta Crystallographica* 8, pp. 291–300.

Holmes, A. (1913). *The Age of the Earth*. London: Harper & Brothers.

Horn, I., R. L. Rudnick, and W. F. McDonough (2000). Precise elemental and isotope ratio determination by simultaneous solution nebulization and laser ablation-ICP-MS: application to U–Pb geochronology. *Chemical Geology* 164 (3-4), pp. 281–301.

Horne, A. M., M. C. van Soest, K. V. Hodges, A. Tripathy-Lang, and J. K. Hourigan (2016). Integrated single crystal laser ablation U/Pb and (U-Th)/He dating of detrital accessory minerals - Proof-of-concept studies of titanites and zircons from the Fish Canyon tuff. *Geochimica et Cosmochimica Acta* 178, pp. 106–123.

Hourigan, J. K., P. W. Reiners, and M. T. Brandon (2005). U-Th zonation-dependent alpha-ejection in (U-Th)/He chronometry. *Geochimica et Cosmochimica Acta* 69 (13), pp. 3349–3365.

Hurley, P. M. (1952). Alpha ionization as a cause of low helium ratios. *Eos, Transactions American Geophysical Union* 33 (2), pp. 174–183.

Hurley, P. M. and H. W. Fairbairn (1953). Radiation damage in zircons: A possible age method. *Bulletin of the Geological Society of America* 64 (June), pp. 659–674.

Hurley, P. M., E. S. J. Larsen, and D. Gottfried (1956). Comparison of radiogenic helium and lead in zircon. *Geochimica et Cosmochimica Acta* 9, pp. 98–102.

Idleman, B. D., P. K. Zeitler, and K. T. McDannell (2018). Characterization of helium release from apatite by continuous ramped heating. *Chemical Geology* 476, pp. 223–232.

J-A, W., S. P. Kelley, R. A. Brooker, M. R. Carroll, I. M. Villa, and M. R. Lee (1999). Direct measurement of Ar diffusion profiles in a gem-quality Madagascar K-feldspar using the ultra-violet laser ablation microprobe (UVLAMP). *Earth and Planetary Science Letters* 170, pp. 141–153.

Jackson, S. E., N. J. Pearson, W. L. Griffin, and E. A. Belousova (2004). The application of laser ablation-inductively coupled plasma-mass spectrometry to in situ U–Pb zircon geochronology. *Chemical Geology* 211 (1-2), pp. 47–69.

Jarosewich, E. and L. A. Boatner (1991). Rare-Earth element reference samples for electron microprobe analysis. *Geostandards Newsletter* 15 (2), pp. 397–399.

Johnson, J. E., R. M. Flowers, G. B. Baird, and K. H. Mahan (2017). “Inverted" zircon and apatite (U-Th)/He dates from the Front Range, Colorado: High-damage zircon as a low-temperature (<50°C) thermochronometer. *Earth and Planetary Science Letters* 466, pp. 80–90.

Jonckheere, R., D. Heinz, B. R. Hacker, D. Rafaja, and L. Ratschbacher (2019). A borehole investigation of zircon radiation damage annealing. *Terra Nova* In press.

Kelley, S. A. and C. E. Chapin (2004). Denudation history and internal structure of the Front Range and Wet Mountains, Colorado, based on apatite fission track thermochronology. *New Mexico Bureau of Geology and Mineral Resources* Bulletin 160, pp. 41–78.

Ketcham, R. A. (2005). Forward and Inverse Modeling of Low-Temperature Thermochronometry Data. *Low Temperature Thermochronology- Techniques, Interpretations, and Applications: Review in Mineralogy & Geochemistry*. Ed. by P. W. Reiners and T. A. Ehlers. 58 (1). Chantilly, VA: Mineralogical Society of America, pp. 275–314.

Ketcham, R. A., W. R. Guenthner, and P. W. Reiners (2013). Geometric analysis of radiation damage connectivity in zircon, and its implications for helium diffusion. *American Mineralogist* 98 (2-3), pp. 350–360.

Ketcham, R. A., P. van der Beek, J. Barbarand, M. Bernet, and C. Gautheron (2018). Reproducibility of thermal history reconstruction From apatite fission-track and (U-Th)/He data. *Geochemistry, Geophysics, Geosystems* 19 (8), pp. 2411–2436.

Kluth, C. F. and P. J. Coney (1981). Plate tectonics of the Ancestral Rocky Mountains. *Geology* 9 (1), pp. 10–15.

Laslett, G. M., P. F. Green, I. R. Duddy, and A. J. W. Gleadow (1987). Thermal annealing of fission tracks in apatite 2. A quantitative analysis. *Chemical Geology: Isotope Geoscience section* 65 (1), pp. 1–13.

Lehnert, R. J. (2000). Beyond Imagination - Image Formation Based on Raman Spectroscopy. *G.I.T. Laboratory Journal* 2, pp. 6–9.

Lenz, C., L. Nasdala, D. Talla, C. Hauzenberger, R. Seitz, and U. Kolitsch (2015). Laser-induced REE^{3+} photoluminescence of selected accessory minerals - An “advantageous artefact" in Raman spectroscopy. *Chemical Geology* 415, pp. 1–16.

Leya, I., H. Busemann, H. Baur, R. Wieler, M. Gloris, S. Neumann, R. Michel, F. Sudbrock, and U. Herpers (1998). Cross sections for the proton-induced production of He and Ne isotopes from magnesium, aluminum, and silicon. *NIM B* 145, pp. 449–458.

Liu, Z., F. Wu, C. Guo, Z. Zhao, J. Yang, and J. Sun (2011). In situ U-Pb dating of xenotime by laser ablation (LA)-ICP-MS. *Chinese Science Bulletin* 56 (27), pp. 2948–2956.

Lovera, O. M., M. Grove, T. M. Harrison, and K. I. Mahon (1997). Systematic analysis of K-feldspar $^{40}Ar/^{39}Ar$ step heating results: I. Significance of activation energy determinations. *Geochimica et Cosmochimica Acta* 61 (15), pp. 3171–3192.

Lovera, O. M. and F. M. Richter (1989). The $^{40}Ar/^{39}Ar$ thermochronometry for slowly cooled samples having a distribution of diffusion domain sizes. *Journal of Geophysical Research* 94 (B12), pp. 17917–17935.

Ludwig, K. R. (2003). Mathematical–statistical treatment of data and errors for $^{230}Th/U$ Geochronology. *Uranium-Series Geochemistry: Reviews in Mineralogy & Geochemistry*. Ed. by B. Bourdon, G. M. Henderson, C. C. Lundstrom, and S. P. Turner. 52. Chantilly, VA: Mineralogical Society of America, pp. 631–656.

Marillo-Sialer, E., J. Woodhead, J. M. Hanchar, S. M. Reddy, A. Greig, J. Hergt, and B. Kohn (2016). An investigation of the laser-induced zircon 'matrix effect'. *Chemical Geology* 438 (C), pp. 11–24.

Marillo-Sialer, E., J. Woodhead, J. Hergt, A. Greig, M. Guillong, A. Gleadow, N. Evans, and C. Paton (2014). The zircon 'matrix effect': evidence for an ablation rate control on the accuracy of U–Pb age determinations by LA-ICP-MS. *J. Anal. At. Spectrom.* 29 (6), pp. 981–989.

McLaren, A. C., J. D. F. Gerald, and I. S. Williams (1994). The microstructure of zircon and its influence on the age determination from Pb/U isotopic ratios measured by ion microprobe. *Geochimica et Cosmochimica Acta* 58 (2), pp. 993–1005.

McLelland, J., M. Hamilton, B. Selleck, J. McLelland, D. Walker, and S. Orrell (2001). Zircon U-Pb geochronology of the Ottawan Orogeny, Adirondack Highlands, New York: Regional and tectonic implications. *Precambrian Research* 109, pp. 39–72.

Meesters, A. G. C. A. and T. J. Dunai (2002). Solving the production–diffusion equation for finite diffusion domains of various shapes. *Chemical Geology* 186 (3-4), pp. 333–344.

Meldrum, A., L. A. Boatner, and R. C. Ewing (2000). A comparison of radiation effects in crystalline ABO4-type phosphates and silicates. *Mineralogical Magazine* 64 (2), pp. 185–194.

Meldrum, A., L. A. Boatner, W. J. Weber, and R. C. Ewing (1998). Radiation damage in zircon and monazite. *Geochimica et Cosmochimica Acta* 62 (14), pp. 2509–2520.

Meldrum, A., L. Boatner, and R. Ewing (1997). Displacive radiation effects in the monazite- and zircon-structure orthophosphates. *Physical Review B* 56 (21), pp. 13805–13814.

Mezger, K. and E. J. Krogstad (1997). Interpretation of discordant U-Pb zircon ages: An evaluation. *Journal of Metamorphic Geology* 15 (1), pp. 127–140.

Monteleone, B. D., M. C. van Soest, K. V. Hodges, G. M. Moore, J. W. Boyce, and R. L. Hervig (2009). Assessment of Alternative [U] and [Th] Zircon Standards for SIMS. *American Geophysical Union Fall Meeting, San Francisco, CA, USA*.

Murakami, T., B. C. Chakoumakos, R. C. Ewing, G. R. Lumpkin, and W. J. Weber (1991). Alpha-decay event damage in zircon. *American Mineralogist* 76, pp. 1510–1532.

Nasdala, L., J. Gotze, J. M. Hanchar, M. Gaft, and M. R. Krbetschek (2004). Luminescence techniques in Earth Sciences. *EMU Notes in Mineralogy* 6, pp. 43–91.

Nasdala, L., M. Wenzel, G. Vavra, G. Irmer, T. Wenzel, and B. Kober (2001). Metamictisation of natural zircon: Accumulation versus thermal annealing of radioactivity-induced damage. *Contributions to Mineralogy and Petrology* 141 (2), pp. 125–144.

Nasdala, L., J. M. Hanchar, A. Kronz, and M. J. Whitehouse (2005). Long-term stability of alpha particle damage in natural zircon. *Chemical Geology* 220 (1-2), pp. 83–103.

Nasdala, L., G. Irmer, and D. Wolf (1995). The degree of metamictization in zircon: A Raman spectroscopic study. *European Journal of Mineralogy* 7 (3), pp. 471–478.

Nasdala, L., C. L. Lengauer, J. M. Hanchar, A. Kronz, R. Wirth, P. Blanc, A. K. Kennedy, and A.-M. Seydoux-Guillaume (2002). Annealing radiation damage and the recovery of cathodoluminescence. *Chemical Geology* 191 (1-3), pp. 121–140.

Nasdala, L., M. Zhang, U. Kempe, G. Panczer, M. Gaft, M. Andrut, and M. Plotze (2003). Spectroscopic methods applied to zircon. *Zircon: Reviews in Mineralogy & Geochemistry*. 53 (1). Chantilly, VA: Mineralogical Society of America, pp. 427–467.

Ni, Y., J. M. Hughes, and A. N. Mariano (1995). Crystal chemistry of the monazite and xenotime structures. *American Mineralogist* 80, pp. 21–26.

Olson, J. C., R. F. Marvin, R. L. Parker, and H. H. Mehnert (1977). Age and tectonic setting of lower Paleozoic alkalic and mafic rocks, carbonatites, and thorium veins in south-central Colorado. *Jour. Research U.S. Geol. Survey* 5 (6), pp. 673–687.

Orme, D. A., W. R. Guenthner, A. K. Laskowski, and P. W. Reiners (2016). Long-term tectonothermal history of Laramide basement from zircon–He age-eU correlations. *Earth and Planetary Science Letters* 453, pp. 119–130.

Ouchani, S., J. C. Dran, and J. Chaumont (1998). Exfoliation and diffusion following helium ion implantation in fluorapatite: implications for radiochronology and radioactive waste disposal. *Applied Geochemistry* 13 (6), pp. 707–714.

Palenik, C. S., L. Nasdala, and R. C. Ewing (2003). Radiation damage in zircon. *American Mineralogist* 88, pp. 770–781.

Parker, R. L. and F. A. Hildebrande (1963). Preliminary report on alkalic intrusive rocks in the northern Wet Mountains, Colorado. *Geol Survey Prof Paper*, E8–E10.

Paton, C., J. D. Woodhead, J. C. Hellstrom, J. M. Hergt, A. Greig, and R. Maas (2010). Improved laser ablation U-Pb zircon geochronology through robust downhole fractionation correction. *Geochemistry, Geophysics, Geosystems* 11 (3).

Paton, C., J. Hellstrom, B. Paul, J. Woodhead, and J. Hergt (2011). Iolite: Freeware for the visualisation and processing of mass spectrometric data. *J. Anal. At. Spectrom.* 26 (12), pp. 2508–11.

Pearson, R. K. (2001). *Exploring Data in Engineering, the Sciences, and Medicine*. Oxford Univ. Press.

Peterman, E. M., J. K. Hourigan, and M. Grove (2014). Experimental and geologic evaluation of monazite (U–Th)/He thermochronometry: Catnip Sill, Catalina Core Complex, Tucson, AZ. *Earth and Planetary Science Letters* 403 (C), pp. 48–55.

Petrus, J. A. and B. S. Kamber (2012). VizualAge: A Novel Approach to Laser Ablation ICP-MS U-Pb Geochronology Data Reduction. *Geostandards and Geoanalytical Research* 36 (3), pp. 247–270.

Powell, J., D. Schneider, D. Stockli, and K. Fallas (2016). Zircon (U-Th)/He thermochronology of Neoproterozoic strata from the Mackenzie Mountains, Canada: Implications for the Phanerozoic exhumation and deformation history of the northern Canadian Cordillera. *Tectonics* 35 (3), pp. 663–689.

Reich, M., R. C. Ewing, T. A. Ehlers, and U. Becker (2007). Low-temperature anisotropic diffusion of helium in zircon: Implications for zircon (U-Th)/He thermochronometry. *Geochimica et Cosmochimica Acta* 71 (12), pp. 3119–3130.

Reiners, P. W. and M. T. Brandon (2006). Using thermochronology to understand orogenic erosion. *Annual Review of Earth and Planetary Sciences* 34 (1), pp. 419–466.

Reiners, P. W., R. W. Carlson, P. R. Renne, K. M. Cooper, D. E. Granger, N. M. McLean, and B. Schoene (2017). The (U-Th)/He System. *Geochronology and Thermochronology*. John Wiley & Sons Ltd. Chap. 11, pp. 291–363.

Reiners, P. W. and K. A. Farley (1999). Helium diffusion and (U-Th)/He thermochronometry of titanite. *Mineralogical Magazine* 62A (2), pp. 1249–1250.

Reiners, P. W., K. A. Farley, and H. J. Hickes (2002). He diffusion and (U-Th)/He thermochronometry of zircon: Initial results from Fish Canyon Tuff and Gold Butte. *Tectonophysics* 349 (1-4), pp. 297–308.

Reiners, P. W., T. L. Spell, S. Nicolescu, and K. A. Zanetti (2004). Zircon (U-Th)/He thermochronometry: He diffusion and comparisons with ^{40}Ar/^{39}Ar dating. *Geochimica et Cosmochimica Acta* 68 (8), pp. 1857–1887.

Renne, P. R., C. C. Swisher, A. L. Deino, D. B. Karner, T. L. Owens, and D. J. DePaolo (1998). Intercalibration of standards, absolute ages and uncertainties in ^{40}Ar/^{39}Ar dating. *Chemical Geology* 145 (1-2), pp. 117–152.

Robinson, K., G. G V, and P. H. Ribbe (1971). The structure of zircon: A comparison with garnet. *American Mineralogist* 56, pp. 782–790.

Ruschel, K., L. Nasdala, A. Kronz, J. M. Hanchar, D. M. Többens, R. Škoda, F. Finger, and A. Möller (2012). A Raman spectroscopic study on the structural disorder of monazite-(Ce). *Mineralogy and Petrology* 105 (1-2), pp. 41–55.

Rutherford, E. (1906). *Radioactive Transformations*. New York: Charles Scribner's Sons.

Saadoune, I., J. A. Purton, and N. H. de Leeuw (2009). He incorporation and diffusion pathways in pure and defective zircon $ZrSiO_4$: A density functional theory study. *Chemical Geology* 258 (3-4), pp. 182–196.

Saadoune, I. and N. H. de Leeuw (2009). A computer simulation study of the accommodation and diffusion of He in uranium- and plutonium-doped zircon ($ZrSiO_4$). *Geochimica et Cosmochimica Acta* 73 (13), pp. 3880–3893.

Samson, S. D. and J. Alexander E C (1987). Calibration of the interlaboratory ^{40}Ar-^{39}Ar dating standard, MMhb-1. *Chemical Geology: Isotope Geoscience section* 66 (1-2), pp. 27–34.

Schoene, B. and S. A. Bowring (2006). U-Pb systematics of the McClure Mountain syenite: Thermochronological constraints on the age of the ^{40}Ar/^{39}Ar standard MMhb. *Contributions to Mineralogy and Petrology* 151 (5), pp. 615–630.

Schoene, B. (2014). U–Th–Pb Geochronology. *Treatise on Geochemistry*. Ed. by H. D. Holland and K. K. Turekian. Elsevier Ltd., pp. 341–378.

Shannon, R. D. (1976). Revised effective ionic radii and systematic studies of interatomic distances in halides and chalcogenides. *Acta Crystallographica Section A* 32 (5), pp. 751–767.

Shuster, D. L. and K. A. Farley (2005). ^{4}He/^{3}He thermochronometry: Theory, practice, and potential complications. *Low Temperature Thermochronology: Techniques, Interpretations, and Applications: Reviews in Mineralogy and Geochemistry*. 58, pp. 181–203.

Shuster, D. L., R. M. Flowers, and K. A. Farley (2006). The influence of natural radiation damage on helium diffusion kinetics in apatite. *Earth and Planetary Science Letters* 249 (3-4), pp. 148–161.

Shuster, D. L. and K. A. Farley (2003). ^{4}He/^{3}He thermochronometry. *Earth and Planetary Science Letters* 217 (1-2), pp. 1–17.

Shuster, D. L. and K. A. Farley (2009). The influence of artificial radiation damage and thermal annealing on helium diffusion kinetics in apatite. *Geochimica et Cosmochimica Acta* 73 (1), pp. 183–196.

Shuster, D. L., K. A. Farley, J. M. Sisterson, and D. S. Burnett (2003). Quantifying the diffusion kinetics and spatial distributions of radiogenic ^{4}He in minerals containing proton-induced ^{3}He. *Earth and Planetary Science Letters* 217 (1-2), pp. 19–32.

Sláma, J. et al. (2008). Plešovice zircon - A new natural reference material for U-Pb and Hf isotopic microanalysis. *Chemical Geology* 249 (1-2), pp. 1–35.

Sliwinski, J. T., N. Kueter, F. Marxer, P. Ulmer, M. Guillong, and O. Bachmann (2018). Controls on lithium concentration and diffusion in zircon. *Chemical Geology* 501, pp. 1–11.

Sliwinski, T. J., M. Guillong, C. Liebske, I. Dunkl, A. von Quadt, and O. Bachmann (2017). Improved accuracy of LA-ICP-MS U-Pb ages of Cenozoic zircons by alpha dose correction. *Chemical Geology* 472, pp. 8–21.

Solari, L. A., C. Ortega-Obregón, and J. P. Bernal (2015). U–Pb zircon geochronology by LAICPMS combined with thermal annealing: Achievements in precision and accuracy on dating standard and unknown samples. *Chemical Geology* 414, pp. 109–123.

Spear, F. S. and J. M. Pyle (2002). Apatite, monazite, and xenotime in metamorphic rocks. *Phosphates - Geochemical, Geobiological, and Materials Importance: Reviews in Mineralogy & Geochemistry*. Ed. by M. J. Kohn, J. Rakovan, and J. M. Hughes. 48. Chantilly, VA: Mineralogical Society of America, pp. 293–335.

Speer, J. A. and B. J. Cooper (1982). Crystal structure of synthetic hafnon, $HfSiO_4$, comparison with zircon and the actinide orthosilicates. *American Mineralogist* 67, pp. 804–808.

Spell, T. L. and I. McDougall (2003). Characterization and calibration of ^{40}Ar/^{39}Ar dating standards. *Chemical Geology* 198 (3-4), pp. 189–211.

Stanley, J. R. and R. M. Flowers (2016). Dating kimberlite emplacement with zircon and perovskite (U-Th)/He geochronology. *Geochemistry Geophysics Geosystems* 17, pp. 4517–4533. arXiv: arXiv:1605.08479.

Steely, A. N., J. K. Hourigan, and E. Juel (2014). Discrete multi-pulse laser ablation depth profiling with a single-collector ICP-MS: Sub-micron U–Pb geochronology of zircon and the effect of radiation damage on depth-dependent fractionation. *Chemical Geology* 372, pp. 92–108.

Stockli, D. F., K. A. Farley, and T. A. Dumitru (2000). Calibration of the apatite (U-Th)/He thermochronometer on an exhumed fault block, White Mountains, California. *Geology* 28 (11), pp. 983–986.

Strutt, R. J. (1905). On the radio-active minerals. *Proceedings of the Royal Society of London* 76 (508), pp. 88–101.

Strutt, R. J. (1908). On the accumulation of helium in geologic time. *Proceedings of the Royal Society of London* 81, pp. 272–277.

Strutt, R. J. (1909). The leakage of helium from radio-active minerals. *Proceedings of the Royal Society of London* 82, pp. 166–169.

Švecová, E., R. Čopjaková, Z. Losos, R. Škoda, L. Nasdala, and J. Cícha (2016). Multi-stage evolution of xenotime-(Y) from Písek pegmatites, Czech Republic: An electron probe micro-analysis and Raman spectroscopy study. *Mineralogy and Petrology* 110 (6), pp. 747–765.

Syme, R. W. G., D. J. Lockwood, and H. J. Kerr (1977). Raman spectrum of synthetic zircon ($ZrSiO_4$) and thorite ($ThSiO_4$). *Journal of Physics C: Solid State Physics* 10, pp. 1335–1348.

Trail, D., J. B. Thomas, and E. B. Watson (2010). The incorporation of hydroxyl into zircon. *American Mineralogist* 96, pp. 60–67.

Tripathy-Lang, A., M. Fox, and D. L. Shuster (2015). Zircon $^4He/^3He$ Thermochronometry. *Geochimica et Cosmochimica Acta* 166, pp. 1–14.

Tripathy-Lang, A., K. V. Hodges, B. D. Monteleone, and M. C. van Soest (2013). Laser (U-Th)/He thermochronology of detrital zircons as a tool for studying surface processes in modern catchments. *Journal of Geophysical Research: Earth Surface* 118 (3), pp. 1333–1341.

Valley, P. M., J. M. Hanchar, and M. J. Whitehouse (2011). New insights on the evolution of the Lyon Mountain Granite and associated Kiruna-type magnetite-apatite deposits, Adirondack Mountains, New York State. *Geosphere* 7 (2), pp. 357–389.

Vallini, D A and Rasmussen, B and Krapež, B and Fletcher, I R and McNaughton, N J (2005). Microtextures, geochemistry and geochronology of authigenic xenotime: constraining the cementation history of a Palaeoproterozoic metasedimentary sequence. *Sedimentology* 52 (1), pp. 101–122.

Vallini, D and Rasmussen, B and Krapež, B and Fletcher, I R and McNaughton, N J (2002). Obtaining diagenetic ages from metamorphosed sedimentary rocks: U-Pb dating of unusually coarse xenotime cement in phosphatic sandstone. *Geology* 30 (12), pp. 1083–1086.

van Soest, M. C., B. D. Monteleone, K. V. Hodges, and J. W. Boyce (2011). Laser depth profiling studies of helium diffusion in Durango fluorapatite. *Geochimica et Cosmochimica Acta* 75 (9), pp. 2409–2419.

Vermeesch, P., S. C. Sherlock, N. M. W. Roberts, and A. Carter (2012). A simple method for in-situ U-Th-He dating. *Geochimica et Cosmochimica Acta* 79, pp. 140–147.

Weber, W. J. (1990). Radiation-induced defects and amorphization in zircon. *Journal of Materials Research* 5 (11), pp. 2687–2697.

Weber, W. (1993). Alpha-decay-induced amorphization in complex silicate structures. *J. Am. Ceram. Soc.* 76 (7), pp. 1729–1738.

Weisberg, W. R., J. R. Metcalf, and R. M. Flowers (2014). Thermochronology of the McClure Mountain syenite; characterization of new He thermochronometers and constraints on the cooling history of the Wet Mountains, Colorado. *Abstracts with Programs - Geological Society of America* 46 (6), p. 512.

Weisberg, W. R., J. R. Metcalf, and R. M. Flowers (2018a). Distinguishing slow cooling versus multiphase cooling and heating in zircon and apatite (U-Th)/He datasets: The case of the McClure Mountain syenite standard. *Chemical Geology* 485, pp. 90–99.

Weisberg, W. R., J. R. Metcalf, and R. M. Flowers (2018b). Response to comment on "Distinguishing slow cooling versus multiphase cooling and heating in zircon and apatite (U-Th)/He datasets: The case of the McClure Mountain syenite standard". *Chemical Geology* 498, pp. 153–156.

Wendt, I. and C. Carl (1991). The statistical distribution of the mean squared weighted deviation. *Chemical Geology* 86, pp. 275–285.

Wiedenbeck, M., P. Allé, F. Corfu, W. L. Griffin, M. Meier, F. Oberli, A. Von Quadt, J. C. Roddick, and W. Spiegel (1995). Three natural zircon standards for U-Th-Pb, Lu-Hf, trace element and REE analyses. *Geostandards Newsletter* 19 (1), pp. 1–23.

Wieler, R. (2002). Cosmic-ray-produced noble gases in meteorites. *Noble Gases in Geochemistry and Cosmochemistry: Reviews in Mineralogy and Geochemistry*. Ed. by D. Porcelli, C. J. Ballentine, and R. Wieler. Washington, DC: Mineralogical Society of America, pp. 125–170.

Willett, C. D., M. Fox, and D. L. Shuster (2017). A helium-based model for the effects of radiation damage annealing on helium diffusion kinetics in apatite. *Earth and Planetary Science Letters* 477, pp. 195–204.

Wolf, R. A., K. A. Farley, and L. T. Silver (1996). Helium diffusion and low-temperature thermochronometry of apatite. *Geochimica et Cosmochimica Acta* 60 (21), pp. 4231–4240.

Wolf, R. A., K. A. Farley, and L. T. Silver (1997). Assessment of (U-Th)/He thermochronometry: The low-temperature history of the San Jacinto mountains, California. *Geology* 25 (1), pp. 65–68.

Woodhead, J. D., J. Hellstrom, J. M. Hergt, A. Greig, and R. Maas (2007). Isotopic and elemental imaging of geological materials by laser ablation inductively coupled plasma-mass spectrometry. *Geostandards and Geoanalytical Research* 31 (4), pp. 331–343.

Yamada, R., M. Murakami, and T. Tagami (2007). Statistical modelling of annealing kinetics of fission tracks in zircon; Reassessment of laboratory experiments. *Chemical Geology* 236 (1-2), pp. 75–91.

York, D., N. M. Evensen, M. L. Martinez, and J. De Basabe Delgado (2004). Unified equations for the slope, intercept, and standard errors of the best straight line. *American Journal of Physics* 72 (3), pp. 367–375.

Zeitler, P. K., A. L. Herczeg, I. McDougall, and M. Honda (1987). U-Th-He dating of apatite: A potential thermochronometer. *Geochimica et Cosmochimica Acta* 51, pp. 2865–2868.

Zhang M S, E. K. H., G. C. Capitani, H. Leroux, A. M. Clark, J. Schluter, and R. C. Ewing (2000). Annealing of α-decay damage in zircon: A Raman spectroscopic study. *Journal of Physics: Condensed Matter* 12, pp. 3131–3148.